8.14 Course Reader

(Dated: February 2, 2010)

This is the Course Reader for 8.14; MIT's advanced undergraduate experimental physics course. Each of the experiments, and the procedures for running them, are described in detail in this reader. Notes on laboratory safety, administrative guidelines and templates for written summaries, oral presentations and curve fitting are also detailed. This volume will be your constant companion in the laboratory. These materials are also available online at http://web.mit.edu/8.13.

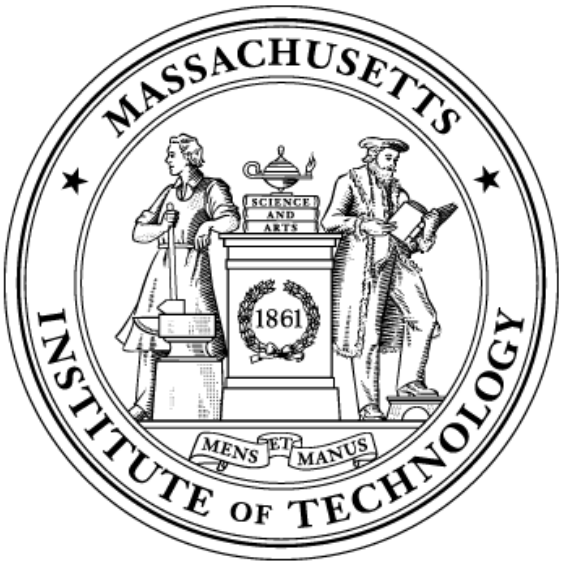

Contents

Policies, Procedures and Safety Information

MIT Department of Physics
(Dated: February 2, 2010)

1. Goals

The purposes of Junior Lab are to give you hands-on experience with some of the experimental bases of modern physics and, in the process, to deepen your understanding of the relations between experiment and theory, mostly in atomic and nuclear physics. You will do experiments on phenomena whose discoveries led to major advances in physics. The data you obtain will have the inevitable systematic and random errors that obscure the relations between the macroscopic observables of our sensory experience and the ideal laws that govern the submicroscopic world of atoms and nuclei. You will be challenged to learn how each of the experimental setups works, to master its manipulation so that you obtain the best possible data, and then to interpret the data in light of theory and a quantitative assessment of the errors. We think you find satisfaction in observing, measuring and understanding phenomena many of which would have won you the Nobel Prize if you had discovered them.

2. Organization

The registrar has preassigned you to one of the sections listed below. If you cannot make the assigned time, you should show up at the section of your choice to see if you can be accommodated (equipment limitations cap each section's enrollment $\leq$ 10 students). Please email spatrick@mit.edu ahead of time so the staff can be prepared for you.

Each section is run independently by one faculty member with the assistance of a graduate teaching assistant. Technical assistance is provided by Dr. Sean Robinson and Regina Yopak. **Outside your regularly scheduled sessions, the labs are open on Fridays from 10:00 am to 4:00 pm. A sign-up sheet for Friday reservations (3-hour block maximum please) is on the bulletin board in 4-361.**

TABLE I: Junior Lab Section Instructors - Spring 2010

Section	Instructor
Monday-Wednesday 2-5	Professor Nergis Mavalvala
Tuesday-Thursday 9-12	Professor Gunther Roland
Tuesday-Thursday 2-5	Professor Gunther Roland

You are expected to work in pairs, sharing as evenly as possible in the measurements, the analysis and the interpretation of the data. The best choice for lab partner may be someone who lives nearby and has a schedule that matches yours so you can get together outside of class to analyze and interpret your results. Most students find they require at least the full 18 hours per week credited to Junior Lab to do the work of the course.

2.0.1. Spring Term: 8.14

Students enrolling in 8.14 are expected to have recently completed 8.13 so as to be prepared to immediately begin conducting investigations. If you have not taken 8.13, please see Professor Roland. The first class period is dedicated to selecting partners, choosing experimental lines and brief introductory notes by section instructors. Students will select 4 different experiments, each of which will require 5 separate lab sessions. The experiments from which you may choose include:

1. The Zeeman Effect
2. Optical Pumping
3. Pulsed NMR
4. Mössbauer Spectroscopy (2 setups available)
5. Superconductivity
6. Doppler-Free Spectroscopy
7. Quantum Information Processing (requires *Pulsed NMR* as a pre-requisite)
8. 21-cm Radio Astrophysics

Note that the additional 5th day (beyond what you had in 8.13) raises the level of expectations regarding the completion of "challenging" aspects of the labguides and an expectation to exceed the standard material. There exist 'extra' sessions at the end of the term in which students can acquire additional data or repeat selected portions of an experiment.

3. Ethics in Science and Science Education

When you read the report of a physics experiment in a reputable journal you can generally assume it represents an honest effort by the authors to describe exactly what they observed. You may doubt the interpretation or the theory they cite to explain the results. But at least you trust that if you repeat the manipulations as described, you will get essentially the same experimental results.

Nature is the ultimate enforcer of truth in science. If subsequent work proves a published measurement is wrong by substantially more than the estimated error limits, a reputation shrinks. If fraud is discovered, a career is ruined. So most professional scientists are very careful about the records they maintain (see the Junior Lab notebook requirements in the next section of the reader) and the results they publish.

Junior Lab is designed to provide pre-professional training in the art and science of experimental physics. What you record in your lab book and report in your written and oral presentations must be exactly what you have observed including **date, time and who did it.**

Sometimes you'll get things wrong because of an error in manipulation, equipment malfunction, misunderstanding, or a miscalculation. Simply cross out errors using a diagonal line in your notebook and start again. The instructor's job is to help you figure out what went wrong so you can do better next time. If circumstances in an experiment are such that you cannot get your own data (e.g. broken equipment, bad weather), you may use somebody else's provided you acknowledge it.

Fabrication or falsification of data, using the results of another person's work without acknowledgement, or copying from "the files" are intellectual crimes as serious as plagiarism, and possible causes for dismissal from the Institute.

The precaution about the acknowledgement of other people's data also applies to acknowledging other people's rhetoric. The appropriate way to incorporate an idea which you have learned from a textbook or other reference is to study the point until you understand it and then put the text aside and state the idea in your own words.

One often sees, in a scientific journal, phrases such as "Following Albert Einstein ..." This means that the author is following the ideas or logic of Einstein not his exact words. If you quote material, it is not sufficient just to include it in the list of references at the end of your paper.

> The quote should be indented on both sides or enclosed in quotes, and attribution must be given immediately in the form of a reference note.[1]

Importing text from a published work, web sites, other student papers, or from the labguide without proper attribution is a serious breach of ethics and will be dealt with by the Committee of Academic Discipline.

Most Junior Lab experiments are concerned with data comparison measurements of well known fundamental constants such as h, e, k, e/m, G, or significant physical quantities such as the mean life of the muon or the cross section of an electron for scattering a photon. The purpose of these experiments is to give you hands-on experience with the manipulation of atomic and nuclear phenomena, a sense of the reality of the concepts and theories you have studied in books and lectures, and the beginning of professional skill in obtaining and recognizing reliable data and extracting meaningful results from them.

There is nothing wrong with "peeking" in the CRC Handbook or any of the many relevant texts to see what your experiment should have yielded. **In fact, in your conclusions, you will compare your values with the established ones — as you would in any of your later scientific publications.**

If the established value is outside your error range, try to find out what went wrong, fix it, and try again. If the established value is in your error range, don't rest easy, but do whatever may be necessary to prove it isn't an accident. **Repetition is the essential key to attaining confidence in a result, whether of a single measurement or an entire experiment!** But whatever the outcome of an experiment is, you must tell exactly what you observed or measured when you present your oral or written report, regardless of how "bad" the results may appear to be.

4. Lab Attendance and Safety

You are required to attend your assigned lab session for the full three hour period. Any exception must be approved by the Professor in charge. The laboratories will be open Monday-Thursday from 9 to 5 and Friday from 10-4 (except Institute holidays) with staff help available to teach physics and maintain equipment. At all other times the laboratories must be kept locked to prevent theft. Junior Lab students may occasionally be permitted access to the lab outside of the normal hours, but only after consulting with their TA or faculty member. **It is each student's responsibility to maintain security by making sure the doors are kept locked at all times outside of the regularly scheduled sessions.** Also, if high voltages are involved, a partner or instructor must be in reach.

4.1. Required Texts

1. **Experimental Lab Guides** Available for download from the Junior Lab website.

2. **Data Reduction and Error Analysis for the Physical Sciences: 3rd Edition, by P.R. Bevington and D.K. Robinson (McGraw-Hill-2003)**

[1] J. Brown: Personal communication. Footnotes may be placed either at the bottom of the page where referenced or at the end among the bibliography.

The latter text contains a comprehensive treatment of error analysis will be useful throughout your future research career.

Recommended textbooks are also on reserve in the Physics Reading Room.

- **Experiments in Modern Physics by Adrian Melissinos (Academic Press, 1966 and 2003)** Please consult these before and during your investigations. Material essential to the understanding of an experiment which can be found in the Melissinos text is generally omitted from the Lab Guide. Note that the Physics Reading Room has both editions which offer different material, you should consult them both!

- **The Art of Experimental Physics by Daryl Preston and Eric Dietz (John Wiley 1991)**

- **An Introduction to Error Analysis 2nd Edition, by John Taylor (University Science Books 1997)**. This book covers much of the same material as Bevington and Robinson and is easier to read.

4.2. Reference Articles and Equipment Manuals

At this stage of your training as an experimentalist, you should realize that there is no 'comprehensive' or perfect textbook. Much of the material you will need to dig into are the early journal papers which originally detailed many of these important discoveries. Many of these references are available online through the Junior Lab Web Site e-Library. References and lending book resources are available through Barker and Hayden Libraries and the Physics Reading Room. For more information on Technical Writing, please refer to The Mayfield Handbook for Technical and Scientific Writing. A few reference books are kept in Room 4-361 for use in the laboratory. They may not by taken from the laboratory, but copies of a few pages may be made on the copier.

5. Grading Policy

5.1. Attendance and Lab Performance - 10%

The regularity of your attendance will be a factor in determining your grade in the course. Also your preparedness for the measurements and alternating as the "lead" (with your partner), to carry them out. Lab instructors will be delighted to accommodate your improvements and corrections to the lab guides! In case of equipment difficulties, students may stay on 30 minutes beyond the end of the normal session, otherwise the lab will be **closed at 5pm** each afternoon.

It is essential that you efficiently use all of the laboratory time assigned to you, and sometimes more. An experienced experimental physicist will be present in every scheduled session. He or she will be assisted by a graduate teaching assistant. In addition, the Junior Lab staff includes technical instructors responsible for the maintenance of the equipment and the development of new experiments. We are ready and eager to help you make things work properly and answer questions. Call for help when you get stuck.

5.2. Quality of Laboratory Notebooks - 10%

Each student's notebook will be evaluated twice during 8.14 by Ms. Edwards: once following the first experiment and once following the third experiment. Students, having already taken 8.13, should be well versed in how to maintain their laboratory notebook. The lab notebook guidelines are posted on the 8.13 web site.

5.3. Preparatory Questions - 10%

Each lab guide has a set of preparatory questions which point you to the essentials of the experiment. Before the first session of each experiment you are required to work out the solutions to the preparatory problems and/or predictions in your lab book. Make a Xerox copy of your solutions and deposit it in your TA's mail box in 4-361. It will be collected shortly after the start of the first session. **Late solutions will not be accepted; since these prepare you for your work, late solutions do not make sense**. Your solutions will be graded by the graduate teaching assistant and returned at the next session.

5.4. Oral Examinations (4 private) - 35%

A one-hour oral review and discussion of each main experiment will be held between the pair of students and one or more of their instructors within ten days of the last scheduled session for that experiment.

Each student should prepare a 20-minute oral report on the theoretical and experimental aspects of a single portion of the experiment. This is a slightly longer presentation than in 8.13 and students are therefore expected to delve deeper into the physics and error analysis of their experiment. We strongly suggest preparing your presentation electronically (e.g. LaTeX) and using the LCD projector for the cleanest most professional presentation possible. See the course web site for more details. The theoretical section should demonstrate a mastery of some portion of theory relevant to understanding the significance of the experimental results. The larger experimental section should demonstrate an understanding of how the equipment works,

what was measured, how the data were reduced, and how the random and systematic errors were estimated. **Each student must discuss motivating theory and experiment; it is not acceptable to discuss theory only or experiment only. Full cooperation with lab partners and others in preparing for the oral reports is encouraged.** This latter aspect is particularly important to ensure that both partners report the same results!

5.5. 4-Page Written Summaries - 35%

You must email an Adobe PDF copy of your ($\leq$4) page, **individually-prepared**, written summary of the purpose, theory, and results of the experiment by midnight on the day you give your oral examination. The delay between oral exam and paper submission allows you to correct any egregious mistakes that were uncovered during the exam so as not to repeat them in your written work and receive a double penalty!!! All your work on the experiment should be summarized, not just the part you chose for your oral presentation. The individual summary you hand in should show evidence of your own mastery of the entire experiment and possess a neat appearance with concise and correct English. Its organization and style should resemble that of a typical abstract that follows the title of an article in the Physical Review Letters (http://prl.aps.org/). **The abstract is essential. It should briefly mention the motivation (purpose), the method (how measured) and most important, the quantitative result WITH uncertainties.** Based on those, a conclusion may be drawn. The report must be type-written in a form that would be suitable for submission as a manuscript and to aid you in this process we have produced a sample paper template written in LaTeXthat we encourage you to study and use for your own submissions. It is downloadable from the course web site.

The paper should include a discussion of motivation and the theoretical issues addressed by the experiment, a description of the apparatus and procedures used, a presentation of the results (including errors!), a discussion of these results, and, finally, a section briefly presenting your conclusions. This last section repeats what was stated in your abstract. The total length (including figures) of your summaries should not exceed four pages in length. It is easiest to read if you include figures and plots in-line within the text and the sample paper template shows you how this is easily done. However, do not inundate the reader with material; you should find a way to summarize your results in at most two or three plots or tables. The figures and tables must be properly captioned. Material and ideas drawn from the work of others must be properly cited, and a list of references should be attached to the summary.

Papers will be graded using the following rough guidelines:

1. Motivation - $\approx$20%
2. Experiment - $\approx$35%
3. Analysis - $\approx$35%
4. Style and English - $\approx$10%

6. Laboratory Notebooks

One critical objective of this course is to instill habits of record keeping that will serve you well in future research. To this end you will be given a standard experimental notebook in which the complete dated record of procedures, events, original data, calculations and results of every experiment is to be kept. **No other form of notebook is acceptable in this course.** Though you will generally work in pairs and are urged to collaborate in all aspects of carrying out the experiments and analyses, each student must keep a complete, dated record of each experiment and its analysis. The cross-hatched paper in the Computation Book is convenient for formatting tabulations, and for guiding line drawings and **making rough plots.** High resolution plots, photos, and Xerox copies of shared data should be glued or taped in place. You must write a sufficient narrative as the experiment proceeds so that, years later, you could reproduce the results you obtained. Notes, tables, and graphs should be neat and compact, leaving as little empty space in the lab notebook as is compatible with clarity and the logic of organization. There should be no loose sheets or graphs floating around.

Analyze data in the lab in a preliminary way as you go along to check for reasonableness. If you are making a series of measurements of one quantity as you vary another, plot the results as you go along so that you can see the trend, catch blunders, and judge where you may need more or less data. **Repeat every measurement at least three times in as independent a manner as possible in order to establish a statistical basis for estimating random error and to reduce the chance of blunders.** If you get through all the manipulations and preliminary analysis of an experiment in less than the five regularly assigned lab sessions, take the opportunity to perfect part or all of the experiment so as to obtain the best possible data set.

Many experiments will require you to transfer your data to a computer and store them in files on disk. Obviously, it is not practical in these cases to print out all your data and paste them into your notebook. However, we expect to see, in your lab notebook, **representative plots or tables**. In addition, we expect a clear description and summary of the **data files** so that when you return to the data days or weeks later, you are able to identify particular files with procedures you carried out in the lab.

Specific requirements for Junior Lab notebooks are detailed on the course web pages.

7. Safety

We are fortunate that there has never been a serious injury in Junior Lab. Prevention of injury is a matter of being aware of and having respect for pieces of equipment that are potentially dangerous. Nevertheless, since it is virtually impossible to set up a reasonably comprehensive and interesting set of experiments in modern physics without using equipment which has potential hazards, it is essential that staff and students be aware of the hazards, and exercise appropriate cautions.

7.1. High Voltage

The first rule is never to work alone. Some years ago a student was electrocuted in Building 4 by a laboratory power supply. Had he not been by himself, someone might have saved him.

All high voltage supplies are clearly marked as dangerous. Do not poke or probe into them. Turn off the supply if you need to change cable connections. The supply may be dangerous even when turned off if the capacitors have not discharged; always keep one hand in your pocket when testing any circuit in which there may be high voltages present so that if you get a shock, it will not be across your chest. Never go barefoot in the lab. Remember that it is current that kills. A good (e.g. sweaty) connection of 6 volts across your body can kill as well as a poor connection of 600 or 6000 volts. If your partner is frozen by an electrical shock, use momentum transfer (tackle them!) to release him or her and start CPR if needed and if a trained person is available.

7.2. Lasers

The Doppler-Free Saturated Absorption Spectroscopy experiment utilizes a near IR laser operating at 40mW of output power. As such, it is classified as a Class 3b laser and all users must previously undergo MIT Laser Safety Training (EHS Course 371C). All students should download http://web.mit.edu/environment/pdf/Laser_Safety.pdf and read, at a minimum, page 13 dealing with Class 3b laser controls. Students must attend a 1.5 hours laser safety training course to be scheduled during the first week of class.

A laser beam may not seem very bright, but if it enters your eye it will be focused by your eye lens to a pinpoint spot on the retina where the intensity is sufficient to destroy retinal cells. It is wise to terminate a laser beam with a diffuse reflector so that the focused beam doesn't reflect around the room. Never examine the performance of an optical system with a laser by viewing the beam directly with your eye.

7.3. Cryogenics

When the cap on a liquid-helium Dewar is left off air flows in and freezes in the neck, forming a strong cement. When a probe is inserted, it may be frozen in solid. Then pressure will build up until something explodes. During the superconductivity experiment, **never leave the Dewar cap off for more than a few seconds**. Always ream out the Dewar before you use it. Check periodically to see that the probe is free. If the probe should freeze in the Dewar, get help immediately from any of the Junior lab staff or a professor or TA.

Liquid nitrogen is chemically inert, but it can cause severe frostbite. Wear gloves and protective glasses when transferring or transporting liquid nitrogen.

7.4. Radiation

Radiation safety at MIT is under the authority of the Radiation Protection Office (N52-496). Junior Lab is accountable to that office for the safe handling and accountability of the sources used in the experiments. During the first class session, a member of the Radiation Protection Office will instruct you in the safe use and handling of radioactive material.

Meticulous care must be taken by all students and staff to insure that every source signed out from the repository be returned immediately after its use and signed in.

Ionizing radiation damages tissue; any exposure should therefore be minimized. The unit of radiation exposure is the rem (roentgen equivalent man). A new unit, called the Sievert (=100 rem) is recommended by the International Commission on Radiation Units and Measurements (ICRU). Your inescapable dosage from cosmic rays and other background sources is 360 millirems/year, which works out to $4.2\text{x}10^{-2}$ millirems/hour. The recommended limit to exposure for a member of the general public is 100 millirem/year, averaged over any consecutive five years. If you follow the Junior Lab guidelines, your exposure will be only a small fraction of the dose you receive from the natural background. A meter is available in room 4-361 for you to check the radiation levels yourself.

Radioactive sources emit three types of radiation: high energy helium nuclei (alpha rays), electrons (beta rays), or photons (gamma rays). Most of the sources in Junior Lab emit only gamma radiation. Of the sources which do emit alpha or beta particles, most are enclosed in plastic or metals, which prevent particulate radiation from escaping. The exceptions are the ^{90}Sr source in the e/m experiment and the ^{241}Am source in the Rutherford Scattering experiment; both sources are in an enclosed apparatus. These sources should never be handled. Handling of open alpha- or beta-emitters can result in dangerous dosages to the skin.

The strength of a radioactive source is measured in curies (Ci). A one-curie source has an activity of 3.7 x

10^{10} disintegrations per second. The "absorbed dose" is a quantity that measures the total energy absorbed per unit mass; it is measured in rads, where 1 rad = 100 erg/gm. The "equivalent dose" is measured in the units discussed above, the rem. The equivalent dose is derived from the absorbed dose by multiplying by a "radiation weighting factor" which is a measure of how damaging a particular type of radiation is to biological tissue. For photons (gamma rays) and electrons and positrons (beta particles), the radiation weighting factor is unity; for helium nuclei (alpha particles), it is 20; for protons with energy greater than 2 Mev it is 5; and for neutrons it ranges from 5 to 20, depending on the energy. When you use the meter in the lab, the readings are in rads, and you must consider the type of particle when you work out the equivalent dose.

For gamma rays with energy greater than 1 MeV, a useful approximation is that the equivalent dose due to a source with an activity of C microcuries is $5.2 \text{ x } 10^{-4} C \frac{E_\gamma}{R^2}$ millirem/hr, where R is the distance from the source in meters and E_γ is the energy of the gamma ray in MeV. For gamma rays with energy less than 1 MeV, this formula is still approximately true for a full-body dose. However, low-energy gamma rays deposit their energy in a smaller mass of tissue than high-energy gamma rays and can cause high local doses. For example, the local dose to the hands from handling a 10 keV source can be up to 25 times the value given by the above formula; hands, however, have a higher tolerance to radiation than inner organs or eyes.

The protective value of shielding varies drastically with the energy of the photons. The intensity of a "soft" X-ray beam (i.e. < 1 KeV) can be reduced by many orders of magnitude with a millimeter of aluminum while 1.2 MeV gamma rays from ^{60}Co are attenuated by only a factor of 2 by a lead sheet one-half of an inch thick. The best way to keep your dosage down is to put distance between you and the source. If you stay a meter away from most sources in Junior Lab, you will be receiving, even without any lead shielding, a dose which is much less than your allowable background dose. If, however, you sit reading the write-up with a box of sources a few inches away, you may momentarily be receiving ten to a hundred times the background level.

We end with a list of precautions:

1. Don't handle radioactive sources any more than you have to.

2. Work quickly when transferring or positioning radioactive sources.

3. Never take a source away from the Junior Lab, even temporarily. The senior staff are legally responsible for the sources and must periodically account for their presence and condition.

4. Replace sources in the lead storage cabinet when they are not in use.

TABLE II: A table showing the radioactive sources used in Junior Lab and their approximate activities.

Experiment	Isotope	$\sim$ Activity (mCi)
Compton Scattering	^{137}Cs	0.4
Mössbauer Spectroscopy	^{57}Co	7
Rutherford Scattering	^{241}Am	0.2
Alpha Decay	Uranium Ore	5×10^{-6}
Relativistic Dynamics	^{90}Sr	8
	^{133}Ba	0.08
X-Ray Physics	^{241}am	10
	^{55}Fe	0.7
	^{90}Sr	0.6
	^{57}Co	0.02
Calibration Sources	^{133}Ba	0.005
	^{109}Cd	0.008
	^{137}Cs	0.007
	^{57}Co	0.0001
	^{60}Co	0.0005
	^{54}Mn	0.0002
	^{22}Na	0.002

5. Keep sources away from your body.

6. Never bring a radioactive source near your eyes because they are particularly sensitive to radiation.

7. Be aware of the sources being used in neighboring experiments.

The Zeeman Effect

MIT Department of Physics
(Dated: February 2, 2010)

The magnetic splitting of spectral lines. A scanning Fabry-Perot interferometer is used to measure the Zeeman effect in mercury. The results are compared with the expectations derived from the vector model for the addition of atomic and nuclear angular momenta. A value of the ratio e/m of the electron is derived from the data.

PREPARATORY PROBLEMS

1. Draw a diagram that shows the effect of a weak magnetic field on the otherwise degenerate substates involved in the transitions which produce the green line (5460.7 Å) and the yellow doublet (5769.6 Å and 5790.7 Å) of mercury. See Melissinos-1966[1],page 334 but beware of the error in the structure diagram for the 5790.7 Åline! Note that there is another (Hg) yellow line at 5789.7 Åbut it is quite weak.

2. Derive the Landé g-factors for the states involved in the production of these lines.

3. What would the Zeeman effect be on the 5461 Å line if the gyromagnetic ratio of the electron were 1 instead of 2.001?

4. What is the expected spread in wavenumbers for the hyperfine structure of natural mercury? What is an appropriate spacing of the Fabry-Perot mirrors to acquire this spectrum?

5. Estimate the Doppler width of the 5461 Åline from the mercury lamp and compare it with the expected Zeeman splittings. Assume the temperature of the emitting vapor is 500 K.

6. Derive a formula for e/m in terms of the measured separations of identified peaks in the interferogram of the Zeeman pattern, the distance between the plates of the interferometer, the strength of the magnetic field, and various physical constants.

1. INTRODUCTION

Since Faraday's discovery in 1848 of magnetically induced circular birefringence (the Faraday Effect), the search for effects of electric and magnetic fields on optical phenomena has been pursued with more and more powerful methods of spectroscopy and stronger and stronger fields. In 1862, in his last experimental work, Faraday himself used the most powerful magnet and best prism spectroscope available in an unsuccessful attempt to detect an effect of a magnetic field on the spectral lines emitted by sodium vapor in a Bunsen burner flame. Three decades later Pieter Zeeman in Leyden, unaware of Faraday's earlier attempt, was induced "by reasons of minor importance" to try to detect a magnetically induced change in the light of a sodium flame [2]. He too failed. However, as Zeeman describes it in his discovery paper of 1896, [3] his attention was subsequently drawn to Maxwell's sketch of Faraday's life in which Faraday's last experiment is mentioned. Zeeman wrote "If a Faraday thought of the possibility of the above mentioned relation, perhaps it might be yet worth while to try the experiment again with the excellent auxiliaries of spectroscopy of the present time." Using a grating ruled on the marvelous engine of Rowland at Johns Hopkins he observed a broadening of the spectral lines emitted by sodium vapor heated in a flame between the poles of a powerful Ruhmkorff magnet which produced a field of 10 kilogauss. Zeeman proposed a theoretical interpretation based on Lorentz's idea that "in all bodies small electrically charged particles with a definite mass are present." Given this concept, the rest of the interpretation is, from a modern point of view, hardly more than a dimensional analysis. Nevertheless this early theory of the "normal" Zeeman effect showed how to interpret the observed line broadening as a measure of e/m, the charge to mass ratio of the electron. The idea was that the frequency of a spectral line emitted by an atom is the frequency of a harmonic vibration of an electron in the atom. Any such vibration can be resolved into two components, one along some particular direction which we take to be the direction of the z axis, and the other in the xy plane. The xy component, in turn, can be represented as the sum of two components of constant amplitude rotating in opposite directions about the z axis. With each such circular component of motion one can associate a central restraining force given by

$$F = mr\omega^2 \tag{1.1}$$

where ω is the angular frequency and r is the radius of the circular motion. If a magnetic field of magnitude B is now imposed in the z direction, the central force will be either increased or decreased by a perturbing (i.e small compared to F) Lorentz force of magnitude $\frac{Be\omega r}{c}$ (cgs units), resulting in a changed frequency of circular motion given by the equation

$$mr(\omega + \Delta\omega)^2 = F \pm \frac{Be\omega r}{c} \tag{1.2}$$

or

$$mr[\omega^2 + 2\omega\Delta\omega + (\Delta\omega)^2] = mr\omega^2 \pm \frac{Be\omega r}{c} \tag{1.3}$$

Neglecting the $(\Delta\omega^2)$ term, one obtains the simple expression

$$\omega + \Delta\omega = \omega \pm \frac{Be}{2mc} \tag{1.4}$$

for the frequencies of light viewed along the direction of the field (as viewed through a hole bored through the magnet pole piece). In directions perpendicular to the field, one sees both these shifted frequencies and the unshifted frequency of the components of vibration along the z axis which, being parallel to the field, is unaffected. With the resolution available to Zeeman the individual frequency-shifted lines were unresolved. However, Lorentz pointed out to Zeeman that the edges of the broadened lines observed parallel to the field, supposedly being light radiated by charges in right and left circular motions, should exhibit circular polarization in opposite senses with respect to one another. With a quarter wave plate and Nicol prism polarizer Zeeman confirmed the prediction. And by rough estimation of $\Delta\omega$ and knowledge of B he obtained a value of 10^7 esu for e/m .

Within a few months of Zeeman's publication magnetically split lines were spectroscopically resolved and found in many cases to consist of more than the "normal" Zeeman triplet, and to have frequency shifts other than $\pm\frac{Be}{2mc}$. The "anomalous" Zeeman effect, which proved to be the rule and not the exception, defied explanation until the advent of quantum mechanics and the discovery of spin.

A modern understanding of the Zeeman effect can be approached on several levels. The vector model, which you should master before starting the experiment, is explained in [4] and in various texts on quantum mechanics and atomic structure listed in the references. It provides a useful image of the atomic machinery involved in the Zeeman effect and yields accurate predictions of the Zeeman effect in atoms whose excited states can be described according to the LS coupling scheme (Russell-Saunders coupling). Information about the mercury spectrum in general and the Zeeman effect on the green and yellow lines of mercury can also be found in Melissinos. (Beware of errors in Melissinos' description of the hyperfine structure of the mercury lines.) Specially useful references are [5, 6]. Additional background material on the quantum theory of the Zeeman effect can be found in [6–14]. Further details of the physical optics of the interferometer can be found in [15, 16].

2. EXPERIMENTAL ARRANGEMENT

In this experiment you will measure the weak-field Zeeman effect on the green and yellow lines of mercury and by means of a Fabry-Perot interferometer. This device provides the high spectral resolution necessary for the detection and measurement of the small fractional changes in wavelength caused by "weak" magnetic fields of several thousands of gauss. The results reveal some of the important properties of angular momenta, spin, and the dipole selection rules, as well as an accurate value of e/m from an interpretation of the data based on the vector model for the quantum mechanical addition of angular momentum. In addition, with sufficient care in the adjustment of the apparatus you can detect and measure the hyperfine structure of the green line of the odd isotopes of mercury due to the interactions between the electronic and nuclear magnetic moments, and the spread in wavelength of the lines of the even isotopes due to the differences in the number of neutrons in their nuclei.

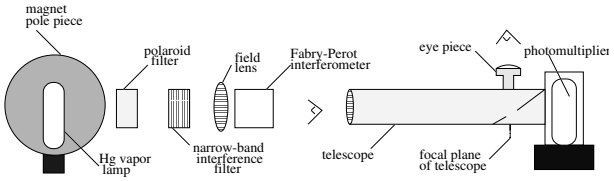

FIG. 1: Schematic diagram of the optical arrangement for recording the intensity at the center of the Fabry-Perot interferogram. The focal length of the collimating field lens is 33 ±0.5 cm and the focal length of the telescope is 43.5 ±0.5 cm. The optical height of the Fabry-Perot is 12.2 ± 0.2 cm.

The optical arrangement is illustrated in Figure 1. Light emitted by a low-pressures mercury vapor lamp passes through a narrow-band interference filter, an optional Polaroid filter, a field lens, the Fabry-Perot interferometer, and a telescope. When properly aligned this system produces at the focal plane of the telescope objective lens interference fringes in the form of circular rings concentric with the axis. A 45° front-aluminized mirror with a small hole in the aluminization centered on the focal plane reflects most of the ring pattern for viewing through the eyepiece, while allowing the light at the center "bulls eye" of the ring pattern to pass through to the photomultiplier. During a spectrum scan the separation of the Fabry-Perot plates is varied by two or three wavelengths by application of a saw-tooth voltage with an amplitude of several hundred volts to three piezoelectric crystals on which one of the plates is mounted. As the separation decreases (increases) the rings in the image plane expand (contract). A plot of the intensity of light passing through the hole located at the center of the ring pattern against the magnitude of the saw-tooth voltage is, in effect, an ultra-high resolution spectrum over a very narrow range of frequencies.

Figure 2 shows the electronic arrangement for recording the central intensity as a function of the voltage applied to the piezoelectric crystal. The photomultiplier output is fed directly to the Y input of an oscilloscope. A signal equal to to the voltage (÷ 100) applied to the piezoelectric crystals is fed from the interferometer controller to the X input of the digital oscilloscope.

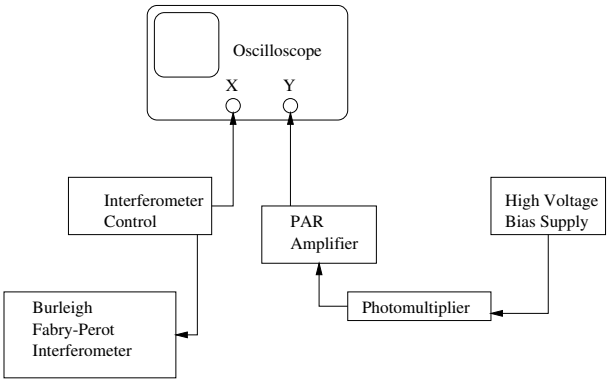

FIG. 2: Schematic diagram of the electronic arrangement for recording the interferogram in the form of a plot of the central intensity versus the separation of the Fabry-Perot plates.

3. PROCEDURE

1. **Determine the optimum mirror separation for measurement of the zeeman splittings** Calculate the separation between the Fabry-Perot mirrors which will provide a "free spectral range" suitable for the desired measurements. What you want to avoid is having the extreme red-shifted Zeeman components of a given line in one order of interference overlap the extreme blue-shifted components of the line in the next order when the field is at maximum strength. Estimate the total width of the Zeeman pattern that you expect at the maximum attainable field strength. Calculate the mirror separation which will give you the necessary free spectral range to accommodate this width.

2. **Align the interferometer** The Burleigh Fabry-Perot interferometer is a delicate instrument capable of providing spectrum measurements of extraordinary resolution and precision. Please treat it with the utmost care. In particular, **do not press the mirrors together by turning the micrometer screws too far as you may crack the sapphire blocks on which the micrometer crews press. The 'zero' position of the mirrors is when the micrometer nearest the edge of the optical table reads 12.212 ± 15 μm.** If you encounter any problems or are uncertain how to adjust the interferometer, call for assistance.

   Mount the mercury spectral calibration lamp between the pole pieces, and turn it on using the AC setting at 18mA. Once the lamp discharge has been initiated, it can be run with a DC current greatly reducing the lamp variability. Adjust the collimating lens (plano-convex, focal length = 33±0.5cm) and the position and orientation of the interferometer so that the light falls on the input mirror and the view through the Fabry-Perot mirrors looking toward the lamp is fully illuminated. Put the interference filter for the 5461 Å green line of mercury in the beam. Begin by adjusting all three micrometers to a setting of 15mm. The micrometers have a range of 25mm where the smallest division on the micrometer shaft corresponds to 10 μm.

   Coarse Alignment of the Fabry-Perot ATTENTION: *Do not look through the interferometer towards the laser. All alignment should be done while viewing the notecard from above the experimental setup.*

   This section is only needed if the interferometer is so poorly aligned that you do not see any circular interference pattern at the output of the Fabry-Perot after turning on the lamp.

   A quick method for course alignment of the Fabry-Perot interferometer is easily accomplished using a laser. Arrange a helium-neon laser to pass through the interferometer mirrors as close to on-axis as possible. Place a white piece of paper a few inches away from the output of the F-P and note the pattern of spots observed. Under coarse alignment, the spots will appear to 'walk' off the card indicating that the mirrors are NOT parallel. Adjustments to the micrometers should be made to cause these helium-neon spots to become more numerous and concentrated (indicating better and better parallelism of the mirrors) until the appear to collapse onto a single point at which point fringing should appear.

   Now, by making small adjustments and taking careful notes on their effects, make the mirrors parallel by adjusting two of the three micrometers while viewing the light coming through the Fabry-Perot mirrors. When coarsely adjusted, you may only see 'arcs' of the interference patterns. As the mirrors are nearly parallel you will see many narrow circular fringes. Fine adjustment will produce comparatively large, sharp circular fringes concentric with the center of your field of view and separated by dark gaps with fainter and narrower rings. When the mirrors are perfectly parallel the circular fringes are sharp and do not change in diameter as you move your eye back-and-forth, and up-and-down.

3. **Align the telescope** Check that the mirror mounted inside the telescope under the eyepiece is inclined at an angle of 45° so that it reflects the light from the telescope lens into the eyepiece. Adjust this angle using the silver screw from the bottom of the assembly. Focus the eyepiece on the tiny aperture (a ragged laser-drilled hole in the aluminization near the center of the mirror). Then point the telescope at a distant object and focus it by adjusting the slide tube.

   Place the telescope so that the light emerging from the interferometer enters the objective lens (focal

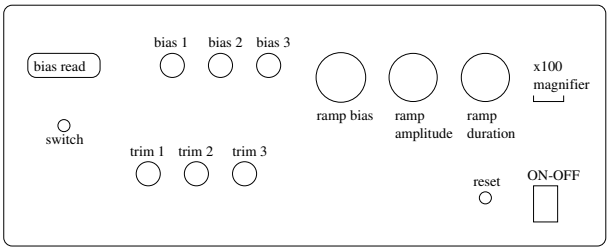

FIG. 3: Diagram of the front panel of the interferometer controller. Note that the knobs are friction-coupled to their shafts so that they turn past the zero and maximum positions without harm.

length = 43.5±0.5cm). (Leave sufficient room between the telescope and the interferometer to insert your head for direct viewing of the interference fringes). Adjust the orientation of the telescope so that the circular fringes seen through the eyepiece are concentric with the tiny aperture in the 45° mirror. (The broad rings are successive orders of interference of the light from the even isotopes of mercury: the breadth of the line is due to the effect of the spread in mass of the isotopes. The faint, narrow rings between the broad ones are the hyperfine lines of the odd isotopes, separated slightly in wavelength from the others as a result of the interaction between the nuclear and electronic magnetic moments.)

4. **Adjust the fabry-perot controller** Turn on the controller and explore its operation with the help of the diagram in Figure 3 and the instrument manual. The function of the controller is to supply a sawtooth voltage to each of three piezoelectric crystals on which the input (left) Fabry-Perot mirror is mounted. The duration and amplitude of the sawtooth voltages are controlled by the correspondingly labeled knobs. The ramp bias knob controls the voltage level of the midpoint of the scan voltage applied to all three crystals; the three bias controls on the left adjust the mean voltages applied to each crystal. The trim controls adjust the slopes of the sawtooth voltages to compensate for any differences that may exist in the electromechanical properties of the crystals. Start with each of the trim controls in their most counterclockwise position.

   With the ramp amplitude turned to zero, set the three bias controls and the three trim controls to near their middle values (∼ 250 V). Application of the bias voltages to the piezoelectric crystal mounts of the input mirror will disturb the parallelism. So, once again, view the fringes directly with your eye close to the output mirror of the interferometer and make the mirrors parallel by adjusting the bottom and top right micrometers. Now view the fringe pattern through the telescope and tweak the bias controls for maximum sharpness. Adjust the telescope orientation so that the aperture hole is exactly at the bull's eye of the circular fringe pattern. You can shift the fringe pattern by adjusting the ramp bias control.

5. **Acquire the spectrum** Put the photomultiplier in its place at the end of the telescope and turn up the Photomultiplier high voltage to ≈ −1000 v. Feed the signal from the photomultiplier tube (PMT) to the voltage preamplifier with the low frequency (LF) roll off control set to DC, and the high frequency (HF) roll off set to a value that satisfactorily reduces the vertical jitter due to electronic noise without suppressing the fine features of the spectrum. Display the output on the y-axis of the digital oscilloscope with the scan signal from the Fabry-Perot controller connected to the x-input. Adjust the scan amplitude so that the piezoelectric drive is activated. Select a bias sweep amplitude and repetition rate that produces a pleasing display of the variation of light intensity at the bullseye of the interferometer pattern over a range of two or three free spectral ranges. Adjust the three bias controls to maximize the amplitudes of the peaks.

   Observe the pattern and identify the hyperfine lines with the help of the plot copied from the American Institute of Physics Handbook and posted on the wall.

6. **Trial Runs** The magnet is capable of producing a field of ∼9.4kG at a current of 50A. **Please do not exceed this current level!**. As a result of such high currents, the magnet coils must be cooled during operation. A Neslab chilled-water circulator (under the left-hand side of the optical table) is installed for this purpose. Turn on the Neslab as soon as you begin your lab sessions to allow time for the water to be cooled. The power switch is on the top left-hand side of the unit. Once the water is circulating, you can turn on the magnet power supply (located under the table), making sure that the current level is at the lowest possible setting.

   When everything is properly adjusted, with the bull's eye of the interference pattern centered on the hole in the 45° mirror and with the bull's eye intensity signal displayed on the oscilloscope, a pattern similar to that in Figures 4 and 7 with $R \approx 0.9$ should be seen.

Observe the fringe pattern through the telescope as you increase the magnet current. Note the behavior of the hyperfine lines. Test the effect on the fringe pattern of inserting a Polaroid filter in the optical path between the source lamp and the Fabry-Perot. Rotate the Polaroid and figure out what is happening. (You can determine the transmission axis of the Polaroid filter by observing light reflected at small angles of grazing incidence from any non-metallic glossy surface like that of the table in the next room.)

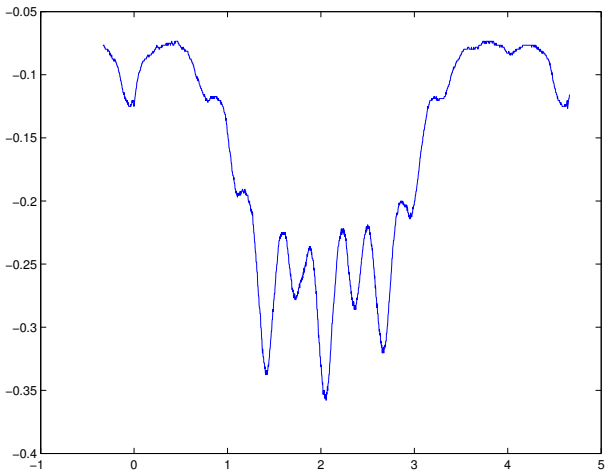

FIG. 4: Sample interferogram of the 5461 Å line of mercury. Magnet current = 50A ∼0.94T. The amplifier gain = 1000 and the PMT bias = -900 VDC. The units of the x-axis are seconds and of the y-axis are volts.

4. QUANTITIES YOU WILL DETERMINE

1. The Zeeman splittings of the green 5461 Å and yellow 5770 Å and 5791 Å lines of mercury.
2. The Landé g-factors for the levels involved in the mercury lines.
3. The value of e/m for the electron.
4. The hyperfine structure of the mercury 5461 Å line.
5. The isotope shift (effect of nuclear mass) of the 5461 Å lines of the even isotopes of mercury.

4.1. The green line of mercury

Using the Hall probe magnetometer explore and record, as a function of the supply current, the intensity of the field between the pole pieces of the magnet in the region that will be occupied by the mercury vapor and up against the centers of the faces of the pole pieces. (Check the Hall magnetometer zero setting by inserting the probe into the magnetically shielded cavity provided, and check the calibration with the 5 kilogauss standard magnet, also provided.)

A convenient way to measure the Zeeman splittings is to record the digital reading of the ramp bias required to move the various interference rings seen in the telescope to a chosen fiducial position marked by a dirt spot on the 45° mirror at the focal plane of the telescope. To do this first stop the scanning action by turning the ramp amplitude to zero. Then select a dirt spot on the mirror at some as your fiducial marker. Adjust the ramp bias control so the spot is on the center line of an interference ring of a particular reference spectrum line, and record the bias reading. Repeat for the other rings of the same order of interference for the spectrum lines whose wavelength shift relative to the reference line you wish to measure. Also record the bias readings for interference rings in several adjacent orders to establish the calibration scale and to provide redundant data from which the random measurement errors can be evaluated.

At zero field tweak up the performance of the interferometer with the bias controls to sharpen up as much as you can the hyperfine components of the green line which appear as the faint, sharper rings between the bright, broad rings of the unresolved emission from the even isotopes. Increase the gain of the oscilloscope y-input to make the hyperfine peaks large enough to be accurately measurable. Here again you can obtain the necessary measurements using the ramp bias control. Beware of confusing interference rings of different orders.

4.2. The yellow doublet of mercury

To observe the mercury yellow lines remove the green interference filter from the optical path and insert the yellow interference filter centered at 5770 Å . Note that there will now be two sets of interference rings present since the filter passes both of the yellow lines. With luck the two sets of rings may be conveniently spaced so that their Zeeman patterns do not overlap at moderate fields. If not, you will have to change the spacing of the mirrors slightly.

Measure the structure and splitting of both components of the mercury yellow doublet. This will require special care because of possible overlapping of the two interference patterns at high field values. Note the slight difference in the Zeeman patterns of the 5769.6 Å and 5461 Å lines. How do they differ and why? A beautiful photograph of the doublet is shown in Fig. 5.

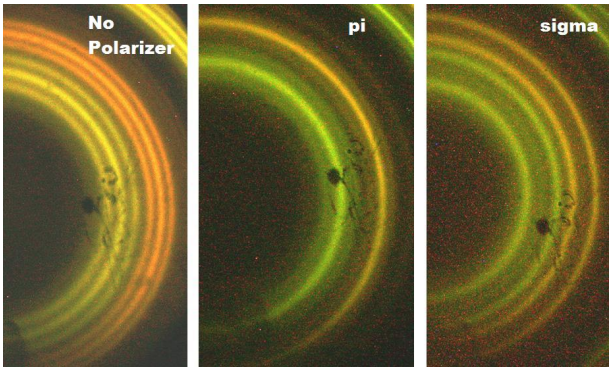

FIG. 5: Photograph of the yellow mercury doublet at 5769.6 and 5790.7 Å showing σ and π transitions. Taken by Matthew Heine and Sarah Trowbridge in 2007.

5. ANALYSIS

To check the results of your ramp bias measurements of the Zeeman splittings you can measure the separations between the peaks of the interferograms utilizing Matlab and fitting the peak locations. **Be sure to measure the separation between the same Zeeman components in adjacent orders**, i.e. the distance in interferogram corresponding to the free spectral range. From these quantities and the separation of the mirrors of the Fabry-Perot interferometer, compute the effective dispersion of the spectroscope, i.e. the shift in wave number per unit distance on the photographs.

1. Tabulate all the measured frequency shifts in units of wave numbers $\frac{\Delta f}{c} = \Delta\frac{1}{\lambda}$ per kilogauss, e.g. $(0.1234 \pm 0.012) cm^{-1} kgauss^{-1}$.
2. Construct energy level diagrams of the mercury transitions and identify the observed Zeeman component frequencies with the various allowed transitions between the magnetic substates.
3. Measure the hyperfine lines, and identify them with the help of the discussion by Steinfeld (1986).
4. Measure the full width at half maximum of a strong hyperfine line to obtain a measure of the effective resolution of the spectrometry. Measure the FWHM of the bright, unresolved composite line of the even isotopes. Derive from these data a measure of the spread in wavelengths of the even isotope lines due to the differences in their nuclear masses. Can you think of a way to make an order of magnitude theoretical prediction of this spread?
5. Compute the Landé g-factors for the upper and lower states involved in the various transitions (Hg 5461 Å, Hg 5770-5790 Å and the magnetic moments of each of the levels in units of the Bohr magneton.
6. If everything makes sense, i.e. all the measured shifts of the π and σ components are consistent with expectations derived from the vector model and selection rules, then determine a best value for e/m for the entire data set.
7. Estimate the random and systematic errors associated with each of your final quantitative conclusions.

5.1. Possible Theoretical Topics

1. The vector model and the Landé g-factor.
2. Hyperfine structure.
3. The isotope shift.
4. Theory of multi-wave interference in the Fabry-Perot interferometer.

6. Theory of the Fabry-Perot Interferometer

A Fabry-Perot interferometer consists of two precisely parallel glass plates with optically flat and highly reflective surfaces facing one another, as illustrated in Figure 6. To use it as a spectrometer one must have, in addition, a lens to focus parallel rays to a point in its image plane and a magnifying eyepiece for examining the intensity pattern of light in the focal plane, i.e. a telescope.

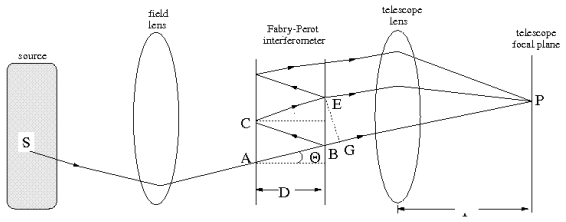

FIG. 6: Geometrical optics of the Fabry-Perot interferometer. Only one of many multiply reflected paths is shown.

Consider a ray of light of wavelength λ emitted by an excited mercury atom at S and making an angle θ with the axis, is incident on the Fabry-Perot from the left at the point A. It will be partially transmitted at each of the two Fabry-Perot mirror surfaces, and will arrive at P after passing through the telescope lens. The portion of the ray reflected at B will be reflected again at C and partially transmitted at E. It will enter the telescope lens parallel to the original ray and will be focussed to the same point P after having traversed an additional distance $2Dcos\theta$. If this additional distance is an integer number of wavelengths, i.e.,

$$2Dcos\theta = m\lambda \tag{6.5}$$

then the two rays (and all the additional multiply reflected rays) will interfere constructively when brought to the focus at P. Constructive interference among all the multiply reflected rays passing through the interferometer at an angle θ to the axis will produce a circle of interference maxima in the focal plane, i.e., a bright ring of the mth order of interference. If the separation of the plates is increased, then the angular radius of the mth order ring will expand so that the decrease in $cos\theta$ compensates for the increase in D.

Suppose you want to measure the difference $\delta\lambda$ between two wavelengths very close together, e.g., the wavelength shift between two lines in a Zeeman pattern. Suppose, further, that the average wavelength λ of the two lines is already known to good accuracy. Viewing the light emerging from the interferometer with your naked eye or through a telescope focused on infinity, you will see two concentric sets of interference rings, corresponding to the two wavelengths. Suppose the mth order ring of wavelength λ_1 coincides with a fiducial mark fixed in the focal plane (e.g. a dirt spot on the 45° mirror in

the Junior Lab setup). Call δD the change in mirror separation required to bring the mth order ring of wavelength $\lambda_1 + \delta\lambda$ into coincidence with the fiducial mark. According to equation 6.5

$$\delta D = \frac{m\delta\lambda}{2cos\theta} \tag{6.6}$$

Call ΔD the change in mirror separation required to bring the $m+1$ ring of wavelength λ_1 into coincidence with the same fiducial mark. In this case

$$\Delta D = \frac{\lambda_1}{2cos\theta} \tag{6.7}$$

Combining equation 6.5, equation 6.6, and equation 6.7 and setting $\cos\theta = 1$ (an accurate approximation since $\theta << 1$) we obtain

$$\delta\lambda = \lambda\frac{\lambda}{2D}\frac{\delta D}{\Delta D} \tag{6.8}$$

which is an expression for the desired wavelength difference in terms of the known wavelength λ, the mirror separation D and the ratio of the changes in separation of the mirrors. In practice the changes can be measured as differences in the digital readings of the bias meter on the Burleigh controller. Since the latter are proportional to the actual changes in mirror separation, the ratio of the meter differences is equal to the ratio of the actual separation changes.

From equation 6.8 one can see that if $\delta\lambda = \lambda\frac{\lambda}{2D} = \frac{\lambda}{m}$, then $\delta D = \Delta D$, i.e., the mirror movement required to shift the ring pattern from the mth order ring of wavelength λ to the mth order ring of wavelength $\lambda + \delta\lambda$ would be the same as the movement required to shift the mth order ring of λ to the mth+1 order of the same wavelength. The quantity $\frac{\lambda}{m}$ is called the free spectral range of the instrument for a particular separation of the mirrors. It represents the difference between two wavelengths such that the mth interference maximum of the larger wavelength coincides with the $(m+1)$ maximum of the smaller wavelength, i.e. $(m+1)\lambda = m(\lambda + \frac{\lambda}{m})$. To avoid confusion as to which interference order a given feature of a complex line may belong, it is generally wise to adopt a mirror separation that gives a free spectral range larger than the wavelength difference to be measured.

The effectiveness of a Fabry-Perot interferometer for high-resolution spectroscopy depends critically on the reflectivity of its mirrors - the higher the reflectivity the sharper, or narrower, the lines. To quantify this relation one must consider the combined effects of the reflection coefficient and additional path length on the contribution that each transmitted beam makes to the total complex amplitude of the optical disturbance at P. If we call r the amplitude reflection coefficient, then the factor by which the amplitude of the ray emerging at E is reduced relative to the direct ray is r^2. In addition the ray is retarded in phase by the angle

$$\alpha = \frac{2\pi D}{\lambda}cos\theta \tag{6.9}$$

Similarly, the nth multiply reflected ray will arrive at P attenuated by the factor $(r^2)^n$ and retarded in phase by $n\alpha$. If the amplitude at P of the wave arriving by the direct path is $Ae^{j(\omega t+\phi)}$, then the total amplitude at P is the complex quantity

$$A_{tot} = Ae^{j(\omega t+\phi)}\left(1+r^2e^{-j\alpha}+\left[r^2e^{-j\alpha}\right]^2+\left[r^2e^{-j\alpha}\right]^3+\ldots\right) \tag{6.10}$$

This is a geometric series of which the sum is

$$A_{tot} = \frac{Ae^{j(\omega t\pm\phi)}}{1-r^2e^{-j\alpha}} \tag{6.11}$$

The intensity at P is proportional to the square of the magnitude of A_{tot} which we obtain by multiplying A_{tot} by its complex conjugate. The ratio of this intensity to the intensity at the center where $\theta = 0$ is then

$$\frac{I}{I_0} = \frac{(1-R)^2}{1-2Rcos\alpha+R^2} \tag{6.12}$$

where we have replaced r^2 by R, the intensity reflectivity of the surfaces. At any fixed wavelength and plate separation, α depends only on the position of P in the focal plane of the telescope lens and not on the position of S. Thus the ratio of the sum of the contributions to the intensity at P from all the incoherent atomic sources in the lamp to the sum at the center of the focused ring pattern is given by equation 6.12 which is, therefore, the general formula for the intensity in the focal plane.

The maxima of the intensity occur where $\frac{\alpha}{2\pi} = \frac{2D}{\lambda}cos\theta = m$, where m is an integer called the order of the interference. Changes in the value of $\frac{\alpha}{2\pi}$ are related to changes in D, λ, and θ by the differential relation

$$\delta\left(\frac{\alpha}{2\pi}\right) = \frac{2cos\theta}{\lambda}\delta D - \frac{2Dcos\theta}{\lambda^2}\delta\lambda - \frac{2Dsin\theta}{\lambda}\delta\theta \tag{6.13}$$

At the center (bull's eye) of the interference ring pattern, where $cos\theta = 1$, the order of interference can be changed from m to $m+1$ either by increasing D by $\Delta D = \lambda/2$ or by decreasing λ by $\Delta\lambda = \lambda\frac{\lambda}{2D} = \frac{\lambda}{m}$. As mentioned previously, quantity $\Delta\lambda$ is called the free spectral range. It is the maximum width of the Zeeman pattern of a given order of interference that can be displayed without overlapping the patterns of the adjacent orders. To express the free spectral range in terms of wave numbers (reciprocal wavelength) one uses the relation

$$\mid \Delta(\frac{1}{\lambda}) \mid \approx \frac{1}{\lambda^2}\Delta\lambda = \frac{1}{2D} \tag{6.14}$$

In a typical setup $D \approx 0.25cm, \lambda \approx 5000$ Å, $m \approx$ 10,000, and the free spectral range in wave numbers is $\frac{1}{2D} = 2.0$ cm^{-1}.

To see what equation 6.12 tells about how the intensity depends on very small displacements of the plates and on very small changes of the wavelength, we define two dimensionless parameters f and g such that $D = (1+f)m_0\lambda_0/2$ and $\lambda = (1+g)\lambda_0$. The parameter f measures the change in separation of the plates in units of $\frac{\lambda_0}{2}$ and is of the order of $\frac{1}{m_0}$. We will be interested in the effects of very small changes in wavelength for which typical values of g are also of the order $\frac{1}{m_0}$ so that $\frac{1}{1+g}$ can be approximated to high accuracy by $(1-g)$. In practical setups $\theta < 1^\circ$ so that we can replace $cos\theta$ by the approximation $1 - \frac{\theta^2}{2}$. Substituting the expressions for D and λ with these approximations in equation 6.12 and dropping the terms of negligible smallness, we obtain

$$\frac{I}{I_0} = \frac{(1-R)^2}{1 - 2Rcos\left[\pi m_0(1+f)(1-g)(1-\frac{\theta^2}{2})\right] + R^2} \tag{6.15}$$

Figure 7 is a plot of the intensity versus angle in the interferograms formed by a Fabry-Perot with $m_0 = 24,818$ and $R = 0.8$, illuminated by light with two wavelengths, $\lambda_1 = 5461$ Åand $\lambda_2 = \lambda_1(1 + 5 \times 10^{-6})$. The four sets of curves are for four different values of the plate separation. The dashed lines are the separate intensity curves for the two wavelengths, and the solid line is their sum. Figure 8 shows the summed intensities versus angle for the same Fabry-Perot and wavelengths, but for four different reflectivities.

Figure 9 shows plots of the intensity at the center of the interferogram $\theta = 0$ as functions of the plate separation for four reflectivities. This is the form of the interferogram/spectrogram you will record in the present experiment.

The intensity function has maxima in the focal plane on concentric circles to which are focused rays leaving the Fabry-Perot at angles θ such that $\frac{2D}{\lambda}cos\theta = m$, where m is an integer. Since we are dealing with small angles we again use the approximation $cos\theta \approx 1 - \frac{\theta^2}{2}$. If $\frac{2D}{\lambda} = m_0$, the mth maximum will lie at the angles $\theta_m = \sqrt{\frac{2(m_0-m)}{m_0}}$.

We now ask "By how much must the phase factor $\alpha = \frac{4\pi D}{\lambda}cos\theta$ change to decrease the intensity from a maximum value to half maximum?". Remembering that at a maximum the phase factor is an integral multiple of 2π, and using the identity $cos(2\pi n + \delta\alpha) = cos(\delta\alpha)$, we have from equation 6.12 the relation

$$\frac{(1-R)^2}{1 - 2Rcos(\delta\alpha) + R^2} = \frac{1}{2} \tag{6.16}$$

from which we obtain

$$cos(\delta\alpha) = 1 - \frac{(1-R)^2}{2R} \tag{6.17}$$

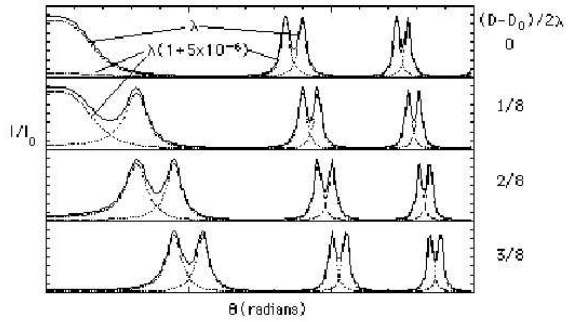

FIG. 7: Plot of intensity against angle in theoretical interferograms of two wavelengths differing in wavelength by 5 parts in a million produced by a Fabry-Perot with $\frac{2D_0}{\lambda_0} = 24,818$, and reflectivity R=0.8. The four plots are for four successively larger plate separations, the first differing from the fourth by $\frac{3}{8}$.

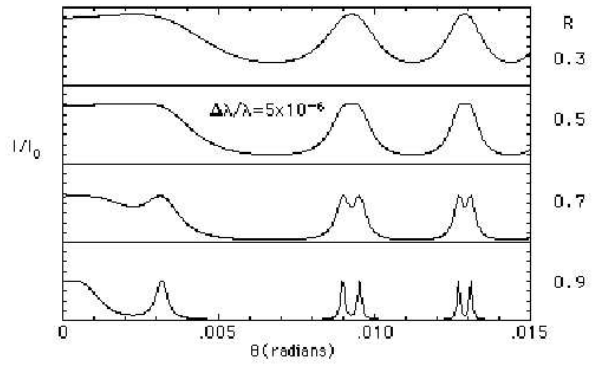

FIG. 8: Plot of intensity against angle in interferograms of light containing two wavelengths, for various reflectivities.

or, to a good approximation

$$\delta\alpha = \frac{1-R}{\sqrt{R}} \tag{6.18}$$

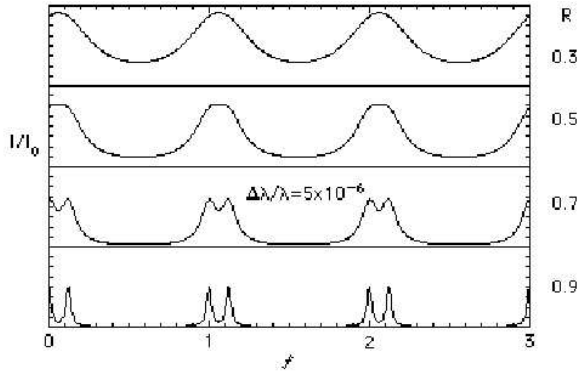

FIG. 9: Plot of intensity at the center of the interferogram against the separation of the FP mirrors for various reflectivities.

If we measure the intensity at $\theta = 0$ as a function of the separation, then the change in D to the half intensity point is

$$\delta D = \frac{\lambda}{4\pi}\frac{1-R}{\sqrt{R}} \tag{6.19}$$

The change in D between successive maxima is $\frac{\lambda}{2}$. Thus the resolution of the interferometer, defined as the ratio of these quantities and called the finesse, is

$$finesse = \frac{2\pi\sqrt{R}}{1-R} \tag{6.20}$$

[1] A. Melissinos, *Experiments in Modern Physics* (Academic Press, 1966).
[2] *Pieter Zeeman's Nobel Prize Lecture* (1902).
[3] P. Zeeman, Phil. Mag **43**, 226 (1897).
[4] A. Melissinos, *Experiments in Modern Physics* (Academic Press, 2003), ISBN QC33.M523, physics Department Reading Room.
[5] H. E. White, *Introduction to Atomic Spectra* (McGraw-Hill, 1934), physics Department Reading Room.
[6] J. Steinfeld, *Molecules and Radiation* (MIT Press, 1986), ISBN QC454.M6.S83, physics Department Reading Room.
[7] S. Gasiorowicz, *Quantum Physics* (John Wiley, 1996), 2nd ed., physics Department Reading Room.
[8] E.U.Condon and G.Shortley, *The Theory of Atomic Spectra* (Cambridge, 1959), ISBN QC454.C746, physics Department Reading Room.
[9] L. Landau and E. Lifshitz, *Quantum Mechanics* (Pergamon, 1974).
[10] E. Merzbacher, *Quantum Mechanics* (Wiley, 1961), ISBN QC174.1.M577, science Library Stacks.
[11] E. K. F.K. Richtmyer and T. Lauritsen, *Introduction to Modern Physics* (McGraw-Hill, 1955), ISBN QC21.R537, physics Department Reading Room.
[12] H. Semat, *Introduction to Atomic and Nuclear Physics* (Holt Rinehart and Winston, 1962), ISBN QC173.S469, physics Department Reading Room.
[13] G. Herzberg, Phil. Mag pp. 82–113 (1944).
[14] H. Schuler and E. Jones, Zeitschrift Fur Physik pp. 630–646 (1932).
[15] E. Hecht, *Optics* (Addison-Wesley, 2002), 4th ed., physics Department Reading Room.
[16] B. B. Rossi, *Optics* (Addison-Wesley, 1957), ISBN QC355.R831, physics Department Reading Room.

Optical Pumping of Rb Vapor

MIT Department of Physics
(Dated: February 2, 2010)

Measurement of the Zeeman splittings of the ground state of the natural rubidium isotopes; measurement of the relaxation time of the magnetization of rubidium vapor; and measurement of the local geomagnetic field by the rubidium magnetometer. Rubidium vapor in a weak (∼.01-10 gauss) magnetic field controlled with Helmholtz coils is pumped with circularly polarized D1 light from a rubidium rf discharge lamp. The degree of magnetization of the vapor is inferred from a differential measurement of its opacity to the pumping radiation. In the first part of the experiment the energy separation between the magnetic substates of the ground-state hyperfine levels is determined as a function of the magnetic field from measurements of the frequencies of rf photons that cause depolarization and consequent greater opacity of the vapor. The magnetic moments of the ground states of the ^{85}Rb and ^{87}Rb isotopes are derived from the data and compared with the vector model for addition of electronic and nuclear angular momenta. In the second part of the experiment the direction of magnetization is alternated between nearly parallel and nearly antiparallel to the optic axis, and the effects of the speed of reversal on the amplitude of the opacity signal are observed and compared with a computer model. The time constant of the pumping action is measured as a function of the intensity of the pumping light, and the results are compared with a theory of competing rate processes - pumping versus collisional depolarization.

1. PREPARATORY PROBLEMS

1. With reference to Figure 1 of this guide, estimate the energy differences (order of magnitude) in eV between each of the following pairs of states of Rb:
   (a) $5^2S_{1/2} - 5^2P_{3/2}$
   (b) $5^2P_{1/2} - 5^2P_{3/2}$
   (c) $5^2S_{1/2}(f = 2) - 5^2S_{1/2}(f = 3)$
   (d) $5^2S_{1/2}(f = 2, m_f = -1) - 5^2S_{1/2}(f = 2, m_f = 0)$ in a magnetic field of 1 gauss.

2. Derive the Landé g-factors for the ground state of the two rubidium isotopes using either the vector model or matrix mechanics for the addition of angular and magnetic moments.

3. In thermal equilibrium at 320K how many atoms in a mole of rubidium would one expect to find in the $5^2P_{1/2}$ state? What is the difference in the population of the lowest and highest magnetic substate of the ground state in a field of 1 gauss at that temperature?

4. Given two plane polarizing filters and a quarter wave plate, how do you make a beam of circularly polarized light?

5. What fractional contributions does the nucleus of a rubidium atom make to its (a) angular momentum (b) magnetic moment?

6. If the earth's field were that of a idealized 'point' magnetic dipole at the center and parallel to the rotation axis, then what would be the direction of the field at the latitude of Boston?

2. Introduction

A. Kastler discovered optical pumping in the 1950's and received the Nobel Prize for his work in 1966. In this experiment you will explore the phenomenon of optical pumping and its application to fundamental measurements in atomic and nuclear physics with equipment originally built for the Junior Lab shortly after the publication of Kastler's work. Various improvements have been made since then. Though its components are simple, the apparatus is capable of yielding accurate results that illustrate several of the fundamental principles of quantum theory and atomic structure. Among other possibilities it can be used to measure collisional relaxation phenomena, and the magnitude and direction of the local geomagnetic field.

3. ANGULAR MOMENTUM AND ATOMIC STRUCTURE

We will be concerned with the angular momentum and energy of neutral atoms of rubidium in a vapor under conditions in which each atom can be treated as a nearly isolated system. Such a system in field-free space has eigenstates with definite values of the square of the total angular momentum, $\vec{F} \cdot \vec{F}$, and of the component of angular momentum with respect to some given direction, F_z. According to the laws of quantum mechanics the eigenvalues of $\vec{F} \cdot \vec{F}$, and F_z are given by the expressions

$$\vec{F} \cdot \vec{F} = f(f+1)\hbar^2 \tag{3.21}$$

and

$$F_z = m_f \hbar \tag{3.22}$$

where f is an integer or half-integer, and m_f has one of the $2f+1$ values $-f, -f+1, ..., f-1, f$. In the absence of any magnetic field, the eigenstates with the same f but different m_f are degenerate, i.e. they have the same energy. However, an atom with angular momentum F generally has a magnetic moment

$$\vec{\mu} = g_f \frac{e}{2m} \vec{F} \tag{3.23}$$

where m is the electron mass, e is the magnitude of the electron charge, and g is a proportionality constant called the Landé g factor. If an external magnetic field is present, then the degeneracy will be lifted by virtue of the interaction between the external magnetic field and the magnetic moment of the atom. If the external field is sufficiently weak so that it does not significantly alter the internal structure of the atom, then the energy of a particular magnetic substate will depend linearly on the field strength, B, and the value of m_f according to the equation

$$E = E_0 + g_f m_f \mu_B B \tag{3.24}$$

where E_0 is the energy of the eigenstate in zero field and : $\mu_B \equiv \frac{eh}{4\pi m_e c} = 9.1 \times 10^{-21}$ ergs/gauss is the Bohr magneton. The g factor depends on the quantum numbers of the particular state and is of order unity. The difference in energy between magnetic substates in a magnetic field is called the magnetic, or Zeeman, splitting. By measuring this splitting in a known field one can determine the value of $g_f \mu_B$. Alternatively, given the value of $g_f \mu_B$ one can use a measurement of the splitting to determine the magnitude of an unknown magnetic field.

3.1. Interactions at the atomic and nuclear scales

A rubidium atom contains nearly 300 quarks and leptons, each with an intrinsic angular momentum of $\frac{\hbar}{2}$. Triplets of quarks are bound by the "color" force to form nucleons (protons and neutrons) with dimensions of the order of 10^{-13}cm. The nucleons are bound in nuclei with dimensions of the order of 10^{-12}cm by the remnants of the color force which "leak" out of the nucleons. Charged leptons (electrons) and nuclei are bound by electromagnetic force in atomic structures with dimensions of the order of 10^{-8}cm. Atoms are bound in molecules by electromagnetic force. Each of these structures - nucleons, nuclei, atoms and molecules - can exist in a variety of states. However, the lowest excited states of nucleons and nuclei have energies so far above the ground states that they are never excited in atomic physics experiments. Moreover, the size of the nucleus is tiny compared to the size of the electronic structure of the atom. Thus, for the purposes of understanding all but the most refined measurements of atomic structure, the nucleus and all it contains can be considered as a point particle characterized by its net charge, angular momentum, magnetic dipole moment, and in some circumstances, weak higher electric and magnetic moments. The problems of atomic physics are thereby reduced to that of understanding how the electrons and nucleus of an atom interact with one another and with external fields.

According to the shell model, the electronic configuration of rubidium is: $1s^2 2s^2 2p^6 3s^2 3p^6 3d^{10} 4s^2 4p^6 5s = 5^2S_{1/2}$ which specifies 36 electrons in closed (i.e. subtotal angular momentum=0) shells with principal quantum number n from 1 to 4 plus a single "optical" electron in a 5s orbital. The letters s, p, and d denote the electron "orbitals" with orbital angular momentum quantum numbers l=0, 1, and 2, respectively. (Note the 5s shell begins to fill before the 4d). The overall designation of the electronic ground state is $5^2S_{1/2}$, which is called "five doublet S one-half." "Five" specifies the principal quantum number of the outer electron. "S" specifies that the total orbital angular momentum quantum number of the electrons is zero. The term "one-half" refers to the subscript 1/2 which specifies the total angular momentum quantum number of the electrons. With only one electron outside the closed shells the total angular momentum of the ground state is due to just the spin of the outer electron. "Doublet" refers to the superscript 2=$2s$ +1 where s=1/2 is the total spin angular momentum quantum number; the word characterizes the total spin by specifying the number of substates that arise from the combinations of $\vec{L}$ and $\vec{S}$. In the alkali metals this amounts to a two-fold "fine structure" splitting of the energy levels of excited electronic states with $l \geq 1$ due to the interaction of the magnetic moments associated with the spin and orbital angular momenta of the outer electron. In such states the orbital and spin angular momenta can combine in just two ways to give $j = l \pm 1/2$. Just as in the case of two bar magnets pivoted close to one another, the state of lower energy is the one in which the spin and orbital magnetic moments are anti-parallel and the total (electronic) angular momentum quantum number is $j = l - 1/2$. The word "doublet" is retained for S states even though there is no spin-orbit interaction because $l = 0$, and consequently the ground state has no fine structure substates [1].

With the shell model as a framework one can explain quantitatively many of the low-energy atomic phenomena, like those involved in the present experiment, in terms of the following hierarchy of interactions, arranged in order of decreasing energy:

1. Interaction between the outer electron(s) and the combined coulomb field of the nucleus and inner closed-shell electrons, giving rise to states specified by the principal quantum numbers and the orbital angular momentum quantum numbers of the outer electrons and differing in energy by $\Delta E \approx 1eV$

2. Interaction between the magnetic moments associated with the spin and orbital angular momenta of

the outer electron(s), giving rise to "fine structure" substates differing in energy by $\Delta E \approx 10^{-3} eV$

3. Interaction between the total electronic magnetic moment and the magnetic moment of the nucleus, giving rise to "hyperfine structure" substates with $\Delta E \approx 10^{-6} eV$

4. Interaction between the total magnetic moment of the atom and the external magnetic field.

The torque resulting from the interaction between the magnetic moments associated with the spin and orbital angular momenta of the electrons causes $\vec{L}$ and $\vec{S}$ to precess rapidly about their sum $\vec{J} = \vec{L} + \vec{S}$. The much weaker interaction between the magnetic moments associated with $\vec{J}$ and the nuclear angular momentum $\vec{I}$ causes $\vec{J}$ and $\vec{I}$ to precess much more slowly about their sum $\vec{F} = \vec{J} + \vec{I}$. And finally a weak external magnetic field $\vec{B}$ exerts a torque on the magnetic moment associated with $\vec{F}$ that causes it to precess about $\vec{B}$ even more slowly. However, if the external field is sufficiently strong that the precession frequency of $\vec{F}$ about $\vec{B}$ approaches that of $\vec{J}$ and $\vec{I}$ about $\vec{F}$, then the dependencies of the separations between the substates on the external field become nonlinear, and the separations become unequal.

The angular momentum quantum numbers of the rubidium nuclei are i=5/2 for ^{85}Rb and i=3/2 for ^{87}Rb. According to the rules for adding angular momenta, the total angular momentum quantum number of the atom must be one of the values $j+i, j+i-1, j+i-2, ...|j-i+1|, |j-i|$. Thus each electronic state with a certain value of j is split into a number of hyperfine substates equal to $2j$+1 or $2i$+1, whichever is the smaller, with a separation in energy between substates that depends on the strength of the magnetic interaction between the total magnetic moment of the electrons and the magnetic moment of the nucleus. Since j =1/2 in the ground state, the number of hyperfine substates is just 2, and the values of f are 5/2+1/2=3 and 5/2-1/2=2 for ^{85}Rb and 3/2+1/2=2 and 3/2-1/2=1 for ^{87}Rb.

The magnetic moments of nuclei are of the order of the nuclear magneton ($\mu_N \equiv \frac{eh}{4\pi m_p c} = 5.0 \times 10^{-24}$ ergs/gauss) which is smaller than the Bohr magneton by a factor equal to the ratio of the proton mass to the electron mass, i.e about 2000 times smaller. The magnitude of the magnetic moment of a nucleus is $g_n \mu_n \sqrt{I(I+1)}$, where I is the angular momentum quantum number of the nucleus, μ_n is the nuclear magneton, and g_n is a gyromagnetic ratio arising from the configuration of the nucleons themselves. Empirically determined values for g_n are: $g_n = 1.3527$ for ^{85}Rb with I = 5/2 $g_n = 2.7505$ for ^{87}Rb with I = 3/2 Thus, regardless of how the electronic and nuclear angular momenta are combined, the nuclear magnetic moment makes a small contribution to the total magnetic moment of the atom. However, the nuclear angular momentum, quantized in units of $\hbar$ like the electronic angular momentum, makes a major contribution to the total angular momentum of the atom and, therefore, to any properties that depend on how the angular momenta are combined such as the Landè g factor and the multiplicities of magnetic substates.

Figures 1 and 2 are schematic energy level diagrams for the ground and lowest excited states of ^{85}Rb and ^{87}Rb in a weak magnetic field, showing how the ground and first excited electronic states can be imagined to split into successive sublevels as the various interactions mentioned above are "turned on". The energy scale is grossly distorted in order to display the hierarchy of structure in one figure. In fact, the separations between the Zeeman levels in a weak external field of $\approx$ 1 gauss are $\approx 10^8$ times smaller than the separation between the unperturbed 5S and 5P levels. The right most portions of Figures 1 and 2 represent the specific level structures with which we will be dealing in this experiment.

In the two lowest excited electronic states, designated $5^2P_{1/2}$ and $5^2P_{3/2}$, the valence electron has orbital angular momentum quantum number l =1. This combines with the electron spin to give a total electronic angular momentum quantum number j of 1/2 or 3/2. The energies of these two states differ by virtue of the "fine structure" interaction between the spin and orbital magnetic moments of the outer electron. Transitions from the hyperfine and magnetic substates of $5^2P_{3/2}$ and $5^2P_{1/2}$ to the hyperfine and magnetic substates of 5S produce photons in two narrow optical spectral regions called the rubidium D-lines at 7800 Åand 7948 Å. Transitions between the various energy levels can occur under a variety of circumstances, which include the following of particular interest in this experiment:

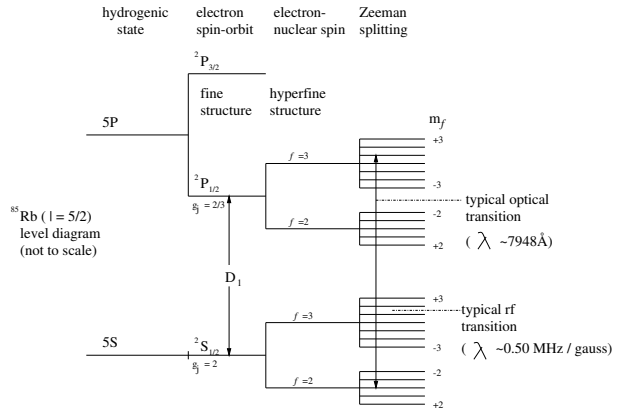

FIG. 1: Energy levels (not to scale) of ^{85}Rb as successively weaker interactions are turned on.

1. Electric dipole transitions between the 5S and 5P states; a) either absorption or stimulated emission induced by interactions with optical frequency photons having energies close to the energy difference between two atomic states. b) spontaneous emission Electric dipole transitions are restricted by the selection rules $\Delta l = \pm 1$, $\Delta f = 0$ or ± 1 except not $f = 0$ to f=0, $\Delta m_f = 0$ or ± 1

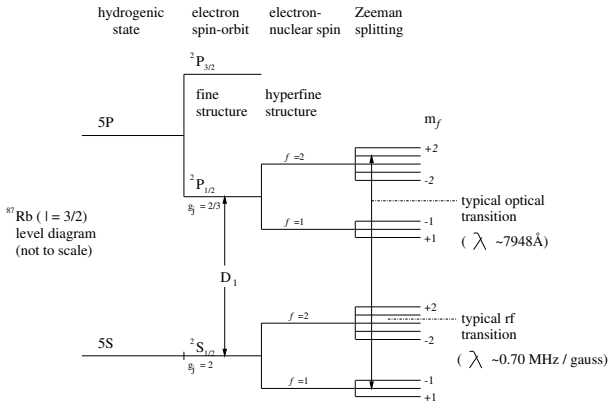

FIG. 2: Energy levels (not to scale) of ^{87}Rb as successively weaker interactions are turned on.

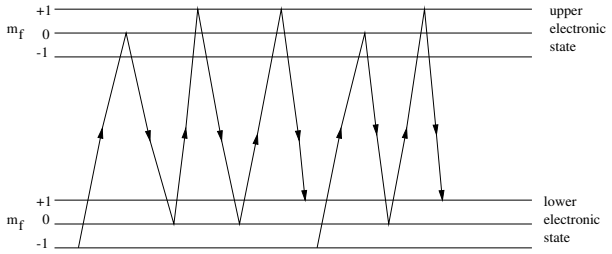

FIG. 3: Schematic histories of several atoms with magnetic substates undergoing optical pumping by circularly polarized light in a magnetic field.

2. Magnetic dipole transitions between magnetic substates induced by radio frequency photons with energies close to the energy differences of two Zeeman levels The selection rule is $\Delta m_f = \pm 1$.

3. Collision-induced transitions between the magnetic substates.

4. OPTICAL PUMPING

Under conditions of thermal equilibrium at temperature T the distribution of atoms among states of various energies obeys the Boltzmann distribution law according to which the ratio $\frac{n_1}{n_2}$ of the numbers of atoms in two states of energy E_1 and E_2 is

$$\frac{n_1}{n_2} = exp\left(\frac{E_2 - E_1}{kT}\right) \tag{4.25}$$

where $k = 8.62 \times 10^{-5}$ eV K^{-1} is the Boltzmann constant. With this formula we can calculate the fraction of rubidium atoms in the first excited electronic state in a vapor at room temperature for which $kT \approx 0.03eV$. The first excited state lies about 2 eV above the ground state. The Boltzmann factor is therefore $\approx exp^{-67} \approx 10^{-29}$, which implies that only about one atom in 10 kilograms is in an excited state at any given moment. On the other hand, the differences between the energies of magnetic substates in the weak fields used in this experiment are very small compared to kT at the temperature of the rubidium vapor. Thus, under equilibrium conditions, there is only a slight difference in the populations of the magnetic substates.

Optical pumping is a process in which absorption of light produces a population of the energy levels different from the Boltzmann distribution. In this experiment you will irradiate rubidium atoms in a magnetic field with circularly polarized photons in a narrow range of energies such that they can induce $5^2S_{1/2} \rightarrow 5^2P_{1/2}$ dipole transitions. However, absorption can occur only if the total angular momentum of the incident photon and atom is conserved in the process. If the incident photons have angular momentum $+\hbar$, the only allowed transitions are those in which $\Delta m_f = 1$. Thus every absorption produces an excited atom with one unit more of projected angular momentum than it had before the transition. On the other hand, the spontaneous and rapid ($\approx 10^{-8}s$) $5^2P_{1/2} \rightarrow 5^2S_{1/2}$ decay transitions occur with only the restriction $\Delta m_f = 0$ or ± 1. The net result is a "pumping" of the atoms in the 5S magnetic substates toward positive values of m.

The process is illustrated schematically in Figure 3 which depicts the histories of several atoms which are initially in various magnetic substates of a lower electronic state. Under irradiation by circularly polarized light they make upward transitions to magnetic substates of an upper electronic state subject to the restriction $\Delta m_f = +1$. Spontaneous downward transitions occur with $\Delta m_f = \pm 1, 0$. When an atom finally lands in the $m_f = +1$ substate of the lower electronic state it is stuck because it cannot absorb another circularly polarized photon.

The rate of spontaneous transitions among the magnetic substates is small. To reduce the rate of depolarizing collisions, the rubidium vapor is mixed with a "buffer" gas (neon) which has no magnetic substates in its ground electronic state and is therefore unable to absorb or donate the small quanta of energy required for magnetic substate transitions. The buffer atoms shield the rubidium atoms from colliding with one another and slow their diffusion to the walls. With the field in the direction of the beam, the most positive substate may be the one of highest energy. Alternatively, with the field in the opposite direction, that same substate would be the one of lowest energy. In either case the population of the extreme substate, whichever it may be, will increase at the expense of the other substates until, as in the actual experiment, there are few atoms left which can absorb the incident circularly polarized photons. Thus the intensity of the transmitted beam increases as the absorbing ability of the vapor diminishes, and it approaches an asymptotic value determined by the rate at which depolarizing collisions restore the atoms to substates which can absorb the polarized photons. In effect, the vapor is magneti-

cally polarized and optically "bleached" by the process of optical pumping, and the resulting distribution of the atoms among their possible quantum states is grossly different from the Boltzmann distribution. (The absorption of the photons also gives rise to a non-Boltzmann population of the $5^2P_{1/2}$ states, but the decay by electric dipole transitions is so rapid that the fraction of atoms in those states at any given time remains extremely small).

In principle, the population of the magnetic substates could be changed by simply turning the beam on and off with a mechanical chopper. Immediately after each turn-off depolarizing collisions would restore thermal equilibrium. When the beam is turned on again one would observe an opacity pulse, i.e. a transmission through the vapor which starts low and increases toward an asymptotic value as the pumping action proceeds and the balance between pumping and collisional depolarization is approached. However, this method has problems caused by the large changes in the signal levels when the pumping beam is turned on and off.

In the present experiment the intensity of the circularly polarized beam is kept steady and changes in the polarization of the vapor are produced by either 1) flooding the vapor with radio photons of the requisite resonant frequency and polarization to induce transitions between the magnetic substates by absorption and/or stimulated emission, or 2) suddenly changing the magnetic field.

With radio photons of the resonance frequency, rapid transitions are induced between the magnetic substates so their populations are kept nearly equal in spite of the pumping action and the vapor can absorb the circularly polarized optical photons. The resonant frequency, indicated by an increase in opacity, is a direct measure of the energy difference between the magnetic substates. Knowing the magnetic field and the resonant frequency, one can derive the value of the magnetic moment of the rubidium atom.

To see how the transitions are induced by a resonance rf field we represent the weak ($\ll 0.2$ gauss) linearly polarized rf magnetic field vector as a sum of two circularly polarized component vectors according to the identity

$$\vec{B}_{rf} = B_{rf}[\cos\omega t, 0, 0] = \frac{B_{rf}}{2}[\cos\omega t, \sin\omega t, 0] + \frac{B_{rf}}{2}[\cos\omega t, -\sin\omega t, 0] \quad (4.26)$$

where $\omega = \gamma B_0$ is the the Larmor precession frequency of the dipoles in the strong ($B_0 \approx 0.2 gauss$) DC field, $\gamma = \frac{g_F e}{2mc}$ is the gyromagnetic ratio of the atoms, and g_F is the Landé g factor. If we confine our attention to the circular component of the rf field rotating in the same sense as the Larmor precession of the moments, then we have the situation discussed by Melissinos (1966, page 344) in the context of nuclear magnetic resonance.

The effects of changing the Z-component of the field on the opacity of the vapor undergoing magnetic pumping depend on the speed, sign and amplitude of the change. One can study the behavior of polarized moments in changing fields and the depolarizing interactions in the vapor by observing the size and shapes of the resulting opacity pulses. The effect on the polarization of changing the field can be described as the effect of a changing torque on a gyroscope. It turns out that the motion of the net angular momentum, $\vec{L}$, of an ensemble of atoms in a magnetic field is governed by the classical equation

$$\frac{d\vec{L}}{dt} = \gamma\vec{L} \times \vec{B} \quad (4.27)$$

where $\vec{B}$ is the magnetic field, and γ is the gyromagnetic ratio of the individual atoms (Abragam 1961). If $\vec{B}$ is steady, the motion is a precession about the field direction with angular velocity γB and a constant value of the angle between $\vec{L}$ and $\vec{B}$. If $\vec{B}$ changes direction at a rate that is small compared to γB, then the angle between $\vec{L}$ and $\vec{B}$ will remain nearly constant, i.e. $\vec{L}$ will, in effect, follow $\vec{B}$. If, on the other hand, $\vec{B}$ changes direction at a rate that is large compared to γB, as in the case where one of its components passes through zero, then $\vec{L}$ cannot follow $\vec{B}$, and the angle between $\vec{L}$ and $\vec{B}$ can change radically. The effect of the field change on the polarization can be deduced from an observation of its effect on the opacity of the vapor.

5. APPARATUS

Figure 3 is a schematic diagram of the apparatus. Photons with energies in the narrow range in which they can induce $5S_{1/2} \rightarrow 5P_{1/2}$ transitions are obtained from a rubidium vapor lamp excited by a radio frequency generator. The latter subjects the vapor to a rapidly oscillating, high amplitude electric field. The result is an "rf discharge" in which free electrons are driven back and forth with sufficient energy to maintain a state of partial ionization as well as to excite valence electrons to the 5^2P and higher levels.

Some of the photons emitted in the decay of excited states pass through a narrow-band interference filter that transmits only the lower energy photons of the D-line doublet, i.e. the D1 photons produced in $5S_{1/2} \rightarrow 5S_{1/2}$ transitions and having wavelengths close to 7948 Å. The D1 photons have an energy distribution whose width, determined by pressure and Doppler broadening in the lamp, is sufficiently large to encompass the spread in energy differences between all the $5S_{1/2}$ and $5P_{1/2}$ magnetic substates.

Next the beam passes through a combination of linear polarizer and quarter-wave plate that transmits only photons with one sense of circular polarization, which means that every transmitted photon has a component of angular momentum in the direction of the beam equal to $\pm\hbar$, as the case may be. The beam traverses rubidium vapor

and a "buffer" gas (neon) contained at low pressure in a glass bulb.

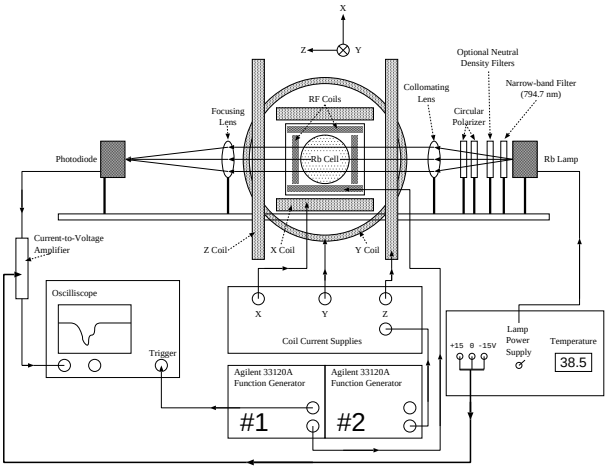

FIG. 4: Schematic diagram of the optical apparatus and electrical control and display equipment. Collimated light of wavelength 794.8 nm passes through Rubidium gas Located at the center of three mutually perpendicular Helmholtz coils. All three components of the magnetic field in the bulb can be controlled. After traversing the cell, the beam is focussed onto a photodiode whose signal is measured with an oscilliscope. When everything is properly adjusted, this configuration can be used to detect very small changes in opacity of the Rubidium Cell.

The rubidium vapor absorption cell is enclosed in a plexiglass oven which allows you to control the vapor pressure of rubidium by adjusting the temperature. The melting point of rubidium is 38.5°C. In addition to rubidium vapor, the cell contains neon gas at a pressure of several mm of mercury. The RF coil is used to irradiate the vapor with very low-energy RF photons to induce transitions between the magnetic substates and thereby depolarize the pumped rubidium atoms. Changes in the intensity of transmitted beam are measured by the solid-state photodiode. The intensity of the signal is displayed on one trace of a dual beam oscilloscope.

NOTE: Electronic equipment and ferromagnetic materials which might have significant effects on the magnetic field should be kept at least a meter away from the vapor cell.

Information on the operation of each component of the setup follows:

5.1. LIGHT SOURCE

The rubidium lamp is a small evacuated glass bulb containing rubidium placed between two coils energized by an RF power supply within the source box. To turn on the lamp:

1. Switch on the lamp power supply;
2. The lamp should reach a stable operating condition (mainly a matter of establishing temperature equilibrium in the lamp) in about 30 minutes. **You should turn on the Rb lamp at the very beginning of a lab session due to this length time required for equilibration.**

5.2. OPTICS

You will position the two lenses so that the beam is nearly parallel as it traverses the vapor and an image of the light source is focused on the photodiode. There is a 715 nm long-pass filter directly in front of the photodiode which is used to block most of the room lights while transmitting wavelengths above 715 nm. There is also a small plastic shroud used to block overhead light. These two components will allow you to conduct the majority of this experiment with the lights on. They can both be removed (be gentle with them) for the purpose of confirming that the focused beam is squarely hitting the detector.

You will want to be sure that your optical components share a common optical axis which should also be collinear with the center of the rubidium cell (the cell itself is already centered within the Helmholtz coils). This optical axis is 6.0" and 6.25" above the top of the optical rail for apparatus #1 and apparatus #2 respectively.

Arrange a polarizing filter and a quarter wave plate so as to circularly polarize the beam entering the bulb containing the rubidium vapor. Near the apparatus you will find a supply of linear polarizers, quarter wave plates, and optical bench mounts with which you can construct and test a circular polarizing system. (Avoid touching the optical surfaces with your fingers.) When you are satisfied that you have a combination that works, mount it between the interference filter and lens 1.

5.3. MEASURING CHANGES IN OPACITY

The current induced by light striking the photodiode is amplified by a Spectra-Physics Current Pre-amplier (mo.# 70710). This is an in-line current-to-voltage converter with a gain that ranges from 10^4 to 10^9. You want to set the gain such that you are getting the highest possible amplification without saturating the system. It is important that changes in the output voltage correspond linearly to changes in light intensity. You can test for this by checking to see that the voltage responds to both increases and decreases in light intensity.

Next, you will need to keep in mind that the changes in light intensity will be very small (probably on the order of millivolts) relative to the over all level of light intensity ($\sim$ 5 to 10 Volts). You can account for this in one of two ways:

- Set the oscilliscope to AC coupling.

- Zooming the scope in as far as possible on the baseline.

5.4. RF GENERATOR (Function Generator 1)

The Agilent 33120A Function Generator will serve as the radio frequency (RF) source. The function generator should be connected directly to the RF coils that are coaxial with the Z-axis. The coils emit RF photons linearly polarized in the Z direction that excite transitions between the magnetic substates of the $5S_{1/2}$ electronic ground state.

The configuration of the function generator will depend on which portion of the experiment you are performing. Specifically, you will use it to sweep through a range of RF, to supply a constant RF, and to possibly emit bursts of RF. An amplitude of 300 mV should work well for generating depolarizing RF.

5.5. HELMHOLTZ COILS

Helmholtz coils are pairs of identical circular coaxial coils separated by a distance equal to their radius and carrying identical currents. They produce a highly uniform magnetic field over an extended region near their geometrical center given by

$$B_I = \frac{\mu_0 R^2 N I}{[R^2 + (R/2)^2]^{3/2}} = \frac{8\mu_0 N I}{\sqrt{125}R} \qquad (5.28)$$

where R is the radius of the coils in meters, I is the current through the coils in Amperes, N is the number of turns and $\mu_0 = 4\pi \times 10^{-7}$ Wb $A^{-1}m^{-1}$. Remember also that 1 Wb m^{-2}=1 Telsa = 10^4gauss. The dimensions of the Helmholtz coils used in this experiment are listed in Table I.

Axis	Quantity	Value 1	Value 2
X	Turns per Coil	50	50
X	Avg. Diameter	14.3	14.3
X	Avg. Separation	7.3	7.1
Y	Turns per Coil	75	75
Y	Avg. Diameter	17.8	18
Y	Avg. Separation	7.5	7.5
Z	Turns per Coil	180	180
Z	Avg. Diameter	22.5	22.4
Z	Avg. Separation	11.0	11.0

TABLE I: Specifications for both sets of Helmholtz Coils. All dimensions in inches

1. Vertical (X-axis) Field Coils: These are used to control the vertical component of the magnetic field. Note that the optical axis of the apparatus is aligned within 17° of the earth's magnetic north-south direction. This means that after cancellation of the vertical component of the earth's field the remaining field will be nearly axial.

2. Lateral (Y-axis) Field Coils: These are used to eliminate any lateral component of the ambient field which results from not having the optical bench perfectly aligned with the magnetic north-south direction.

3. Longitudinal (Z-axis) Field Coils: As with the X and Y-axis coils, the current through the Z-axis coils is controled through the Helmholtz Coils Power Supplies Panel. However, in the case of the Z-axis coils, there is a switch to toggle the current source for these coils between the adjustable DC power supply and an external source, namely the second Agilent Function Generator. You will use the function generator when a time-varying (sawtooth or square-wave) current is needed.

   The function generator is designed to output to a 50 Ω load. The resistance of the Z-Axis Helmholtz coils will probably only be about 13 Ω. However an additional resistor has been added to the Helmholtz Coils panel to make the total resistance of the external input terminal $\sim 50\Omega$. Yet you will need a way to know how much current is flowing through the Z Coils as a function of time. Thus when using the function generator, you will want to use a BNC T-connector to look at the output of the function generator on the oscilliscope to see what voltage is really being applied to the coils. If you combine this with a measurement of the total resistance of the circuit, you should be able to convert this voltage to a current.

   You will use the square wave feature to simultaneously flip the Z-axis field and change its magnitude. The effect this has on the magnetization of the rubidium vapor depends on how the switching time compares with the precession period of the atoms. This may be important in understanding how changes in the magnitude of the X-coil current effects the waveform of the opacity signal. (You can explore the effect of switching time with the program called "Optical Pumping Simulation" on the Junior Lab PC's - see Appendix A.)

5.6. OVEN HEATER

The vapor cell is in an oven made of plexiglass heated by forced hot air from a blower beneath the table. Turn on the blower, and adjust the Variac for proper temperature. The heating systems on the the two appartuses are different; each Variac has been marked to indicate what setting will provide a stable oven temperature of

$38 - 40°$ C. Start out with the Variac 20% above this setting for the first ten minutes and then reduce to this setting to maintain the desired temperature **You should turn on the heater at the very beginning of the lab session so that an equilibrium temperature is reached after about 30 minutes.**

6. EXPERIMENTS

QUANTITIES YOU CAN MEASURE

1. Separation between the magnetic substates of the ground states of the two natural rubidium isotopes as a function of magnetic field strength.
2. The Landé g-factors and their ratio for the ground states of the two isotopes.
3. e/m
4. The relative abundance of the two isotopes.
5. The magnitude and direction of the ambient field.

6.1. DEPOLARIZATION BY RF RESONANCE: MEASUREMENT OF THE MAGNETIC MOMENTS OF THE RUBIDIUM ISOTOPES; MEASUREMENT OF THE AMBIENT MAGNETIC FIELD

In this experiment the vapor is continuously optically pumped, resulting in a high degree of polarization of the atomic angular momenta in the gas traversed by the pumping beam. After about one-tenth of a second of pumping, an equilibrium is reached at which the rate of polarization by pumping of the atoms along the beam equals the rate of depolarization by collisions. At that point the vapor becomes relatively transparent because the number of atoms capable of absorbing the circularly polarized photons becomes constant.

6.1.1. Constant Magnetic Field, Varying Radio Frequency

The rate of depolarization can be increased by flooding the vapor with low-energy RF photons tuned to the frequency of the magnetic substate transitions,

$$f = \frac{\Delta E}{h} = \frac{g_F \mu_B B_z}{h} \tag{6.29}$$

where ΔE is the difference in energy between adjacent magnetic substates. (The frequency required to induce transitions in ^{85}Rb ($i = 5/2$) is approximately 0.5 megahertz per gauss). Photons with the resonant frequency of a particular isotope induce both upward transitions (absorption) and downward transitions (stimulated emission) among the magnetic substates of the ground electronic state of that isotope. The result is an increase in the absorption of the pumping beam.

The resonant frequencies depend on the magnitude of the total field $|\vec{B}|=(B_x^2 + B_y^2 + B_z^2)$and not just on its Z-axis component. It is left to you to compute the field produced by the Helmholtz coil from measurements of the coil parameters and the current.

The digital oscilloscope will serve as a high resistance voltmeter with the trigger mode set to "auto". Estimate at what frequency you expect to see the ^{85}Rb resonance and then use the knob on the function generator to slowly sweep through this frequency range. If things are set up correctly you should see a noticeable shift in the baseline. Before you attempt this, do you expect the signal level to increase or decrease as you pass through a resonance?

Once you have found the ^{85}Rb resonance you should be able to quickly calculate (in your head) the frequency at which the ^{87}Rb resonance will occur. Once you have successfully identified both of these resonances manually, you can program the function generator to perform a sweep through an appropriate frequency range in order to determine the resonant frequencies more precisely. To do this adjust the oscilloscope so that the entire horizontal axis spans a time equal to twice the sweep time (this way you will be able to distinguish real resonant features from noise). Then use the function generator's SYNC output to trigger the scope.

In both manual and programmed sweeps you will need to watch out for the effects of harmonics of the fundamental oscillator frequency. These harmonic resonances will occur if the amplitude of the frequency generator is set too high.

In this part of the experiment you should aim to obtain the following results:

- magnetic moments of the rubidium atoms in their ground state
- precise determination of the ratio of the Landè g-factors of the two isotopes
- the magnitude and direction of the ambient magnetic field

The following is an outline of a possible procedure:

1. Set the Z, Y, and X-coil currents to zero.
2. Search for the resonance frequencies of the two isotopes in the ambient field.
3. Adjust the X-coil current step-by step so as to minimize the resonant frequency (by bucking out the vertical component of the ambient field. Tabulate and plot (in your lab book) the X-current and the two resonance frequencies at each step. Trace the hyperbolic relations of frequency versus current on either side of the minima.

4. With the X current set at the value for the minimum resonance frequencies, adjust the Y-coil current in the same manner, and set it to the value for the new minimum resonance frequencies.

5. Finally, tabulate and plot the Z-coil current and resonance frequencies on both sided of the minimum, and see how low a resonance frequency you can achieve (it should be possible to go as low as 10 kHz).

With the data obtained in this way and the coil dimensions, you will have all the information you need to derive the required results. You can use the Digital Magnetometer (with milligauss resolution) to measure and verify your results for the magnitude and direction of the ambient field. It can also be useful for checking that the helmholtz coils are producing the fields you expect.

6.1.2. Constant Radio Frequency, Varying Magnetic Field

By inspection of (6.29), one can see that the resonance depends on the relation between the magnetic field and the frequency of the RF. So in addition to sweeping through a range of frequencies for a constant magnetic field, we can also detect resonances by linearly varying the magnetic field in a constant RF. Rearranging (6.29), we see that:

$$B_z = \frac{hf}{g_F \mu_B} \tag{6.30}$$

To implement this experimentally, start by setting Function Generator 1 to a constant frequency, say 100 KHz. Use your results from the previous section to buck out the X and Y components of the magnetic field. Then you will want to configure Function Generator 2 with a sawtooth ramp that will cover an appropriate range of the Z-axis magnetic field.

From (6.30), you can quickly calculate the magnetic field at which resonance will occur for both ^{85}Rb and ^{87}Rb. Then, you can determine the current that will be required to generate this field from (5.28) and measurements of the Z-axis Helmholtz coils.

Then you are left with the task of calculating the voltage range you must specify for the sawtooth on the function generator. To determine this, you will need to measure the resistance of the Helmholtz coils (and the cables that connect it to the function generator). Use a multimeter to measure the total resistance of the Helmholtz coils and associated cables.

Remember that you will need to measure either the voltage across or the current through the coils directly since you cannot trust the values on the function generator.

How many resonant peaks do you expect to see? To answer this, first recall that magnetic substate splitting depends only on the magnitude of the magnetic field and not on the direction. In other words, it does not matter if the resonant value of the field is positive or negative. This would suggest an even number of resonant peaks. However, if you are sweeping through both positive and negative values of the magnetic field, what will happen when the field is very close to zero? What do you expect to happen as you sweep through the value for zero magnetic field (i.e. the current that will produce a field in the Helmholtz coils that will exactly cancel the ambient magnetic field)?

This procedure should provide you with an alternate way of determining the Z-component of the ambient magnetic field.

6.2. ALTERATION OF THE POLARIZATION BY CHANGES OF THE MAGNETIC FIELD

Buck out the vertical and lateral components of the earth's field with the X and Y coils, as above. The Z-coil current can be alternately turned on and off by using a square wave on the the second function generator. The waveforms representing the opacity as a function of time after turn-on and turn-off can be observed and captured on the digital oscilloscope with the opacity signal displayed on one beam, the Z-coil current displayed on the other beam, and the sweep triggered by the `SYNC` output of the function generator. Precise measurements of the waveforms in the form of amplitude versus time can be made with the horizontal (TIME) and vertical (VOLTAGE) cursors of the digital oscilloscope. (Note that the time constants of the rise and fall of the current in the Helmholtz coil are different.) Record and explain the effects on the waveforms of various changes in the conditions. For example:

1. Change the strength of the field.

2. Change the pumping rate by interposing neutral density filters in the light beam. Several filters of optical density 0.1 are provided. Recall that optical density, D, is related to transmission, T, by $D = \log_{10} 1/T$

3. Change the density of the rubidium vapor by changing the bulb temperature.

The time constant of the change in opacity following a sudden change in the magnetic field is determined by two competing factors - the intensity of the pumping beam and the rate of disorientation of the atoms through collisions which enhances the "relaxation" and return of the pumped system to its normal state.

You should work out the mathematical theory of the competition between pumping and collisional depolarization in order to interpret your results. (The problem is analogous to that of filling a bucket with a leak in the bottom.)

7. Possible Theoretical Topics

1. Derivation of the Landè-g factors for the two rubidium isotopes, including the effects of the nuclear magnetic moments.

2. Variation of the opacity a) when the field is flipped; b) if the pumping beam were suddenly turned on, and after some time, turned off.

3. Theory of the Helmholtz coils and numerical calculation of the field off axis.

---

[1] S. Gasiorowicz, *Quantum Physics* (Wiley, New York, 1974), qC174.12.G37 Physics Department Reading Room.

[2] A. Abragam, *Principles of Nuclear Magnetism* (Oxford University Press, New York, 1961), qC762.A158 Physics Department Reading Room.

[3] R. Bernheim, *Optical Pumping: An Introduction* (W.A. Benjamin, New York, 1965), qC357.B527 Physics Department Reading Room.

[4] A. C. Melissinos, *Experiments in Modern Physics* (Academic Press, Orlando, 1966), qC33.M523 Physics Department Reading Room.

[5] R.K.Richtmyer, E.H.Kennard, and T.Lauritsen, *Introduction to Modern Physics* (McGraw-Hill, New York, 1955), qC21.R537 Physics Department Reading Room.

[6] R. Benumof, Amer. Journ. of Phys. **33**, 151 (1965), physics Department Reading Room - Journal Collection.

[7] Nagel and Hayworth, Amer. Journ. of Phys. **34**, 553 (1966), physics Department Reading Room.

[8] R. Evans, *The Atomic Nucleus* (McGraw-Hill, New York, 1955), chap. 5.5, qC174.12.G37 Physics Department Reading Room.

[9] H. Semat and J. Albright, *Introduction to Atomic and Nuclear Physics* (Holt, Rinehart and Winston, New York, 1972), chap. 9: "Optical Spectra and Electronic Structure", pp. 256–300.

Pulsed NMR: Spin Echoes

MIT Department of Physics
(Dated: February 2, 2010)

Magnetic resonances of protons in various substances are studied by the techniques of pulsed NMR and the measurement of spin echoes. Various substances containing protons (water, glycerine, etc.) are placed in a uniform magnetic field and subjected to pulses of a transverse ∼7 MHz rf magnetic field in near resonance with the Larmor precession frequency of the protons. The spin-lattice and spin-spin relaxation time constants are determined from measurements of the free-induction signals and the spin echoes produced by various combinations of rf pulses. Temperature effects are observed in glycerine, and the effects of paramagnetic ions on the relaxation time constants in water are measured. The magnetic moments of the proton and of the fluorine nucleus are derived from the data.

1. PREPARATORY QUESTIONS

1. Show that the Larmor precession angular velocity with which a particle with spin angular momentum $\left|\vec{I}\right| = I\hbar$ and magnetic dipole $\vec{\mu} = \gamma\vec{I}$ precesses in a uniform magnetic field $\vec{B_0}$ is independent of the angle between $\vec{\mu}$ and $\vec{B_0}$ and given by

$$\omega_0 = \gamma B_0 = (g\mu_N/\hbar)B_0. \tag{1.31}$$

   g is the counterpart of the Landé g-factor in atomic spectroscopy and is given by

$$g = (\mu/\mu_N)/I, \tag{1.32}$$

   where μ_N is the nuclear magneton, $e\hbar/2m_p$.

   For protons, $g = 5.58$, so $\gamma = 26.8$ x10^3 radians sec^{-1} gauss^{-1} , corresponding to 4.26 MHz / kGauss. (1 Gauss = 10^{-4} Tesla.)

2. Derive the classical expression for the potential energy of a magnetic dipole in a magnetic field.

3. According to quantum mechanics the component of angular momentum in a given direction, e.g. the direction of $\vec{B_0}$, is an integer or half-integer multiple of $\hbar$. Write an expression for the energies U_m, for the various possible states of a nucleus with total angular momentum quantum number I in a magnetic field. Draw diagrams of U vs B_0 over the range 0 to 10,000 Gauss, showing the variation with B_0 ("splitting") of the energy levels of the proton and fluorine magnetic moments.

4. Show on the above diagrams the frequencies of photons which would cause transitions among the various levels at $B_0 =$ **1770 Gauss**. Confirm that the photon frequencies are the same as the corresponding Larmor frequencies.

5. The samples used in the NMR measurements contain very large numbers of the dipoles being studied. These interact with one another and are in thermal equilibrium at room temperature. The relative populations of their allowed energy states therefore follow the Boltzmann distribution, namely $N \propto \exp^{-E/kT}$. Calculate the fractional difference in the populations of the magnetic states of the proton in a sample at room temperature in a magnetic field of **1770 Gauss**, i.e. $(n_+ - n_-)/(n_+ + n_-)$.

2. Progress Check

By the end of your 2nd session in lab you should have a determination of the nuclear magnetic moment of fluorine in units of the nuclear magneton. You should also have a preliminary value of t_2 for 100% glycerine.

3. Introduction

The NMR method for measuring nuclear magnetic moments was conceived independently in the late 1940's by Felix Bloch and Edward Purcell [1–3]. Both investigators, applying somewhat different techniques, developed methods for determining the magnetic moments of nuclei in solid and liquid samples by measuring the frequencies of oscillating electromagnetic fields that induced transitions among their magnetic substates resulting in the transfer of energy between the sample and the measuring device. Although the amounts of energy transferred are extremely small, the fact that the energy transfer is a resonance phenomenon enabled it to be measured. Bloch and Purcell both irradiated their samples with a continuous wave (cw) of constant frequency while simultaneously sweeping the magnetic field through the resonance condition. Cw methods are rarely used in modern NMR experiments. Radiofrequency (rf) energy is usually applied in the form of short bursts of radiation (pulse nmr) and the effects of the induced energy level transitions are observed in the time between bursts. It is experimentally much easier to detect the extremely small effects of the

transitions if this detection phase is separated in time from the multi-watt rf burst phase. More importantly, as we shall see, it is much easier to sort out the various relaxation effects in pulse nmr experiments. The present experiment demonstrates the essential process common to all NMR techniques: the detection and interpretation of the effects of a known perturbation on a system of magnetic dipoles embedded in a solid or liquid. In addition, the effects of perturbations caused by the embedding material yield interesting information about the structure of the material.

3.1. Classical Picture of Spin Dynamics

One can describe the dynamics of a particle with spin in a magnetic field by drawing an analogy with a gyroscope in a gravitational field. The spin vector precesses about the field direction and then, as energy is transferred to or from the particle, the angle between its spin axis and the field axis gradually changes. This latter motion is called nutation.

The trouble with the gyroscope analogy would appear to be that an individual spin which obeys quantum mechanics cannot nutate continuously, since its projection on the field direction is quantized. Bloch, in 1956, proposed a vector model in which he showed that although nuclear spins obey quantum laws, the ensemble average taken over a large number of spins behaves like a classical system, obeying the familiar laws of classical mechanics. Thus one can gain significant insight by a classical analysis of a spinning rigid magnetized body in a magnetic field.

Following the discussion given by [4], we consider the motion of a nucleus with angular momentum $\vec{I}\hbar$ and magnetic moment $\vec{\mu} = \gamma\hbar\vec{I}$ in a magnetic field $B = B_0 + B_1$ composed of a strong steady component $B_0\hat{k}$ and a weak oscillating component $B_1 \sin(\omega t)\hat{\imath}$ perpendicular to B_0, where $\hat{\imath}, \hat{\jmath}, \hat{k}$ are the unit vectors in the laboratory reference frame xyz. The quantity γ is called the gyromagnetic ratio. (In the present experiment, the strong steady field has a magnitude of several kiloGauss; the weak oscillating field is the field inside a small solenoid 2 cm long, wound with 10 turns, and connected to a crystal-controlled fixed-frequency generator and wideband power amplifier producing an rf alternating current with a peak amplitude of $\sim$ 1 mA at 5.00 x 10^6 Hz. A simple calculation will confirm that under such conditions $B_1 \ll B_0$). The equation of motion of the particle is

$$\frac{d\vec{I}}{dt} = \gamma\vec{I} \times \vec{B} \tag{3.33}$$

If $B_1 = 0$, the motion in a reference frame fixed in the laboratory is a rapid precession of the angular momentum about the direction of $\vec{B_0}$ (the z axis) with the Larmor precession frequency γB_0, as shown in one of the preparatory questions. To understand the perturbing effects of the small-amplitude oscillating field on the motion we first represent it as the vector sum $\vec{B_1} = \vec{B_r} + \vec{B_l}$ of two counter-rotating circularly polarized components given by the equations

$$\begin{aligned} \vec{B_r} &= \tfrac{1}{2}(B_1 \cos\omega t\ \hat{\imath} + B_1 \sin\omega t\ \hat{\jmath}) \\ \vec{B_l} &= \tfrac{1}{2}(B_1 \cos\omega t\ \hat{\imath} - B_1 \sin\omega t\ \hat{\jmath}), \end{aligned} \tag{3.34}$$

where the subscript l denotes the component rotating in the direction of rapid precession (the proton precesses in the left hand direction as can be seen by solving Eq. 3.33), and r denotes the component rotating in the opposite direction.

Next we consider the situation from the point of view of an observer in a reference frame $x'y'z'$ rotating in the direction of precession with angular velocity ω and unit vectors:

$$\begin{aligned} \hat{\imath}' &= \cos\omega t\ \hat{\imath} + \sin\omega t\ \hat{\jmath} \\ \hat{\jmath}' &= -\sin\omega t\ \hat{\imath} + \cos\omega t\ \hat{\jmath} \\ \hat{k}' &= \hat{k}. \end{aligned} \tag{3.35}$$

In this rotating frame $\vec{B_r}$ is a constant vector $(B_1/2)\hat{\imath}'$, $\vec{B_l}$ is rotating with angular velocity -2ω, and the rapid precession will have angular frequency $\gamma(B_0 - \omega/\gamma)$, as though the particle were in a field whose z component is B_0 plus a fictitious field in the opposite direction of magnitude ω/γ. Suppose now that ω is adjusted so that $\omega = \gamma B_0$. Then the rapid precession will vanish, i.e. its frequency in the rotating frame will be zero, and the particle will precess slowly about the direction of the steady field $(B_1/2)\hat{\imath}'$ with angular velocity $\gamma B_1/2$, with only a tiny flutter averaging to zero due to the counter-rotating component. If I is initially parallel to B_0 (quantum mechanics not withstanding to the contrary), then in time $\pi/(\gamma B_1)$ the spin direction will precess exactly 90°. Putting I in the $x'y'$ plane, perpendicular to B_0. If the oscillating field is now turned off, the particle will be left with its magnetic moment in the $x'y'$ plane and, from the point of view of an observer in the laboratory frame, it will be rotating in the xy plane with angular frequency γB_0 about the z direction.

According to the Bloch theorem, the result of this classical treatment of the motion of a single magnetized spinning body is actually valid for an ensemble of quantized magnetic moments. Consider such a sample containing protons (hydrogen nuclei) placed between the poles of the magnet. According to the Boltzman distribution law, if the sample is in thermal equilibrium at temperature T, then the ratio of the number of protons n_+ with z components of spin up to the number with z components down is

$$n_+/n_- = \exp^{(E_+ - E_-)/kT} = \exp^{\mu_p B_0/kT}, \tag{3.36}$$

where μ_p is the magnetic moment of the proton. At room temperature in a field of several kilogauss this ratio is only slightly greater than one, which means that the magnetization due to alignment of the proton moments in the z direction is very slight. Nevertheless, if the ensemble is rotated 90 deg by application of an rf field under the conditions described above for just the correct amount of time (a " 90 deg rf burst"), then the nuclear magnetization will end up in the plane perpendicular to B_0 and precess with angular velocity γB_0 about the z direction. The precessing magnetization creates an alternating magnetic flux in the solenoid which, according to Faraday's law, induces an rf voltage. This rf voltage can be readily detected after the rf burst has been terminated, thereby proving that the resonance condition was achieved and that the applied frequency was equal to or very close to the precession frequency of the protons. Knowledge of the field strength and the resonance frequency allows the determination of the gyromagnetic ratio of the proton, which is a measurement of fundamental importance in nuclear physics.

To detect the nuclear-induced rf signal of angular frequency γB_0 that appears across the terminals of the solenoid immediately after the 90 deg rf burst, it is mixed with a steady signal of frequency ω from the fixed oscillator to produce a beat signal of comparatively low frequency $|\gamma B_0 - \omega|$ which can be observed directly on an oscilloscope. Of course, if ω is adjusted to be precisely equal to γB_0, as in the above discussion, then the beat frequency is zero and the output is a dc voltage proportional to the sine of the difference in phase between the induced signal and the reference voltage. In this mode the rf mixer becomes a phase detector. The 90° rotation of magnetization still works even if ω is slightly off the resonant condition, in which case the beat signal is readily observed. However, it doesn't last forever. It decays because of three distinct effects:

1. The field of the magnet is not perfectly uniform so that the protons in different parts of the sample precess at slightly different frequencies and get out of phase with one another, thereby gradually decreasing the net magnetization of the sample. This effect, although physically the least interesting, is always the dominant effect.

2. Protons in any given substance are generally located in several different molecular environments in each of which the precession frequency will be perturbed in a slightly different amount by magnetic dipole interactions. As in 1) the result is a gradual loss of phase coherence and a decay of the resultant magnetization.

3. Electromagnetic interactions between the protons and the surrounding particles cause transitions between the spin up and spin down states whose coherent combination is manifested as magnetization rotating in the xy plane. The result is a gradual decay of these coherent combinations and a return to the state of thermal equilibrium in which the magnetization is in the z direction and therefore no longer capable of inducing a signal in the solenoid.

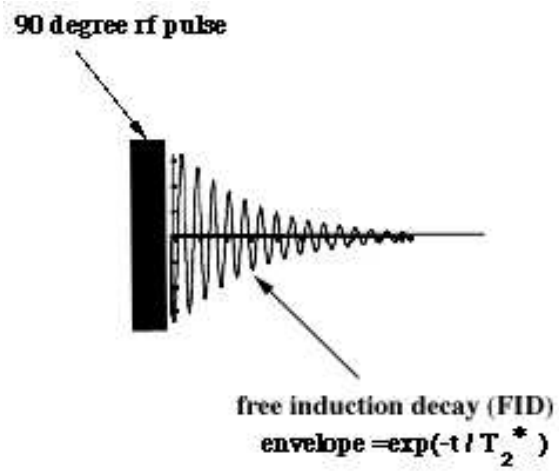

FIG. 1: The Free Induction Decay.

The oscillatory induced signal modulated by a decaying exponential Figure 1 is referred as the Free Induction Decay (FID.) An excellent reference describing these relaxation effects is given in [5] and is available from the Junior Lab e-library.

3.2. Spin-Lattice Relaxation Time, T_1

Effect number 3) is thermal relaxation, and its rate is an interesting measure of the coupling of the protons to their environment. It is characterized by a time constant denoted by T_1, called the spin-lattice or longitudinal relaxation time. T_1 is the lifetime of the spins in a given energy state and is equal to the time constant for the exponential return to the Boltzmann distribution after the Z-component of the magnetization has been disturbed from equilibrium. This decay process is governed by the ease with which the nuclei are able to give up their energy to their surroundings. In effect, spin-lattice relaxation is a cooling process; an even population distribution implies an infinite temperature and as cooling occurs, after the pulse, the temperature falls, allowing the excess population to return to its equilibrium state. Transfer of energy from the spins to the lattice requires that there be a fluctuating magnetic field with Fourier components vibrating near the Larmor precession frequency in order to induce NMR transitions. The field originates from magnetic dipoles which are in thermal agitation.

3.3. Spin-Spin Relaxation Time, T_2

Fig. 1 characterizes the FID (Free Induction Decay). T_2^* is the name given to the observed value of the decay constant and is the time for the transverse magnetization to decrease to 1/e of the value it had immediately after the pulse. This normally observed phenomena consists of two components

$$1/T_2^* = 1/T_2 + \gamma \Delta H_0 \tag{3.37}$$

where T_2 is the spin-spin, or transverse relaxation time and ΔH_0 is the inhomogeneity of the magnetic field over the sample volume. The second term on the right is always larger than $1/T_2$ and is sometimes referred to in the literature as $1/T_2'$.

Effect number 2) above is characterized by T_2. It is the basis for the powerful method of pulsed NMR chemical analysis based on measurement of the various perturbed precession frequencies due to the various locations of the protons within the molecule. Given the spectrum of these frequencies for a new complex organic compound, an expert can practically write out the chemical formula. The time it takes for the transverse magnetization to die out after a sample is perturbed by an rf pulse is a measure of this process. As we discussed above, a 90° pulse leaves the sample with a net magnetization that lies in the x-y plane and precesses about the z axis. With the passage of time, the magnetic moments interact with one another, and lose their phase coherence in the x-y plane. This process does not involve the loss of any energy from the spin system.

In many cases, the same physical mechanisms determine T_1 and T_2 so that they are equal. The cases of interest are those where there are additional mechanisms for spin-spin relaxation such that T_2 is shorter than T_1. After a 90° pulse all phase coherence may be lost before any substantial z magnetization is recovered. The transverse magnetization, and thus also the rf voltage induced in the sample coil, fall off as the phase coherence is lost. The dominant effect of magnet inhomogeneity, which could be fatal for such precision measurements, can be virtually eliminated by the remarkable invention of Hahn who discovered the phenomenon of "spin echoes" [6, 7].

3.4. Spin Echoes

To see how a spin echo is produced, consider a typical sample which has an enormous number of protons, of the order of 10^{23}. They can be divided into millions of ensembles, each one of which consists of a still enormous number of protons in a region where the external field has values within a very narrow range. Each ensemble will have a certain net magnetization which contributes to the total magnetization, but each such magnetization

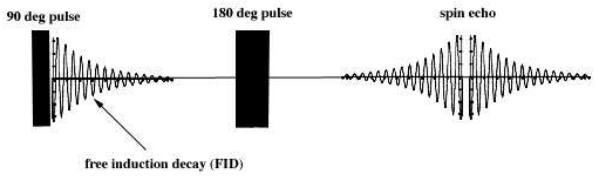

FIG. 2: The NMR signal observed when the applied rf frequency is offset slightly from the Larmor frequency. The fast oscillations corresponds to the beat between the two frequencies.

will precess with a slightly different frequency and therefore gradually get out of phase with respect to the others. Suppose that after a decent interval a second rf burst of double duration, i.e. a 180° burst, is applied to the sample. The magnetization of each ensemble will be precessed through 180°, ending back in the xy plane where it will resume its precession motion. But now the accumulated phase differences between the various ensembles are all precisely reversed. Those that were ahead of the average are now behind by the same amount, and as the precession proceeds, the dephasing of the ensembles is gradually reversed. After precisely the same time interval τ all the ensembles are back in phase, the total magnetization reaches a maximum, and a "spin echo" signal is induced in the solenoid. The amplitude of the echo is usually smaller than that of the original FID. There will be some loss in magnitude of the magnetization due to thermal relaxation and the effects of random fluctuations in the local fields that perturb the precession of the nuclear moments and it is precisely the relaxation time of this loss that we wish to measure. The spin-echo method enables one to eliminate the otherwise dominant effects of the nonuniformity of the magnetic field. If the two-pulse sequence is repeated for several different values of τ, the height of the echo should vary as $\exp(-t/T_2)$.

A necessary assumption implied in the spin-echo technique is that a particular spin feels the same constant magnetic field before and after the "refocusing" 180° pulse. If, because of Brownian motion, a spin has diffused to a different region of magnetic field before the echo, then that spin will not be refocused by the 180° pulse. This is often the case for non-viscous liquids and will result in a decay of echoes which is not quite exponential and somewhat faster than that observed in viscous liquids. The **Carr-Purcell** technique, described in [8, 9] and summarized below, elegantly addresses this difficulty. The section of this lab guide entitled "measurements" will ask you to take data to measure the apparent T_2 for two samples (e.g. a viscous sample such as glycerine and a non-viscous one such as Fe^{+++} doped H_2O) to compare with later measurements taken from the same samples by the Carr-Purcell technique.

3.5. The Measurement of T_1

3.5.1. $90° - 90°$

As mentioned above, the spin-lattice relaxation time can be measured by examining the time dependence of the z magnetization after equilibrium is disturbed. This can be done by saturating the spins with a 90° pulse, so that the z magnetization is zero. Immediately after the first pulse one should be able to observe a free induction decay (as in Fig.1) whose amplitude is proportional to the z-magnetization just before the pulse. One then waits a measured amount of time, t, so that some magnetization has been reestablished, and then applies a 90° pulse to the recovering system. The second 90° pulse will rotate any z magnetization into the x-y plane, where it will produce a FID signal proportional to the recovered magnitude it had just before the second pulse. If the two-pulse sequence is repeated varying the time between the 90° pulses the amplitude of the FID as a function of t will give the value of T_1.

3.5.2. $180° - 90°$

Another sequence, the $180° - \tau - 90°$, is also used. A 180° pulse is applied to the equilibrium system, causing the population of the states to be precisely inverted, and thus leaving the $x-y$ magnetization at zero. In this case, there should be little or no FID immediately after the first pulse. The system is then allowed to approach equilibrium for a specified delay, after which a 90° pulse is applied to rotate the partially recovered z magnetization into the $x-y$ plane. The magnitude of the FID gives a measure of the size of the magnetization which can be plotted against the delay to give the exponential time constant. In this case, the magnetization actually reverses going through zero at time $T_1 \ln 2$.

3.5.3. $180° - \tau - 90° \; 180°$

It was mentioned earlier that it is experimentally much easier to detect the extremely small effects of transitions if they are separated in time from the multi-watt rf bursts. Unfortunately, the usual "Inversion Recovery" method requires observation of the FID immediately after the second rf pulse. This problem was addressed several years ago by two Junior Lab students[1]. who proposed the "Three-Pulse" sequence[10]. See Figure 3 for a sample data set using this technique.

[1] Both of these students, Rahul Sarpeshkar and Isaac Chuang, are now M.I.T. professors. Creativity in Junior Lab is one indicator of future success in science!

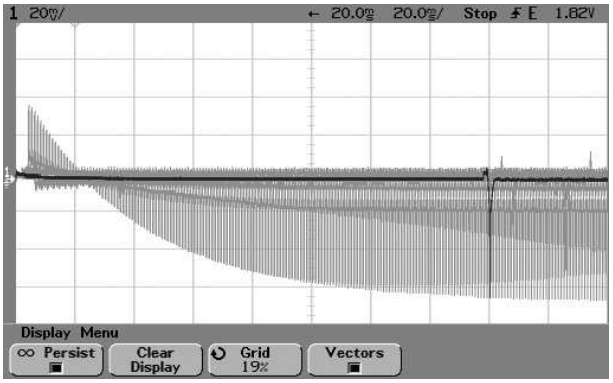

FIG. 3: An example data set using the "Three-Pulse" technique with the oscilloscope set to infinite-persist.

The first pulse (180°) inverts the population along the -Z axis as in the normal Inversion-Recovery method. After a delay of t, the second and third pulses can be understood as a normal 90-T-180 sequence which is used to measure the fraction of spins which are in the $|+z>$ state at the moment that the pulses are applied. The time between the second and third pulses is kept small to minimize T_2 effects. The amplitude of the echo is therefore related to the amount of T_1 decay (or recovery) during t and will have the form $A(1-2*e^{(-t/T1)})$.

The three experiments mentioned so far, (i.e. the spin-echo, the $90° - 90°$ and the $180° - 90°$ sequences) have each been performed successfully many times in this lab. However each has its intrinsic difficulties leading to various modifications which will be discussed.

4. Experimental Apparatus

This experiment uses a permanent magnet whose field is **1770 Gauss** (0.177 Tesla). Care should be taken to avoid bringing any magnetizable material (such as iron or steel) near the magnet as this may be pulled in and damage the magnet.

The experimental apparatus, shown in Figure 4 consists of a gated rf pulse generator with variable pulse widths and spacings, a probe circuit that delivers rf power to the sample and picks up the signal from the sample, a preamp that amplifies the signal, and a phase detector which outputs an audio signal whose frequency corresponds to the difference between the Larmor frequency and the frequency of the signal generator. Details of how to design and build NMR probes can be found in [11].

The rf pulse generating system is made up of a 15 MHz frequency synthesizer (Agilent 33120A), a digital pulse programmer based on a STAMP micro-controller, a double-balanced mixer used as an rf switch (Mini-Circuits ZAS-3), a variable attenuator, and an rf power amplifier capable of 2 watts output.

The frequency synthesizer feeds a +10dBm RF sine wave to the power splitter . The power splitter keeps

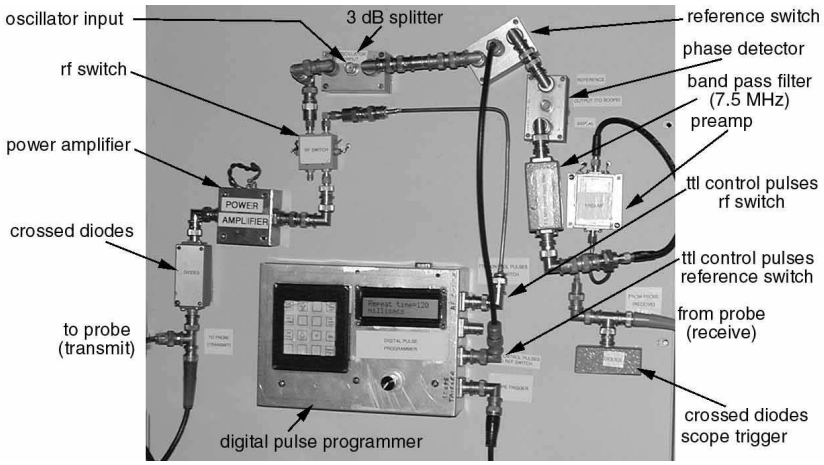

FIG. 4: The Experimental Setup. The magnet and the probe circuit are not shown

all impedances appropriately matched while feeding one half of the RF power to a double-balanced mixer (DBM) used as a gate for the RF. The other half is used as a reference signal in the phase detector. The gate is opened and closed by TTL pulses provided by the digital pulse programmer. After the switching stage, the RF pulses pass into a constant-gain (+33 dBm) RF power amplifier. The power amplifier feeds the amplified pulsed RF into the probe circuit.

The signal out of the sample, as well as a considerable amount of leakage during pulses, comes out of the probe circuit, and is amplified by a sensitive preamp (Tron-Tech W110F). The signal then goes into a phase detector (Mini-Circuits ZRPD-1), where it is mixed with the reference signal coming out of the other port of the power splitter. Since the NMR signal is, in general, not precisely at the frequency of the transmitter, when the two signals are mixed, a signal is produced at the difference frequency of the resonance signal and the applied rf. Since we are looking at NMR signals in the vicinity of 1-8 MHz, mixing this down to a lower frequency makes it easier to see the structure of the signal.

4.1. The probe circuit

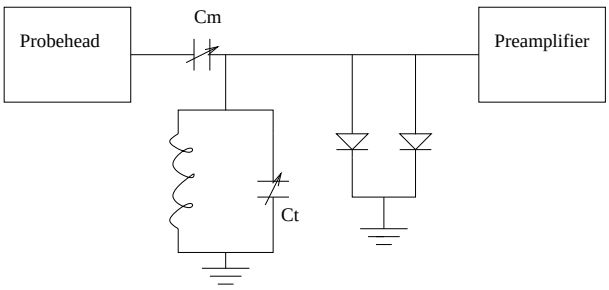

FIG. 5: Schematic of the probehead circuit.

The probe circuit is a tuned LC circuit, impedance matched to 50 ohms at the resonant frequency for efficient power transmission to the sample. The inductor L in the circuit is the sample coil, a ten turn coil of #18 copper wire wound to accommodate a standard 10mm NMR sample tube. The coil is connected to ground at each end through tunable capacitors C_m and C_t, to allow frequency and impedance matching. Power in and signal out pass through the same point on the resonant circuit, so that both the power amplifier and the signal preamp have a properly matched load. Between the power amplifier and the sample is a pair of crossed diodes, in series with the probe circuit from the point of view of the power amplifier. By becoming non-conducting at low applied voltages, these serve to isolate the probe circuit and preamp from the power amplifier between pulses, reducing the problems associated with power amplifier noise, but they pass the high rf voltages that arrive when the transmitter is on. The signal out of the probe circuit passes through a quarter-wavelength line to reach another pair of crossed diodes, which go directly to ground, at the input of the preamp. The diodes short the preamp end of the cable when the transmitter is on, causing that end of the cable to act like a short circuit. This helps to protect the delicate preamp from the high rf power put out by the power amplifier. Any quarter-wave transmission line transforms impedance according to the following relation:

$$Z_{in} = Z_0^2/Z_{out} \tag{4.38}$$

where Z_0 = the characteristic impedance of the line.

Therefore during the rf pulse, the preamp circuit with the quarter-wave line looks like an open circuit to the probe and does not load it down. Between pulses, the voltage across the diodes is too small to turn them on, and they act like an open circuit, allowing the small NMR signal to pass undiminished to the preamp.

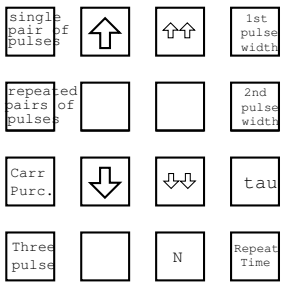

FIG. 6: The Pulse Programmer Interface.

5. Experimental Procedure

Although it is the policy in Junior Lab to discourage the use of pre-wired experiments, there are two reasons why the present set-up should not be (lightly) changed. Several of the components, particularly the double-balanced mixers (DBM) and the low-level TRONTECH pre-amplifier, are easily damaged if the rf power level they are exposed to exceeds their specified limit. Furthermore, the lengths of some of the cables have been specially selected to fix the relative phase relationship of different signals.

Most of the controls that you will manipulate are on the digital pulse programmer, the oscilloscope or the function generator. The keypad of the Digital Pulse Programmer is shown in Figure 6. Press any of the four buttons on the right and then use the arrow buttons to set the corresponding time. The default times are: First Pulse Width (PW1) = 24μs, Second Pulse Width (PW2) = 48μs, τ = 2ms, Repeat Time = 100ms. The first two buttons on the left determine whether the two-pulse sequence occurs only once or repeats continuously 10 times sec^{-1} (or at a different repeat time if you change this parameter).

Set the delay, τ, to the minimum position and observe the amplified rf pulses from the port marked "transmitter" on channel two of the oscilloscope. The pulses should be approximately 20-30 volts peak-to-peak. Choose the slowest possible sweep speed which will enable both pulses to be viewed simultaneously. A good starting pair of pulse-widths might be 24 μs and 48 μs corresponding to approximately 90° and 180°. Now switch to channel one which displays the output of the phase detector (through the low-pass filter). Incidentally, there is another low-pass filter which is part of the scope itself. On the Tektronix analog scope there is a button marked "BW limit 20 MHz". This button should be pressed in (active). On the HP digital scope the BW limit is set by one of the soft keys. Set the y-sensitivity to about 10 mV/div at first. Channel one will display the nmr signal. Place the glycerine vial in the probe and place the probe in the magnet. Now the fun begins!!

Refer to Figure 2 which is a highly stylized version of the signals you might obtain. The form of the voltage displayed during the two bursts is unimportant. You will be focusing your attention on the (FID) signals which appear after each burst and on the echo. For five or ten microseconds after the rf pulse the amplifier is still in the recovery phase and this part of the signal should be ignored.

5.1. Free Induction Decay (FID)

As mentioned above, the oscillations following the first pulse represent a beat between the applied rf frequency and the Larmor frequency. Since the latter is proportional to B_0, you should see high-frequency oscillations as you raise ω from below the resonance condition. They will spread out in time, pass through a zero-beat condition and then begin to increase in frequency again as the field continues to increase. These oscillations with their exponentially decaying envelope is referred to as the Free Induction Decay (FID).

5.2. Setting Pulse Widths

It is sometimes easiest to set the pulse widths with the magnetic field slightly off resonance so that the FID is well displayed. The size of the FID should be maximum after a 90° or 270° pulse, minimum or zero after a 180° pulse. It is usually easiest to set the pulse-width to 180° by minimizing the FID. Then, if you want a 90° pulse, reduce the pulse-width in half.

You have four or more degrees of freedom: these include the widths of each of the two pulses, the delay between the pulses, and the frequency of the applied current. Experiment with all of them. Look for free induction decays (FID); vary the FID so that you get varying amounts of oscillations (beats) and try to explain the beats. Once you find oscillatory FID's, move the probe slightly between the pole pieces of the magnet in a direction perpendicular to the magnetic field. Explain the changes you see. Use these changes to find the most homogeneous position in the field, then leave the probe there for the remainder of the experiment. Measure T_2^*. Using various combinations of 90° and 180° rf pulses, obtain data from which you can determine T_1 and T_2 in several samples (see section entitled "Measurements".)

5.3. The Carr-Purcell Experiment

As mentioned above, if diffusion causes nuclei to move from one point of an inhomogeneous magnetic field to another in a time less than 2τ, the echo amplitude is reduced. It can be shown that the echo amplitude for a pulse separation τ is

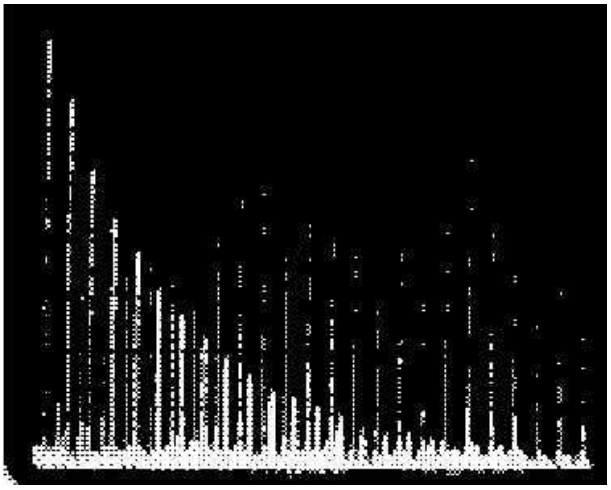

FIG. 7: The Carr-Purcell pulse and echo sequence

$$E(2\tau) = E(0)\exp[-(2\tau/T_2) - (\frac{2}{3})\gamma^2 G^2 D\tau^3] \quad (5.39)$$

where G is the gradient of the inhomogeneous field and D is the diffusion constant. Because of the τ^3 dependence the effects of diffusion are pronounced for large values of t and thus affect the measurement of long T_2's. Carr and Purcell [8] introduced a pulse sequence which can be described as follows: $\pi/2, \tau, \pi, 2\tau, \pi, 2\tau, \pi, 2\tau...$ (i.e. 90 deg pulse at time 0, followed by 180 deg pulses at times $\tau, 3\tau, 5\tau$, etc.) Echoes will be observed at times $2\tau, 4\tau, 6\tau$, etc.

When you are ready to do a Carr-Purcell, set up the pulse width and magnetic field first with a two-pulse spin echo and then switch to the Carr-Purcell. The picture should resemble Figure 7.

6. MEASUREMENTS

6.1. Magnetic Moments of Hydrogen and Fluorine

With this apparatus, we can measure the magnetic moments of two nuclei: the proton ^1H and the Fluorine nucleus ^{19}F. One of the strongest signals is due to hydrogen in glycerine. Once you have obtained a good resonance, remove the sample and replace it with the transverse probe of the Hall Gaussmeter. From the magnetic field strength (**1770 gauss=0.177 Tesla**) and the measured frequency you can calculate the magnetic moment. Repeat the measurement for fluorine using the trifluoric acetic acid sample or the hexafluorobenzene (you may wish to consult the CRC or another source to get an idea of what resonant frequency you are looking for). The former is a strong acid and should be handled with extreme care. Before looking for the fluorine resonance, move the knob on the probe circuit in the magnet to point to "FLUORINE". Also note that the T_1 relaxation time for our fluorine sample is long and if you use the default (100 ms) repetition rate of the pulse sequence, the observed signal will be small! Finally, be creative with the pulse programmer... by setting pw2 = 1μs you can effectively create a one pulse sequence...

6.1.1. *Relaxation constants for Water*

In the case of water, the relaxation times (T_1 equals T_2 for most non-viscous liquids) is of the order of several seconds. The measurement of T_2 is quite difficult but the equivalent measurement of T_1 can be done as follows:

Set up a $90° - 180°$ echo sequence with the shortest possible delay between pulses. As mentioned above, one must usually wait at least 5 times T_1 between successive repeats of this pulse sequence to allow sufficient time for equilibrium to be re-established. If less time is taken, the echo signal is diminished. Taking advantage of this fact, one can vary the repeat rate and plot the echo height against the repeat time. For times less than about 3 s, you can read this repeat time from the small numerical display on the scope (push the button marked "per"). For slower rates switch to the manual ("one-shot") mode and use your watch to wait a specified amount of time in between pulses. Repeat the measurement for both tap-water and distilled water.

The first measurements of T_1 in distilled water stood for about thirty years. Since then careful measurements have produced a number which is about 50% higher. The difference is due to the effect of dissolved oxygen in the water (O_2 is paramagnetic). As an optional experiment, you might try to carefully remove the dissolved oxygen from a sample of distilled water. Bubbling pure nitrogen through the water will work as will other methods in the literature. A challenging question which you might discuss in your oral examination is why O_2 is paramagnetic while N_2 is diamagnetic.

6.1.2. *Effects of Paramagnetic ions.*

An extremely small amount of any substance with unpaired electron spins has a very dramatic effect of reducing T_1. There is a bottle of $FeCl_3.6H_20$ in the lab. The standard starting solution has a molarity of 0.166M corresponding to approximately 10^{20} Fe^{+++} ions/cc. There are 10 molar dilutions made from the standard solution with which measurements of both T_1 and T_2 should be taken. Repeat your measurements across the dilutions several times to ensure accuracy and precision. Plot the relaxation times versus concentration on a log-log scale.

Viscosity of Aqueous Glycerine Solutions in Centipoises/mPa s

Glycerine percent weight	Temperature (°C)										
	0	10	20	30	40	50	60	70	80	90	100
0 [1]	1.792	1.308	1.005	0.8007	0.6560	0.5494	0.4688	0.4061	0.3565	0.3165	0.2838
10	2.44	1.74	1.31	1.03	0.826	0.680	0.575	0.500	–	–	–
20	3.44	2.41	1.76	1.35	1.07	0.879	0.731	0.635	–	–	–
30	5.14	3.49	2.50	1.87	1.46	1.16	0.956	0.816	0.690	–	–
40	8.25	5.37	3.72	2.72	2.07	1.62	1.30	1.09	0.918	0.763	0.668
50	14.6	9.01	6.00	4.21	3.10	2.37	1.86	1.53	1.25	1.05	0.910
60	29.9	17.4	10.8	7.19	5.08	3.76	2.85	2.29	1.84	1.52	1.28
65	45.7	25.3	15.2	9.85	6.80	4.89	3.66	2.91	2.28	1.86	1.55
67	55.5	29.9	17.7	11.3	7.73	5.50	4.09	3.23	2.50	2.03	1.68
70	76	38.8	22.5	14.1	9.40	6.61	4.86	3.78	2.90	2.34	1.93
75	132	65.2	35.5	21.2	13.6	9.25	6.61	5.01	3.80	3.00	2.43
80	255	116	60.1	33.9	20.8	13.6	9.42	6.94	5.13	4.03	3.18
85	540	223	109	58	33.5	21.2	14.2	10.0	7.28	5.52	4.24
90	1310	498	219	109	60.0	35.5	22.5	15.5	11.0	7.93	6.00
91	1590	592	259	127	68.1	39.8	25.1	17.1	11.9	8.62	6.40
92	1950	729	310	147	78.3	44.8	28.0	19.0	13.1	9.46	6.82
93	2400	860	367	172	89	51.5	31.6	21.2	14.4	10.3	7.54
94	2930	1040	437	202	105	58.4	35.4	23.6	15.8	11.2	8.19
95	3690	1270	523	237	121	67.0	39.9	26.4	17.5	12.4	9.08
96	4600	1580	624	281	142	77.8	45.4	29.7	19.6	13.6	10.1
97	5770	1950	765	340	166	88.9	51.9	33.6	21.9	15.1	10.9
98	7370	2460	939	409	196	104	59.8	38.5	24.8	17.0	12.2
99	9420	3090	1150	500	235	122	69.1	43.6	27.8	19.0	13.3
100	12070	3900	1410	612	284	142	81.3	50.6	31.9	21.3	14.8

[1] Viscosity of water taken from "Properties of Ordinary Water-Substance." N.E. Dorsey, p. 184. New York (1940)

FIG. 8: The viscocity of water-glycerine mixtures. From http://www.dow.com/glycerine/resources/table18.htm

6.1.3. Effect of Viscosity.

It has been shown that the major contribution to both T_1 and T_2 processes comes from the fluctuating dipolar fields of other nuclear (and unpaired electron) spins in the immediate region. Only those fluctuations which have a sizeable Fourier component at the Larmor frequency can affect T_1, but spin-spin relaxation is also sensitive to fluctuations near zero frequency. It is for this reason that viscous liquids (whose fluctuations have a sizeable low-frequency component) exhibit a T_2 less than T_1. You will find a series of samples of glycerine-water mixtures in different ratios. Each will be marked with its viscosity [2]. Measure T_2 by the Carr-Purcell method and T_1 by the $180° - 90°$ method, the three-pulse method or the method suggested in paragraph 1 of this section. With the aid of Figure 8, compare your results with those found in the extraordinary thesis of Bloembergen [12] started in the year that NMR was discovered.

7. Supplemental Questions

Each of the magnetic moments in a sample is influenced by the magnetic fields of other moments in its neighborhood. These differ from location to location in the sample, depending on the relative distance and orientation of neighbor moments to one another. An approximate measure of the magnetic field variation experienced by the proton moments in the water molecule is the range corresponding to parallel alignment of two interacting protons at one extreme to opposite alignment at the other.

1. Using μ/r^3 for the field of the neighbor moment, show that the half-range in the Larmor precession frequencies is given by $\Delta\omega \approx (g\mu_n)^2/hr^3$.

2. The return to normal of the transverse distribution of the protons following resonance occurs as moments with different precession frequencies become more and more randomly orientated in the precession angle. Estimate the transverse relaxation time T_2 for the water sample by finding the time required for two moments, differing by the average $\Delta\omega$ calculated in part a., to move from in-phase to π-out-of-phase positions.

As you've probably guessed, this lab is merely a stepping off point for an incredibly varied set of potential investigations. Some good general references for this lab (beyond the ones already cited in the text) are [13–19].

[1] F. Bloch, Phys. Rev. **70**, 460 (1946).
[2] N. Bloembergen, E. Purcell, and R. Pound, Phys. Rev. **73**, 679 (1948).
[3] *Nobel Lecture for Felix Bloch and Edward Mills Purcell* (1952).
[4] A. Abragam, *Principles of Nuclear Magnetism* (Oxford University Press, 1961), ISBN QC762.A158, physics Department Reading Room.
[5] Derome, Mod. NMR Technique. For Chem. Research (1987).
[6] E. Hahn, Phys.Rev. **80**, 580 (1950).
[7] E. Hahn, Phys Today **Nov. 1953**, 4 (1953).
[8] H. Carr and E. Purcell, Phys. Rev **94**, 630 (1954).
[9] S. Meiboom and D. Gill, Rev. Sci. Inst. **29**, 668 (1958), a short paper with a major modification of the Carr-Purcell sequence. Without such a modification, it is not possible to generate a long train of echoes. This is an early application of a complex multiple-pulse sequence with phase shifts which have become routine.
[10] I. Chuang, Junior Lab Paper (1990).
[11] R. Ernst and W. Anderson, Rev. Sci. Instrum. **37**, 93 (1966).
[12] N. Bloembergen, *Nuclear Magnetic Relaxation* (W.A. Benjamin, 1961), ISBN QC173.B652, physics Department Reading Room.
[13] G. Pake, American Journal of Physics **18**, 438 (1950).
[14] T. Farrar and E. Becker, *Pulse and FT NMR* (Acad. Press, 1971), ISBN QC454.F244, physics Department

Reading Room.
[15] Feynman, Leighton, and Sands, *Lectures on Physics*, vol. Volume II, Chapter 35 (Addison-Wesley, 1965), ISBN QC23.F435, interesting discussions of angular momentum, the Stern-Gerlach Experiment and NMR, Physics Department Reading Room.
[16] E. Fukushima and S. Roeder, *Experimental Pulse NMR* (Addison-Wesley, 1981), ISBN QC762.F85, an excellent practical reference, Science Library Stacks.
[17] R. Freeman, *A Handbook of Nuclear Magnetic Resonance* (Farragut Press, 1997), 2nd ed., ISBN QD96.N8.F74, spin-Lattice Relaxation, Science Library Stacks.
[18] G. Pake, Annual Review of Nuclear Science **19**, 33 (1954).
[19] G. Pake, Sci. Amer. **Aug.** (1958), an excellent introduction, Science Library Journal Collection.

APPENDIX A: QUANTUM MECHANICAL DESCRIPTION OF NMR

Recall that for all spin-1/2 particles (protons, neutrons, electrons, quarks, leptons), there are just two eigenstates:

$$spin\ up \Rightarrow |m_l, m_s\rangle = |\frac{1}{2}, \frac{1}{2}\rangle \implies |0\rangle \tag{A1a}$$

$$spin\ down \Rightarrow |m_l, m_s\rangle = |\frac{1}{2}, \frac{-1}{2}\rangle \implies |1\rangle \tag{A1b}$$

where the simplified abbreviations for these two states are noted. Using these as basis vectors, the general state of a spin-1/2 particle can be expressed as a two-element column matrix called a **spinor**.

$$|\psi\rangle = u|0\rangle + d|1\rangle = \begin{bmatrix} u \\ d \end{bmatrix} \tag{A2}$$

where normalization imposes the constraint that $|u|^2 + |d|^2 = 1$.

The physics is governed by the Time Dependent Schrödinger Equation:

$$i\hbar \frac{d}{dt}|\psi\rangle = H|\psi\rangle \tag{A3}$$

which has the solution $|\psi(t)\rangle = U|\psi(t=0)\rangle$, where $U = e^{-iHt/\hbar}$ is unitary. In pulsed NMR, the Hamiltonian

$$H = -\vec{\mu} \cdot \vec{B} \tag{A4}$$

is the potential energy of a magnetic moment placed in an external magnetic field. In matrix representation this is

$$H = -\mu[\sigma_x B_x + \sigma_y B_y + \sigma_z B_z] \tag{A5}$$

where the Pauli spin matrices,

$$\sigma_x \equiv \begin{bmatrix} 0 & 1 \\ 1 & 0 \end{bmatrix} \quad \sigma_y \equiv \begin{bmatrix} 0 & -i \\ i & 0 \end{bmatrix} \quad \sigma_z \equiv \begin{bmatrix} 1 & 0 \\ 0 & -1 \end{bmatrix} \tag{A6}$$

are 'spin operators' or 'generators' of unitary transformations. Inserting Eqs.A6,A2 and Eq.A5 into Eq.A3:

$$i\hbar \frac{d}{dt}\begin{bmatrix} u \\ d \end{bmatrix} = i\hbar \begin{bmatrix} \dot{u} \\ \dot{d} \end{bmatrix} \tag{A7}$$

$$= -\mu \left(\begin{bmatrix} 0 & 1 \\ 1 & 0 \end{bmatrix} B_x + \begin{bmatrix} 0 & -i \\ i & 0 \end{bmatrix} B_y + \begin{bmatrix} 1 & 0 \\ 0 & -1 \end{bmatrix} B_z \right) \begin{bmatrix} u \\ d \end{bmatrix} \tag{A8}$$

$$= -\mu \left(\begin{bmatrix} d \\ u \end{bmatrix} B_x + \begin{bmatrix} -i & d \\ i & u \end{bmatrix} B_y + \begin{bmatrix} u \\ -d \end{bmatrix} B_z \right) \tag{A9}$$

The equations of motion then become:

$$\begin{aligned} \dot{u} &= i\mu B_x d + \mu B_y d + i\mu B_z u \\ &= \mu\left[iB_x + B_y\right] d + i\mu B_z u \qquad \text{(A10)} \\ \dot{d} &= \mu\left[iB_x - B_y\right] u - i\mu B_z d \qquad \text{(A11)} \end{aligned}$$

If $B_z \neq 0$ and $B_x = B_y = 0$ and the equations reduce to

$$\begin{aligned} \dot{u} &= i\mu B_z u \qquad \text{(A12)} \\ \dot{d} &= -i\mu B_z d \qquad \text{(A13)} \end{aligned}$$

Integrating with respect to time yields

$$\begin{aligned} u &= u_0 e^{i\mu B_z t} = u_0 e^{i\omega_0 t} \qquad \text{(A14)} \\ d &= d_0 e^{-i\mu B_z t} = d_0 e^{-i\omega_0 t} \qquad \text{(A15)} \end{aligned}$$

where

$$\omega_0 = \frac{\mu B_z}{\hbar} \tag{A16}$$

is the **Larmor Precession Frequency**. If an atom undergoes a spin-flip transition from the 'spin-up' state to the 'spin-down' state, the emitted photon has energy $E = 2\omega_0\hbar$.

Now let's add a small external magnetic field B_x but still keeping $B_y = 0$ and such that $B_x \ll B_z$. Eqn. A11 becomes:

$$\begin{aligned} \dot{u} &= i\mu B_x d/\hbar - i\mu B_z u/\hbar \qquad \text{(A17)} \\ \dot{d} &= i\mu B_x u/\hbar + i\mu B_z d/\hbar \qquad \text{(A18)} \end{aligned}$$

For a time varying magnetic field of the type produced by an 'RF-Burst' as in pulsed NMR, $B_x = B_{x0}\cos\omega t$ where $\cos\omega t = \left(e^{i\omega t} + e^{-i\omega t}\right)/2$ from **Euler's Theorem**. Now, we can see that

$$\begin{aligned} \dot{u} &= -i\omega_0 u + i\omega_x/2\left(e^{i\omega t} + e^{-i\omega t}\right) d \qquad \text{(A19)} \\ \dot{d} &= i\omega_0 d + i\omega_x/2\left(e^{i\omega t} + e^{-i\omega t}\right) u \qquad \text{(A20)} \end{aligned}$$

Using $\omega_x \ll \omega_0$ since $B_x \ll B_0$.
We can try for a solution of the form

$$u = C_u(t)e^{-i\omega_0 t} \quad \text{(A21)}$$
$$d = C_d(t)e^{i\omega_0 t} \quad \text{(A22)}$$

From this general form, use the **Chain Rule** to determine $\dot{u}$ and $\dot{d}$. Note that the terms C_u and C_d drop out as they appear on both sides and then, dividing by $e^{-i\omega_o t}$ yields:

$$\dot{C}_u = \frac{i\omega_x}{2} C_d \left[e^{i(\omega - 2\omega_0)t} + e^{-i(\omega - 2\omega_0)t} \right] \quad \text{(A23)}$$
$$\dot{C}_d = \frac{i\omega_x}{2} C_u \left[e^{i(\omega - 2\omega_0)t} + e^{-i(\omega + 2\omega_0)t} \right] \quad \text{(A24)}$$

Now we use the approximation $\omega \ll \omega_0$ to show that the leading terms are very small. If we run at **resonance** ($\omega = 2\omega_0$):

$$\dot{C}_u = \frac{i\omega_x}{2} C_d \quad \text{(A25)}$$
$$\dot{C}_d = -\frac{i\omega_x}{2} C_u \quad \text{(A26)}$$

Taking the next derivatives, we can demonstrate that these coefficients act like **harmonic oscillators**

$$\ddot{C}_u + \left(\frac{\omega_x}{2}\right)^2 C_u = 0 \quad \text{(A27)}$$
$$\ddot{C}_d + \left(\frac{\omega_x}{2}\right)^2 C_d = 0 \quad \text{(A28)}$$

This harmonic oscillator equation has the general solution

$$C_u = a\cos\omega t + b\sin\omega t \quad \text{(A29)}$$
$$C_d = a\cos\omega t + b\sin\omega t \quad \text{(A30)}$$

or without loss of generality

$$C_u = a\cos(\omega_x t/2) + b\sin(\omega_x t/2) \quad \text{(A31)}$$
$$C_d = a\cos(\omega_x t/2) + b\sin(\omega_x t/2) \quad \text{(A32)}$$

Doting these solutions and solving for C_u and C_d

$$C_u = a\cos(\omega_x t/2) + b\sin(\omega_x t/2) \quad \text{(A33)}$$
$$C_d = ia\sin(\omega_x t/2) - ib\cos(\omega_x t/2) \quad \text{(A34)}$$

Recall Eq.A22 to finally write down what are known as **Rabi Oscillations** valid for $\omega_x \ll \omega_0$.

$$u = u(t) = [a\cos(\omega_x t/2) + b\sin(\omega_x t/2)]\, e^{-i\omega_0 t} \quad \text{(A35)}$$
$$d = d(t) = i\,[a\sin(\omega_x t/2) - b\cos(\omega_x t/2)]\, e^{i\omega_0 t} \quad \text{(A36)}$$

The important thing to note is that a 'spin-up' state is defined as when $a \to 1$ and $b \to 0$ and the opposite for a 'spin-down' state.

APPENDIX B: BLOCH SPHERE REPRESENTATION

A single qubit in the state $a|0\rangle + b|1\rangle$ can be visualized as a point (θ, ϕ) on the unit sphere, where $a = \cos(\theta/2)$, $b = e^{i\phi}\sin(\theta/2)$, and a can be taken to be real because the overall phase of the state is unobservable. This is called the Bloch sphere representation, and the vector $(\cos\phi\sin\theta, \sin\phi\sin\theta, \cos\theta)$ is called the Bloch vector.

The Pauli matrices give rise to three useful classes of unitary matrices when they are exponentiated, the *rotation operators* about the $\hat{x}$, $\hat{y}$, and $\hat{z}$ axes, defined by the equations:

$$R_x(\theta) \equiv e^{-i\theta X/2} = \cos\frac{\theta}{2} I - i\sin\frac{\theta}{2} X = \begin{bmatrix} \cos\frac{\theta}{2} & -i\sin\frac{\theta}{2} \\ -i\sin\frac{\theta}{2} & \cos\frac{\theta}{2} \end{bmatrix} \quad \text{(B1)}$$

$$R_y(\theta) \equiv e^{-i\theta Y/2} = \cos\frac{\theta}{2} I - i\sin\frac{\theta}{2} Y = \begin{bmatrix} \cos\frac{\theta}{2} & -\sin\frac{\theta}{2} \\ \sin\frac{\theta}{2} & \cos\frac{\theta}{2} \end{bmatrix} \quad \text{(B2)}$$

$$R_z(\theta) \equiv e^{-i\theta Z/2} = \cos\frac{\theta}{2} I - i\sin\frac{\theta}{2} Z = \begin{bmatrix} e^{-i\theta/2} & 0 \\ 0 & e^{i\theta/2} \end{bmatrix}. \quad \text{(B3)}$$

One reason why the $R_{\hat{n}}(\theta)$ operators are referred to as rotation operators is the following fact. Suppose a single qubit has a state represented by the Bloch vector $\vec{\lambda}$. Then the effect of the rotation $R_{\hat{n}}(\theta)$ on the state is to rotate it by an angle θ about the $\hat{n}$ axis of the Bloch sphere. This explains the rather mysterious looking factor of two in the definition of the rotation matrices.

An arbitrary unitary operator on a single qubit can be written in many ways as a combination of rotations, together with global phase shifts on the qubit. A useful theorem to remember is the following: Suppose U is a unitary operation on a single qubit. Then there exist real numbers α, β, γ and δ such that

$$U = e^{i\alpha} R_x(\beta) R_y(\gamma) R_x(\delta)\,. \quad \text{(B4)}$$

APPENDIX C: FUNDAMENTAL EQUATIONS OF MAGNETIC RESONANCE

The magnetic interaction of a classical electromagnetic field with a two-state spin is described by the Hamiltonian $H = -\vec{\mu}\cdot\vec{B}$, where $\vec{\mu}$ is the spin, and $B = B_0\hat{z} + B_1(\hat{x}\cos\omega t + \hat{y}\sin\omega t)$ is a typical applied magnetic field. B_0 is static and very large, and B_1 is usually time varying and several orders of magnitude smaller than B_0 in strength, so that perturbation theory is traditionally employed to study this system. However, the Schrödinger equation for this system can be solved

straightforwardly without perturbation theory, in terms of which the Hamiltonian can be written as

$$H = \frac{\omega_0}{2} Z + g(X\cos\omega t + Y\sin\omega t)\,, \tag{C1}$$

where g is related to the strength of the B_1 field, and ω_0 to B_0, and X, Y, Z are the Pauli matrices as usual. Define $|\phi(t)\rangle = e^{i\omega t Z/2}|\chi(t)\rangle$, such that the Schrödinger equation

$$i\partial_t|\chi(t)\rangle = H|\chi(t)\rangle \tag{C2}$$

can be re-expressed as

$$i\partial_t|\phi(t)\rangle = \left[e^{i\omega Zt/2} H e^{-i\omega Zt/2} - \frac{\omega}{2} Z\right]|\phi(t)\rangle\,. \tag{C3}$$

Since

$$e^{i\omega Zt/2} X e^{-i\omega Zt/2} = (X\cos\omega t - Y\sin\omega t)\,, \tag{C4}$$

(B3) simplifies to become

$$i\partial_t|\phi(t)\rangle = \left[\frac{\omega_0-\omega}{2} Z + gX\right]|\phi(t)\rangle\,, \tag{C5}$$

where the terms on the right multiplying the state can be identified as the effective 'rotating frame' Hamiltonian. The solution to this equation is

$$|\phi(t)\rangle = e^{i\left[\frac{\omega_0-\omega}{2} Z + gX\right]t}|\phi(0)\rangle\,. \tag{C6}$$

The concept of *resonance* arises from the behavior of this solution, which can be understood to be a single qubit rotation about the axis

$$\hat{n} = \frac{\hat{z} + \frac{2g}{\omega_0-\omega}\,\hat{x}}{\sqrt{1+\left(\frac{2g}{\omega_0-\omega}\right)^2}} \tag{C7}$$

by an angle

$$|\vec{n}| = t\sqrt{\left(\frac{\omega_0-\omega}{2}\right)^2 + g^2}\,. \tag{C8}$$

When ω is far from ω_0, the spin is negligibly affected by the B_1 field; the axis of its rotation is nearly parallel with $\hat{z}$, and its time evolution is nearly exactly that of the free B_0 Hamiltonian. On the other hand, when $\omega_0 \approx \omega$, the B_0 contribution becomes negligible, and a small B_1 field can cause large changes in the state, corresponding to rotations about the $\hat{x}$ axis. The enormous effect a small perturbation can have on the spin system, when tuned to the appropriate frequency, is responsible for the 'resonance' in nuclear magnetic resonance.

In general, when $\omega = \omega_0$, the single spin rotating frame Hamiltonian can be written as

$$H = g_1(t)X + g_2(t)Y\,, \tag{C9}$$

where g_1 and g_2 are functions of the applied transverse RF fields.

APPENDIX D: MODELING THE NMR PROBE

The material in this appendix was provided by Professor Chuang of the MIT Media Laboratory. A tuned circuit is typically used to efficiently irradiate a sample with electromagnetic fields in the radiofrequency of microwave regime. This circuit allows power to be transferred from a source with minimal reflection, while at the same time creating a large electric of magnetic field around the sample, which is typically placed within a coil that is part of it.

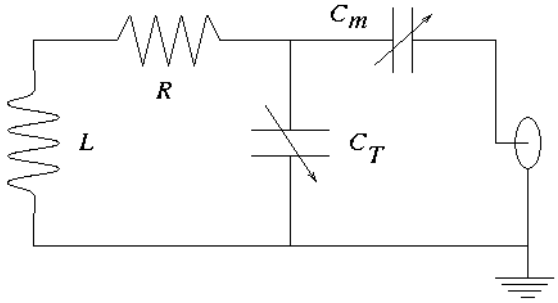

FIG. 9: Schematatic diagram of NMR probe circuit. The connector on the right goes off to the source and any detection circuitry.

1. Circuit and Input Impedance

A typical probe circuit, as shown in Figure 7, consists of an inductor L, its parasitic coil resistance R, a tuning capacitor C_T, and an impedance matching capacitor C_m. We can analyze the behavior of this circuit using the method of complex impedances, in which the capacitors have impedance $Z_C = 1/j\omega C$, inductors $Z_L = j\omega L$, and resistors $Z_R = R$, with $\omega = 2\pi f$ being the frequency in rad/sec, and $j = \sqrt{-1} = i$ (dropping the minus sign that sometimes appears in EE).

The input impedance is thus

$$\begin{aligned}
Z &= Z_{C_m} + \left[\frac{1}{Z_{C_T}} + \frac{1}{R+Z_L}\right]^{-1} && \text{(D1)}\\
&= Z_{C_m} + \left[j\omega C_T + \frac{1}{R+j\omega L}\right]^{-1} && \text{(D2)}\\
&= Z_{C_m} + \left[\frac{jR\omega C_T + 1 - \omega^2 LC_T}{R+j\omega L}\right]^{-1} && \text{(D3)}\\
&= \frac{1}{j\omega C} + \left[\frac{R+j\omega L}{1+jR\omega C_T - \omega^2 LC_T}\right] && \text{(D4)}\\
&= \frac{1+jR\omega C_T - \omega^2 LC_T + j\omega RC_m - \omega^2 LC_m}{j\omega C_m(1+jR\omega C_T - \omega^2 LC_T)} && \text{(D5)}\\
&= \frac{1+j\omega R(C_T+C_m) - \omega^2 L(C_T+C_m)}{j\omega C_m(1+jR\omega C_T - \omega^2 LC_T)}\,. && \text{(D6)}
\end{aligned}$$

2. Tune and Match Conditions

The resonant frequency of this circuit is set by

$$\omega^2 = \frac{1}{L(C_T + C_m)}\,, \tag{D7}$$

and at this frequency, the input impedance is

$$Z_0 = \frac{R(C_T + C_m)}{C_m(1 + jR\omega C_T - \omega^2 L C_T)}\,. \tag{D8}$$

We would like this impedance to be 50 ohms, because that is the typical impedance expected by RF or microwave sources and the coaxial cable which carries in the signal. Setting $Z_0 = 50$ we obtain:

$$\frac{50}{R} = \frac{C_T + C_m}{C_m(1 + jR\omega C_T - \omega^2 L C_T)} \tag{D9}$$

$$= \frac{C_T + C_m}{C_m\left[1 + jR\omega C_T - \frac{C_T}{C_T + C_m}\right]} \tag{D10}$$

$$= \frac{(C_T + C_m)^2}{C_m\left[C_m + jR\omega C_T(C_T + C_m)\right]}\,. \tag{D11}$$

To good approximation, the $jR\omega C_T(C_T + C_m)$ term in the demoniator may be neglected, giving, finally

$$\frac{50}{R} = \left(1 + \frac{C_T}{C_m}\right)^2\,. \tag{D12}$$

The two important results give the resonant frequency, Eq. (B7), and the impedance matching condition, Eq. (B12), in terms of the capacitor settings. When the matching condition is satisfied, then all the source power goes into the tuned resonator at the resonant frequency, thus creating the strongest possible oscillating magnetic field inside the coil L.

Mössbauer Spectroscopy

MIT Department of Physics
(Dated: February 2, 2010)

The Mössbauer effect and some of its applications in ultra-high resolution , $\frac{\Delta E}{E} \sim 10^{-12}$, gamma-ray spectroscopy are explored. The Zeeman splittings, quadrupole splittings, and chemical shifts of the 14 keV Mössbauer gamma-ray line emitted in the recoilless decay of the first excited state of the ^{57}Fe nucleus are measured in iron and in various iron compounds and alloys. From the data and knowledge of the magnetic moment of the ^{57}Fe ground state one determines the magnetic moment of the first excited state, and the strengths of the magnetic field at the sites of the iron nuclei in metallic iron, Fe_2O_3, and Fe_3O_4. The natural line widths of the 14 keV transitions are determined from measurements of the absorption line profiles in sodium ferrocyanide absorbers of various thicknesses. Relativistic time dilation is demonstrated by a measurement of the temperature coefficient of the energy of the 14 keV absorption lines in enriched iron.

PREPARATORY PROBLEMS

1. Derive an exact relativistic expression for the recoil energy of the nucleus of mass M that emits a gamma ray of energy E, and evaluate it for an iron nucleus and $E = 14.4$ keV.

2. Suppose the above atom is embedded in an iron crystalite which has a mass of $10^{-6}g$ grams and is free to move. Compute the recoil energy of the crystal. If the emission of the gamma ray is "recoilless", i.e. the nucleus does not acquire momentum relative to the center of mass of the crystal, what would be the energy shift of the gamma ray photon due to the recoil of the crystal?

3. Draw an energy level diagram of the $^{57}_{26}$Fe nucleus in a magnetic field and show the transitions which give rise to the Zeeman pattern you expect to see in this experiment.

4. Why is the multiplicity of energy levels of a nucleus due to electric quadrupole interaction with an electric field gradient acting alone (quadrupole splitting) less than the multiplicity of levels due to magnetic dipole interaction with a magnetic field (Zeeman splitting)?

5. How fast must the source be moved relative to the absorber to shift the frequency of resonant absorption by the natural line width?

6. Why can't you do this experiment with the 6.4 keV photons also emitted by the source?

1. Introduction

The resolution of a spectrum measurement is characterized by the ratio $\frac{E}{\Delta E}$, where E is the energy of the spectrum line and ΔE is a measure of the line width , e.g. the full width at half maximum. The NaI scintillation spectrometer in the Compton experiment produces a spectrum of 662 keV gamma rays with a resolution of about 10. At the same energy the spectrum obtained with the germanium solid state cryogenic detector in the X-ray Physics experiment has a resolution of 200. The high resolution gratings used in the hydrogenic atom experiment for measurements in the visible portion of the spectrum has a resolution on the order of 5 x 10^4.

Now imagine spectroscopy with a resolution of 10^{12}! Recoilless emission and resonance absorption of gamma radiation by nuclei, discovered by Rudolf Mössbauer in 1957, makes possible such ultra- high resolution spectroscopy in the gamma-ray region of the spectrum. Mössbauer spectroscopy has been used in many areas of physics and chemistry, for example in the determination of life-times of excited nuclear states, in the measurement of nuclear magnetic moments, in the study of electric and magnetic fields in atoms and crystals, and in the testing of special relativity and the equivalence principle. The phenomenon itself is also of great interest. In this experiment you will observe the Mössbauer effect and explore several of its applications in ultra-high resolution spectroscopy.

Mössbauer himself provided a particularly lucid introduction to the physics and application of recoilless gamma-ray emission and absorption in his 1961 Nobel Lecture which is available in the Junior Lab E-Library [1]. More technical discussions are found in [2, 3]. An excellent reference is "The Mössbauer Effect" by Hans Frauenfelder [4] which contains historical and theoretical background and reprints of articles bearing on all the topics in this set of experiments.

You will use as the source of recoilless gamma rays a commercial Mössbauer source consisting of $^{57}_{27}$Co diffused into a platinum substrate. The $^{57}_{27}$Co nucleus decays by K-electron capture to an excited state of $^{57}_{26}$Fe according to the scheme shown in Figure 1. The newly created iron atom settles down in the crystal lattice of the substrate and the d-shell vacancies in its electronic structure are filled in such a way as to eliminate the magnetic field at the nucleus. 91% of the excited iron nuclei decay by gamma-ray emission to the first excited state (3/2-). The latter has a comparatively long half-life of 9.8 x 10^{-8} seconds (beware that both Melissinos (2003) and Fraunfelder (1962) list the lifetime incorrectly as 0.14 μs) and decays to the ground state with the emission of 14.4 keV

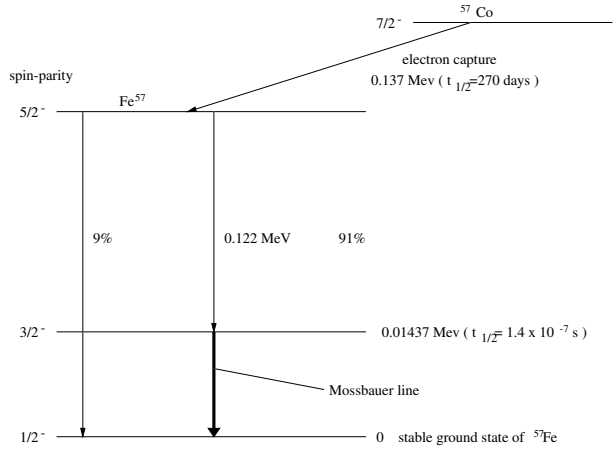

FIG. 1: Decay scheme of $^{57}_{27}$Co. The 14.4-keV transition $3/2- -> 1/2$ is the one used in many Mössbauer experiments. From http://isotopes.lbl.gov/.

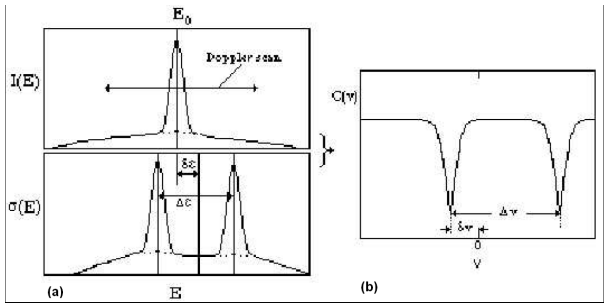

FIG. 2: (a) Schematic plots against energy, E, of (top) the intensity, I(E), of gamma rays from a single line Mössbauer source moving with velocity v relative to a Mössbauer absorber, and (bottom) absorption cross section $\sigma(E)$ of the absorber. (b) Schematic plot of counting rate C(V) of a detector exposed to the gamma rays after they have traversed the absorber against velocity V. In (a) the energy separation of the two absorption lines is $\Delta\epsilon$, and the Doppler shift due to the motion of the source is $\delta\epsilon$. In (b) the velocity separation of the two lines is $\Delta V = c\frac{\Delta\epsilon}{E_0}$, where Eo is approximately the average energy of the two lines.

gamma rays of which a substantial fraction are emitted without recoil or Doppler broadening. The natural line width of the 14.4 keV line is $\Gamma = \frac{h \ln 2}{2\pi\tau_{1/2}} = 4.7 \text{ x } 10^{-9}$ eV corresponding to a fractional width of $\approx 3 \text{ x } 10^{-13}$. In the absence of a field, the magnetic substates of the excited and ground states are degenerate. Under this condition the spectrum of gamma rays from the recoilless emissions appears as a single ultra-narrow line on top of a Doppler-broadened and recoil-shifted "normal" emission line, as illustrated in Figure 2a.

In a similar way, absorbers containing $^{57}_{26}$Fe can have ultra-narrow recoilless resonance absorption lines on top of a normal Doppler-broadened and recoil-shifted 14.4 KeV line. Mössbauer absorption lines may be shifted slightly in energy with respect to the emission line by virtue of the different electronic environments of the nuclei in the source and the absorber (the "chemical" shift), and they may be split by the interactions between the nuclear magnetic dipole and/or electric quadrupole moments with internal or external fields in the absorber (Zeeman or electric quadrupole splittings). In a famous experiment that tested the red shift predicted by the general theory of relativity, the shift was caused by a ≈ 100 foot difference in height of the source and absorber!

Figure 2b is a schematic representation of the absorption cross section of $^{57}Fe^{++}$ in an ionic compound in which the iron nuclei are in a nonuniform electric field which produces an electric quadrupole splitting $\Delta\epsilon$ in addition to an isomer shift $\delta\epsilon$ (see below). The measurement process in Mössbauer spectroscopy uses the Doppler shift produced by controlled motion of the source to scan the emission line back and forth in energy over the absorption spectrum of a sample containing the same isotope in its ground state and in a particular chemical or physical environment of interest. The advantage of using a source with a single emission line for performing such a scan is apparent from a consideration of the complications that occur if a multi-line source is used to scan the absorption spectrum of a multi-line absorber.

A primary objective of this experiment is to determine the width of the convolved recoilless emission and absorption lines of the 14.4 keV transition in $^{57}_{26}$Fe. The velocity width Γ_ν corresponding to a given energy width Γ is given by the simple formula $\Gamma_\nu = c\frac{\Gamma}{E_0}$ where E_0 is the mean energy (14.4 keV) of the gamma rays in the line, and c is the speed of light. The velocity width corresponding to the natural line width estimated above is $1 \text{ x } 10^{-4}$ m s^{-1}. Clearly, one will require a velocity resolution at least an order of magnitude smaller to obtain a useful profile of the line shape.

Suppose that the recoilless photons are emitted with a distribution in energy, $I(E)$, centered around E_0. When the source moves at a velocity V toward the absorber, a photon emitted with energy E in the rest frame of the source has an energy

$$E' = E\left(1 + \frac{V}{c}\right) \tag{1.1}$$

in the rest frame of the absorber. (By convention, positive velocity indicates the source moving toward the absorber.) Call $\sigma(E)$ the cross-section for absorption by the absorber atoms of photons of energy E, and call η the effective area of the detector which we assume to be constant over the narrow energy range of the 14.4 keV line. Then the counting rate when the emitter is moving with velocity V will be

$$C(V) = \eta \int_0^\infty I(E) e^{-\frac{\sigma(E')Nx}{A}} dE \qquad (1.2)$$

where x is the thickness of the absorber in g cm^{-2}, A is the atomic weight, and $N = 6.022$ x 10^{23} mol^{-1} is Avogadro's number. We assume that both the emission line intensity and the absorption cross section have the Lorentzian form, i.e.

$$I(E) = \frac{I_0(\frac{\Gamma}{2})^2}{(E - E_0)^2 + (\frac{\Gamma}{2})^2} \qquad (1.3)$$

and

$$\sigma(E) = \frac{\sigma_0(\frac{\Gamma}{2})^2}{(E - E_0 - \Delta E)^2 + (\frac{\Gamma}{2})^2} \qquad (1.4)$$

where ΔE is the intrinsic shift of the resonance energy in the absorber relative to the source due to chemical or other effects, and I_0 and σ_0 are the values at the line centers. The counting rate of a detector placed in the beam of gamma rays after the beam has traversed the absorber is then

$$C(V) = \eta I_0 \int_0^\infty dE \frac{(\frac{\Gamma}{2})^2}{(E - E_0)^2 + (\frac{\Gamma}{2})^2} e^{-\frac{\sigma_0 \frac{\Gamma}{2}^2}{(E[1+\frac{V}{C}] - E_0 - \Delta E)^2 + (\frac{\Gamma}{2})^2} \frac{Nx}{A}} \qquad (1.5)$$

For thin absorbers $\frac{\sigma_0 Nx}{A} \ll 1$, and one can obtain an approximate expression for the line profile by expanding the exponential factor in Eqn. 1.5 and keeping only the first two terms. The integral can then be evaluated by contour integration in the complex plane to obtain

$$C(V) = C_0\Big(1 - \frac{B}{(\frac{E_0 V}{c} - \Delta E)^2 + \Gamma^2}\Big) \qquad (1.6)$$

where C_0 is a constant that depends on the strength of the source and the thickness of the absorber and B is a constant that depends only on the thickness of the source. This function has a minimum at $V = \frac{\Delta E}{E} c$ and a full width at half maximum (FWHM) of $\frac{2c\Gamma}{E_0}$. For thick absorbers one must resort to numerical integration of equation (1.5). Figure 3 shows the line profiles for various thicknesses of absorber corresponding to values of $\alpha = \frac{\sigma_0 Nx}{A}$ ranging from 0.1 to 10. The width of the absorption line at half amplitude clearly increases with increasing absorber thickness in the range of thickness where nearly all the recoilless emission is absorbed near the line center, i.e. in the range of "line saturation". One can correct for this saturation effect by measuring the line width as a function of absorber thickness and extrapolating to zero thickness. (Note that in an actual observation the non-recoilless emission causes a background counting rate that does not vary with velocity but does decrease with increasing thickness of the absorber.)

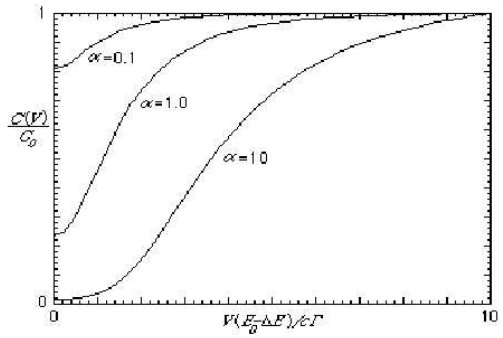

FIG. 3: Calculated shapes of recoilless gamma-ray absorption lines for various thicknesses of absorber. The normalized counting rates are plotted as functions of velocity expressed in units of $\frac{c\Gamma}{E_0 - \Delta E} \approx \frac{c\Gamma}{E_0}$.

Many interesting effects can be observed in absorption spectra; several are discussed below.

2. Observable Effects

2.1. Zeeman splitting in an internal magnetic field

The nucleus of an iron atom in metallic iron and certain iron compounds is in an intense magnetic field produced primarily by unpaired electrons of the same atom. Since both the nuclear states involved in the 14.4 keV transition have spin and associated magnetic moments, both are split by the interactions between the nuclear magnetic moment and the magnetic field of the electrons. In an isolated atom the effect of this interaction on optical transitions is characterized as hyperfine splitting. When the atom is bound in a crystal lattice the orientation of the internal magnetic field due to the electrons is fixed with respect to the lattice. As a result, the effect of the electronic magnetic field on the energy of the nucleus may be thought of and analyzed simply as the Zeeman effect in a new context. The number of absorption peaks and their separations depend on the angular momenta and associated magnetic moments of the absorber nucleus in each state. A measurement of the internal Zeeman splitting can be combined with knowledge of the magnetic moment of the ground state (which can be derived from other experiments) to deduce the magnetic field at the iron nucleus in the absorber, and the magnetic moment of the first excited state.

2.2. Isomer shift

If the chemical environment of the iron nuclei in the source and absorber are different then the electron den-

sities will, in general, be different. Since the electromagnetic interaction between the electrons and the nucleus depends, albeit only slightly, on the electron density at the nucleus and on the nuclear radius, and since the radius of the iron nucleus changes slightly in the 14.4 keV transition, there is, in general, a shift of the resonance energy from source to absorber if the host materials are different. This is called the "isomer shift" because the excited states of nuclei were originally called isomers. The magnitude of the shift depends on the s-electron density at the nucleus. If there is greater electron density at the absorbing nucleus than at the emitting nucleus, additional energy must be given to the gamma-ray by moving the source toward the absorber. There are differences on the order of a factor of ten between the isomeric shifts of Fe in the +2 and+3 ionization states in the lattice, and these differences may easily be measured. An isomer shift in a Zeeman or quadrupole pattern appears as a shift of the "center of gravity" of the lines.

2.3. Electric Quadrupole Splitting

The nucleus may be in an electric field with a gradient due to nearby ions with unfilled atomic levels. If the nucleus has a quadrupole (or higher) electric moment, i.e. if its electric charge distribution is not spherically symmetric, its energy levels will be split by amounts that depend on the projections of its spin in the direction of the field gradient. The ground state is shifted by the quadrupole interaction, and the first excited level is split into two levels: thus two transitions with energies $\Delta E_2 \pm \frac{1}{2}\Delta E_3$, are possible, yielding two absorption peaks, as shown in Figure 2.

2.4. Anisotropic emission by polarized nuclei

Each of the possible transitions that give rise to the Zeeman spectrum of lines of an absorber with ^{57}Fe nuclei in a strong internal magnetic field has a particular anisotropic radiation pattern relative to the direction of the field. The orientation of the internal field of a ferromagnetic material can be controlled by a much weaker external field. Thus changes in the relative intensities of the lines in the Zeeman pattern can be caused by placing the absorber in the field of a strong permanent magnet. Figure 4 shows the expected intensities of the Zeeman absorption lines in an absorber with no preferred orientation (unmagnetized) and in an absorber magnetized in a direction perpendicular to the direction of propagation.

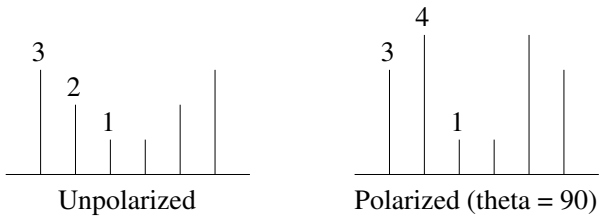

FIG. 4: Expected relative intensities of the Zeeman pattern of ^{57}Fe for an unpolarized absorber and for an absorber polarized perpendicular to the direction of propagation[5].

2.4.1. Effect of the relativistic time dilation (2nd order doppler shift) on the frequency of the 14.4 keV line through measurment of the temperature coefficient

Vibration frequencies of atoms in a crystal at room temperature are of the order of 10^{13} Hertz. Therefore, a ^{57}Fe nucleus in its first excited state makes many oscillations before it decays and, is whizzing around with a mean square velocity of $\approx \frac{kT}{m}$ during this time. According to the special theory of relativity, a clock aboard the moving nucleus runs slow relative to one at rest in the laboratory by the fraction

$$\frac{1}{\gamma} = \sqrt{1 - \frac{\nu^2}{c^2}} \tag{2.1}$$

Thus the center energy of a Mössbauer line emitted from a source at temperature T is shifted down in energy by an amount of the order $< (\frac{\nu}{c})^2 > E = \frac{kT}{mc^2}E$, where E is the unshifted energy. The center energy of an absorption line is similarly shifted. This effect was discovered in the gravitational red-shift experiment by Pound and Rebke (1960). They had to take special care in their experiment to maintain the source and absorber at the same temperature within a fraction of a degree so that the temperature shifts did not mask the gravitational red shift. The temperature effect provides a clear demonstration of the so-called "twin paradox" of special relativity and resolves any doubt as to whether the accelerations involved in return trips negate the dilation of time suffered by clocks in motion. The exact theory of the effect can be found in the collection of reprints contained in [4].

3. APPARATUS

Figure 5 is a schematic of the experimental arrangement. A beryllium side window proportional gas counter (LND Model 45431, see Melissinos, p 181) and associated measurement chain are used to selectively detect the 14.4 keV photons emitted by excited ^{57}Fe nuclei produced by the beta decay of ^{57}Co in a specially prepared "Mössbauer" source (i.e. ^{57}Co diffused into a platinum substrate). An efficiency curve for the proportional

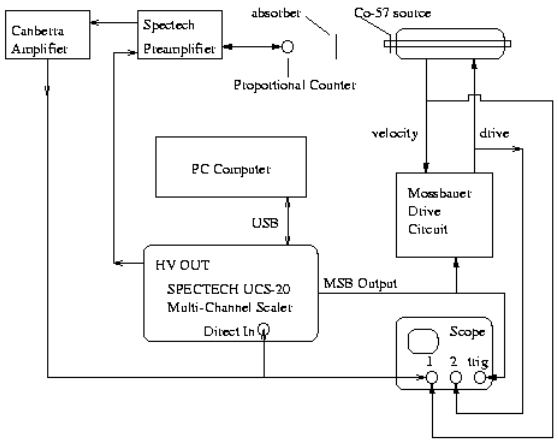

FIG. 5: Block diagram for the Mössbauer spectroscopy experiment. Note that for pulse height analysis measurements of the Co-57 spectrum, the output of the preamplifier should be sent to the 'amp in' input on the back of the UCS20.

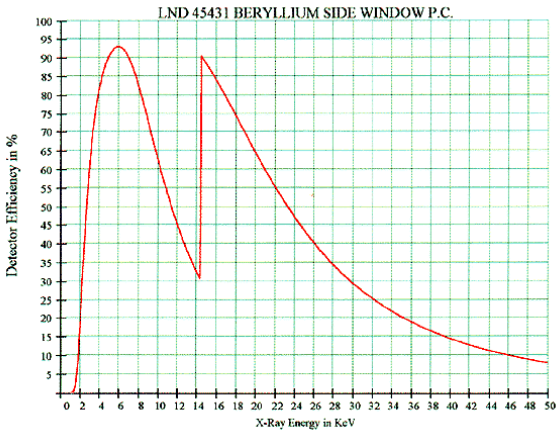

FIG. 6: X-Ray detection efficiency curve for the LND 45431 beryllium side window proportional counter.

counter is shown in Figure 6. Some of the 14.4 keV photons are emitted by nuclei that share the recoil momentum with macroscopic bits of the matter in which they are imbedded ("recoilless emission") with the result that their fractional spread in energy, or line width, $\frac{\Delta E}{E}$, is extraordinarily narrow, of the order of 10^{-12}.

A sample containing ^{57}Fe atoms in an environment that permits recoilless absorption of 14.4 keV photons, is placed between the source and the proportional counter. The source is mounted on a piston which moves back and forth with a velocity that is a periodic sawtooth function of time. This motion causes a corresponding sawtooth Doppler shift in the energies of the photons that traverse the sample. In effect, the narrow emission line is swept back and forth in energy over the recoilless absorption lines of the ^{57}Fe in the absorber. Meanwhile, an external MCA (Spectrum Technologies UCS-20), connected to a PC over a USB bus, operated in its Multi-Channel Scaler or 'MCS' mode, is triggered at the start of each velocity cycle to count clock pulses in a scaler. When a 14.4 keV photon, having traversed the absorber, triggers the proportional counter, the resulting pulse is counted in the memory channel of the MCS with the address given by the current number in the clock scaler. Thus, after a given exposure, each channel of the MCS contains a number of counts proportional to the number of photons that traversed the absorber within the narrow range of energies corresponding to the narrow range of velocities of the piston during which the clock scaler dwelled on the address of that channel.

The detector contains primarily 800 Torr of Krypton with a small amount of methane quench gas. The recommended operating voltage is +1800 VDC with a range of 1700-1950. Typical resolution (%FWHM Cd-109) is 10%. A 14.4 keV photon entering the chamber through the mylar window ionizes some of the Kr atoms, the creation of each ion/electron pair requiring $\geq$ 30 eV. The positive ions drift to the outer wall and the electrons to the center wire. In the viscinity of the wire, E ($\propto 1/r$) is so high that electrons in one mean free path pick up enough energy to ionize more atoms, the effective gas gain being approximately 1000. The methane suppresses the sparking by absorbing the UV quanta generated in the process. Of secondary importance, the methane also supresses the random motion of the electrons, thus shortening the travel time to the center wire and the rise time of the signal pulse. The overall absorption efficiency at 14.4 keV is 30%. The 122 keV and 136 keV photons entering the counter Compton scatter and produce a broad background of lower energy signals. The single channel analyzer (SCA) discriminates against most of these, but about 20% of the pulses falling in the 14.4 keV window of the SCA are from this Compton background. The charge pulse from the counter is amplified and differentiated by the preamp which is mounted as close to the counter as possible. Further amplification of the pulse is provided by the main amplifier.

The contents of each count register are displayed on the computer monitor. In the absence of a Mössbauer absorption line the average number of counts in the various velocity intervals will be equal within the Poisson statistics of counting. If there is a Mössbauer absorption line at an energy equal to the Doppler-shifted energy at some particular velocity, then the counting rate during the time that pulses are addressed to that velocity channel will be reduced, and the accumulated deficiency of counts in that and neighboring channels will be seen as an "absorption line" on the MCS screen.

Detailed instructions for operation of the drive circuit are in a binder located near the equipment. The piston on which the source is mounted is driven by the magnetic force produced by a drive current in the coil of the transducer. The resulting motion induces a current in a sense coil that is proportional to the velocity. This sense

current is compared to a reference current ramp, and the difference (error) signal is fed back to the drive-current amplifier in such a manner as to reduce the difference between the sense current and the reference current, keeping the velocity of the piston precisely proportional to the reference current.

The reference current is a sawtooth function of time with a slow, linear rise from $-I_0$ to $+I_0$ with a rapid flyback to $-I$. The corresponding velocity of the piston is therefore also a sawtooth function of time with a slow, linear rise from $-V_0$ to $+V_0$ and a rapid flyback. The MSB signal (most significant bit of the channel address scaler) of the MCS is used to trigger an independent ramp generator in the velocity drive circuit. The circuit is designed for a nominal trigger rate of 6Hz; it functions satisfactorily at $\approx$ 5Hz which is the closest rate that can be obtained from the MCA with the thumb wheels set at 2,2 (200 μs per channel). It is essential that this setting be used. The thumb wheel on the Austin drive adjusts the amplitude of the motion, and hence, with the fixed frequency, the amplitude of the velocity sweep (the rotary switch just below the thumb wheel is not used).

Display both the drive and velocity signals on an oscilloscope and check that 1) the velocity ramp is linear and 2) the drive signal has an average value near zero and is not in high frequency oscillation. The gain in the servo feedback loop, controlled by the FIDELITY knob, should be adjusted to achieve a linear velocity ramp. Start with the knob in the fully CCW position and then cautiously increase until you hear a high pitched tone or until the DRIVE signal begins to oscillate at about 12 kHz. Then, back it off slightly. If you hear a sound emanating from the drive motor, the gain is way too high. The D.C. component should be zero (or nearly so), both on the oscilloscope and as seen on the two LED's just below and on either side of the velocity thumbwheel switch. The COMP. AMP.0 adjustment (on either front panel or on the top of the unit) is used to zero out the D.C. component. At lower velocities, both LED's will be off when adjusted properly. The proper setting of the FIDELITY control is essential to obtaining good and reproducible Mossbauer spectra. There should be a slight ringing after each point in the DRIVE waveform where the sense of the acceleration changes, but this should die out rapidly. The ASYM UL potentiometer control on the top of the unit is used for the flyback generator and should be set for the best straight VELOCITY waveform.

Caution #0: If anything requires adjustment such as changing the thumbwheels to adjust the velocity range, or even if you simply wish to erase the MCS spectrum (clearing the spectrum reinitializes the bistable MSB output) from the software interface, be sure to turn off the MOTOR switch and turn off the software before making the change. Wait about 30 seconds before turning on the motor switch. This allows the unit to stabilize after the bistable has been removed and reapplied.

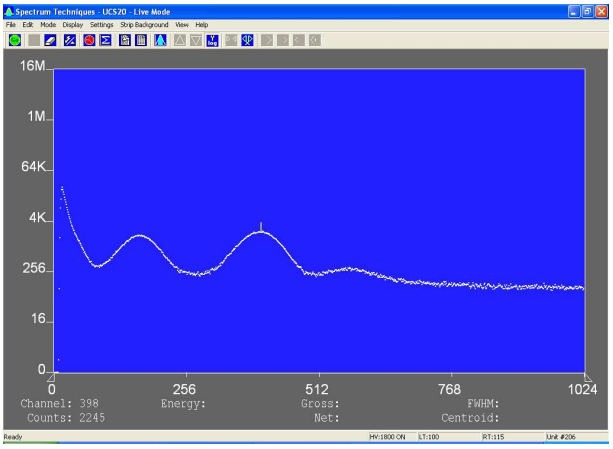

FIG. 7: Typical Co-57 pulse height spectrum acquired by the Spectech UCS-20 multi-channel analyzer. Distance between Co-57 and proportional counter detector window is ~10cm. Integration time = 100s. Co-57 had ~5mCi of activity.

Caution #1: The motor switch on the electronic drive generator should be ON only when the MCS is in the 'acquire' mode so the motors are receiving proper ramp voltages.

Caution #2: Do not touch the fragile window on the proportional counter detector.

3.1. Mössbauer Start-Up Check List

1. Setup the apparatus as shown in Figure 5.
2. Turn on the power switch of the electronics rack and adjust the thumb wheels on the Mössbauer drive to 80. Place the knob marked "Fidelity" in roughtly the central position. (leave the Mössbauer drive switch in OFF position). Turn on the power switch to the SPECTECH UCS-20 Universal Computer Spectrometer.
3. Run the UCS20 Software from the adjacent Windows XP Computer desktop.
4. Use the software menu bar (Settings – Amp/HV/ADC) to turn on the high voltage bias to the propotional counter at +1800 VDC. Also set the conversion gain to 2048.
5. Set the Canberra 816 Amplifier gain to approximately 20.
6. Remove any absorber present in the circular aperture between the Co-57 source and the proportional counter detector. Adjust the carriage holding the source so that it is about 10 cm away from the detector window.
7. Run the MCA in pulse height analysis mode for about 60 seconds and examine the resultant spectrum. It should appear similar to Figure 7. Adjust

the gain controls so that the pulses in the strong 6.4 keV iron K-line have an amplitude of about 2.0 volts. Identify the fainter 14.4 keV Mössbauer line at about twice the amplitude of the iron K-line. Hint: a stack of papers roughly the size of this labguide will block the 6.4 keV line but pass the 14.4 keV line.

8. Adjust the lower and upper level discriminators of the MCA (using the mouse to move the traingles under the 'X' axis) so that only pulses in the 14.4 keV peak are accepted by the ADC.

9. Place the enriched ^{57}Fe iron foil absorber (found in the white box on the shelf above the apparatus) in the spring clamps between the source and the detector, attempt to center the foil in the circular aperture.

10. Using the software, change the mode from Pulse Height Analysis to Mössbauer. Go to the settings – Mossbauer menu and set the dwell time per channel to 100μs per channel (to give a sweep repetition rate of $\approx$ 5 Hz). Note that if you change the resolution or "gain conversion" of the software, you must adjust the dwell time per channel to maintain this 5Hz sweep rate. Set the number of passes to 1500 (5 minutes). Start the MCS acquisition.

11. Turn on the drive and verify that it is moving the piston back and forth at the frequency ($\approx$ 5 Hz) of the MCS sweep. Check the drive and velocity signals using an oscilloscope.

12. Clear the MCS momentarily, start recording, and watch the Mössbauer spectrum of the Zeeman-split 14.4 keV line build up on the MCS screen. After about 5 minutes, you should see something resembling Figure 8.

4. Experiments to perform

1. Natural width of the 14.4 keV Mössbauer line of ^{57}Fe. The observed linewidths are larger than the intrinsic width of 0.19 mm/s since some broadening is always introduced by inhomogeneity of the environment of the iron in the source and sample. Additional broadening arises from imperfections in the source driving mechanism.

2. Ratio of the magnetic moments of the ^{57}Fe nucleus in its ground and first excited states.

3. Magnetic field at the iron nuclei in metallic iron and in Fe_2O_3.

4. Quadrupole splitting of the first excited state of the ^{57}Fe nucleus in the bivalent and trivalent state of the iron atom.

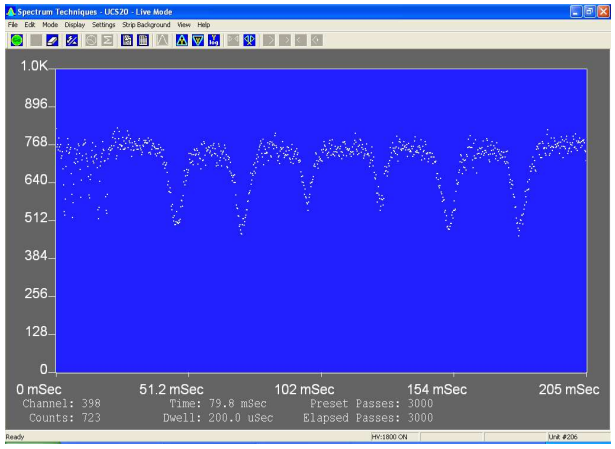

FIG. 8: Typical Mossbauer spectrum using an enriched Fe-57 foil acquired by the Spectech UCS-20 multi-channel analyzer. Distance between Co-57 and proportional counter detector window is ~10cm. Integration time = 3000 passes ~10 minutes. Co-57 had ~5mCi of activity.

5. Relative isomer shifts of the 14.4 keV line in metallic iron, steel and compounds of iron.

6. Effect of relativistic time dilatation (second-order Doppler shift) on the frequency of the 14.4 keV line through measurement of the temperature coefficient.

4.1. Preliminary Experimental Calculations

We now consider the time required to record a Mössbauer spectrum. A typical sample will have 1 mg cm^{-1} of iron in the gamma-ray beam. For purposes of illustration, we assume the spectrum has two absorption peaks. If the Fe57 is present in its natural 2% abundance, there will be 2 x 10^{17} Fe57 nuclei cm^{-2}. The peak resonant cross section is approximately 2 x 10^{-18} cm^2 (Frauenfelder, 1963). We divide this value by 8 because of the finite source linewidth, the two absorption peaks of the spectrum, and the estimated product of the recoil free fraction of the source and absorber. The observed intensity will be 5%. The spectrometer will typically divide the velocity scale into 256 channels. For a 10 mCi source the total counting rate is usually about 10,000 counts/s of which about 85% will be 14.4 keV radiation. The spectrometer duty cycle is about 66% and r, the 14.4 keV counting rate per channel, is typically 44 counts/s/channel (you should measure this for yourself!). The signal-to-noise ratio, S/N, is given by $S/N = a_p\sqrt{rT}$where a_p is the peak absorption intensity and T is the running time. If we want a S/N of 40, then for $a_p = 0.05$, T = 14,500s or about 4 hours. For a given S/N, the run time is inversely proportional to the square of the peak absorption.

4.2. Zeeman splitting of the ground and first excited states of ^{57}Fe in an iron foil

The primary purpose of this part of the experiment is to record and understand the Zeeman splitting of the 14.4 keV gamma-ray line emitted by ^{57}Fe nuclei in an iron foil. The other purpose is to establish a convenient secondary calibration standard.

Record the absorption spectrum for a sufficient time to obtain at least several thousand counts per channel so that you can measure accurate centroid values, intensities, and shapes of the six lines of the pattern. Measure the channel positions of each of the absorption peaks in the MCS display.

Next, without changing any of the settings, carry out an absolute calibration of the drive motion with the interferometer, as described below. Derive from your measured spectrum and the velocity calibration data the separation in velocity (mm/s) between adjacent pairs of lines in the six-line Zeeman pattern. With these results in hand you can use the quickly observable Zeeman pattern of the enriched iron foil as a secondary calibration standard for each of your subsequent Mössbauer spectrum measurements.

Convert the velocity separations between the lines of the Zeeman pattern into energy separations. The magnetic moment of the ground state of ^{57}Fe has been measured by electron spin resonance techniques to be (0.0903 $\pm$ 0.0007 μ_N. Using this fact, and interpreting the Zeeman pattern in terms of the energy level diagram (see Melissinos, p. 277), determine the internal magnetic field at a nucleus of iron in the iron foil absorber, and the magnetic moment of the first excited state. Discuss the experimental errors in the values you have obtained. With the data in hand can you verify the discovery of Hanna et al. (1960) [5] that the magnetic moments of the ground and first excited states have opposite signs?

4.3. Absolute calibration

Calibration of the velocity sweep is accomplished with the aid of a Michelson interferometer shown schematically in Fig. 9. A beam of coherent light from a laser is split by partial reflection from a glass slide oriented at 45° so that the two parts traverse different paths before striking the same spot on a photodiode. While the length of one path is fixed, the length of the other path varies because it includes a reflection from a mirror mounted on the moving piston. When the piston moves a distance equal to one-half of the wavelength of the laser light, the length of the path increases by one wave length, the phase of the beam at the photodiode changes by 360°, and the intensity of the recombined beam at the photodiode goes through one cycle of constructive and destructive interference. Every cycle of interference produces one cycle of a sinusoidal voltage signal from the photodiode that can be registered as one pulse by the multichannel scaler.

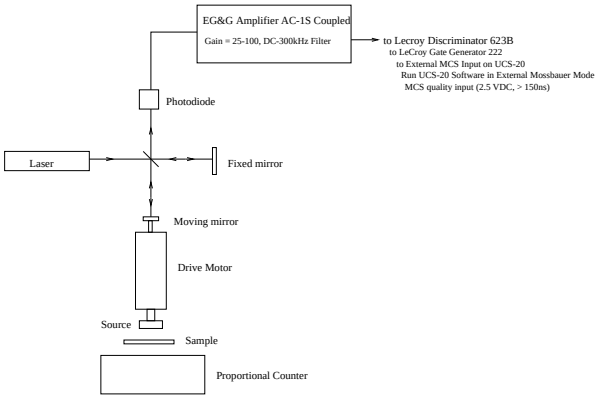

FIG. 9: Schematic diagram of the Michelson interferometer for calibration of the velocity sweep. **Be particularly sensitive to try and block any stray reflections of the HeNe laser from interferometer into another another portion of the lab. Block as necessary using black posterboard or index cards.**

Call V_i the average velocity of the moving mirror during the time interval corresponding to the ith channel of the multichannel scaler display. The average rate of pulses during the ith time interval is $\frac{2V_i}{\lambda}$. If we call T the time interval during which pulses are directed to a given channel by the clock register, i. e., the dwell time per channel, and N the number of sweeps made during the course of a calibration run, then the total number of counts recorded in the ith channel will be

$$C = NT\Big(\frac{2V_i}{\lambda}\Big) \tag{4.1}$$

Solving for the velocity corresponding to the ith channel, we find

$$V_i = \frac{C\lambda}{2NT} \tag{4.2}$$

The orientations of the laser, the beam splitter (glass slide), and the two adjustable mirrors should be adjusted so that the incident and reflected beams all strike the beam splitter as close to the same spot as possible without allowing a reflected beam to go straight back into the laser where it may disrupt the performance of the laser. **Be sure to prevent unwanted laser light from crossing the room potentially harming another investigator.** Adjust the mirrors to superpose the two beams of the interferometer on the photodiode.

Operate the UCS20 in 'External Mössbauer' mode and turn on the Mössbauer drive motor. Watch the oscilloscope for the interference signal as you make small adjustments of the mirrors. When you see some interference fringes on the photodiode output, send the signal to the EG&G 5113 Amplifier with a gain of about 10-100 and AC couple the A-input. Apply a low-pass filter with a cutoff of about 300 kHz. This signal is then sent

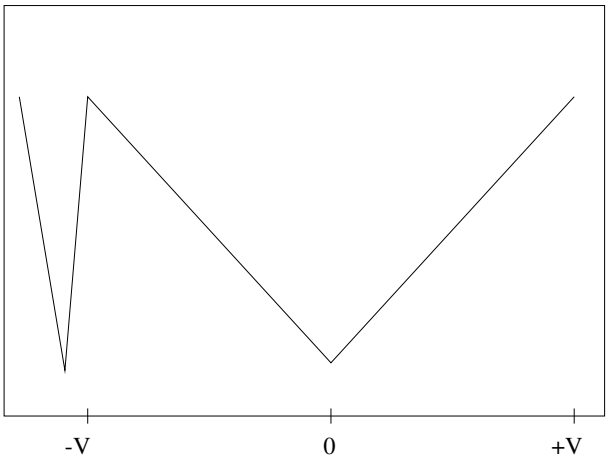

FIG. 10: Ideal appearance of the multichannel scaler screen after several minutes of operation with the interferometer velocity calibrator. The sharp feature at the start is produced during the rapid reversal of the velocity of the piston at the high speed end of its stroke. In reality, the bottom of the "V" will probably be truncated due to the low amplitude of the pulses during the low-velocity portion of the sweep.

to the LeCroy 623B discriminator converting the analog interference signal into a fast rise time logic level pulse. In order to generate an "MCS-friendly" input, we process the output of the discriminator with the LeCroy 222 Gate Generator. Set the pulse width to 10 microseconds and send the TTL output into the External MCS input on the back of the Spectrum Techniques UCS-20 instrument. When everything is working properly, the multichannel scaler look similar to Fig. 10.

When you have mastered the calibration procedure, run the Mössbauer setup with an enriched iron foil absorber and adjust the amplitude of the velocity sweep to obtain the 6-line Zeeman pattern that will be your secondary calibrator. Record the channel numbers of the absorption line centroids. Without changing any of the settings of the Mössbauer drive circuit except to turn it off and on, proceed with the interferometer calibration by replacing the proportional counter pulses with the interferometer pulses. If everything is working properly, the velocity sweep should be precisely linear so that $V_i = ai + b$ where 'a' and 'b' are constants. Thus two measurements of the velocity in good (smooth) portions of the calibration "V" pattern are sufficient to determine 'a' and 'b'. Since realigning the interferometer each time a velocity change is made, subsequent velocity calibrations may be made using the known splittings of either metallic iron or Fe_2O_3. Please see the 'ASA-700 Mossbauer Drive' document under the 'Selected Resources' section of the Junior Lab web site for these data.

The following is a menu of possible investigations:

1. Properties of the Resonant Line Shape. In this experiment, you will use an absorber of sodium ferrocyanide $Na_3Fe(CN)_6 \cdot 10H_2O$ which has no magnetic field or electric field gradient at the crystal sites of the iron nuclei. Absorbers of three different thicknesses are available. This allows you to measure the line width as a function of thickness so that you can extrapolate your results to zero thickness. Derive a value for the intrinsic width of the 14.4 keV first excited state of ^{57}Fe and compute the implied lifetime of the excited state. What other causes of line broadening may be present in your data?

2. Temperature coefficient of the Mössbauer lines and the twin "paradox". The temperature effect is a shift in the resonant frequency of an absorption line due to the second order Doppler effect which amounts to a slowing of the atomic "clocks" in a heated sample due to their thermal motion relative to the reference atomic clocks in the lab. According to the theory of relativity, the effect should be of the order of $(\frac{\nu}{c})^2 \approx \frac{kT}{mc^2} \approx 10^{-13}$. That is small indeed, but accessible to Mössbauer spectroscopy. It is also a proof that the so-called "twin paradox" (not really a paradox since it follows logically from the theory of relativity) is really true, i.e. that if you send your twin on a fast round trip rocket flight he/she will return younger than you. See Reference [4], page 63 for more details. The strategy of this experiment is as follows:

   (a) Operate the spectrometer at very high dispersion and calibrate it by measuring the separation between the two central peaks of the ^{57}Fe spectrum;

   (b) Measure the fractional shift position $\frac{\Delta E}{E}$ of the single peak of stainless steel between room temperature T and $T + \Delta T$;

   (c) Compare the result with the theory of Josephson (page 252 within the Frauenfelder collection).

   To measure the temperature effect reduce the velocity amplitude of the Mössbauer drive so that the two central components of the Zeeman pattern are widely separated, say by 400 channels, i.e. increase the dispersion of the spectrometer so that the small effect of temperature will be able to cause a shift of several channels in the centroids of the Zeeman lines. Calibrate the velocity scale by recording the locations of the central two peaks of the ^{57}Fe spectrum. Place the aluminum-block oven with the Mylar windows, containing the thin stainless steel and attached heater and thermocouple, in position between source and counter. Accumulate a spectrum with sufficient counts so that the positions of the peaks of the absorption line can be determined with an uncertainty no greater than 11 channel.. Adjust the temperature control to $120°C$ and turn on the heater. When the temperature has stabilized record a high-temperature spectrum. Repeat cold

and hot measurements several times to reduce and evaluate your random error. Determine the temperature coefficient from your data, i.e. the fractional change in the peak energies per degree centigrade, and compare your results with the theoretical prediction (see the discussion in Frauenfelder, 1962, page 63).

3. Quadrupole splitting and isomer shifts in Fe^{++} and Fe^{+++} ions. Measure the absorption spectra in samples of $FeSO_4 \cdot 7H_2O$ and $Fe_2(SO_4)_3$ and determine the quadrupole splittings (if any) and the isomer shifts. Accumulations of 30 to 60 minutes should be sufficient to show the absorption spectra and permit accurate measurement of the splittings. See [6] for a discussion of the implications of such measurements.

4. Combined Zeeman and quadrupole effects in Fe_2O_3. Measure the absorption spectrum of an isotope-enriched sample of red (ferrous) iron oxide, Fe_2O_3. (Note that the red oxide, otherwise known as rust, is not ferromagnetic, i.e. it is not attracted by a magnet.) Allowing for the combined effects of Zeeman and quadrupole splitting, and using the value for the magnetic moment of the first excited state obtained above, derive the strength of the magnetic field at the iron nuclei in red oxide, and the magnitude of the product of the quadrupole moment and the electric field gradient.

5. The absorption spectrum of magnetite (Fe_3O_4; the black magnetic oxide of iron). Try to figure out what is going on. The available samples of magnetite require long exposures because they have only the natural abundance of 2%. The Mössbauer spectrum of magnetite has provided important clues to the structure of this peculiarly complex substance. You will probably need to dig into the literature for help in the interpretation of the spectrum. There is an extensive series of reviews on Mössbauer spectroscopy in the Science Library. Incidentally, the black sand that you may have seen on ocean beaches is magnetite.

6. Other iron-bearing materials, like rust, cast iron filings, spring steel, medicinal iron pills, black sand.

Other references related to this experiment are [7–12]

[1] *Nobel Lectures from Robert Hofstadter and Rudolph Ludwig Mössbauer* (1961).
[2] A. C. Melissinos, *Experiments in Modern Physics* (Academic Press: Orlando, 2003), ISBN QC33.M523, physics Department Reading Room.
[3] S. Gasiorowicz, *Quantum Physics* (Wiley: New York, 1996), 2nd ed., ISBN QC174.12.G37, physics Department Reading Room.
[4] H. Frauenfelder, *The Mössbauer Effect* (Benjamin: New York, 1962), ISBN QC477.F845, physics Department Reading Room.
[5] S. S. Hanna, J. Heberle, C. Littlejohn, G. J. Perlow, R. S. Preston, and D. H. Vincent, Phys. Rev. Letters **4**, 177 (1960).
[6] S. DeBenedetti, Sci. Amer. (1960).
[7] Boyle and Hall, Reports on Progress in Physics, XXV **Aug**, 442 (1962), qC.R425, Science Library Journal Collection, London.
[8] O. C. Kistner and A. N. Sunyar, Phys. Rev. Letters **4**, 412 (1960).
[9] O. C. Kistner, A. N. Sunyar, and D. H. Vincent, American Institute of Physics: New York (1963).
[10] S. L. Ruby, L. M. Epstein, and K. H. Sun, Rev. Sci. Instr. **31**, 580 (1960), qC.R453, Physics Department Reading Room.
[11] E. Oldfield and R. Kirkpatrick, Science **227**, 1537 (1985).
[12] U. Gonser, *Mössbauer Spectroscopy*, vol. 5 of *Topics in Applied Physics* (Springer-Verlag, 1975), ISBN QC491.M6, pp 16-17.

APPENDIX A: MÖSSSBUAER EFFECT EQUIPMENT LIST

Model	Description	Source
ASA S-700A	Mössbauer Drive	NA
ASA K-4	Mössbauer Motor	NA
ASA PC-200	Scintillator	no longer available
Canberra 3002D	HV Power Supply	canberra.com
Canberra 815	Amplifier	canberra.com
MG 05-LHR-111	Laser	mellesgriot.com
Ortec 109PC	Pre-Amp.	ortec-online.com
MIT	Low Freq Amp	homemade
MIT	Interferometer Setup	homemade
MIT	St. Steel Absorber/Oven	homemade
MIT	Mössbauer Absorbers	webres.com

APPENDIX B: VERIFICATION OF VELOCITY CALIBRATION

To first order, T, the dwell time per channel is simply that which was set under the Mossbauer settings submenu in the UCS-20 software.

This can be confirmed, if desired by feeding pulses from a pulse generator to both the input of the pulse amplifier and to a frequency meter. Integrate for sufficient

time to obtain a smooth horizontal pattern and count the number of sweeps. From the number of sweeps, the average number of pulses recorded per channel, and the frequency of the pulses, you can compute T, the dwell time per channel.

Example: Suppose you record N=1000 sweeps and find C=2000 counts in a particular channel. With the ASA-700 thumb-wheel sweep controls set at 80 mm s^{-1}, you may have found in the frequency-generator calibration that T=170μs ch^{-1}. The wavelength of the HeNe laser light is $\lambda = 6328\mathring{A}$, or 6.328×10^{-5}cm. According to Equation 4.2, the piston velocity at that part of the cycle is

$$V = \frac{6.328 \times 10^{-5} \times 2000}{1000 \times 0.000170 \times 2} = 0.367\ cm\ s^{-1} \qquad \text{(B1)}$$

Table 1.2. Mössbauer parameters and effects

Symbol	Definition and units used	Corresponds in wave or particle picture, respectively	Physical parameter	Cause of the effects	Observed or predicted effects	Formulation	Fe^{57} energy level diagram with allowed transitions: Source (S) / Absorber (A)	Schematic representation of observation (resonance absorption vs. velocity)
f	Number of recoil free γ-ray events (emission or absorption) divided by total number of γ-ray events, dimensionless (Debye-Waller factor)	Relative intensity of resonance line Probability of recoil-free events	Probability of phonon creation or annihilation by the emitting or absorbing atom or mean square of vibrational amplitude		Intensity of Mössbauer line	$f = \exp - k^2 \langle x^2 \rangle$	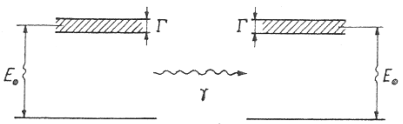	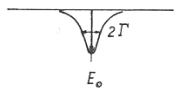
				Vibrational modes of the resonating atom (as function of direction, temperature and pressure, in different lattices, phases, near critical temperatures, at surfaces and close to other lattice defects)	Intensity dependence			
				Vibrational modes of the resonating atom in non-cubic symmetry of single crystals, and polycrystalline materials	Change in the relative line intensities of hyperfine split spectra (Goldanskii-Karyagin effect)			
Γ	Full width at half maximum in energy units	Line width or spread in wave length Uncertainty or spread in energy	Mean lifetime of the excited state Apparent mean lifetime of the excited state Atomic, magnetic electric relaxation processes		Natural line width	$\Gamma_{\text{eff}} = \frac{\hbar}{\tau_{\text{eff}}}$	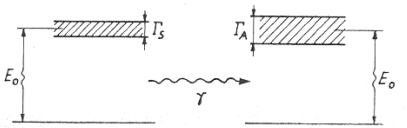	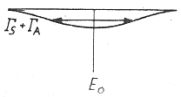
				Saturation effects Diffusion and Brownian motion of the atoms or molecules, Relaxation processes, Spin-flip processes, Superparamagnetism, Fluctuations near critical temperatures (magnetic, ferroelectric and other phase transitions)	Line broadening			
				Delay coincidence measurements Thermal spike	Line narrowing			
				Change in the mean lifetime of the excited state	Line narrowing or line broadening			
E_γ	Mean energy of radiation in energy units	Mean wavelength of γ-radiation Mean energy of γ-radiation	Energy difference between excited and ground state	Interaction of the nuclear charge distribution with the electron density at the nuclei in source and absorber (electric monopole interaction)	Isomer shift	$\delta = C \frac{\delta R}{R} [\lvert\psi_A(0)\rvert^2 - \lvert\psi_S(0)\rvert^2]$	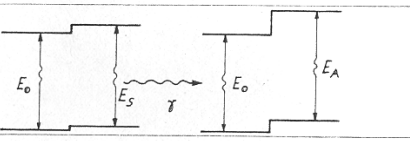	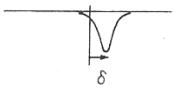
				Interaction of the nuclear magnetic dipole moment with a magnetic field at the nucleus (magnetic dipole interaction); Angular dependence of the nuclear Zeeman effect in single crystals, preferred oriented materials (texture) and polycrystalline materials; Symmetry tests in γ-decay (time reversal invariance, parity conservation); Boltzmann population of the hyperfine sublevels at low temperature ($\ll 1$ K)	Nuclear Zeeman effect Change in the relative line intensities, polarization of the γ-radiation (linear, elliptical, circular) Change in relative line intensities Change in relative line intensities	$E_m = -g_N \beta_N H m_I$	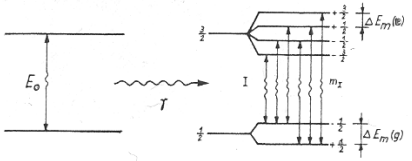	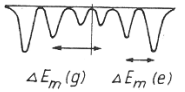
				Interaction of the nuclear quadrupole moment with EFG at the nucleus (electric quadrupole interaction) Angular dependence of the quadrupole interaction in single crystals, preferrentially oriented materials (texture) and polycrystalline materials	Quadrupole splitting Change in the relative line intensities, polarization of the γ-radiation	$E_Q = \pm \frac{1}{4} eQV_{zz} (1 + \frac{1}{3}\eta^2)^{\frac{1}{2}}$	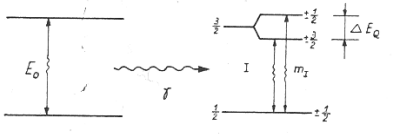	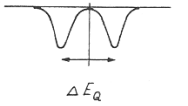
				Change in temperature Change in pressure Acceleration and gravitational fields	Relativistic effects Temperature shift Pressure shift Acceleration and gravi tational red shift	$\delta_R = \frac{v^2}{2c^2} E_\gamma$	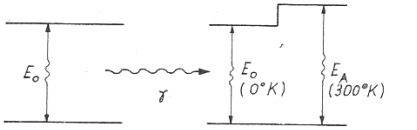	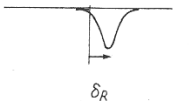

FIG. 11: From Mössbauer Spectroscopy, Edited by U. Gonser, Springer-Verlag, 1975

Superconductivity

MIT Department of Physics
(Dated: February 2, 2010)

Several of the phenomena of superconductivity are observed in three experiments carried out in a liquid helium cryostat. The transition to the superconducting state of each of several bulk samples of Type I and II superconductors is observed in measurements of the exclusion of magnetic field (the Meisner effect) from samples as the temperature is gradually reduced by the flow of cold gas from boiling helium. The persistence of a current induced in a superconducting cylinder of lead is demonstrated by measurements of its magnetic field over a period of a day. The tunneling of Cooper pairs through an insulating junction between two superconductors (the DC Josephson effect) is demonstrated, and the magnitude of the fluxoid is measured by observation of the effect of a magnetic field on the Josephson current.

1. PREPARATORY QUESTIONS

1. How would you determine whether or not a sample of some unknown material is capable of being a superconductor?

2. Calculate the loss rate of liquid helium from the dewar in L d^{-1}. The density of liquid helium at 4.2 K is 0.123 g cm^{-3}. At STP helium gas has a density of 0.178 g L^{-1}. Data for the measured boil-off rates are given later in the labguide.

3. Consider two solenoids, each of length 3 cm, diameter 0.3 cm, and each consisting of 200 turns of copper wire wrapped uniformly and on top of one another on the same cylindrical form. A solid cylinder of lead of length 3 cm and diameter 0.2 cm is located inside the common interior volume of the solenoids. Suppose there is an alternating current with an amplitude of 40 mA and a frequency of 5 KHz in one of the solenoids. What is the induced open circuit voltage across the second solenoid before and after the lead is cooled below its critical temperature?

4. What is the Josephson effect?

5. Calculate the critical current for a 1mm diameter Niobium wire at liquid Helium temperatures (4.2 K). Use equation 3.1 to evaluate the critical magnetic field at 4.2 K and knowing that Bo = 0.2 Tesla for Niobium.

2. INTRODUCTION

In this experiment you will study several of the remarkable phenomena of superconductivity, a property that certain materials (e.g. lead, tin, mercury) exhibit when cooled to very low temperature. As the cooling agent you will be using liquid helium which boils at 4.2 K at standard atmospheric pressure. With suitable operation of the equipment you will be able to control the temperatures of samples in the range above this boiling temperature. The liquid helium (liquefied at MIT in the Cryogenic Engineering Laboratory) is stored in a highly insulated Dewar flask. Certain precautions must be taken in its manipulation. **It is imperative that you read the following section on Cryogenic Safety before proceeding with the experiment.**

2.1. CRYOGENIC ASPECTS AND SAFETY

The Dewar flask shown in Figure 6 contains the liquid helium in a nearly spherical metal container (34 cm in diameter) which is supported from the top by a long access or neck tube (length about 50-60 cm and diameter about 3 cm) of low conductivity metal. It holds ∼25 liters of liquid. The boiling rate of the liquid helium is determined by the rate of heat transfer which is slowed by a surrounding vacuum space which minimizes direct thermal conduction and multiple layers of aluminized mylar which minimizes radiative coupling from the room. The internal surfaces are all carefully polished and silver plated for low radiation emissivity. Measurement shows that helium gas from the boiling liquid in a quiet Dewar is released with a flow rate of gas at STP (standard temperature and pressure = 760 torr and 293K) about 5 $cm^3 s^{-1}$.

The only access to the helium is through the neck of the Dewar. Blockage of this neck by a gas-tight plug will result in a build-up of pressure in the vessel and a consequent danger of explosion. The most likely cause of a neck blockage is frozen air (remember everything except helium freezes hard at 4 K) in lower sections of the neck tube. Thus it is imperative to inhibit the streaming of air down the neck. In normal quiet storage condition, the top of the neck is closed with a metal plug resting loosely on the top flange. When the pressure in the Dewar rises above $p_0 = W/A$ (where W is the weight of the plug and A is its cross-sectional area) the plug rises and some pressure is released. Thus the pressure in the closed Dewar is regulated at p_0 which has been set at approximately 0.5 in. Hg.This permits the vaporized helium gas to escape and prevents a counterflow of air into the neck. When the plug is removed, air flows downstream into the neck where it freezes solid. You will have to remove the plug for measurements of the helium level and

for inserting probes for the experiment, and **it is important that the duration of this open condition be minimized. Always have the neck plug inserted when the Dewar is not in use.**

In spite of precautionary measures, some frozen air will often be found on the surface of the neck. This can be scraped from the tube surface with the neck reamer, consisting of a thin-wall half-tube of brass. Insertion of the warm tube will liquefy and evaporate the oxygen/nitrogen layer or knock it into the liquid helium where it will be innocuous. **If you feel any resistance while the probe is being inserted in the Dewar, remove the probe immediately and ream the surface (the whole way around) before reinserting the probe.** The penalty for not doing this may be sticking of delicate probe components to the neck surface. Warmed and refrozen air is a strong, quick-drying glue!

In summary:

1. Always have the neck plug on the Dewar when it is not in use.
2. Minimize the time of open-neck condition when inserting things into the Dewar.
3. Ream the neck surface of frozen sludge if the probe doesn't go in easily.

3. THEORETICAL BACKGROUND

3.1. Superconductivity

Superconductivity was discovered in 1911 by H. Kamerlingh Onnes in Holland while studying the electrical resistance of a sample of frozen mercury as a function of temperature. On cooling with liquid helium, which he was the first to liquify in 1908, he found that the resistance vanished abruptly at approximately 4 K. In 1913 he won the Nobel prize for the liquification of helium and the discovery of superconductivity. Since that time, many other materials have been found to exhibit this phenomenon. Today over a thousand materials, including some thirty of the pure chemical elements, are known to become superconductors at various temperatures ranging up to about 20 K. Within the last several years a new family of ceramic compounds has been discovered which are insulators at room temperature and superconductors at temperatures of liquid nitrogen. Thus, far from being a rare physical phenomenon, superconductivity is a fairly common property of materials. Exploitation of this resistance-free property is of great technical importance in a wide range of applications such as magnetic resonance imaging and the bending magnets in particle accelerators such as the Tevatron at Fermi Lab.

Zero resistivity is, of course, an essential characteristic of a superconductor. However superconductors exhibit other properties that distinguish them from what one might imagine to be simply a perfect conductor, i.e. an ideal substance whose only peculiar property is zero resistivity.

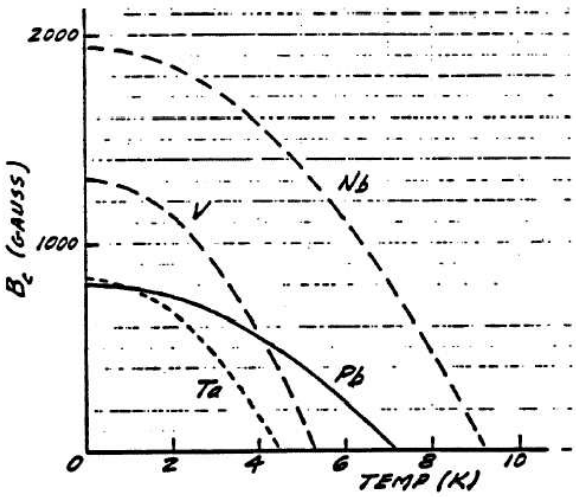

FIG. 1: Critical field plotted against temperature for various superconductors.

The temperature below which a sample is superconducting in the absence of a magnetic field is called the critical temperature, T_c. At any given temperature, $T < T_c$, there is a certain minimum field $B_c(T)$, called the critical field, which will just quench the superconductivity. It is found (experimentally and theoretically) that B_c is related to T by the equation

$$B_c = B_0\Big[1 - \Big(\frac{T}{T_c}\Big)^2\Big] \tag{3.1}$$

where B_0 is the asymptotic value of the critical field as $T \to 0$ K. Figure 1 shows this dependence for various materials including those you will be studying in this experiment.

Note the extreme range of the critical field values. These diagrams can be thought of as phase diagrams: below its curve, a material is in the superconducting phase; above its curve the material is in the non-conducting phase.

3.2. Meissner Effect and the Distinction Between a Perfect Conductor and a Super Conductor

An electric field $\vec{E}$ in a normal conductor causes a current density $\vec{J}$ which, in a steady state, is related to the electric field by the equation $\vec{J} = \sigma\vec{E}$ where σ is called the electrical conductivity. In a metal the charge carriers are electrons, and at a constant temperature, σ is a constant characteristic of the metal. In these common circumstances the relation between $\vec{E}$ and $\vec{J}$ is called "Ohm's law". A material in which σ is constant is called an ohmic conductor.

Electrical resistance in an ohmic conductor is caused by scattering of the individual conduction electrons by lattice defects such as impurities, dislocations, and the displacements of atoms from their equilibrium positions in the lattice due to thermal motion. In principle, if there were no such defects including, in particular, no thermal displacements, the conductivity of a metal would be infinite. Although no such substance exists, it is interesting to work out the theoretical consequences of perfect conductivity according to the classical laws of electromagnetism and mechanics. Consider a perfect conductor in the presence of a changing magnetic field. According to Newton's second law, an electron inside the conductor must obey the equation $e\vec{E} = m\dot{\vec{v}}$, where $\dot{\vec{v}}$ represents the time derivative of the velocity vector. By definition $\vec{J} = ne\vec{v}$ where n is the conduction electron density (number per unit volume). It follows that $\vec{E} = \frac{m}{ne^2}\dot{\vec{J}}$ or more conveniently for later purposes $\vec{E} = \frac{4\pi}{c^2}\lambda^2\dot{\vec{J}}$ where $\lambda^2 = \frac{mc^2}{4\pi ne^2}$. (Note how this relation differs from Ohm's law). From Maxwell's equations we have the relation (CGS units), $\nabla \times \vec{E} = -\frac{1}{c}\dot{\vec{B}}$.

Thus

$$\frac{4\pi\lambda^2}{c}\nabla \times \dot{\vec{J}} = -\dot{\vec{B}} \tag{3.2}$$

Another of Maxwell's equations is $\nabla \times \vec{B} = \frac{1}{c}\left(4\pi\vec{J} + \dot{\vec{E}}\right)$ from which it follows that $\lambda^2\nabla \times (\nabla \times \dot{\vec{B}}) = -\dot{\vec{B}}$ where we assume the low frequency of the action permits us to drop the displacement term $\dot{\vec{E}}$. The latter equation can then be expressed as $\nabla^2\dot{\vec{B}} = \dot{\vec{B}}$ The solution of this equation is $\dot{\vec{B}}(z) = \dot{\vec{B}}(0)e^{\frac{-z}{\lambda}}$ where z is the distance below the surface. Thus the rate of change of $\vec{B}$ decreases exponentially with depth leaving $\vec{B}$ essentially constant below a characteristic penetration depth λ. If a field is present when the medium attains perfect conductivity, that field is retained (frozen-in) irrespective of what happens at the surface. If we attempted to change the magnetic field inside a perfect conductor by changing an externally-applied field, currents would be generated in such a way as to keep the internal field constant at depths beyond λ. This may be thought of as an extreme case of Lenz's law. If a perfect conductor had a density of conduction electrons like that of copper (approximately one conduction electron per atom), the penetration depth would be of order 100 $\mathring{A}$. A magnetic field can exist in a medium of perfect conductivity providing it was already there when the medium attained its perfect conductivity, after which it cannot be changed. It came as quite a surprise when Meissner and Ochsenfeld in 1933 showed by experiment that this was not true for the case of superconductors. They found instead that the magnetic field inside a superconductor is always zero, i.e. $\vec{B} = 0$, rather than the less stringent requirement $\dot{\vec{B}} = 0$. This phenomenon is now referred to as the Meissner Effect.

Shortly after the Meissner effect was discovered it was given a phenomenological explanation by F. and H. London [1]. They suggested that in the case of a superconductor, equation 3.2 above should be replaced by the equation

$$\frac{4\pi\lambda}{c}\nabla \times \vec{J} = -\vec{B} \tag{3.3}$$

which is called the London equation. Continuing as before, one obtains

$$\vec{B} = \vec{B}(o)e^{-\frac{z}{\lambda_L}} \tag{3.4}$$

which implies that $\vec{B} \approx 0$ for depths appreciably beyond λ_L, in agreement with the Meissner Effect.

London's idea was based originally on thermodynamic arguments. However, it is also useful to think of a superconductor as being a perfect diamagnetic material. Turning on a magnetic field in the neighborhood of a perfect diamagnetic material would generate internal currents which flow without resistance and annul the field inside.

The constant λ_L, called the London penetration depth, is the depth at which the internal field has fallen to 1/e of its surface value. Experiments have demonstrated the universal validity of equation 3.4 and have measured its value for many superconducting materials. The magnitude of λ_L may well differ from that of λ since the density of superconducting electrons is not necessarily the same as that of conduction electrons in a normal metal. It varies from material to material and is a function of temperature.

3.3. IMPLICATIONS OF THE MEISSNER EFFECT

The Meissner Effect has remarkable implications. Consider a cylinder of material which is superconducting below T_c. If the temperature is initially above T_c, application of a steady magnetic field $\vec{B}$ will result in full penetration of the field into the material. If the temperature is now reduced below T_c, the internal field must disappear. This implies the presence of a surface current around the cylinder such that the resulting solenoidal field exactly cancels the applied field throughout the volume of the rod. Elementary considerations show that a current in a long solenoid produces inside the solenoid a uniform field parallel to the axis with a magnitude determined by the surface current density (current per unit length along the solenoid axis), and no field outside the solenoid. In the case of the superconducting cylinder in a magnetic field, the surface current is in a surface layer with a thickness of the order of λ_L. Any change of the externally applied field will cause a change of the surface current that maintains zero field inside the cylinder. The

difference between this behavior and that of a perfectly conducting cylinder is striking. As mentioned previously, if such a cylinder underwent a transition to a state of perfect conductivity in the presence of a magnetic field, the internal field would remain unchanged and no surface current would appear. If the field were then reduced, a surface current would be induced according to Faraday's law with the result that the flux of the internal field would remain constant.

Next we consider the case of a hollow cylinder of material which is superconducting below T_c. Just as in the solid rod case, application of a field above T_c will result in full penetration both within the material of the tube and in the open volume within the inner surface. Reducing the temperature below T_c with the field still on gives rise to a surface current on the outside of the cylinder which results in zero field in the cylinder material. By itself, this outside-surface current would also annul the field in the open space inside the cylinder: but Faraday's law requires that the flux of the field inside the cylinder remain unchanged. Thus a second current must appear on the inside surface of the cylinder in the opposite direction so that the flux in the open area is just that of the original applied field. These two surface currents result in zero field inside the superconducting medium and an unchanged field in the central open region. Just as before, the presence of these two surface currents is what would be expected if a magnetic field were imposed on a hollow cylinder of perfectly diamagnetic material.

If now the applied field is turned off while the cylinder is in the superconducting state, the field in the open space within the tube will remain unchanged as before. This implies that the inside-surface current continues, and the outside-surface current disappears. The inside-surface current (called persistent current) will continue indefinitely as long as the medium is superconducting. The magnetic field inside the open area of the cylinder will also persist. The magnetic flux in this region is called the frozen-in-flux. In effect, the system with its persistent currents resembles a permanent magnet. Reactivation of the applied field will again induce an outside-surface current but will not change the field within the open space of the hollow cylinder. One should also be aware of the obvious fact that magnetic field lines cannot migrate through an **SC (superconductor)**.

Various parts of the experiment will demonstrate the striking features of the superconducting state, which differ so markedly from the hypothetical perfect-conducting state.

Incidentally, no perfect conductors are known. However, partially ionized gas of interstellar space ($\approx$ 1 hydrogen atom cm^{-3}) is virtually collisionless with the result that it can be accurately described by the theory of collisionless plasma under the assumption of infinite conductivity.

4. SUPERCONDUCTIVITY THEORY TODAY

4.1. BCS Theory

We note that the London equation, equation 3.3, is not a fundamental theory of superconductivity. It is an ad hoc restriction on classical electrodynamics introduced to account for the Meissner Effect. However, the London equation has been shown to be a logical consequence of the fundamental theory of Bardeen, Cooper, and Schrieffer - the BCS theory of superconductivity for which they received the Nobel Prize in 1972 [2]. A complete discussion of the BCS theory is beyond the scope of these notes, but you will find an interesting and accessible discussion of it in [3] (vol. III, chapter 21) and in references [2, 4, 5]

According to the BCS theory, interaction between electrons and phonons (the vibrational modes of the positive ions in the crystal lattice) causes a reduction in the Coulomb repulsion between electrons which is sufficient at low temperatures to provide a net positive and long-range attraction. This attractive interaction causes the formation of bound pairs of remote electrons of opposite momentum and spin, the so-called Cooper pairs. Being bosons, many Cooper pairs can occupy the same quantum state. At low temperatures they "condense" into a single quantum state (Bose condensation) which can constitute an electric current that flows without resistance. The quenching of superconductivity above T_c is caused by the thermal break-up of the Cooper pairs. The critical temperature T_c is therefore a measure of the pair binding energy. The BCS theory, based on the principles of quantum theory and statistical mechanics, is a fundamental theory that explains all the observed properties of low-temperature superconductors.

4.2. RECENT DEVELOPMENTS IN HIGH-T_c SUPERCONDUCTING MATERIALS

The BCS theory of superconductivity led to the conclusion that T_c should be limited by the uppermost value of phonon frequencies that can exist in materials, and from this one could conclude that superconductivity was not to be expected at temperatures above about 25 K. Workers in this field were amazed when Bednorz and Müller [6], working in an IBM laboratory in Switzerland, reported that they had found superconductivity at temperatures of the order 40 K in samples of La-Ba-Cu-0 with various concentrations. This is all the more surprising because these are ceramic materials which are insulators at normal temperatures.

The discovery of high-temperature superconductors set off a flurry of experimental investigations in search of other high-T_c materials and theoretical efforts to identify the mechanism behind their novel properties. It has since been reported that samples of Y-Ba-Cu-0 exhibit T_c at 90 K with symptoms of unusual behavior at even higher temperature in some samples. Many experiments have

been directed at identifying the new type of interaction that triggers the high-T_c transitions. Various theories have been advanced, but none has so far found complete acceptance.

5. EXPERIMENTAL APPARATUS

5.1. Checking the level of liquid Helium in the dewar

A "thumper" or "dipstick" consisting of a 1/8" tube about 1 meter long with a brass cap at the end is used for measuring the level of liquid helium in the Dewar. The cap is closed with a thin sheet of rubber so that pressure oscillations in the tube can be more easily sensed (thumpers are often used without this membrane). The tube material, being a disordered alloy of Cu-Ni, has very low thermal conductivity (over three orders of magnitude less than that of copper!) particularly at low temperature and will conduct very little heat into the helium. The measurement consists in sensing the change of frequency of pressure oscillations in the tube gas acting on the rubber sheet between when the lower end is below and above the liquid level.

After removing the neck plug, hold the dipstick vertically above the Dewar and lower it slowly into the neck at a rate which avoids excessive blasts of helium gas being released from the Dewar. During the insertion, keep your thumb on the rubber sheet and jiggle the tube up and down slightly as you lower it so as to avoid stationary contact with the neck surface and possible freezing of the tube to the neck. When the bottom end has gotten cold with no noticeable release of gas from the Dewar neck, you will notice a throbbing of the gas column which changes in frequency and magnitude when the end goes through the liquid helium surface. Vertical jiggling of the dipstick may help to initiate the excitation. This pulsing is a thermal oscillation set up in the gas column of the dipstick by the extreme thermal gradient, and it changes upon opening or closing the lower end of the tube.

When the probe is in the liquid, the throbbing is of low frequency and constant amplitude. When pulled above the surface of the liquid, the frequency increases and the amplitude diminishes with distance away from the liquid surface. Identify this change by passing the thumper tip up and down through the surface a number of times, and have your partner measure the distance from the stick top to the Dewar neck top. With a little experience you should be able to establish this to within a millimeter or so. Following this measurement, lower the dipstick to the bottom of the Dewar and repeat the distance measurement. Once the dipstick has been lowered to the bottom, it may get clogged with frozen sludge which has collected in the bottom of the Dewar, and you may have trouble in exciting further throbbing. If this occurs and you want to continue measurements, raise the stick until the tip just comes out of the Dewar and start again. Both partners

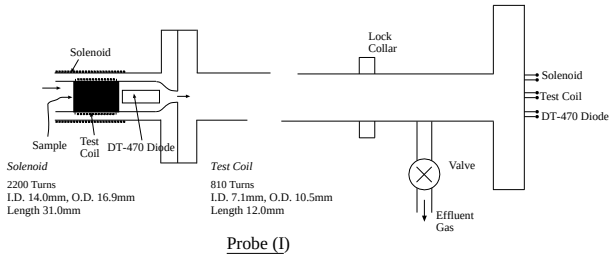

FIG. 2: Diagram of probe I. The distance from the top of the lock collar to the bottom of the probe is 30.5".

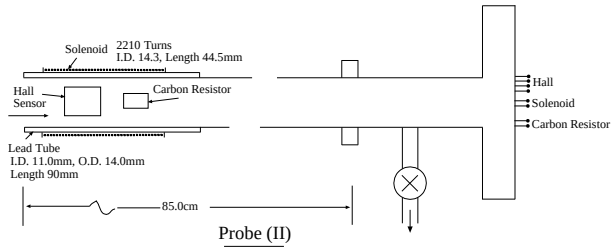

FIG. 3: Diagram of probe II. The distance from the top of the lock collar to the bottom of the probe is 30.5".

should assess the level independently. A depth-volume calibration curve for the Dewar is taped to the wall next to the experiment.

Straighten the dipstick before and after insertion - it is easily bent, so take care. Be sure to record the depth reading on the Usage Log Sheet on the clipboard above the experimental station before and after Dewar use.

You will be using three different insert probes which contain different active components. Each probe is essentially a long, thin-walled stainless steel tube which can be inserted and positioned in the neck tube of the Dewar. A rubber flange is provided on the probe for sealing between the probe and Dewar neck so that the helium gas can escape only through the probe tube. Various labeled electrical leads from the thermometer, coils and field-sensor emerge from the top of the probe tube. Helium gas flows up the probe tube, cooling it, and escapes through a side valve at the top, either directly to the atmosphere or through a gas flow gauge – needle valve – vacuum pump system which permits accurate control of the sample temperature.

Probe I has provision for changing the samples (Pb, V and Nb), each in the form of a small cylinder of common diameter 0.60 cm. The samples are inserted in a thin-wall hollow brass cylinder around which is wound a test coil of dimensions given in Figures 2, 3 and 5. Around the test coil is wound a solenoid coil which is longer than the test coil and sample, and which can produce a magnetic field penetrating both test coil and sample cylinder. Immediately above the centered sample is a small commercial silicon diode (Lakeshore Model DT-470). All electrical lines run up the probe tube to the connections at the top.

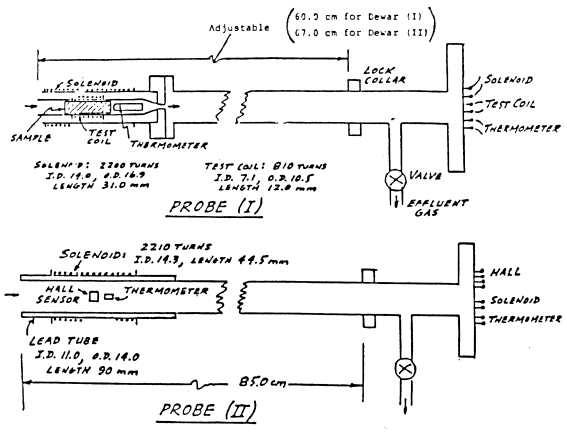

FIG. 4: Diagrams of probes I and II. The distance from the top of the lock collar to the bottom of the probe is 30.5".

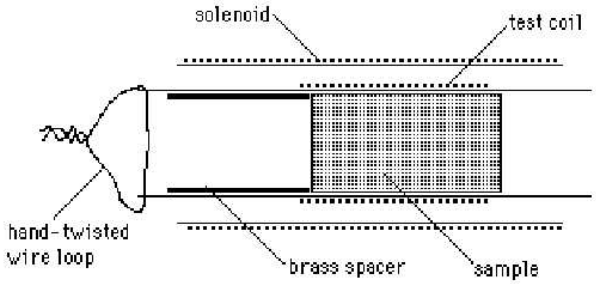

FIG. 5: Placement of the sample in probe I. The test coil has 810 turns of wire with a 7.1mm ID and a 10.5mm OD. It's length is 12.3mm

The rubber flange connection on each probe seals the Dewar neck tube to the probe tube, thereby forcing the helium gas to escape through the probe tube. The rubber flange should be stretched over the lip of the Dewar neck and tightened. A knurled, threaded ring at the top of the flange connector permits one to slide the probe tube up or down relative to the rubber flange connector (which of course is in fixed position on the Dewar). This controls the position of the sample in the Dewar neck. A small back-and-forth twisting motion during the process eases the motion. Never apply excessive force in sliding the probe tube along the flange. The lock collar on the tube and the side valve tube may be used with reasonable restraint as pressure points for providing sliding or twisting. On the top part of the rubber flange assembly, a small gas exit line contains a check valve which serves as a safety release if the pressure in the Dewar exceeds a set point. **Do not disturb it.**

The insert probes are delicate and must be handled with care. This means that they should not be bumped against other objects nor strained when maneuvering them into or out of the Dewar. A storage rack is provided for holding them when not in use. When inserting or withdrawing the probes, keep them strictly vertical, no bending please!!!

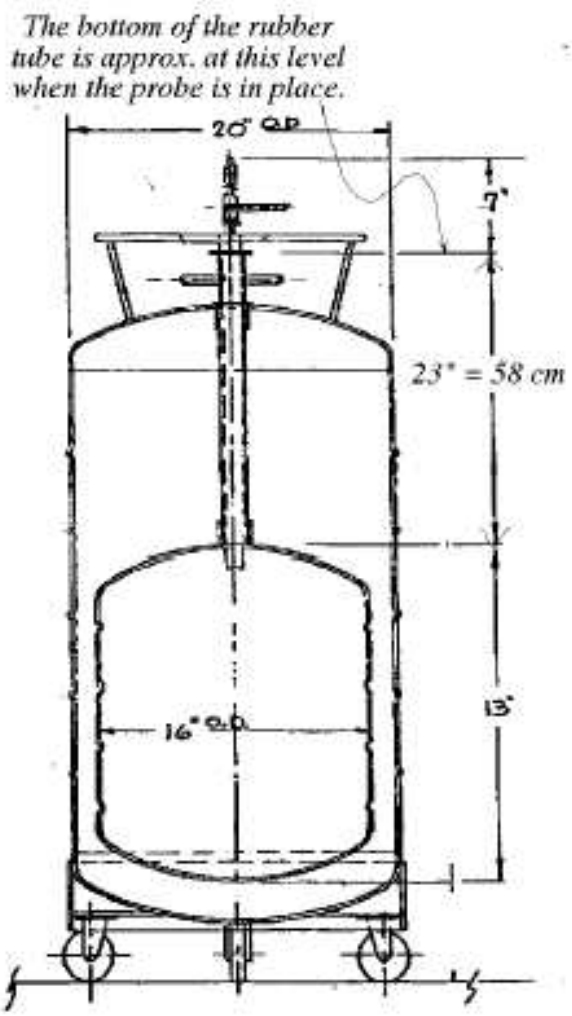

FIG. 6: Illustration of typical storage Dewar.

5.2. TEMPERATURE CONTROL OF SAMPLES

Temperature control of the various samples is achieved by control of the flow rate of cold helium gas passing the samples and thermometers in the probe tips.

The probes are designed so that all exiting helium gas must pass by the sample and its nearby thermometer once the probe is sealed on the Dewar. A large temperature gradient exists along the Dewar neck tube. By judiciously positioning the tip of the probe in the Dewar neck tube and varying the gas flow, we can control the temperature of the sample. This can be done by pumping the gas through a needle valve (for control) and a flow gauge (for measurement). In this procedure the normal liquid helium boiling rate is accelerated so that more cold gas passes by the sample, thereby reducing its

temperature.

Experience with our probes has shown that a good operating position of the bottom of the probe is found to be about x=10 cm (for probe I) and about x=4 cm for probe II above the bottom of the Dewar neck. At these insert positions, variation of the flow over the gauge range will provide temperature control over the range of interest (4-20 K). Gas flow is controlled with a small-angle needle-valve connected in series with the flow gauge. Use the OPEN-CLOSE valve to isolate the vacuum-pump from the system and stop the pumping. **Never close the gas flow by tightening the metal needle valve to its fully closed position.** This can damage the fine needle-surface.

Measure the length of the probes using the lock collar (Fig 4) as a reference so that you know how to position the probes to their desired x-positions. Make a sketch in your lab notebook, **it is important!**

5.3. TEMPERATURE MEASUREMENT

In Probe I, a Silicon diode, located 1 cm above the sample is used to measure the temperature. The 10μA current from the source box through the diode in the forward direction causes a voltage drop of $\sim$ 0.5V at 300K, which changes little until $\sim$ 20K, but there changes rapidly to $\sim$1.6V. Using the table in the Appendix (Table I) you can determine the temperature of the sample material.

6. EXPERIMENTAL PROCEDURE:

6.1. Preparing the probe

1. Place the probe on the table near the helium gas tank. The probe assembly should be at room temperature and dry. If it is damp from condensation, use the warm (not hot) air blower and Kleenex for blotting.

2. If you are using probe I, slide the selected sample cylinder into the small brass tube. Notice that the sample fits loosely in the brass tube: this permits cold helium gas to pass by the sample and thermometer (see Figure 5) and up the probe tube. Secure the sample in the brass tube by threading a small loop of copper wire through holes in the brass tube and hand-twisting the wire ends.

   Take special care that the sample and spacer cannot fall out into the Dewar when the probe is in the Dewar. When the probe is properly sealed onto the Dewar, all exiting gas must pass up the brass tube and out from the probe at the top.

3. The rubber flange assembly (for sealing the probe tube to the Dewar neck) can be slid on the probe tube by releasing the 0-ring pressure with the knurled ring. We try to keep a very light film of grease on the probe tube to facilitate easy sliding. A combination of twisting while sliding will ease the sliding operation. Slide the rubber flange assembly towards the bottom of the probe tube so that it contacts the upper bumper guard. Tighten the knurled ring.

4. Flush the probe tube with low pressure helium gas from the helium gas bottle to displace the air in the probe tube and expel or evaporate any condensed water droplets that may have collected in constricted sections of the probe tube during the previous use. Use a gentle flow of dry helium gas from a high-pressure storage tank to do this. The top center valve on the tank (turning counter-clockwise looking down opens it) releases high-pressure gas (as read on the gauge) to a pressure-regulating valve on the side. Turning the pressure-regulating handle, clockwise, controls the pressure of exiting gas. After turning this handle counter-clockwise so that no gas is released, connect the exit tubing to the local flow gauge and then to the top exit valve (set OPEN) of the probe tube.

Carefully turn the handle clockwise to start the gas flow through the tube until you can just hear it flowing from the bottom of the probe. You should feel a modest flow of gas emanating from the bottom tube holding the sample. Continue this flushing operation for 5 - 10 secs then close the valve on the probe. Important: Keep the open end of the probe pointed down so that the trapped helium gas will not escape!

6.2. Precooling the probe

1. Start with the probe in the extended position using the knurled knob assembly. After clearing the inside surface of Dewar neck tube with the neck reamer, hold the probe tube assembly vertically above the neck and lower it into the Dewar. Get your instructor or TA to help you with this and the following operation the first time it is done. Seat the rubber flange over the Dewar neck lip and push (with some twisting) the rubber flange down as far as it goes. The bottom of the rubber will touch the nitrogen vent tubes. Tighten the lower hose clamp around the Dewar neck but do not tighten (or release) the top clamp ring. The probe tube is now sealed to the Dewar and all exiting gas must escape through the top exit valve, which should now be in the OPEN position.

2. Connect the probe cable to the 9-pin D-connector at the top. We will want to follow the temperature during the precooling operation, so connect the thermometer leads to the 10 microamp source

and adjust according to the instructions given previously. The voltage across the silicon diode in probe I should be about 0.5 V since we are still close to room temperature (in probe II the resistance should be about 300 Ω).

3. Slowly lower the probe tube in the rubber flange assembly by releasing the O-ring pressure with the knurled ring. **CAUTION: if the pressure is released too much, the weight of the probe may cause it to fall abruptly.** Avoid this by holding the probe tube when releasing the pressure. A slight twisting of the probe tube in the O-ring may be helpful in achieving a smooth sliding movement. Continue lowering the probe tube until signs of increased exit gas flow appear. Stop at this position, tighten knurled ring, and look for signs of thermometer cooling. Watch the temperature develop using the table in the Appendix (Table I). Depending upon the liquid helium level in the Dewar, you should notice an increased gas flow and this is cooling the bottom of the probe. The thermometer resistance will show very little change until its temperature gets into the 40-70 K range.

   After waiting a couple of minutes at this 2 cm position to see what happens, continue the lowering over the remaining distance in small steps (perhaps 0.5 cm) always waiting a minute after making a change and locking the knurled ring. The system takes a while to respond to a change in position. In a few minutes the voltage across the temperature sensor should be about 1.6 V indicating that the sample is close to 4.2 K.

   During this critical precooling operation, there should be a modest flow of cool exit gas – if the gas release becomes uncomfortably cold to your hand held 4 inches from the exit tube, back up a little and let the system settle down before continuing the operation. You should be seeing a thermometer response depending upon this gas flow. Continue the lowering to the lock collar limit and allow the system to equilibrate, at which time the gas flow should have decreased.

4. If you do not see cold gas being released through the top exit valve (and an associated increase of thermometer resistance) during the lowering operation over the last few centimeters, the probe tube may be blocked and the precooling operation must be stopped. Cold gas escaping from the safety-release tube on the side of the rubber flange assembly (with consequent cooling and frosting of nearby metallic components) is another indication that the probe tube is blocked. With a normal precooling gas flow, only the top section of the metal components of the probe tube will get cold and frosted. This frosting will melt and should be wiped with a cloth once the small equilibrium gas flow has been attained. If there is any evidence of blockage in the probe tube, remove it from the Dewar, place it on the table, warm the assembly to room temperature with the cold air blower, dry, and flush with helium gas. Then reinsert the tube into Dewar as above. *IF YOU SEE BEHAVIOR OTHER THAN THAT DESCRIBED OR ANYTHING NOT ANTICIPATED, CONSULT YOUR INSTRUCTOR.*

5. After you have attained precooling thermal equilibrium (with a very small exit gas flow), the thermometer resistance should indicate a temperature below about 30 K. You can then proceed with the experiments. These are best performed with the sample located in the neck of the dewar. For Probe I, place the sample 10cm above the bottom of the neck and for Probe II, place the sample 4cm above the bottom of the neck. Temperature control at this working position is performed by pumping on the helium vapor at various rates with the mechanical pump beneath the experimental station and the flow-meter/needle valve assembly above the pump.

6.3. Measuring T_c for Vanadium

After loading probe I with the vanadium sample and following the precooling procedures described earlier with the probe assembly at the optimum operating height, you are ready to experiment with controlling the sample temperature. Connect the probe gas exit to the flow gauge-control valve- vacuum pump system. With the ON-OFF valve closed, turn on the vacuum pump. Slowly open the ON-OFF valve so as to see gas flow on the gauge. This can be controlled by adjustment of the metal control valve and with fine adjustment through the teflon micrometer valve. Notice the thermometer response after making an adjustment. Remember that the system takes some time to adjust to a new equilibrium condition – be patient and don't hurry the operations.

Determine T_c by observing the change of mutual inductance between the solenoid and the test coil when the electrical conductivity of the enclosed sample changes abruptly. High conductivity implies that surface currents will be induced in a sample if the external field (from the solenoid) is changed with correspondingly less field penetration into the sample volume. If an AC current is passed through the solenoid, the flux passage through the test coil (and hence the inductive signal in the test coil) will depend upon the sample conductivity. If conditions were ideal, the existence of the Meissner Effect would imply no flux passage in the superconductor and hence zero test coil signal at temperatures below T_c. Our conditions are not ideal, but there will still be a recognizable change at the transition, permitting an accurate determination of T_c.

Connect a function generator, set for a 200 Hz sine wave, at 500 mV_{RMS} amplitude to Channel 1 of the

oscillosope and tee-it to the solenoid marked "OUTER COIL". Because of the low impedence of the outer coil (5.8Ω), the function generator will be loaded down and the measured amplitude on the scope will be ∼100 mV_{RMS}. Connect the "TEST COIL" output to Channel 2 of the oscilloscope and observe the induced signal (it should be about 5-6 mV_{RMS} with the sample in the normal state). Observe the sudden reduction of the test coil signal when the sample is cooled through the transition, and vice-versa, by manipulation of the gas flow rate. Watch out for the inductance between the signal conductors to the "OUTER COIL" and the "TEST COIL" near the point where they enter the cable together.

To measure T_c, record both the test coil signal and the temperature sensor voltage simultaneiously. With experience, you can adjust the gas flow rate so that the temperature drifts slowly through the transition value during which you and your partner can record both signal and temperature sensor values. A slow drift of the temperature will achieve close agreement between sample and thermometer temperatures. A graph of these quantities can be used to assess the resistance of the thermometer at the transition, and hence T_c. Do this a number of times, in both directions, upward and downward in temperature, looking out for possible hysteresis action, and noting how reproducibly the transition can be established. T_c values are usually taken at the midpoints. Make graphs of these drift runs as you take them – seeing them displayed can help with the next one.

Experience has shown that the hysteresis difference between cool-down and warm-up transition curves is strongly dependent upon the speed of passage through the transition. This is probably due to different time constants associated with temperature flow in (or out) of the sample rod relative to that of the temperature sensor.

6.3.1. CHANGE OF T_c IN VANADIUM WITH MAGNETIC FIELD

According to the phase diagrams of Figure 1 and equation (1), the presence of a constant DC magnetic field on the sample will shift the superconducting transition to a lower temperature. We can see and measure this shift if we apply DC current to the solenoid in addition to the AC current needed in the measurement process. Since there is a limitation on the magnitude of the DC magnetic field that can be used (I^2R losses in the solenoid fine wire would perturb the temperature distribution), the magnitude of the transition temperature shift will be very small and careful measurements must be made to observe the effect.

This is best done by fine-tuning the flow rate so that the test coil inductive voltage is being held fixed in time at the midpoint between the SC and NC signal levels which you have established from the transition graphs of the previous section. If this is accomplished then the drift rate effects are eliminated and the thermometer resistance at the mid-range set point can be used as a temperature marker. Repeating the same type of measurement with the magnetic field on can then observe the shift in critical temperature. We note that this procedure for measuring ΔT_c also eliminates the effect of a possible temperature difference between sample and thermometer caused by their different positions in the gas stream.

After getting the mid-range set point data for zero DC magnetic field, connect the output of the solenoid DC Current Supply Box in parallel with the AC current supply and adjust to a DC current of 150 mA. In connecting the DC and AC sources in parallel, the output AC voltage from the audio oscillator will drop (there is extra load on it). You should readjust this to a standard 70 mv RMS. Now redetermine the SC and NC (non-conducting) test coil signal levels (they may differ from the earlier levels) by varying the gas flow rate and again establish the thermometer resistance at the mid-range test signal value which is being held constant in time.

You can calculate the magnetic field at the sample from the solenoid parameters given earlier and what you expect for ΔT, as indicated by Figure 1. Note that from Equation (1), we have the useful relation

$$\frac{dB_c}{dT}|_{@T_c} = \frac{2B_0}{T_c} \tag{6.1}$$

Both measurements, DC ON and DC OFF, should be made under identical conditions.

6.4. TRANSITION TEMPERATURE OF OTHER SAMPLES

After you have finished the measurements on vanadium, withdraw the probe from the Dewar neck in the prescribed manner, close the Dewar neck, and carefully place the probe tube horizontally on the lab table. Parts of the probe tube are very cold and will frost-up. There is an air blower available to speed its warm-up. (CAUTION: the air blower blows either room-temperature air or very hot air according to the switch setting – DO NOT direct hot air on the probe or you will damage insulation components on the probe). It is prudent to keep one hand hand in the air stream to guard against this. After the probe has warmed to room temperature and the frosting has disappeared, water droplets will remain. They should be gently blotted (not rubbed) dry with a Kleenex tissue. Be careful never to insert anything with moisture on its surface into the Dewar neck.

The vanadium rod will slide out from the probe into your hand (NOT dropped on the floor) after removing the twisted clamp wire. **The small sample cylinders are delicate (and expensive), so do not mishandle them – keep them in the storage box when not in use so that they don't get lost.**

6.4.1. TRANSITION TEMPERATURE OF LEAD

Replace the vanadium sample with the lead sample and its brass spacer and follow the same procedure described ealier for obtaining its transition temperature. You will find for the lead sample that the inductive signal in the test coil decreases slowly with lowering temperature as you approach T_c followed by an abrupt, discontinuous change when the sample becomes superconducting. This small change, occurring when the sample is still a normal conductor, reflects the temperature dependence of the lead normal conductivity above T_c but is NOT part of the superconducting transition. Lead is a good conductor at these temperatures.

You may also notice that the magnitude of the fractional change in inductive signal in going through T_c for lead is smaller than it was for vanadium. This again reflects the higher conductivity of lead above T_c. If you are careful in adjusting the RMS value of the voltage being applied to the solenoid so that it is the same for the lead case as it was for the vanadium case, you should find the same value for the SC inductive signal. The sample geometry is the same and infinite conductivity below T_c characterizes both samples. On the other hand, the magnitude of the inductive signal above T_c depends upon the normal state conductivity and this varies from sample to sample, and in fact is a measure of it.

6.4.2. MEISSNER EFFECT IN LEAD

When you have the lead sample in probe I for determining its T_c value, you can do another experiment that unequivocally demonstrates the Meissner Effect, namely, the flux exclusion from a superconductor. By applying a DC magnetic field to the sample in the NC state and then simply cooling it below T_c, the flux should be suddenly expelled in a transient manner. This would induce a transient voltage (and current) in the test coil of our assembly. We can see this transient signal by connecting the test coil to a current integrating circuit (for total charge measurement) as available in a circuit box.

The transient current integrator is simple op-amp circuit, with the induced voltage delivered from the test coil being amplified and driving a speaker.

Apply a DC field with the solenoid current supply (≈200 mA) in the normal state and connect the test coil output into the current integrator box with the box output to the oscilloscope. Set the oscilloscope for a slow 'rolling display mode' (≈ 2 sec/division) and for AC-couple the input, so that you can see the transient change in potential. Upon cooling the sample through T_c with gas flow regulation, a kick in the oscilloscope beam should be observed (up or down) indicating flux passage outward through the test coil. Warming the sample through T_c should give an oppositely directed kick when the field goes back in. You can check the absolute sense of the direction by merely turning off the solenoid current when the sample is in the normal state. With our charge-measuring circuit, the inductive kick is on the scale of 100 mV, so set the oscilloscope sensitivity appropriately.

It is to be emphasized that this test for the presence of the Meissner Effect is a most unequivocal one for a superconductor. It does not occur in a PC. There have been reports in the literature of experiments in which the sample's electrical conductivity (σ) was found to change drastically with T_c (so one would observe an AC test coil signal change), yet the Meissner action failed to appear. An abrupt change in normal conductivity could accompany, for example, a crystallographic transition occurring at low temperatures, and this could mimic a superconducting transition in producing an AC mutual inductance change.

6.5. TRANSITION IN NB

Determine the transition temperatures for Nb in the same way as you have done for vanadium and lead above. Lead is a Type I superconductor which means that the transition is very sharp, unlike Type II superconductors. Type II superconductors have "vortices" in them which allow for small regions with magnetic fields – as long as the "width" of these vortices are smaller than the penetration depth, this behaviour is allowed. These vortices act to slow the transition from "normal" to "superconductor." This is why the Niobium and Vanadium (two of the only three elemental Type II superconductors) show rather wide transitions compared with that of lead.

7. PERSISTENT CURRENT IN A SUPERCONDUCTOR (PROBE II)

We can demonstrate the existence of a persistent current in a superconductor using the hollow lead cylinder sample in Probe II. According to an earlier discussion, if we apply an axial magnetic field to the sample above T_c, cooling the sample below T_c will generate two oppositely-flowing persistent currents on the inside and outside surfaces of the cylinder. Thereafter, removing the external field will remove the outside-surface current but leave the inside-surface current producing the frozen-in-flux inside the cylinder. We can measure this flux, or magnetic field, with the Hall magnetic field sensor, which is positioned along the tube axis of Probe II as indicated in Fig.4.

Probe II contains a hollow cylindrical sample of pure lead (I.D. 1.11 cm, O.D. 1.43 cm, length about 9 cm) around which is wound a solenoidal coil of fine Cu wire (2210 turns, length 4.45 cm). Current in the solenoidal coil will produce a reasonably uniform magnetic field throughout its volume. The field strength can be calculated from the dimensions of the coil and the current. Inside the lead cylinder and along its axis is a tiny magnetic field sensor (a Hall field probe described later) and also a small thermometer (a carbon resistor). The elec-

trical lines run inside the probe tube to the connections at the top of the probe. All of the components of probe II are in a fixed assembly and will remain unchanged during the experiment.

Probe II uses a small carbon resistor to determine the sample temperature. It's resistance varies from $\sim 300\Omega$ at room temperature to $\sim 2000\Omega$ below 20K. Simply using an ohmeter to measure the resistance would produce too much heating ($I^2R = 10^{-4}$W). We therefore limit the current I to 10μA using the current source box and measure the voltage drop in which case the power dissipated is $\sim 10^{-6}$W. The calibration is not given, you will have to establish it using T_c for lead.

In a Hall probe a longitudinal DC current is passed through a semiconductor (InSb in our probe) in the presence of the magnetic field to be measured. A transverse potential appears across the material which varies linearly with the magnetic field and with the DC current. Our Hall probe has a sensitivity of about 20 mV gauss^{-1}, as you will determine, when operated with a standard DC current of 35 mA at low temperature. A Hall-probe circuit box is located at the experiment station. Before using it for field measurement, it must be balanced with a bias voltage in zero magnetic field.

Probe II should be flushed first with helium gas as described earlier. The lock collar on probe II is in fixed position 85.0 cm above the sample and thus this probe can be lowered farther into the Dewar than probe I. It is imperative that you use Figure 6 to help determine the position of the probe bottom after it is inserted into the Dewar. After insertion, follow the same precooling sequence as with probe I and approach low temperature thermal equilibrium at the position where the probe bottom is 2 cm above the Dewar neck bottom. The resistance of the carbon thermometer will be about 2800Ω at $T_c \approx 7$ K for lead (and 300Ω at room temperature). The thermometer response and gas release pattern offer guidance in this precooling. After stability is attained, raise the probe to X ≈ 4 cm where the experiment is best performed and connect the gas pumping system for temperature control. Practice controlling the temperature.

Connect the DC solenoid current supply box to the solenoid and the Hall-sensor current and potential leads to the Hall probe box, taking care to match the color codes. After bringing the probe temperature to low temperature but above T_c so that the lead sample is in the normal state, turn on the Hall current (35 mA by adjustment of rheostat control). With zero solenoid current (hence zero magnetic field), adjust the bias control so that zero Hall voltage (less than 2 mV) is read on the most sensitive voltage scale of the Agilent 34401A multimeter. This bias adjustment must be done at low temperature, namely when the thermometer resistance is about 1400-1500Ω. Now apply 100 mA of DC solenoid current from its supply box and measure the Hall voltage (it should be around one millivolt) corresponding to the magnetic field at the Hall-sensor that is produced by the solenoid current. This serves to calibrate the Hall-sensor since you can calculate the field produced by the solenoid current. The Hall voltage should be proportional to the field and you can get a calibration curve for the Hall probe by measuring the Hall voltage for several values of the solenoid current.

After activating the Hall-sensor when the lead sample is NC and measuring the field, reduce the sample temperature so that it is SC (by increasing the gas flow) thereby inducing the two persistent surface discussed earlier. For ideal conditions (long solenoid, long tube, complete Meissner effect), we expect no change in the field at the Hall-sensor. With our geometry, you will probably notice a small drop in the magnetic field at the transition T_c, but the important observation is that the field inside the open area of the tube is maintained. This small change in Hall voltage at T_c can be used to identify the onset of the transition and in essence it serves to calibrate the carbon resistance thermometer at T_c. With the DC field on, arrange the gas flow so that the temperature drifts down slowly through the transition region. Record your thermometer resistance and Hall voltage readings as the change occurs. Graphing these data as you go along will help you to determine the resistance of the thermometer at the transition.

Now in this SC state, turn off the solenoid current supply (and this is the "punch-line"), and observe that the field remains. This shows that there is a persistent current on the inside surface of the lead cylinder with no outside field. Flowing without resistance, the current should continue indefinitely as long as the lead sample is in the superconducting state. You have thus made a "Persistent Current Superconducting Magnet" like those which are now commercially available and which have almost entirely replaced electromagnets in technical applications where steady, uniform high-intensity fields are required. If the sample is now warmed slowly by reducing the cooling gas flow, the internal frozen-in field will suddenly disappear (quench) at the transition. Record the resistance and Hall voltage readings during this change and compare with the earlier cool-down graph. (What happens to the magnetic field energy when a quench occurs?)

Another series of observations will show that one can generate a "frozen-in zero-flux" state. With zero field, cool the sample below T_c and then turn on the field by passing a DC current through the solenoid. What is the Hall probe response during these steps, and how do you explain it? You can now understand why superconducting assemblies are sometimes used to provide nearly perfect shields against electromagnetic disturbances, as in the experiment now under development at Stanford University to detect the Lense-Thirring effect on a gyroscope in orbit about the earth.

QUESTIONS:

1. Is there an upper limit to the magnitude of this persistent current and frozen field that we can generate in our sample? Why?

2. What current can we pass along a long SC wire of radius 1 mm and still expect the wire to remain superconducting (use lead wire at 4 K)?

3. What is the areal current density (amp cm^{-2}) in the persistent current that you measured (assume $\lambda_L = 10^{-6}$cm), and how does it compare with that flowing in a wire (1 mm diameter) supplying a household 100-watt light bulb?

8. THE JOSEPHSON EFFECTS

The passage of electrons through a thin (<50 Å) insulating barrier is a well-known example of quantum-mechanical tunneling. The current-voltage (I-V) characteristic of such a barrier is ohmic (linear) at low bias. In accordance with the exclusion principle, the current is proportional to the number of electron states per unit energy in the conductors on either side of the barrier.

Giaever [7] discovered that if the electrodes are superconducting the curve becomes highly non-linear with the current remaining nearly zero for voltages up to $V = 2\Delta/e$, where Δ is the superconducting energy gap, as illustrated in Figure 7.

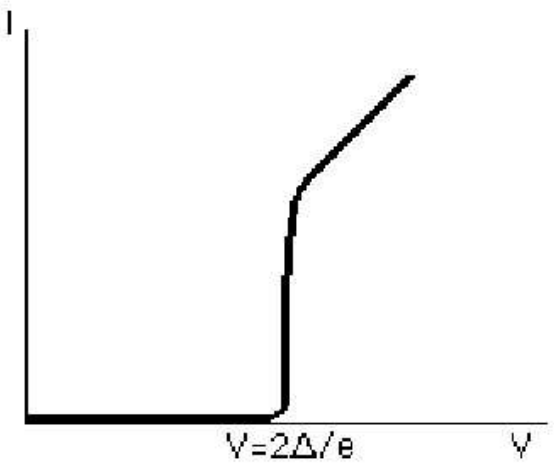

FIG. 7: Single particle tunneling at T = 0 K

According to the BCS theory of superconductivity, all of the electrons near the Fermi level (at 0 K) are condensed into pairs of opposite spin and momentum. Single electrons are not available for the tunneling process nor are there any available electron states to receive them. As the voltage is raised to the energy gap, pairs are broken up into normal single electrons (quasi-particles) which exhibit ohmic tunneling.

The remarkable discovery of Josephson [8] was his theoretical prediction that not only can the quasiparticles tunnel through the insulating barrier but the Cooper pairs can also do so, provided that the barrier is small compared to the decay length of the wave function of the Cooper pairs in the barrier ($< 10\mathring{A}$). This is a consequence of the inapplicability of the exclusion principle to pairs which are, in effect, bosons.

When the two superconductors are separated by a large insulating barrier, the condensed state of the Cooper-pair bosons in each can be described by a wave function with a single value of phase. But as the barrier becomes smaller, phase correlations extend across the intervening space and the two superconductors act like coupled oscillators. The isolated pieces of superconductor begin to act like a single superconductor although the superconductivity in the insulating region is weak (i.e. the order parameter, which is a measure of the ratio of pairs to single electrons is small) and electromagnetic potentials can be sustained within the barrier.

Perhaps the most accessible description of the theory of the Josephson effect has been provided by Feynman [3]. He derives the following relations:

$$J(t) = J_0 \sin\delta(t) \tag{8.1}$$

and

$$\delta(t) = \delta_0 + \frac{2e}{h}\int V(t)dt \tag{8.2}$$

where J is the Josephson current density, $\delta(t)$ is the phase difference across the junction, and V is the voltage across the junction. These simple equations are the basis of the theory of both the dc and ac Josephson effects.

8.1. THE DC JOSEPHSON EFFECT

If the coupled superconductors are linked to a current source by an external circuit, the tunneling current that flows without a voltage is given by the first equation. The maximum critical current, j_0, which corresponds to a phase difference of $\pi/2$, is proportional to the strength of the coupling across the barrier, and is determined by the dimensions of the barrier region, the materials and the temperature. It is inversely proportional to the normal ohmic resistance of the junction at room-temperature.

With a dc voltage across the junction, the current will oscillate at a frequency given by

$$\nu = \frac{2e}{h}V_0 = 484\ MHz\ \mu V^{-1} \tag{8.3}$$

In the $V \neq 0$ region the current oscillates too fast to be seen on the low frequency I-V plot, averaging to zero. As Feynman points out, one obtains the curious situation that, with no voltage across the junction, one can have a large current but if any voltage is applied, the current oscillates and its average goes to zero. The current will remain zero as the dc voltage is raised until, as mentioned above, the (Giaever type) quasiparticle tunneling region is reached at the gap voltage, $V = 2\Delta/e$. This type of curve, illustrated in Figure 8, is sometimes obtained but, more commonly, with the circuitry that we will be

using, the results look like Figure 9. In this experiment the current will be swept by a symmetrical sine wave so that the current-voltage characteristics will appear in two quadrants of the plane. Note the hysteresis which is usually too fast for the oscilloscope to record. It can, however, be observed by reducing the bandwidth of the Y amplifier on the oscilloscope.

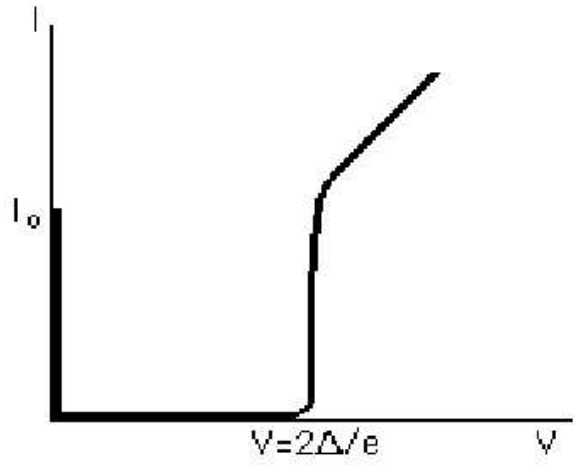

FIG. 8: Tunneling I-V curve showing both Josephson tunneling and single-electron (quasiparticle) tunneling

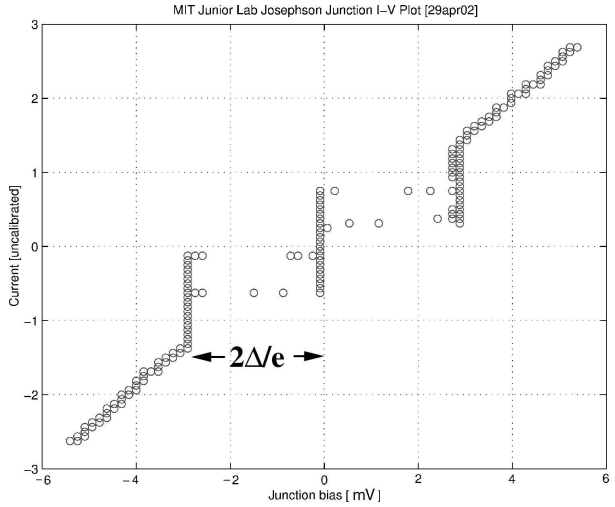

FIG. 9: Typical oscilloscope trace of Josephson junction I-V curve.

8.2. THE AC JOSEPHSON EFFECT

There are two categories of high frequency effects which can be observed in these systems, though not with the equipment of this experiment. We have seen that the application of a dc voltage across the junction causes the current to oscillate at the frequency shown in Equation 8.3. An applied voltage of approximately 50 μV produces 24 GHz oscillations, corresponding to K-band microwaves. Such oscillations have been detected with extremely sensitive apparatus. Feynman explains that if we apply a high-frequency voltage in addition to a dc voltage to the junction, and if the frequency is related to the dc voltage by the above relation, we will get a dc component of the Josephson current. This can be seen as steps in the I-V curve at voltages corresponding to harmonics of the applied frequency.

8.3. JOSEPHSON JUNCTIONS

Thin-film tunnel junctions are commonly made by depositing a narrow stripe of the superconducting metal on an insulating substrate, usually glass, and then causing an oxide layer of the desired thickness to build up on the exposed surface. Next another stripe, running perpendicular to the first stripe and consisting of the same or different superconducting metal, is deposited on top of the oxide layer. Tunneling occurs between the two stripes in the rectangle of oxide in the crossing area.

The niobium-niobium junctions used in this experiment and shown in Figure 10.

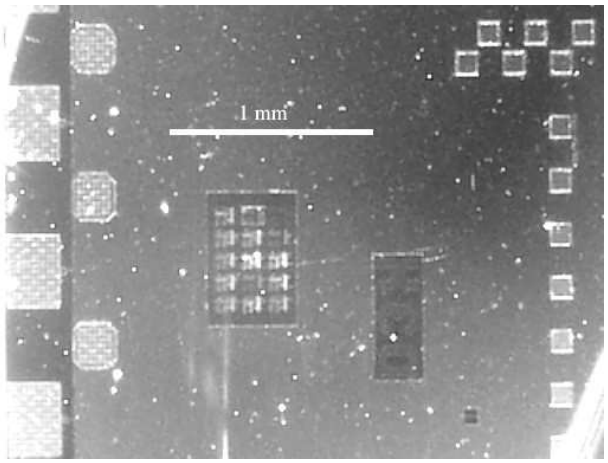

FIG. 10: Photograph of the Junior Lab Josepshson Junction chip provided by Dr. Will Oliver of MIT's Lincoln Laboratory and Professor Terry Orlando of MIT.

The dimensions of the junction are 5 μm x 5 μm and the critical current is 10μA μm^{-2}. The aluminum oxide barrier thickness is 1.5 - 2.0nm. There is an additional very thin layer of aluminum between the oxide layer and the Nb but this should have a negligible effect on the penetration depth. This The London penetration depth for Nb at $T = 0$K is 39nm. This value changes slightly at $T = 4.2$K, through a correction factor that is $= \sqrt{1-(T/T_c)^4}$ which is about 1.02 at $T = 4.2$K. Thus

$$\lambda_L \approx 39nm \times 1.02 \tag{8.4}$$

The junction is mounted on the bottom of the third probe, and 6 electrical lines (4 for the junction I-V measurements and 2 for the solenoid) run up the inside of

the probe tube to the blue junction box on the top of the probe.

The Josephson Junction chip used in this lab actually has two junctions in the circuit (Figure 11), but only one of them is active in the experiment. The active junction is 5μm $\times$ 5μm in area, and is probed by sourcing current from I+ to I-, while measuring the voltage drop from V+ to V-.

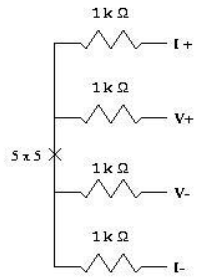

FIG. 11: Schematic circuit for Josephson Junction chip. The junctions are denoted by $\times$ symbols, and represent regions where two niobium layers overlap with a thin layer of insulating oxide between them.

A photograph of a Josephson Junction probe assembly is shown in Figure 12.

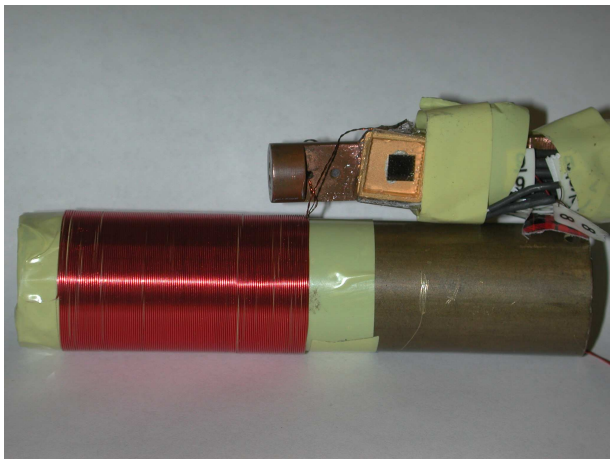

FIG. 12: Photograph of the Junior Lab Josepshson Junction Probe Assembly. Note that the outer solenoid is shown disassembled.

8.4. JOSEPHSON JUNCTION EXPERIMENTS

The Josephson Junction probe is a very delicate instrument and needs to be handled with extreme care! Before hooking up the cables between the blue box at the top of the probe and the 'make-and-break' circuit panel mounted in the 19" rack, please ensure that all the switches are in the 'DOWN' position. This will ground and short together the leads of the josephson junction which is extremely sensitive to electrical discharges. Only raise the switches to the 'UP' position when the current supply and the voltage preamplifier have been turned on and their settings verified. Please NEVER exceed 200mA through the solenoid coil surrounding the josephson junction. Now let's begin!

1. Connect the V_p and V_n signals from the 'make-and-break' switch panel to the voltage preamplifier inputs using two BNC cables. Configure the preamplifier inputs as DC Coupled A-B and initially set the filtering to 'FLAT' or 'DC'. Start with a gain of 100.

2. Connect the output of the voltage preamplifier to scope channel 1 (the X input).

3. Use a BNC-T connector to send the output of the function generator (Agilent 33220A) to the I_{pos} and I_{neg} BNC input on the 'make-and-break' switch panel (the coax's shield provides the return path for I_{neg}). Use the other half of the BNC-T connector to monitor the current on the channel 2 (the Y input) of the oscilloscope. Start with a 200 Hz sinewave at 1.5Vpp amplitude.

4. With all the 'make-and-break' switches still in their 'DOWN' position, you should be able to see a vertical line on the scope operating in XY mode. This is simply the oscillating output of the function generator being monitored on the scope.

5. Now connect the cables from the temperature sensor readout box and from the 'make-and-=break' panel to the blue box on the top of the Josephson Junction probe.

6. Carefully insert the probe into the dewar, clamping the flange to the dewar neck with the junction itself in the RAISED postion. VERY SLOWLY lower the probe until it begins to cool when it reaches the helium vapor above the liquid. SLOWLY cool the probe at no more than a few degrees per second. It should require about 5-10 minutes to reach Tc (about 9.2 K for Niobium). When you've reached about 200K you can raise all the 'make-and-break' switches into their 'UP' position. You should observe an 'ohmic' IV trace.

7. As you reach Tc, the ohmic trace on the scope should distort into the nonlinear IV trace similar to that shown in Figure 9.

The current spike at V=0 represents the Josephson current (tunnelling by Cooper pairs!!!). Record this current; you can deterimine its magnitude by finding the vertical distance between the two points where the I-V curve becomes nonlinear. There are 1kΩ resistors in series with each of the four Josephson Junction leads which will enable you to convert the scopes measured voltage

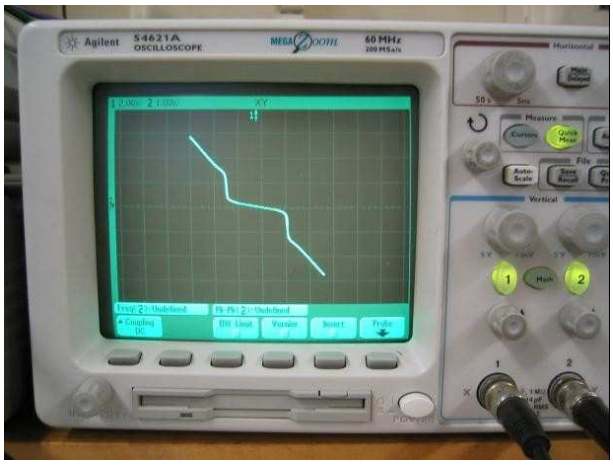

FIG. 13: Typical results with the Junior Lab Josepshson Junction

into a true 'current'. The curve obtained should resemble Figure 9 although the horizontal parts switch so fast they may not show up on the scope. It should be possible to estimate the superconducting energy gap from this curve. The magnitude of the zero-voltage Josephson current is strongly dependent upon magnetic field, and it is just this dependence which provides the basis for Josephson devices such as SQUIDs (superconducting quantum interference devices.)

8.4.1. Determination of the Flux Quantum

The probe includes a solenoid coil which can be used to produce a magnetic field in the plane of the junction. Using a DC power supply as your current source, vary the coil current in the range ± 150mA. (you should use the known value of the flux quantum and the dimensions of the junction to calculate *aprori* the range of B-fields to explore). The coil was produced by wrapping 2000 turns of 36 AWG magnet wire (Belden 8058) around a brass cylinder and produces a field of 540 Gauss A^{-1}. Explore both positive and negative currents to back out the local effect of the earth's magnetic field! The best results are obtained by reducing the function generator output voltage to about 350mV P-P to minimize local heating of the junction which can obscure the effect you're looking for.

Record and plot the zero-voltage Josephson current against the solenoid current and its magnetic field. You should be able to see at least two zeros. Be careful not to apply very large currents to the solenoid. You may also want to have the scope average the preamp output signal to reduce its noise. From this and the dimensions of the junction cited above, you can estimate the magnitude of the flux quantum (see Reference [9]).

Congratulations on your first investigations into superconductivity! Feel free to use the experiments in this labguide as a spring board for your own investigations... Other useful references include **Superconductivity:** [10–12], for **Josephson Effects:** [13–15], for **Miscellaneous Topics:** [16, 17].

[1] F. London and H. London, in *Proc. Roy. Soc.* (1935), pp. 71–88.

[2] L. C. J.R. Schrieffer and J. Bardeen, Physics Today pp. 23–41 (1973), qC.P592 Physics Department Reading Room.

[3] R. Feynman, *Lectures on Physics*, vol. III (Addison-Wesley, New York, 1966), qC23.F435 Physics Department Reading Room.

[4] R. L. Liboff, *Introductory Quantum Mechanics* (Holden-Day, 1980), qC174.12.L52 Physics Department Reading Room.

[5] C. Kittel, *Introduction to Solid State Physics*, vol. III (Wiley, New York, 1976), qC176.K62 Science Library Stacks.

[6] Bednorz and Müller, Z. Phys. **B64** (1986), qC.Z483 Science Library Journal Collection.

[7] L. Esaki and I. Giaever, *Nobel lectures: Experimental discoveries regarding tunneling phenomena in semiconductors and superconductors* (1973).

[8] B. D. Josephson, *Nobel lecture: Theoretical predictions of the properties of a supercurrent through a tunnel barrier, in articular those phenomena which are generally known as josephson effects* (1973).

[9] D. Scalapino, in *Encyclopedia of Physics*, edited by R. Lerner and G. Trigg (Addison-Wesley, 1991), pp. 479–481, 2nd ed.

[10] Tinkham, *Introduction to Superconductivity* (McGraw-Hill, 1996), 2nd ed.

[11] D. Ginsberg, American Journal of Physics **32** (1964).

[12] *Superconductivity: Selected Reprints* (1964).

[13] D. J. S. D. N. Langenberg and B. J. Taylor, Scientific American **214**, 30 (1966), t.S416 Science Library Journal Collection.

[14] J. Clarke, American Journal of Physics **38**, 1071 (1970).

[15] S. S. P.L. Richards and C. Grimes, Anerican Journal of Physics **36**, 690 (1968).

[16] L. D. Landau, *Pioneering theories for condensed matter, especially liquid helium*, Nobel Lectures (1962).

[17] C. S. W.S. Corak, B.B. Goodman and A. Wexler, Physical Review **102** (1954).

Voltage	**Kelvin**	**Voltage**	**Kelvin**
1.69812	1.4	1.13598	23
1.69521	1.6	1.12463	24
1.69177	1.8	1.11896	25
1.68786	2	1.11517	26
1.68352	2.2	1.11212	27
1.67880	2.4	1.10945	28
1.67376	2.6	1.10702	29
1.66845	2.8	1.10263	30
1.66292	3	1.09864	32
1.65721	3.2	1.09490	34
1.65134	3.4	1.09131	36
1.64529	3.6	1.08781	38
1.63905	3.8	1.08436	40
1.63263	4	1.08093	42
1.62602	4.2	1.07748	44
1.61920	4.4	1.07402	46
1.61220	4.6	1.07053	48
1.60506	4.8	1.06700	50
1.59782	5	1.06346	52
1.57928	5.5	1.05988	54
1.56027	6	1.05629	56
1.54097	6.5	1.05267	58
1.52166	7	1.04353	60
1.50272	7.5	1.03425	65
1.48443	8	1.02482	70
1.46700	8.5	1.01525	75
1.45048	9	1.00552	80
1.43488	9.5	0.99565	85
1.42013	10	0.98564	90
1.40615	10.5	0.97550	95
1.39287	11	0.95487	100
1.38021	11.5	0.93383	110
1.36809	12	0.91243	120
1.35647	12.5	0.89072	130
1.34530	13	0.86873	140
1.33453	13.5	0.84650	150
1.32412	14	0.82404	160
1.31403	14.5	0.80138	170
1.30422	15	0.77855	180
1.29464	15.5	0.75554	190
1.28527	16	0.73238	200
1.27607	16.5	0.70908	210
1.26702	17	0.68564	220
1.25810	17.5	0.66208	230
1.24928	18	0.63841	240
1.24053	18.5	0.61465	250
1.23184	19	0.59080	260
1.22314	19.5	0.56690	270
1.21440	20	0.54294	280
1.17705	21	0.51892	290
1.15558	22	0.49484	300

TABLE I: Probe I Si-diode (DT-470) calibration.

21-cm Radio Astrophysics

MIT Department of Physics
(Dated: February 2, 2010)

Measurement of the Doppler spectrum of interstellar atomic hydrogen and the dynamics of the galactic rotation. A 7.5 foot computer-controlled azimuth-elevation parabolic dish antenna, located on a roof of MIT, is used with a heterodyne measurement chain and digital correlator to observe the Doppler spectrum of the 21-cm hyperfine line of interstellar atomic hydrogen in various directions along the Milky Way. Features of the spiral-arm structure of the Galaxy are deduced from the measured radial velocities of the hydrogen clouds in the galactic disc.

1. PREPARATORY PROBLEMS

1. Explain the origin of the 21-cm line of atomic hydrogen.

2. Describe the size and shape of the Galaxy, giving our position from the center in light-years and parsecs (pc). What is the maximum Doppler shift you can expect to observe in the 21-cm line?

3. The parabolic dish antenna used in this experiment has a diameter of 7.5 feet. Suppose it is set so that a source of 21-cm radio emission drifts through its field of view. Plot the signal strength at the output of the diode detector as a function of angle from the center of the field of view.

4. Explain the 21-cm spectrum at 150° and 60° as shown in Figure 7.

5. Explain the signal chain in this experiment (e.g. how the hardware and software serve to convert the signal received by the telescope into a display of signal strength versus frequency.

2. Progress Check for 2nd Session

What is the approximate temperature of the sun at 1420 MHz? Plot the power spectrum of galactic hydrogen at 40 degrees galactic longitude and identify all the salient characteristics of the spectrum. Does it agree with Van de Hulst?

3. General Structure of the Milky Way

The sun is one among the approximately 10^{11} stars that comprise our Galaxy[1]. From a distant vantage point this vast array of stars would appear as a rotating spiral galaxy, rather like our famous neighbor galaxy, M31, in the constellation of Andromeda. Detailed examination would reveal a spheroidal component and a concentric disk component. The spheroidal component consists mostly of small (M< $0.8M_\odot$), old (10-15 billion years) stars (so-called population II) of which most are concentrated in a central "bulge" with a diameter of 3 kpc and the rest are distributed in an extensive "halo" that extends to a radius of 30 kpc or more. The disk component is a thin, flat system of stars, gas and dust ∼200 pc thick and ∼30 kpc in radius. The disk stars (called population I) are extremely heterogenous, ranging in age from newborn to the age of the halo stars, and with masses from 0.1 to 100 $M_\odot$.

The solar system is imbedded in the disk component at a distance of 8.0±0.5 kpc from the center at which radius the circular motion of the Galaxy has a period of approximately $2x10^8$ years. The naked eye can distinguish about 6,000 of the nearby stars (apparent brightness down to 6 mag) over the entire sky; the myriads of more distant stars of the disk blend into what we perceive as the Milky Way, which is our Galaxy seen edge on.

Between the stars of the disk is the interstellar medium (ISM) of gas and dust comprising approximately 10% of the total mass of the disk. The gas consists primarily of hydrogen and helium with a mass density ratio of 3 to 1 and an average total number density of about 1 atom cm^{-3}. The dust is composed mostly of graphite, silicates and other compounds of the light and common elements in microscopic grains containing a small fraction of higher-Z elements, primarily iron. The effect of dust in blocking the light of more distant stars is clearly seen in the "dark lanes" that are conspicuous features of the Milky Way in the region of, e.g., the constellations Cygnus and Aquilla.

The pressure in the ISM is conveniently characterized by the product nT, where n is the density in atoms cm^{-3} and T is the temperature in Kelvins. It is roughly constant in the disk and of the order of 3000 K cm^{-3}. A wide range of observations across the electromagnetic spec-

[1] This description of the Galaxy is a summary of the material contained in Galactic Astronomy by Mihalas and Binney [1], a very useful reference for this experiment. It also contains in Chapter 8 a detailed presentation of the theoretical basis for interpreting the data on galactic kinematics obtained from observations of the Doppler profile of the 21-cm line. Another very nice introduction to the structure of the Milky Way is on-line at http://cassfos02.ucsd.edu/public/tutorial/MW.html. Other useful references for this lab are [2–8].

trum show that the ISM tends to exist in one of three different states: hot, warm and cool, with temperatures of 10^6, 10^4, and 10^2 K, respectively, and corresponding low, medium and high densities. Within the cool regions there are particularly dense cold regions (T$\approx$ 20K) known as molecular clouds, containing H_2, OH, and other more complex molecules. These clouds are the birthplaces of stars that are formed by gravitational contraction of the cloud material. When a burst of star formation occurs in a molecular cloud, the massive stars heat the surrounding ISM to form a warm region of 10^4 K. After short lives of a few million years the massive stars explode as supernovas that spew into the ISM portions of the heavy elements that have been synthesized by nuclear fusion in their interiors and by neutron capture during their explosions. The explosions blow "bubbles" of 10^6 K gas that merge to form an interconnecting network of hot regions. The hot gas eventually cools and is recycled through molecular clouds in a continuous process that gradually enriches the ISM with the Z>2 elements of which the Earth and we are composed. Dynamical studies show that there also exists "dark matter" of unknown nature with a mass comparable to or even larger than the total mass of the luminous stars.

An essential key to the development of modern astrophysics was the invention of the spectroscope and its application with photography near the turn of the century to the study of stars and hot nebulae in the visible range of the spectrum. Comparison of stellar spectra with the line spectra of elements in the laboratory yielded information on the composition and temperature of celestial objects, and measurement of wavelength shifts due to the Doppler effect provided determinations of radial velocities which revealed the dynamical properties of systems such as double stars and the general expansion of the universe in the motions of distant galaxies. Most of the interstellar medium, however, is too cold to radiate in the visible part of the spectrum and remained undetectable and its properties largely unknown until fifty years ago. Then, in the midst of World War II, a young Dutch astronomer, H. van de Hulst, examined the theoretical possibilities for detecting cosmic radio waves of some distinct frequency, i.e. a spectral line in the radio portion of the electromagnetic spectrum which would permit measurements of physical conditions and radial motions like those available in the visible spectrum. He predicted that the spin-flip transition of atomic hydrogen would produce such a line at a wavelength near 21 centimeters, and that the unique conditions of low density and temperature in interstellar space are such as to allow time for hydrogen atoms, excited by collision to their hyperfine triplet state (F=1), to decay by radiation to the ground state (F=0). The line was observed in 1951 by Ewing and Purcell at Harvard, by Christiansen in Sydney, and by Muller and Oort in the Netherlands. Radio observations at 21 cm soon became a major tool of astronomy for exploring and measuring the structure of our Galaxy and the many distant galaxies accessible to the giant radio telscopes such as the giant single dish antenna at Arecibo in Puerto Rico, the 20-km diameter aperture synthesis array (Very Large Array) in New Mexico, and the transcontinental aperture synthesis array called the VLBA (Very Long Baseline Array).

Atomic hydrogen is the principal constituent of the interstellar medium, and one of the most interesting tracers of galactic structure. Whereas visible light emitted by stars is heavily obscured by interstellar dust, photons with a wavelength of 21 centimeters, emitted in spin-flip transitions of atomic hydrogen in its electronic ground state, reach us from all parts of the Galaxy with little absorption. Measurements of the Doppler shifts of the frequency of the 21-centimeter line determine the radial components (projections onto the line of sight) of motions of the interstellar medium. Analysis of the Doppler shifts in various directions around the galactic plane (i.e. around the Milky Way) reveal the kinematic structure of the galaxy, e.g., the tangential velocity of the matter in the Galaxy as a function of the distance from the center, and, by implication, the geometry of the spiral arms.

4. EXPERIMENTAL APPARATUS

4.1. Antenna & Motors

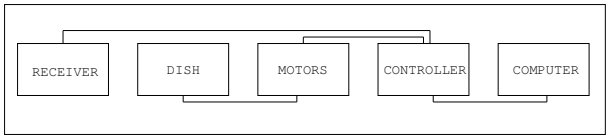

FIG. 1: SRT

The small radio telescope, SRT, is a 7.5 foot diameter parabolic dish and receiver designed by Haystack Observatory and sold by Cassi Corporation.[2]. It has a focal length of 85.7cm. It has a beam width of approximately 7.0 degrees.[3]. The dish is mounted on a two-axis azimuth/elevation mount. It is supported by a aluminum frame constructed from C/Ku band mesh that will reflect all incident microwave energy if the surface holes are less than 1/10th of the incident wavelength. The system is controlled using a computer running a java applet that communicates via serial connection with the controller housing a Basic-Stamp microcontroller. The microcontroller in turn controls the motor functions, one drive at a time. A very basic block diagram of the system is shown in Fig. 1. The software calculates galactic coordinate positions from the azimuth-elevation coordinates

[2] Complete specifications for the antenna, mount and receiver are available at www.haystack.edu/edu/undergrad/srt/index

[3] The first minimum of the antenna diffraction pattern is given (see any text on optics) by $1.22\frac{\lambda}{d}\frac{180}{\pi} =\approx 7^\circ$.

and a knowledge of the local sidereal time (LST). A brief summary of celestial geometry is provided in Appendix A.

4.2. RECEIVER

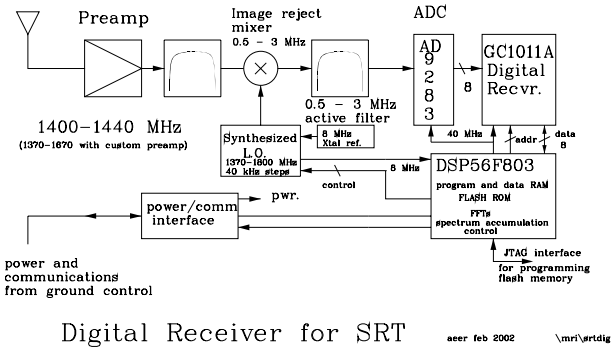

FIG. 2: Receiver

The SRT uses a phasing type single sideband scanning receiver. Fig. 2 shows a block diagram of the radio receiver and subsequent signal processing stages. Radio power arriving from directions close to the axis of the parabolic antenna is focused by reflection to an antenna feed horn. Signals then pass through a band pass filter, low noise pre-amplifier and mixer. The baseband signal is digitized and sent back to the controlling computer over a serial RS-232 link. The central frequency of the synthesized local oscillator (LO) used in the mixer is user selectable from within the JAVA program. This permits the investigator to look at different spectral regions around 1420 MHz.

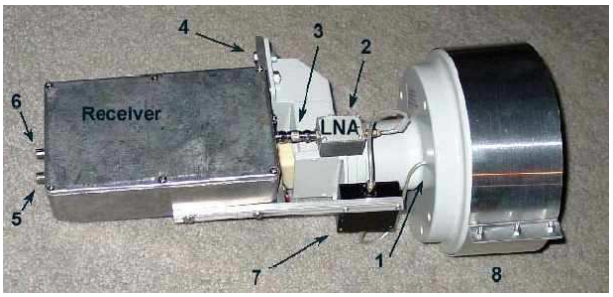

FIG. 3: Feedhorn

1 - L-Band probe
2 - Low Noise Amplifier
3 - Universal Male F to F Coupler
4 - Receiver mounting bracket
5 - Video Port - Analog signal
6 - Power and Communication - Digital Signal
7 - Band Pass Filter
8 - Feed Horn Extension

Signals pass from the feed horn to the low noise amplifier. The LNA provides a 24dB gain whose output passes through a 40MHz bandpass filter that prevents out of band signals from producing intermodulation in the image rejection mixers. Mixers are circuit elements that form the product of two analog waveforms (in NMR these elements are also called "phase detectors"). It's two inputs and output are related by the trigonometric relationship:

$$\cos\omega_1 t\cos\omega_2 t = \frac{1}{2}\cos(\omega_1+\omega_2)+\frac{1}{2}\cos(\omega_1-\omega_2) \quad (4.1)$$

Note that both sum and difference frequencies are generated in a mixer. For our application, we band-pass filter the output and throw away the sum frequency contribution. A "balanced" mixer is one in which only the sum and difference frequencies, and not the input signals or their harmonics, are passed, see http://www.haystack.edu/edu/undergrad/srt/receiver/receiver_circuit.html for more information.

4.2.1. Electronic Noise Calibration

Complete details of the SRT calibration are available at http://www.haystack.edu/edu/undergrad/srt/receiver/SRT_calibration.html. Temperature calibration is performed using a noise diode, whose intensity and spectral distibution is approximately equivalent to a 115 Kelvin blackbody.

The electronic noise calibrator is a diode (Noise/Com NC302L) connected to a small dipole antenna attached to the center of the SRT dish. A small (6mA) current is sent through a controlled bulk avalanche mechanism, resulting in a wide band of frequencies. The dipole emits the signal which is detected by the receiver. To generate the correct wavelength signal, the dipole was fabricated to be 1/2 wavelength, or approximately 10.5 cm. To minimize signal from behind the dipole, the poles are set 1/4 wavelength, or approximately 5.25 cm, above the circular plate at the center of the SRT dish.

Calibration: The software temperature calibration measures the ratio of the received power when the noise diode is turned on and then off again. Both of these power measurements will necessarily contain contributions from spillover and sky. The power ratio is given by

$$\frac{P_{on}}{P_{sky}} = \frac{T_{receiver}+T_{noisecal}+T_{spillover}+T_{sky}}{T_{receiver}+T_{spillover}+T_{sky}} \quad (4.2)$$

$T_{noisecal}$ is the temperature the electronic noise calibrator radiates and P_{on} is the power measurement with the calibrator on. The value of $T_{noisecal}$ was determined by the manufacturer in comparison with an independent vane calibration method.

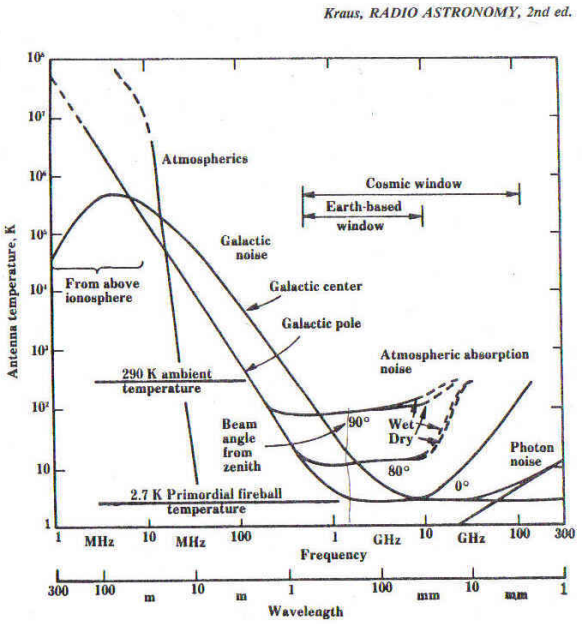

Fig. 8-6. Antenna sky noise temperature as a function of frequency and angle from zenith. A beam angle (HPBW) of less than a few degrees and 100 percent beam efficiency are assumed. (*After Kraus and Ko*, 1957, *cosmic noise between* 10 MHz *and* 1 GHz; *Penzias and Wilson*, 1965, *cosmic noise above* 1 GHz; *Croom*, 1964, *atmospheric noise*; *CCIR*, 1964, *atmospherics*; *and Radio Astronomy Explorer Satellite* RAE-2, *Novaco and Brown, cosmic noise below* 10 MHz.)

FIG. 4: Noise Temperature versus angle from zenith. Taken from Kraus, 2nd Edition.

4.3. Ground Controller and Software Interface

The SRT control software interface is run from a computer in 4-361 which communicates with the ground controller box located in 26-630. The ground controller serves as the interface between the computer and the antenna stepper motors as well as the digital receiver located next to the antenna feed. RS-232 is used to send commands to the motors and to receive back the digitized spectral temperatures from the receiver[4]. The ground controller should be left ON so that students can remotely operate the dish from 4-361. A printed copy of the SRT Manual is located next to the computer in 4-361 and is also available online.[5]

Login to the SRT computer using the instructions from the technical staff. Double click on the SRTCassi icon on the desktop to start the program. The first thing that happens is that the telescope will be moved to the 'stow' position (roughly due north and at zero degrees elevation). Once the command console has been loaded, the user may access a series of functions via the command toolbar located along the top of the console. Pointing and clicking on any of these buttons will either initiate an automatic sequence response or wait on text input by the user. Perhaps the most useful thing to do right away is to begin a log file which will provide you with a continual record of your experiment. To do this, click on the text entry box at the bottom of the Java interface screen and type in the path and filename you wish to log to (e.g. c:\srt\users\username\15aug03.rad). Make sure to create the path first! You can transfer data from this directory to your athena account using Secure FX.

The control program calculates the Local Sidereal and Universal Time based on the computer clock settings within the information sidebar on the right-hand side. **Since Universal Time = Eastern Time + 5 hours (under Standard Time) and = Eastern Time + 4 hours (under Eastern Daylight Savings Time), you must make sure the box "Automatically adjust clock for daylight savings" is checked when setting the computer's clock.** It also indicates the antenna direction in both Equatorial (RA and DEC) and Galactic ('l' and 'b') here.

When turning on the system, pay special attention to any error messages that may appear within the Message Board below the Total Power Chart Recorder. They may indicate that the system has failed to communicate through the coaxial cable (i.e. gnd 0 radio 1). If movement of the dish stops prematurely, "antenna drive status.." or "lost count" may appear in the Motion Status Display Area. If this occurs please turn off the control system (which in turn ends motor power) and have a technical staff member take a look at the motor drive gears. Before powering down the system please return the dish to the stow position.

4.4. DATA COLLECTION

The SRT is continually acquiring and processing RF signals incident upon the dish. The upper right plot shows individual power spectra updated every few seconds. The plot to the left in RED, shows an integrated power spectrum which may be cleared by pressing the "CLEAR" button. It is convenient to check this now by generating a test signal at 1420.4 MHz. This is done by turning on the Marconi RF synthesizer (press the "CARRIER ON/OFF" button and the LED should toggle between ON and OFF). Make sure that you don't leave this synthesizer on except for brief tests and system calibrations.

To deliver a command to the SRT through the JAVA interface, the operator enters text commands into the text box at the bottom of the control console and then clicks the appropriate command button which acts on this data input.

Note that some command button requests must be supplemented with manual command entries. Azimuth and elevation locations are set using the Horizon Coordinate system. Simply enter the azimuth and elevation in de-

[4] Full details and schematics of the ground controller are available at http://www.haystack.edu/edu/undergrad/srt/receiver/schemgndctl2.pdf

[5] The SRT Manual is available online at http://www.haystack.edu/edu/undergrad/srt/SRTSoftware/SRTManual.pdf

grees of the position to be observed and the software will check to see if the requested position is currently visible within the mechanical limits of the dish. The control program computes the number of pulses required to turn the telescope and the PC then sends the pulses to the stepping motors. When the telescope reaches the position, if "tracking mode" is on (button text is YELLOW), the PC continues to generate pulses at the rate required to compensate for the earth's rotation so as to keep the telescope pointing to the specified position in the sky. To turn tracking off, simply click on the button and it should turn RED.

Try the following to get started:
Enter "180 40" in the text window and then press the Azel button. The dish should slowly move to point due south. Press STOW to return the dish to it's "parked" position at Azimuth=95°,Elevation=4°. Press the "RECORD" button to stop writing to the log file and open it up using a text editor. Think about how you might process such a log file using Matlab's IMPORT command.

5. OBSERVATIONS

You will first test and calibrate the equipment by aligning a noise diode and centering the telescope feed on a peak source, the radio emission of the Sun. The beamwidth of a radio telescope is the solid-angle measure of the half-power point of the main lobe of the antenna pattern. Measure the half-power beamwidth (HPBW) of the SRT by moving the telescope in a continuous scan across a very bright radio source (e.g. the Sun, Cygnus-X or certain geosynchronous satellites) and plot temperature K vs. degree offset. Measurement of the beam pattern can help the user discover problems with optical alignment or aid in the determination of antenna focus.

Finally, you will observe the power spectrum of the 21-cm hydrogen emission from a sequence of positions along the Milky Way **(identifying which positions is a key task for the student!)**. Derive the Galactic rotation curve, and estimate the mass of the Galaxy interior to the circle tangent to the line of sight among your observations that is farthest from the Galactic center. Observe the non-uniformities in the hydrogen distribution revealed by the doppler-induced structures of the line profiles. The multiple-component line profiles are evidence of the spiral-arm structure of the Galaxy.

A list of these and other possible student projects are listed at http://web.haystack.mit.edu/SRT/srtprojects.

5.1. The Sun's Brightness Temperature

To prepare yourself for these measurements, start by reading the Haystack 'SRT Projects' page about Solar Observations available on-line through http://www.haystack.edu/edu/undergrad/srt/index.html.

Calibrate the system temperature T_{sys} and set the frequency to "1420.4 4" in order to set the bandwidth as wide as possible to reduce noise variations. To perform a system calibration press the "Cal" button. The noise source is then enabled for approximately 1 second while data is collected. Data is then taken with the noise source off for an additional 1 second. The system software then calculates T_{sys}, and reports it in the right information sidebar. For the off-source calibration, an area at least two beamwidths (in azimuth, positive or negative) away from the sun is desirable.

There are a couple of different ways to measure T_{sun}. By clicking on the "npoint" button, a series of measurements surrounding the sun in a 5x5 grid are made with the step size set by the antenna beamwidth defined in the "srt.cat" file. The default value for the beamwidth is 5.0°. The measured power/temperature at each of these grid points is displayed just above the text input box and at the completion of the scan, a 2-D contour plot of the grid is displayed in the graph box at the top of the page. Information about the sweep is then displayed in the information sidebar. The telescope offsets are also adjusted so as to point the dish to the maximum observed signal within the sampled region.

The "npoint" scan is also useful for verifying the targeting accuracy of the system. If the computer clock is set incorrectly or the local latitude and longitude have been inadvertently changed, the sun will NOT appear well centered in this gridded scan. See for example, Figure 5.

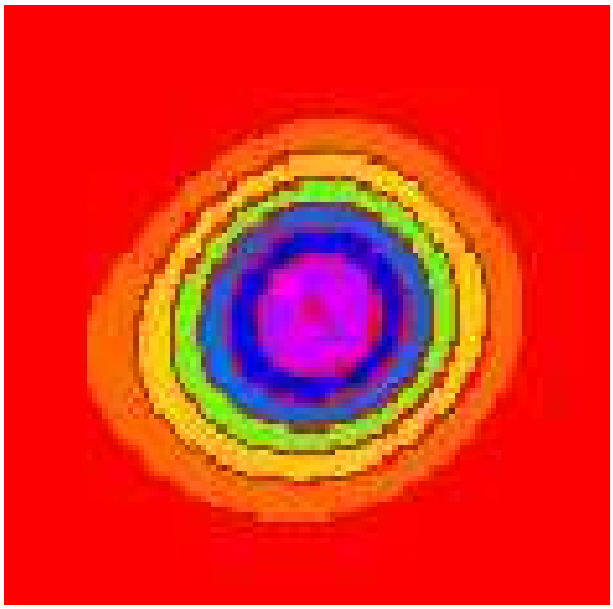

FIG. 5: Typical result from an "npoint" measurement of the Sun's brightness temperature. The countour plot is generated from a 5x5 series of measurements spaced by 1/2 the antenna beamwidth as specified in the srt.cat text file within the CassiSRT folder on the hard drive.

The "npoint" scan will focus the dish at the maximum temperature location for the sun when completed. Pointing corrections should be set to the location of peak intensity before continuing the observation session.
To manually specify offsets, enter the offset in the command text area.

```
enter azimuth(degrees) elevation(degrees)
Press ‘‘offset’’ button
```

If you've entered something like -5 -5 the effect is that the npoint plot will move right and up.

5.1.1. *Alternative T_{sun} measurement*

You can also use the "drift" button to cause the dish to be pointed "ahead in time" and then stopped. This will permit the sun, or any other object, to drift through the antenna beam. Recording this data and then plotting the results in Matlab, one can derive an empirical value for the beamwidth of the antenna to compare it with the theoretical value. What is the convolution of a finite source with the radiation pattern of the antenna beam? Can you model this? An interesting comparison can be made by comparing your results with the solar flux measured by other antennas around the world, see http://web.haystack.mit.edu/SRT/solar.html.

Measure the power seen by the antenna versus offset to find an estimate for the half-power beam width (HPBW). Your graph should resemble Figure 6.

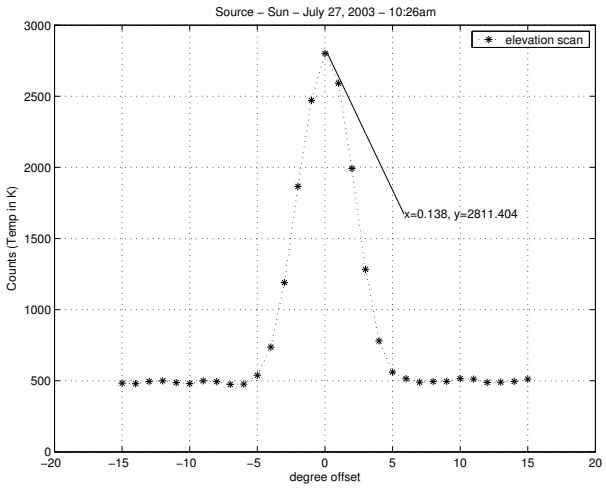

FIG. 6: Sun Scan Elevation

5.2. Measuring the Galactic Rotation Curve

To measure the rotation curve of the Milky Way, you will need to record hydrogen line profiles and a known set of galactic coordinates. Your first job is to figure out at which coordinates you will need to point the telescope! Use the software to determine when these regions of the galaxy will be visible from our Northern hemisphere vantage point. Since the visible portion of the galaxy varies with time, you may find it necessary to share observation time with student pairs from other sections.

6. ANALYSIS

Compare your plot of the angular response function of the antenna, obtained in the drift scan of the sun, with the theoretical diffraction pattern of a circular aperture. You may need to consult a text on physical optics and use of a computer computation of a Bessel function.

Derive an estimate of the brightness temperature of the sun at 21 cm from your measurements and calibration, taking account of the fraction of the effective solid angle of the antenna response function that is occupied by the sun. Here you may need to study the portion of Shklovski's book or other reference dealing with brightness temperatures, antenna temperatures and the relation to actual source temperatures.

Reduce the data of your 21-cm line profiles to plots of relative antenna temperature against radial velocity relative to the sun, taking account of the motion of the earth and the antenna around the sun. They should look similar to that obtained in the original Hulst survey shown in Figure 7.

With the help of the discussions presented in Mihalas and Binney and by Shu, derive from your data a plot of the velocity curve of the Galaxy as a function of radius. Why are you only able to do so for locations interior to the radial position of our solar system?

6.1. Possible Theoretical Topics

1. Hyperfine splitting of the hydrogen ground state.
2. Radiative processes in the sun.
3. Antenna theory.
4. The structure and dynamics of our Galaxy.
5. Radiative transfer.

[1] D. Mihalas and J. Binney, *Galactic Astronomy* (San Francisco, 1968).
[2] F. H. Shu, *The Physical Universe - Chapter 12* (University Science Books, Mill Valley, CA, 1982), this reference gives a clear description of the interpretation of 21cm spectra in terms of the rotation curve of the Galaxy.
[3] K. Rohlfs and T. L. Wilson, *Radio Astronomy, 2nd. ed.* (Springer, 1996), a modern handbook of radio astronomy techniques. Section 5.5 describes the relationship between antenna temperature and brightness temperature.[6] Chapter 6 provides a useful discussion of antenna theory.
[4] e. a. H. C. van de Hulst, *Bull. of the Astron.*, vol. XII, 117 (Institutes of the Netherlands, 1954).
[5] P. Duffett-Smith, *Practical Astronomy With Your Calculator* (Cambridge, 1988), 3rd ed.
[6] I. S. Shklovski, *Cosmic Radio Waves* (Cambridge; Harvard University Press, 1960).
[7] H. Horowitz and W. Hill, *The Art of Electronics, 2nd Edition* (Cambridge University Press, 1989).
[8] F. J. Kerr, Ann. Rev. Astron. Astroph. **Vol.7**, 39 (1969).

[6] Note, however, the following errors in Section 5.5: The equation between equation (5.59) and equation (5.60) should read $I_\nu = 2kT/\lambda^2$. Equation (5.62) should read $W = \frac{1}{2}A_e \int\int \frac{2kT_b(\theta,\phi)}{\lambda^2} P_n(\theta,\phi) d\Omega$.

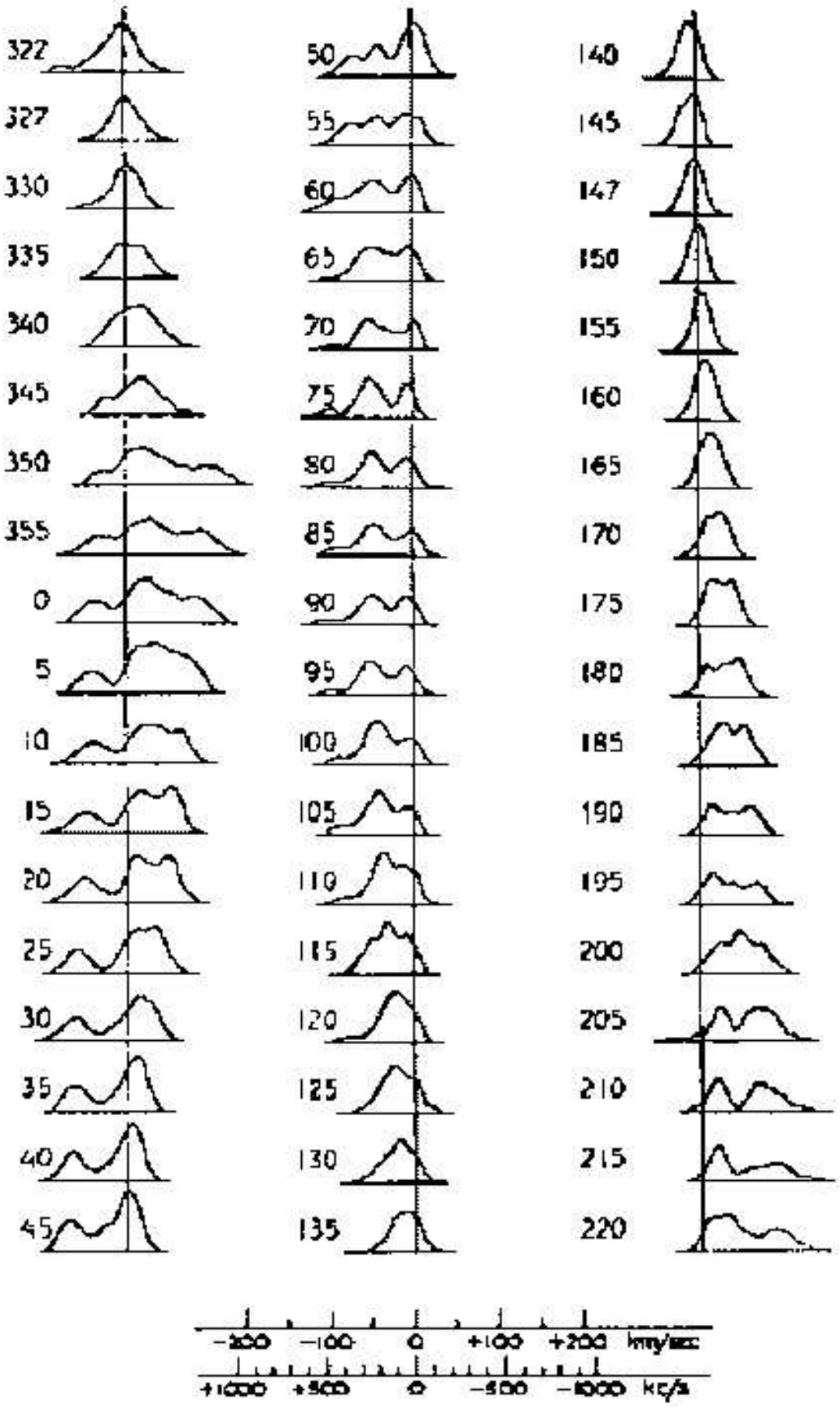

FIG. 7: Survey of hydrogen line profiles at various galactic longitudes. (from H.C. van de Hulst et. al., Bull. of the Astron. Inst. of the Netherlands, XII, 117, May 14, 1954) Note: Pictures are reversed from our images and longitude is given in the old system (l^I,b^I). $l^{II} = l^I + 32.31°$

APPENDIX A: THE SRT.CAT FILE

The text file srt.cat, located in SRTCassi, is the primary configuration file for the SRT java interface program that is used to control the telescope.

The srt.cat file may be updated, but upon doing so, please stow the telescope, shut down the control program, and restart it so that it recognizes any updates made to the srt.cat control file.

The srt.cat file contains keywords which are case sensitive. Lines that are preceeded by a "*" are ignored. Blank lines are ignored.

Keywords:
AXISTILT* - Use to set the azimuth and elevation axis tilt. Default is 0 0
AZEL* - Allows user to catalog a fixed catalog location by name.
AZLIMITS - This may be set to allow movement in a clockwise position from stow from 90° to 270°. At the midpoint the telescope will face due south. Degree limits should be set slightly below the physical limitations of the telescope. It is recommended to use 95° and 265°. The telescope movement is clockwise as seen from above through increasing degree.
BEAMWIDTH* - Antenna beamwidth in degrees, default is 7.0°.
CALCONS* - Gain correction constant. This is the ratio of temperature (K) per count. Change this during calibration (should be 1 to 1 ratio). Default is 1.0. This will be changed by software after calibration occurs and value will be available in the status bar.
COMM* - Communication port, default 1, use 0 for linux.
COUNTPERSTEP* - Counts per step for stepped antenna motion. The default is no stepped motion.
CURVATURE* - Optional correction for curvature in spectrum. The default is 0.
DIGITAL - Indicates that a digital receiver is being used. Comment out if using the analog receiver (set via jumper removal).
ELBACKLASH* - Optional correction for elevation backlash to improve pointing in flipped mode. The default is 0.
ELLIMITS - This may be set to allow movement in a clockwise position from stow from 0° to 180°. At the midpoint the telescope will face up. Degree limits should be set slightly below the physical limitations of the telescope. It is recommended to use 10° and 175°. The telescope movement is clockwise as seen from above through increasing degree.
GALACTIC - Set a galactic cordinate by location and name.
MANCAL* - Calibrates vane. 0 indicates auto-calibration, 1 indicates manual calibration. Is not a requirement of the digital setup.
Moon - Add the Moon to the catalog.
NOISECAL - Calibration temperature of the noise diode located at center of dish. Temperature is in K.
RECORDFORM* - Adds tabs to separate columns in output file. The default is space delimited. "VLSR" adds vlsr and "DAY" forces a file change at each new day.
SOU - Set a source in the catalog by location and name. For negative declination us "-" in from of dd.
SSAT* - Satellite ID and location (satellite name then longiture west).
STATION - Used to set latitude (in degrees), longitude (in degrees), and station name.
Sun - Add the Sun to the catalog.
TLOAD* - Load temperature. Default is 300K.
TOLERANCE* - Counts of error which can accumulate before command to drive stow occurs. Default value is 1.
TSPILL* - Antenna spill over temperature in K. Default is 20K.

File Format:
STATION deg(latitude) deg(longitude) name
AZLIMITS deg(lower limit) deg(upperlimit)
ELLIMITS deg(lower limit) deg(upper limit)
CALCONS value
TLOAD value(in temp K - default 300K)
MANCAL value(0 or 1 - default is 0)
TSPILL value(in temp K - default 20K)
BEAMWIDTH value(in degrees - default 7)
AXISTILT deg(azimuth axis tilt - default 0) deg(elevation axis tilt - default 0)
SSAT deg
AZEL deg(azimuth) deg(elevation) name
GALACTIC deg(longitude) deg(latitude) name
SOU ra(hh mm ss) dec(dd mm ss) name [epoc]
SUN
MOON
DIGITAL
NOISECAL value(in temp K)
TOLERANCE value(in counts)
COUNTPERSTEP value(in counts)
ELBACKLASH value(default 0)
CURVATURE value(default 0)
RECORDFORM value(i.e. "TAB", "—", default is " ")

*** - represents required fields or fields that should be set by user**

[ ] - represents optional field

APPENDIX B: COORDINATE SYSTEMS

This material is taken in part from Duffett-Smith's book "Practical Astronomy With Your Calculator, 3rd Edition 1988, Cambridge Press". It contains many useful algorithms and is worth checking out of the library or purchasing. There are several coordinate systems which you may meet in astronomy and astrophysical work and here we shall be concerned with four of them: the horizon system (Figure 8), the equatorial system (Figure 10), the ecliptic system (Figure 13) and the galactic system (Figure 9).

Horizon Coordiates "Az" and "El" The horizon system, using Azimuth and Altitude (Elevation) is the system underwhich the SRT is operated.

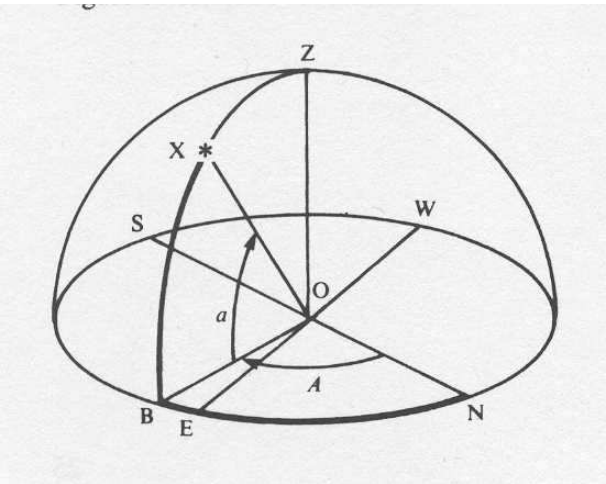

FIG. 8: Diagram of the Horizon coordinate system. Imagine an observer at point 'O'; then her horizon is the circle 'NESW' where North is the direction of the north pole on the Earth's rotation axis and not the magnetic north pole. **Azimuth** increases from 0° (north) through 360°. The **altitude** or **elevation** is 'how far up' in degrees (negative if below the horizon).

Galactic Coordinates, "l" and "b" When describing the relations between stars and other celestial objects within our own Galaxy, it is convenient to use the galactic coordinate system. The fundamental plane is the plane of the Galaxy and the fundamental directions the line joining our Sun to the center of the Galaxy as depicted in Figure 9.

Equatorial or Celestial Coordinates, "RA" and "DEC" are the spherical coordinates used to specify the location of a celestial object (Figures 10, 11 and 12). The north celestial pole (NCP) is the direction of the earth's rotation axis, and the celestial equator is the projection onto the sky of the plane of the earth's equator.

Right ascension (RA) is the celestial analog of geographic longitude. RA is measured eastward along the celestial equator from the vernal equinox ("V" in Figures 11 and 12) which is the ascending node of the plane defined by the sun's apparent motion (caused by the orbital motion of the earth around the sun) and the celestial equator. In catalogs of celestial objects RA is generally specified in units of hours, minutes and seconds from 0 to 24 hours, but it is often more conveniently specified in degrees from 0° to 360° with a decimal fraction. Declination (DEC) is the celestial analog of geographic latitude. DEC is measured north from the celestial equator along a celestial meridian which is a great circle of constant RA. In catalogs DEC is generally specified in degrees, arc minutes (') and arc seconds ("), but it is also often more conveniently specified in degrees from -90° to +90° with a decimal fraction. (1 hour of RA at constant DEC corresponds to an angle of 15°*cos(DEC) degrees subtended at the origin).

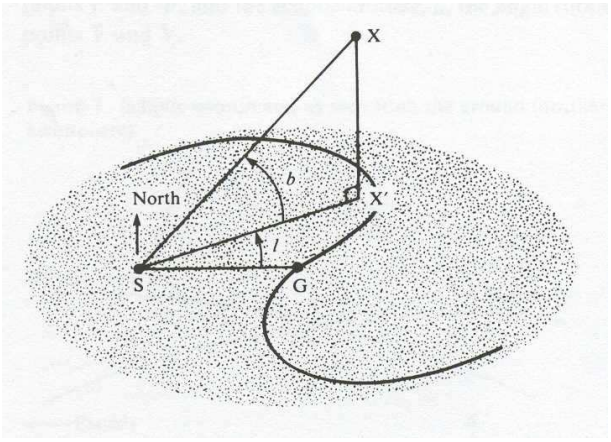

FIG. 9: Diagram of the Galactic coordinate system. The point marked "S" represents the Sun, "G" is the center of the Galaxy and "X" is a star which does not lie in the galactic plane.

The **ecliptic** is the intersection of the earth's orbital plane with the celestial sphere. To an observer on earth the sun appears to move relative to the background stars along the ecliptic with an angular velocity of about 1° per day. The angular velocity is not exactly constant due to the eccentricity of the earth's orbit (e=0.016722). The period of the earth's orbit is 365.256 days. The **inclination** (ie) of the earth's equator to the ecliptic is 23° 27'. The **ascending node** of the ecliptic with respect to the celestial equator is the intersection of the ecliptic and the celestial equator (the vernal equinox) where the sun in its apparent motion crosses from south to north declinations on March 21. **Precession of the equinoxes** is the motion of the equinoxes along the ecliptic due to precession of the earth's rotational angular momentum about the ecliptic pole. The precession is caused by the torque of the gravitational attractions between the sun and moon and the earth's equatorial bulge. The period of the precession is approximately 25,000 years.

Ecliptic coordinates (Figures 14 and 13) are generally used to specify the positions and orientations of objects in the solar system. **Ecliptic longitude** (elon) is measured along the ecliptic eastward from the vernal

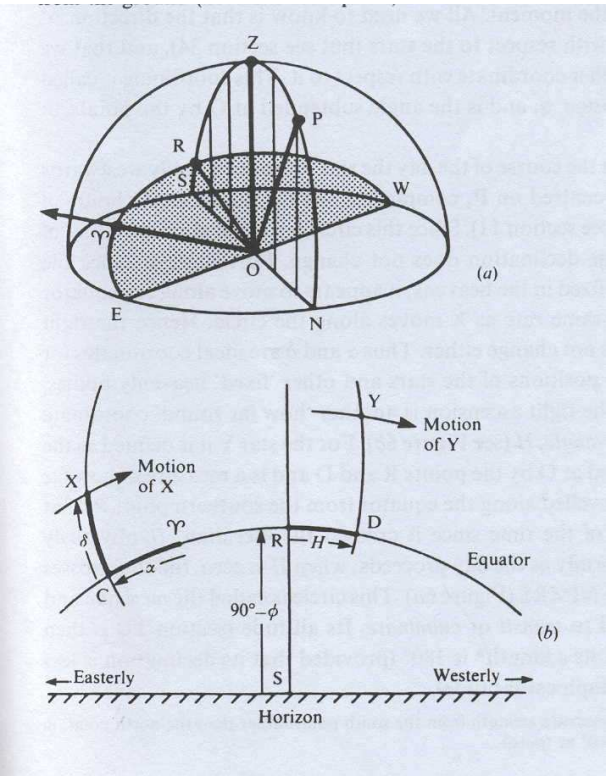

FIG. 10: Diagram of the Equatorial coordinate system

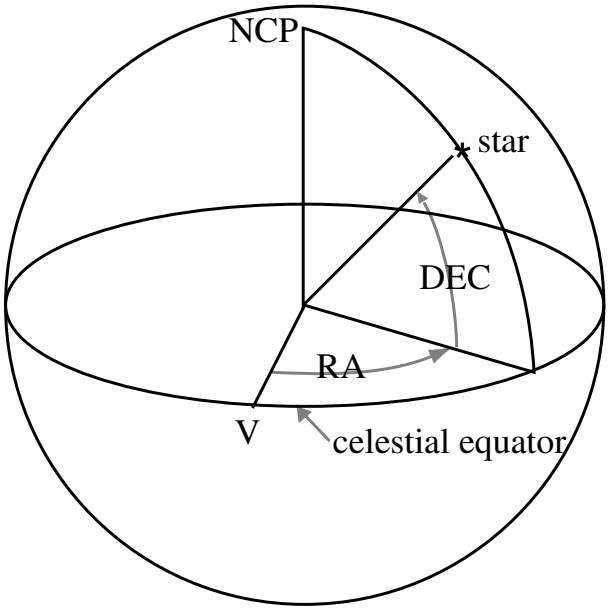

FIG. 11: Diagram of the celestial coordinate system

equinox. **Ecliptic latitude** (elat) is measured along a great circle northward from the ecliptic.

The orientation of the orbit of a planet is specified by 1) the ecliptic longitude of the ascending node of the orbital plane and 2) the inclination of the orbit to the ecliptic. Similarly, the orientation of a planet's rotation or the

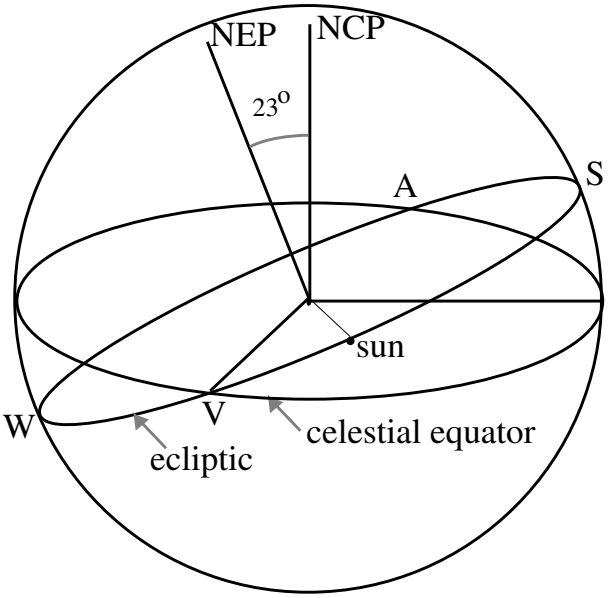

FIG. 12: Diagram of the celestial sphere, showing the celestial north pole (NCP), the celestial equator, the north ecliptic pole (NEP) and the ecliptic. The points labeled V, S, A, and W are, respectively, the vernal equinox, summer solstice, autumnal equinox, and winter solstice corresponding to the directions of the sun on March 21, June 21, September 21, and December 21. The point labeled "sun" is the direction of the sun on approximately April 21.

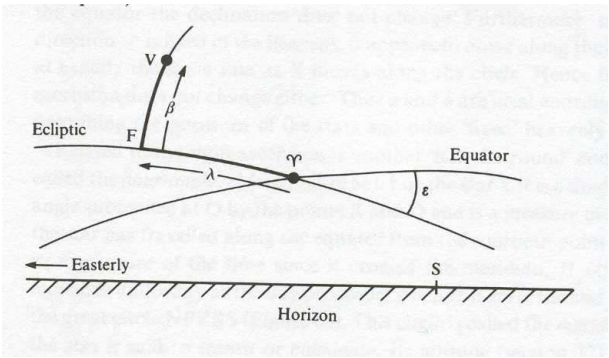

FIG. 13: Diagram of the Ecliptic coordinate system

rotation of the sun itself, as illustrated in Figure 14, is specified by the ecliptic longitude (ELON) of the ascending node of its equator and the inclination (INCL) of the equator to the ecliptic.

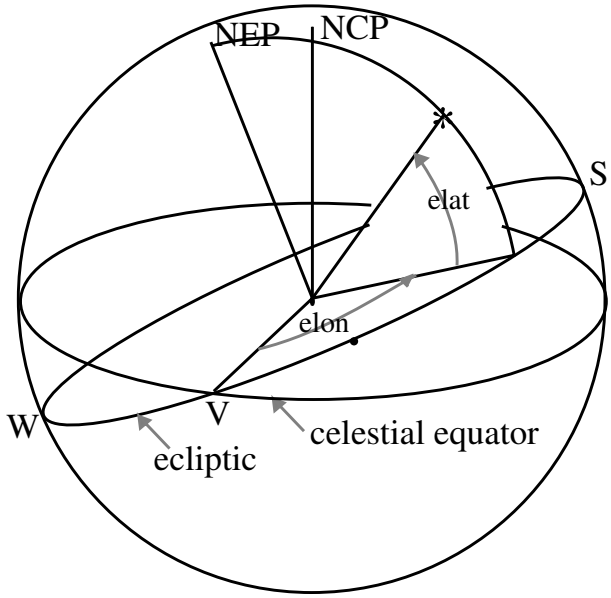

FIG. 14: Diagram showing the relation between the ecliptic and celestial coordinate systems

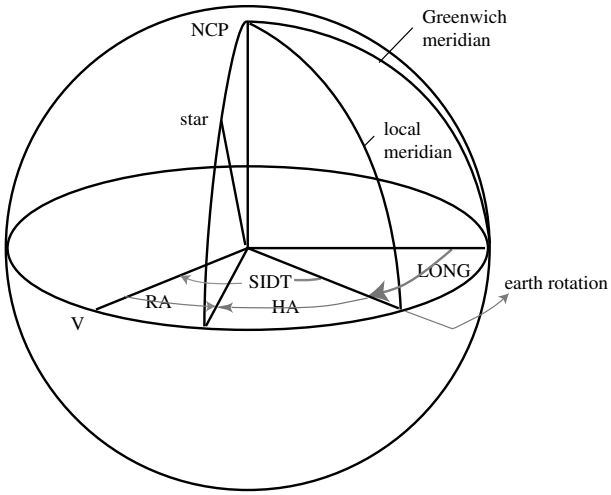

FIG. 15: Diagram of the relations between the quantities involved in setting the position of the telescope about the polar (HA or RA) axis

APPENDIX C: SIGNAL PROCESSING IN 21-CM RADIO ASTROPHYSICS

For a voltage $v(t)$ measured in the time domain we can compute the Fourier transform $V(\nu)$:

$$V(\nu) = \int v(t) e^{-2\pi i \nu t} dt \tag{C1}$$

Note that $V(\nu)$ is *complex*, giving us an amplitude and a phase for each frequency component. In our experiment we are not interested in the phase information. Taking the square modulus of the Fourier transform gives us the voltage power spectrum:

$$S(\nu) = [V(\nu)]^2 \tag{C2}$$

$S(\nu)$ is the quantity plotted by the data acquisition software. For the voltage power spectrum, the units are volts^2 (rms), and a sine wave with amplitude V$_o$rms will produce a signal of amplitude V$_o$rms/4, which becomes V$_o$rms/2 in the one-sided spectrum that is displayed (see below). The spectrum displayed on the Junior Lab computer screen has units dBm, which is power expressed in dB referred to one milliwatt. The spectrum values are converted to milliwatt units by taking into account the characteristic impedance of the transmission line, $Z_o = 50\ \Omega$. This is done according to $dBm = 10log\frac{Vrms^2}{.2236^2}$ where the 50 Ω's in the numerator and denominator have canceled. The power you measure $\frac{V_{rms}^2}{Z_0}$ is the power going down the cable to the A/D converter, related to, but not equal to, the power received at the antenna.

The above expression for the Fourier Transform, refer to a continuous signal measured for an infinite length of time. In practice, instead of $v(t)$, we in fact measure $v_i(t)$, discrete samples separated by a time interval δt, over a period of time Δt. Thus the number of points measured is $N = \Delta t/\delta t$. Our Fourier transform is now the sum

$$V_j(\nu) = \sum_{i=1}^{N} v_i(t) e^{-2\pi i \nu_j t} \delta t \tag{C3}$$

This differs from the ideal $V(\nu)$ computed above in some important ways. We have to consider the effects of *sampling* and *windowing*. We also note that the power spectrum has the property of *symmetry about zero frequency*.

Sampling: We sample the signal at a rate $1/\delta t$, which means that only signals with frequency $2/\delta t$ or smaller can be reconstructed. In a properly designed spectrometer the sampling range and the *anti-aliasing filter* are chosen with this in mind. This is the reason for the 3 MHz bandpass filter (see Figure 2) and the sampling rate of just over 6 MHz. A strong signal with frequency larger than 6 MHz that "leaks" through the filter will appear in our power spectrum at an *aliased* frequency with the 0-3 MHz band. Thus, strong interference signals can corrupt your spectra, even though they are outside the bandpass.

Because we use the Fast Fourier Transform (FFT) algorithm to compute the Fourier transform, the spectra are also sampled with values known only at certain values of the frequency. Our frequency "channels" are centered at these values and are separated by

$$\delta\nu = \frac{1}{N\delta t} \tag{C4}$$

Windowing: Because the time series is truncated (i.e., we only measure the voltage signal for a finite period of time), the features in the frequency domain are broadened. In other words, a pure harmonic signal, which in principle would appear as a delta function in the frequency domain, in fact appears as a feature with nonzero width. We can express this effect of the limited time span by multiplying by a "window function" $w(t)$ in the time domain:

$$v_m(t) = w(t)v(t) \tag{C5}$$

For the simplest window function with no weighting, $w(t)$ is unity during the times of the measurements and zero otherwise:

$$w(t) = 1 \text{ for } -\frac{\Delta t}{2} \le t \le \frac{\Delta t}{2} \tag{C6}$$

By the convolution theorem, the Fourier transform of $v_m(t)$ is the convolution of the Fourier transforms of $v(t)$ and $w(t)$:

$$V_m = W(\nu) * V(\nu) \tag{C7}$$

The Fourier transform of the uniform $w(t)$ function above is a sinc function in the frequency domain (see Figure 1):

$$W(\nu) = \frac{\sin \pi\nu\Delta t}{\pi\nu} \tag{C8}$$

The width of the sinc function is proportional to Δt. For example, the half width at the first null (HWFN) is $1/\Delta t$. Thus, each frequency "spike" in the frequency domain is broaded into a feature shaped like a sinc function with a width determined by the length of the data stream. Note that that the spacing between the nulls is equal to $1/\Delta t$ and that this is also the channel spacing. The spectral line is also characterized by "sidelobes," a sort of ringing that can extend far from the main spectral feature. For this choice of window and sampling, the width and sidelobes do not appear in the sampled values of the spectrum if the spectral line is at the center of a channel.

The uniform window is only one possible weighting scheme that can be applied to the data. By changing the weights, we can change the shape of the spectral line

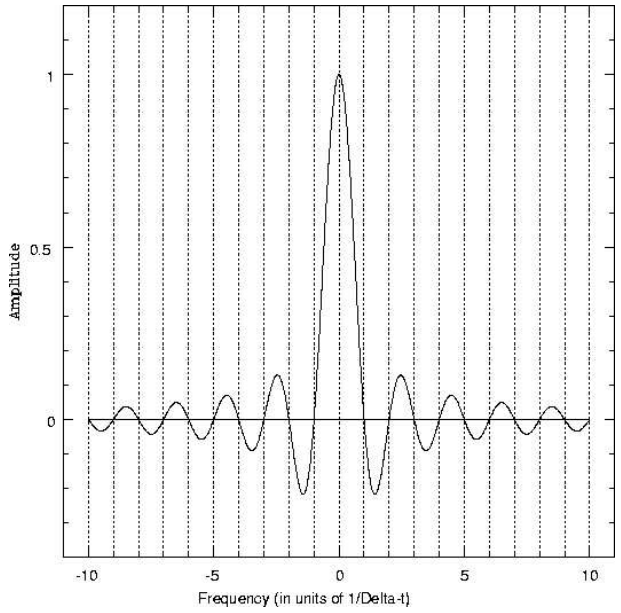

FIG. 16: The Fourier transform of a uniform window of width Δt. The vertical dotted lines show the centers of the frequency channels in the sampled power spectrum, assuming the spectral line is exactly at the center of one channel (which it may not be).

in the frequency domain. The choice should be based on considerations of the expected properties of the spectrum. For example, if we were interested in resolving two closely spaced spectral features, we would choose a weighting scheme that would produce a narrow spectral peak. If we were concerned about interfering signals, it would be prudent to choose a weighting function that produces small sidelobes, even at the cost of a broader spectral peak.

Symmetry About Zero Frequency It can be shown that the Fourier transform of a real function is symmetric about zero frequency. For nonzero frequency components, the power is equally divided between $\pm\nu$. When we display the spectrum, we just sum the frequency components at $\pm\nu$ and present a "one-sided" spectrum. Thus, the first frequency bin is at $\nu = 0$, and the last frequency bin is at $\nu = \delta\nu(\frac{N}{2} - 1)$.

1. Fourier Transform Spectroscopy

The radio astrophysics data acquisition program presents you with choices of:

- Blocks to average = $N_{\rm blocks}$
- 2 Sided PS bins = $N_{\rm bins}$ (corresponds to "n" above)
- Window

From these quantities the duty cycle and the frequency channel spacing are computed and displayed.

Blocks to average Each "block" of data consists of $2^{19} = 524288$ samples collected in the time domain (taking approximately 79msec at a sampling rate of 6.67Msamples/sec). This is the minimum amount of data the program can take. After collecting a block of data, the computer is occupied for some time calculating the power spectrum from $n\delta t$ segments of the data, applying any user selected windowing function and converting to dBm. A power spectrum is calculated for each block of data, and these spectra are averaged. The fraction of time that the computer is collecting data (as opposed to processing it) is the "duty cycle" that is displayed on the screen. As computers get faster and faster, this duty cycle should approach unity.

2 Sided PS bins The signal we measure is real, so the power spectrum we compute is symmetric about zero frequency. The spectrum presented on the PC screen has been "folded" so that the channels at plus and minus the same frequency have been summed. The channel spacing, $\delta\nu$, displayed on the screen is

$$\delta\nu = \frac{1}{N_{\rm bins}\delta t} = \frac{6.67\ {\rm MHz}}{N_{\rm bins}}$$

Doppler-Free Laser Spectroscopy

MIT Department of Physics
(Dated: February 2, 2010)

Traditionally, optical spectroscopy had been performed by dispersing the light emitted by excited matter, or by dispersing the light transmitted by an absorber. Alternatively, if one has available a tunable monochromatic source (such as certain lasers), a spectrum can be measured one wavelength at a time' by measuring light intensity (fluorescence or transmission) as a function of the wavelength of the tunable source. In either case, physically important structures in such spectra are often obscured by the Doppler broadening of spectral lines that comes from the thermal motion of atoms in the matter. In this experiment you will make use of an elegant technique known as Doppler-free saturated absorption spectroscopy that circumvents the problem of Doppler broadening. This experiment acquaints the student with saturated absorption laser spectroscopy, a common application of **non-linear optics**. You will use a diode laser system to measure hyperfine splittings in the $5^2S_{1/2}$ and $5^2P_{3/2}$ states of ^{85}Rb and ^{87}Rb.

1. PREPARATORY PROBLEMS

1. Suppose you are interested in small variations in wavelength, $\Delta\lambda$, about some wavelength, λ. What is the expression for the associated small variations in frequency, $\Delta\nu$? Now, assuming $\lambda = 780nm$ (as is the case in this experiment), what is the conversion factor between wavelength differences ($\Delta\lambda$) and frequency differences($\Delta\nu$), in units of GHz/nm?

2. Suppose you have a laser cavity of length, L, and with index n. What are the frequency and wavelength spacings $\Delta\nu$ and $\Delta\lambda$ of the longitudinal cavity modes for radiation at wavelength λ? Compute the value of $\Delta\nu$ and $\Delta\lambda$ for (a) a diode laser with: $\lambda = 780$ nm, $L = 250$ μm, $n = 3.5$ and (b) a 2 cm external cavity diode laser with: $\lambda = 780$ nm, $L = 2$ cm, $n = 1$.

3. Draw an energy level diagram for ^{85}Rb and ^{87}Rb including the ground state (5S) and first excited state (5P) showing the fine structure (spin-orbit coupling) and hyperfine structure (nuclear angular momentum). Include estimates of the energy scales for the different interactions.

4. Make a chart or diagram of as many different frequency (e.g. energy, wavelength, etc.) scales in this experiment as you can using approximate values and units of MHz: Laser linewidth, laser longitudinal mode spacing, natural atomic linewidth, fine structure, hyperfine structure, Doppler width, Fabry-Perot free spectral range, Fabry-Perot resolution, wavemeter resolution, ...

5. Explain how a diode laser works, including what elements constitute the resonant optical cavity, the gain medium and the source of pump energy.

2. LASER SAFETY

You will be using a medium low power ($\approx$ 40 mW) near-infrared laser in this experiment. The only real damage it can do is to your eyes. Infrared lasers are especially problematic because the beam is invisible. You would be surprised how frequently people discover they have a stray beam or two shooting across the room. Additionally, laser work is often done in the dark, which causes the pupil of the eye to dilate, making you that much more vulnerable.

ALWAYS USE THE APPROPRIATE LASER SAFETY GOGGLES WHEN THE LASER IS ON.

Keep the doors closed and windows covered, to protect people outside the room. To the industrious student, we leave the following theoretical exercise: compare the power per unit area hitting your retina if where you to look directly at the sun with that if you where you to look directly into a 10 mW laser beam of 1 mm diameter (but don't actually try it!).

CAUTION: FRYING THE DIODE LASER

The diode laser is an extremely delicate electronic device. It can very easily be destroyed or damaged by static electricity or by subjecting it to relatively small currents. The maximum current is limited by the sophisticated laser controller you will be using, but generally you should stay around a setting of 70 mA. Additionally, there are omnipresent current spikes from static electricity and the switching on and off of nearby electrical equipment, including the laser power supply itself. Such current spikes are regularly implicated in the frequent and untimely deaths of diode lasers. Diode lasers cost money, they can be hard to obtain, and it is definitely not any fun to install a new one and realign the laser diode head. So help us out by following theses rules:

DO NOT DISCONNECT THE LASER HEAD FROM THE CONTROLLER OR ATTEMPT TO DRIVE THE LASER WITH A DIFFERENT POWER SUPPLY.

CAUTION: CARE OF THE OPTICS

You will be using expensive precision optical instru-

ments, so treat the equipment with great care. Even a good front-surface mirror can cost quite a bit.

ALL OPTICAL SURFACES (INCLUDING MIRRORS) SHOULD ONLY BE CLEANED WITH COMPRESSED AIR OR DELICATELY SWABBED WITH LENS TISSUE MOISTENED WITH LENS CLEANER. NEVER SCRUB.

3. Introduction

There are many varied references which may prove useful in performing this lab. They are listed in the bibliography [1–13].

Saturated absorption laser spectroscopy requires a quasi-monochromatic, tunable, highly directional, laser beam to excite atoms from lower levels, $|g\rangle$, to excited levels, $|e\rangle$. For stationary atoms, absorption from the laser beam is maximum when the laser frequency ν_L exactly coincides with an atomic transition ν_0. The resonance is sharp in this case, meaning that absorption is confined to a very narrow range of frequencies. This situation changes, however, when the atoms are moving. Consider an atom *moving* toward the laser with a velocity v along the beam. If this atom is to experience maximum absorption, ν_L must now be reduced because of the Doppler effect: an atom moving toward a source of light "observes" the light to be upshifted in frequency due to the relative motion. Hence, a reduction in ν_L is mandatory if, after this upshifting, the frequency of the light in the atom's frame is to match the transition frequency ν_0 . The magnitude of the required shift is $\delta\nu \cong \nu_0\left(\frac{\nu}{c}\right)$, which calls for a downshift or upshift in the laser frequency depending on whether the atom is approaching ($v < 0$) or receding ($v > 0$) from the laser.

Consider a gaseous sample of atoms through which a laser beam passes. The number of atoms $N(v)dv$ lying within some velocity interval dv, when plotted as a function of velocity v along the beam, yields a bell-shaped "Maxwellian" distribution centered at $v = 0$. Since a majority of the atoms exhibit only modest velocities, most of these velocities will fall near the middle of the distribution. The remaining atoms, with larger velocities along the beam, populate the wings of the distribution. One can show that a majority of the atoms in the sample have velocity components v on the order of $\sqrt{\frac{2kT}{M}}$, where M is the mass of the atom, k is Boltzmann's constant, and T the absolute temperature. It follows that a gaseous target exhibits a range of absorption frequencies due to this spread in velocities and associated Doppler shifts. The width [FWHM] of this inhomogeneously-broadened Doppler spectral profile is

$$\Delta\nu_D = 7.16\ \nu_0\sqrt{\frac{T}{A}} \times 10^{-7} \qquad (3.1)$$

where A is the atomic weight. According to this expression, a sample of rubidium atoms, maintained at 297 K and excited at 780 nm ($\nu_0 = 3.8\times10^{14}$ Hz), will exhibit a Doppler width of 502 MHz. This is one prediction that is to be tested in the present experiment.

For many years, Doppler widths on the order of 500 MHz served to limit the resolution of optical spectroscopy. Various atomic and molecular interactions, presumed to be small but capable of producing significant features in optical spectra, were never observed because of shrouding and broadening due to the Doppler effect.

The primary feature of saturated absorption laser spectroscopy is its avoidance of or insensitivity to the Doppler effect.

Hence spectra produced by this technique are referred to as "Doppler-free." As such, they exhibit much greater sharpness/resolution, and they reveal spectroscopic features that were heretofore unobservable.

The term "velocity group" is important in saturated absorption laser spectroscopy. It is an abbreviation for a group of $N(v)dv$ atoms, all of which have velocities between v and $v + dv$ along the laser beam. Velocity groups exhibit different sizes - groups near the center of the distribution are large while groups located in the wings of the distribution are small. The term "population" is also important; it is short for the number of atoms or atomic population that occupies a specific atomic state $|n\rangle$. Ground-state populations are much larger than excited-state populations although saturated absorption laser spectroscopy is capable of producing significant redistributions within these populations. The dots in Fig. 1a depict relative populations; in the case shown here, the ground-to-excited-state population ratio is 5:2. The bell-shaped curves in Fig. 1b go a step further by depicting the Maxwellian velocity distributions $N_g(v)dv$ and $N_e(v)dv$ for the ground and excited-state populations.

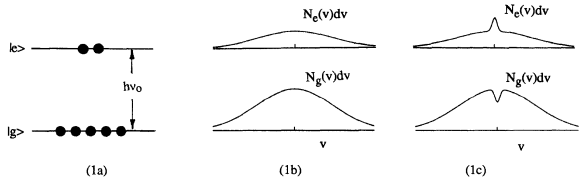

FIG. 1: Population and Maxwellian velocity distributions in a ground-state, $|g\rangle$, and and excited-state, $|e\rangle$, for a hypothetical two-state atom. The hole-burning and population redistribution shown in part (c) correspond to a laser frequency $\nu = \nu_0$.

Consider next the case of a laser beam with frequency $\nu = \nu_0$. Fig. 1c indicates what happens when such a beam passes through a gaseous sample. Only the $v = 0$ group in the ground state interacts with this beam, and hence this group is the only one that suffers depopulation due to promotion of atoms into the excited state.

One says that the laser has burned a "hole" in the middle of the ground-state distribution since fewer $v = 0$

atoms remain to absorb laser light. Such hole-burning or depopulation is central to saturated absorption laser spectroscopy. In the two-level case considered here, this phenomenon requires considerable laser power and/or a relatively long excited-state lifetime τ. The long lifetime helps because it delays the atom's return to the original state. The probability for such decay per unit time is $\Gamma = \frac{1}{\tau}$. Since τ is 28 nsec for the $5^2P_{3/2}$ state of Rb, the spontaneous decay rate here is $\Gamma = 0.36 \times 10^8$ sec^{-1}.

Suppose that the laser frequency ν exceeds the resonant frequency ν_0. It follows that ground-state atoms in the $v = 0$ velocity group can no longer absorb. The only group that can absorb is the group that is moving away from the laser with the right velocity $v > 0$ so as to see the laser frequency ν downshifted to the correct resonant frequency ν_0. Due to the absorption, a hole or relative shortage of atoms develops in this particular $v > 0$ group. We see that as the laser frequency ν continues to scan through the resonance, this hole shifts from group to group.

Saturated absorption laser spectroscopy employs two laser beams derived from a single laser to insure that they both have the same frequency. The beams are arranged to propagate in opposite directions and overlap one another as they pass through the target. One beam, the "pump" beam, is more intense. The other, usually 1/10 as intense, is called the "probe" beam.

Consider the effects of two such beams on a gaseous sample as the laser frequency ν scans upward toward ν_0. For a specific $\nu < \nu_0$, the group of atoms that interacts with the pump beam is that group which counterpropagates along this beam with the requisite velocity $v < 0$ that tunes the beam and atoms into resonance. The only other group of affected atoms is the group that counterpropagates with the same speed relative to the probe beam. These two velocity groups lie in opposite wings of the ground-state distribution. The pump beam burns a significant hole in its $v < 0$ group, but the probe beam, because of its low intensity, causes negligible redistribution within its group.

To perform saturation spectroscopy, one monitors the amount of absorption that the probe beam undergoes as it passes through the sample. If $P(\nu)$ represents the power carried by the probe beam after passage through the sample, one can define an absorption signal $A(\nu) = P_b - P(\nu)$ where $P(\nu)$ is assumed to approach a constant or "baseline" level of transmitted power P_b far from the resonance. We assume P_b to be frequency independent and note that $A(\nu)$ provides a direct measure of the frequency-dependent absorption by the sample. As the laser frequency ν continues to approach ν_0, the sample's absorption $A(\nu)$ from the probe beam gradually increases due to the increasing population of the velocity groups.

If the pump beam happens to be blocked while the laser scans right through ν_0, the absorption signal $A(\nu)$ associated with the probe beam shows a simple, Doppler-broadened lineshape that reflects the varying sizes of the velocity groups in the ground-state distribution.

Now we return to the two-beam case, and let the laser $\nu = \nu_0$. Now the pump and probe beams interact with the same group of atoms, the $v = 0$ group. The pump beam proceeds to depopulate this group, and the probe finds as a result that there are fewer $v = 0$ atoms than in nearby groups. It follows that the absorption of energy $A(\nu)$ from the probe beam exhibits a sharp dip at ν_0 due to this depopulation by the pump. According to the probe, the sample's absorption capacity at $\nu = \nu_0$ shows fatigue or "saturation," and $A(\nu)$ no longer reflects just the gradual variation in $N_g(v)dv$. Instead, the lineshape $A(\nu)$ exhibits the sharp dip called a Lamb dip characteristic of "saturated absorption." A Lamb dip can be several orders of magnitude narrower than the Doppler-broadened spectrum on which it sits. Therein lies the reason why saturated absorption signals can resolve previously shrouded features and offer the prospect of increased spectroscopic accuracy and precision.

The width of the Lamb dip is finite, however, for several reasons, the most fundamental being the uncertainty principle. In the limiting case for which (1) the laser beams are monochromatic and weak, (2) atomic collisions are rare, and (3) the atomic dwell time in the laser beam is long, the width of the Lamb dip is $\delta\nu = \frac{\Gamma}{2\pi}$ which is the "natural width" of the transition. In the present case of Rb, $\delta\nu = 6$ MHz [FWHM]. Lamb dips this narrow are not achieved in the current experiment because our free-running diode laser is insufficiently monochromatic. Since the spectral width of the laser used here is about 30 MHz, the widths of our Lamb dips are 30-40 MHz.

3.1. Fine and Hyperfine Structure

As an alkali metal with one valence electron, Rb has an energy-level scheme that resembles hydrogen. The ground state is designated $5^2S_{1/2}$ and the first excited states, the $5^2P_{1/2}$ and $5^2P_{3/2}$, derive their splitting (their fine-structure splitting) from the spin-orbit interaction. This experiment involves the $5^2P_{3/2}$ state, which lies an energy equivalent of 780 nm above the $5^2S_{1/2}$ ground state.

If the rubidium nuclei were spinless, the $5^2S_{1/2}$ and $5^2P_{3/2}$ energy levels would be singlets in the absence of external fields. Such is not the case, however; natural rubidium contains two isotopes, the 28% abundant ^{87}Rb (I=3/2) and the 72% abundant ^{85}Rb (I=5/2). These non-zero nuclear spins dictate that rubidium nuclei exhibit magnetic and possibly quadrupolar moments (in addition to charge and mass). Nuclear moments interact with the atomic electrons to generate structural subtleties called hyperfine structure (hfs) and hyperfine energy splittings.

To characterize the hfs, it is useful to define a total angular momentum quantum number F, which, in the case of the $5^2S_{1/2}$ state of ^{87}Rb, assumes the values 1 and 2. In the $5^2P_{3/2}$ state of ^{87}Rb, F can be 0, 1, 2, or 3. A transition between some hyperfine sublevel in

the $5^2S_{1/2}$ state and a hyperfine sublevel in the $5^2P_{3/2}$ manifold must satisfy the selection rule $\Delta F = \pm 1$ or 0. The energies, or more precisely, the frequencies ν_F of the various hyperfine sublevels within a given $^{2S+1}L_J$ manifold such as the $5^2P_{3/2}$ can be expressed in terms of two hyperfine coupling constants A and B:

$$\nu_F = \nu_J + \frac{AC}{2} + \frac{B\left[\frac{3C(C+1)}{4} - I(I+1)J(J+1)\right]}{2I(2I-1)J(2J-1)} \quad (3.2)$$

where $C = F(F+1) - J(J+1) - I(I+1)$. For the $5^2S_{1/2}$ ground state of ^{87}Rb, C assumes the values -5/2 or +3/2 corresponding to $F = 1$ or 2. It follows that the third term in Eq. 3.2 is zero, and thus the hfs in the ground state of ^{87}Rb is characterized by the single coupling constant A($5^2S_{1/2}$). The same is true for the ground state of ^{85}Rb. As for the $5^2P_{3/2}$ state of ^{87}Rb, C varies from -15/2 to +9/2 as F ranges from 0 to 3. In this case, both coupling constants A and B are nonzero. By subtracting Eq. 3.2 from itself for adjacent pairs of hfs sublevels in the $5^2P_{3/2}$ manifold, one can derive three linear equations which relate three experimentally-determined hfs splittings $\Delta\nu = \nu_F - \nu_{F-1} = \alpha, \beta$ and γ to a single pair of coupling constants A and B. **The determination of such a pair (A, B) is the major objective of this experiment**.

4. Apparatus

All lasers rely of several common principles for operation: most notably stimulated emission of radiation and population inversion. According to quantum mechanics, all atoms and molecules have discreet energy states which correspond to different periodic motions of the constituent nuclei and electrons. The lowest possible energy states are called the ground state of the particle while all other states are referred to as excited states. In certain circumstances, an atom or molecule can change its energy level by absorption or emission of a photon in what is called an optically allowed transition according to the resonance condition $\Delta E = h\nu$, where ΔE is the difference between initial and final energy states, h is Planck's constant and ν is the photon frequency.

There are two different emission processes, spontaneous emission and stimulated emission. Spontaneous emission is what occurs when an atom or molecule undergoes a transition from an excited energy level to a lower energy level by emitting a resonance photon, conserving total energy. In stimulated emission, a photon of energy hν perturbs the excited particle and causes it to relax to a lower level, emitting a photon of the same frequency, phase, and polarization as the perturbing photon. Stimulated emission is the basis for photon amplification and the fundamental mechanism underlying all laser action. A simplified look at laser action is now described. Einstein defined two coefficients A and B which are parameters related to a particular transition of a given material. The coefficient A relates to the spontaneous emission probability while B relates to the absorption and stimulated emission probabilities (both are equal in terms of quantum mechanical rules).

Given a very simple two level system with lower level 1 and upper level 2, the relative transition rates can be expressed in terms of N_1 and N_2 which represent the relative populations of the respective levels and the Einstein coefficients A_{21} and B_{12} ($=B_{21}$). The subscripts denote the direction of the transition. Under normal conditions, $N_1 >> N_2$ as predicted by statistical thermodynamics. When a resonant photon passes through a volume of these particles, it may interact with a level 1 particle and be destroyed in an absorption process, the probability of which is proportional to $N_1 \times B_{12}$. Alternatively, it may interact with an excited level 2 particle and generate a second photon of identical nature through stimulated emission with a probability proportional to $N_2 \times B_{21}$. In order for laser action to occur, a population inversion is necessary, defined by $N_2 > N_1$. Spontaneous emission also competes to deplete the N_2 level yet only produces unwanted photons of an indiscriminate character. Because of this and other losses, every laser has a minimum value of $N_2 - N_1$ which can give rise to laser output, called threshold inversion.

In order to sustain laser emission, it is necessary to enclose the excited material within an optical cavity (i.e. between two reflecting surfaces). In this case, photons are reflected many times through the lasing medium, greatly increasing the probability of interacting and producing stimulated emission. This multipass nature of the optical cavity results in interference-induced longitudinal mode structure. Only laser light whose wavelength satisfies the standing wave condition, $ml = 2nL$, will be amplified. L is the cavity length, n is the refractive index of the material, and m is an integer corresponding to the mode number of the standing wave pattern. The spacing of adjacent modes is given by $\Delta\nu = \frac{c}{2nL}$, where c is the speed of light. For $n = 6$, $L = 250$ μm then the spacing is about 3.3cm^{-1} or 100 GHz. In addition to longitudinal mode structure, the radiation field may have nodes and antinodes in the plane perpendicular to the laser axis. The best mode structures follow a gaussian distribution, have minimal diffraction losses and can therefore be focused to the smallest size spot.

Broad tuning characteristics of the diode laser are controlled by the shift of the band gap with diode temperature, roughly 2 to 5 cm^{-1} K^{-1}. In our experiment the operating temperature typically ranges between 293-323 K, which is achieved by controlling the temperature of the cold plate mount to which the diode laser package is mounted. Single mode tuning is obtained by changing the laser current. Small changes in laser current cause small changes in the crystal's temperature and thus causes a change in the refractive index n, of the semiconductor material. This refractive index (in the range of 5.5 to 6.5 for Pb-salt materials) change causes a frequency

shift according to the relation

$$\Delta\left(\frac{1}{\lambda}\right) = \frac{1}{2L(n - \lambda\frac{\partial n}{\partial \lambda})} \tag{4.1}$$

where L is the length of the laser cavity (the change of L with temperature is negligible). Note that a combination of different operating temperatures and currents will provide a selection of different frequencies of emitted radiation. Diode lasers tend to emit energy in fewer modes at lower current levels (relative to threshold) and single mode operation generally occurs at higher operating temperatures. Thus it is desirable to access absorption features using combinations of low current and high temperatures. The tuning rate of the laser is determined by the thermal resistance of the device as well as by the electrical contact resistance (.005 to .05 ohm) which is much greater than the bulk resistance of the material. Typical rates are between .001 to .017 cm^{-1} mA^{-1} (250 MHz mA^{-1}). Since the thermal resistance of the diode laser package increases with temperature, tuning rates are typically larger at higher operating temperatures.

Radiation emitted from diode lasers consists of energy which is highly divergent as well as being quite astigmatic. Half-angle divergence in the direction perpendicular to the active or junction layer is typically between 12 and 30 degrees (with 90 degrees occurring as well) while the radiation divergence in the plane parallel to this layer is typically 2 to 6 times less.

You will be using a commercial external cavity diode laser system manufactured by TUI Optics, in this experiment. This unit consists of a laser head and a controller. The head contains the 780nm AlGaAs semiconductor diode laser together with a collimating lens, mounted on a temperature controlled stage. The design incorporates a diffraction grating placed in front of the diode, which acts as a wavelength selective mirror; since this mirror forms one of the two reflective surfaces of the laser cavity its orientation thus allows fine tuning of the output frequency of the laser. Such an *external cavity diode laser* can output single mode light with a spectral width of 30 MHz or less. Changing the diode current and the diode temperature can also change the output frequency, but more drastically (often causing mode hopping, and also changing the output power).

The controller (Fig. 2) is turned on by rotating the key clockwise; be sure to turn it off after you are done. It consists of four modules: the main DC100 monitor, the DTC100 temperature controller, the DCC100 current controller, and the SC100 scan controller. The DC100 shows the diode's current and temperature. The DTC and DCC have fine adjustment knobs to set the temperature and current, and incorporate feedback loops with limit settings to allow these parameters to settle gracefully. Note that the diode temperature may take several minutes to settle down when you first turn on the system, or change the temperature. Do not modify any settings other than the large multi-turn potentiometers.

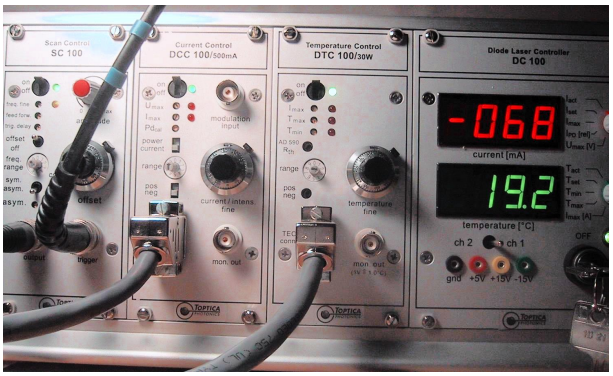

FIG. 2: Front panel of the TUI Laser.

The SC100 allows the diode's output frequency to be swept in a ramp; the three knobs of interest control the width of the sweep (the red knob), the sweep speed (small grey knob left of the multiturn potentiometer), and the sweep offset (the multiturn pot). A frequency sweep of approximately 10 GHz is possible, with periods from seconds to milliseconds. The SC100 has two outputs; one goes to the diode laser, and the other (the trigger) is a TTL (0/+5V) level signal used to trigger acquisition by the oscilloscope. The SC100 can be turned off when no frequency sweep is desired.

The laser's manual, and further references on diode lasers in general, are available on the Junior Lab web site (go to the page for this lab).

4.1. Balanced detector

The other piece of equipment special to this experiment is a balanced optical detector, used to sense the intensity *difference* of two optical beams. This is used to remove an undesirable sloping baseline in the absorption spectra which can result from scanning the laser frequency; it also allows Doppler-broadened components to be removed from the spectra, and suppresses common-mode signals that arise from stray light.

The detector is comprised of two reversed-biased PIN photodiodes wired with opposite polarities to the summing point of a current-to-voltage converter. By this means we monitor only the difference $A_{12}(\nu) = A_1(\nu) - A_2(\nu)$ between the absorption signals riding on the separate probe beams.

These beams, the rubidium vapor cell, and the dual detector-amplifier are carefully positioned so that in the absence of a pump beam, the differential absorption signal $A_{12}(\nu)$ is null throughout the sweep. Even with the reintroduction of the pump beam, which crosses only one probe beam, the null in $A_{12}(\nu)$ persists as long as ν differs from ν_0. At resonance, however, one gets a pure saturation signal, devoid of Doppler character and riding on a flat baseline.

4.2. Frequency meter

A Burleigh Wavemeter Jr. optical wavelength meter is available for optional use. This uses a calibrated Michaelson interferometer to measure the wavelength of light which is coupled in through an optical fiber. The input is a fiber input coupler mounted on an optical post with a special magnetic base so that it can easily be placed and removed from in front of the laser. The input angle must be aligned carefully to couple light into the fiber; it is helpful to monitor the wavemeter's photodiode current while doing this, using the BNC connector on the back. It may take several minutes to achieve good alignment. The wavemeter is good to ± 0.2 nm or so around 780 nm.

4.3. Optical Path

The layout for this experiment is shown in Fig. 3. Light comes out of the laser head through a sliding shutter which can be used to temporarily block the beam. The laser head should be aligned (if not already done) so that the laser beam is everywhere parallel with the breadboard surface. You should always begin a session by double checking this and noting the beam height in your notebook.

The beam passes first through a Faraday isolator to reduce laser instabilities and is then split into two legs by a simple glass slide beam splitter. The reflected beam is directed into a Fabry-Perot interferometer, used to monitor the laser's frequency during a sweep. This is comprised of two partially reflective mirrors and a silicon detector. The mirrors must be aligned such that they are plane parallel. Interferometric traces generated by this cavity show that the nonlinearity of the laser sweep is about 0.2% for sweeps of 2 GHz or less.

The main laser beam is transmitted through the glass slide beam splitter and passed through a variable neutral density filter wheel. This is used to control the overall power in the pump and probe beams and thus to minimize the power broadening of the Rb spectral lines. Following the variable neutral density filter, the beam is split again by a prism. Two weak, parallel beams are reflected from its surfaces; these are used as the probe beams. The un-reflected high-power beam is the pump. Two mirrors reflect the pump and probe beams toward each other, intersecting at the Rb cell. All three beams pass through the cell, but only one probe beam intersects the pump inside the cell. The two probe beams then go into the balanced detector. Additional neutral density filters can be placed inline with the probe and pump beams to control their levels independently.

Our choice of the D_2 transition in atomic Rb is prompted by several considerations:

1. single-mode external cavity laser diode systems work well at the requisite 780 nm wavelength;
2. in a darkened room, the 780 nm light is visible and easily tracked with the help of a phosphorescent beam plate;
3. the atomic target consisting of a static Rb cell at room temperature is very convenient;
4. natural rubidium, with its $^{85}Rb(72\%)$ and $^{87}Rb(28\%)$ isotopes, invites measurement of ground and excited-state hyperfine splittings as well as Doppler widths and isotope shifts; and
5. the energy-level scheme of Rb automatically provides optical pumping, which significantly enhances the saturated absorption effect.

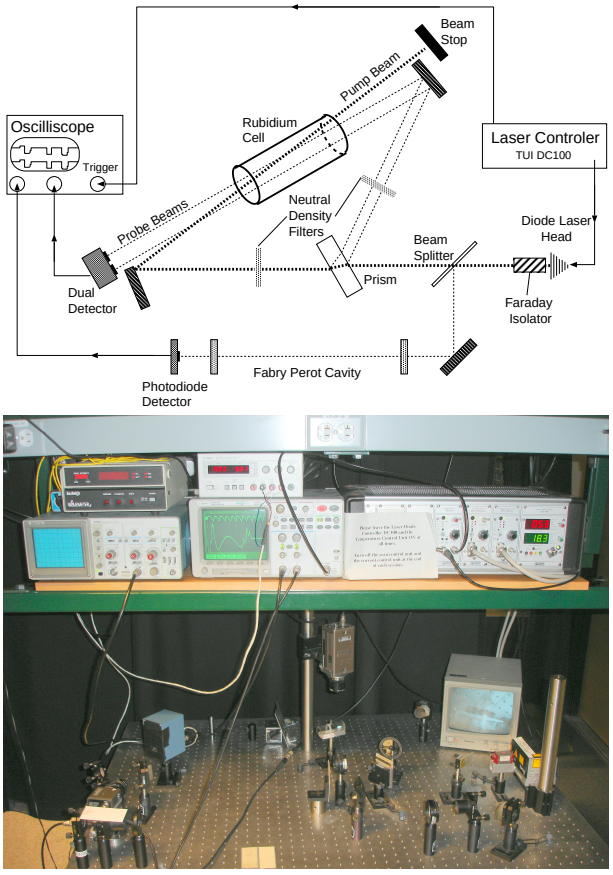

FIG. 3: Experimental Layout: (top) schematic, (bottom) actual photo of optical breadboard.

5. OBSERVATIONS and MEASUREMENTS

A typical experiment will involve the following steps:

1. Align the Fabry-Perot cavity and tune the laser such that interference fringes are visible with a reasonable sweep range.
2. Align the pump and probe beams through the Rb cell and find the ^{87}Rb fine and hyperfine transitions using the diode settings you found.

3. Try different pump and probe beam attenuation levels using different neutral density filters, to observe the doppler broadened peak, the Lamb dip, and finally sharp doppler-free spectra.

4. Quantitatively measure the splittings of the peaks and the peak separations, using the Fabry-Perot interference fringes for frequency difference calibration.

5. Derive the coupling constants A and B of Eq. 3.2 from your measurements.

5.1. Lineshape Considerations

One of the chief difficulties of this experiment is achieving a good balance of pump and probe power to minimize the observed linewidths, and some theory can help explain what we should observe. Pappas et al. [4] have analyzed the present situation in which optical pumping significantly enhances saturated absorption effects. These authors show that in this case, the differential lineshape $A_{12}(\nu)$ for saturated absorption by a low-density target is

$$A_{12}(\nu) = A_s\Big(\frac{\Delta}{2}\Big)^2\left[(\nu-\nu_0)^2+\Big(\frac{\Delta}{2}\Big)^2\right]^{-1} \tag{5.1}$$

where A_s scales as

$$I_{probe}\frac{I_{pump}}{I_{sat}}\frac{1-\Gamma_i T}{2+\Gamma_i T}\left[F+F^2\right] \tag{5.2}$$

and $\Delta = \frac{\gamma(1+F)}{4\pi}$ is the power-broadened width [FWHM] of the signal in Hz. The quantities I_{probe} and I_{pump} are beam intensities, $F = \sqrt{1+\frac{I_{pump}}{I_{sat}}}$ is the broadening factor, $\gamma = \frac{1}{\tau}+\frac{2}{T}+2\pi\delta\nu_{laser}$ is the homogeneous linewidth of the transition in rad/sec, and $I_{sat} = \frac{h\nu_0}{\sigma_0\tau}(1+\frac{\tau}{T})(2+\Gamma_i T)^{-1}$ is a convenient yardstick by which to measure of the intensity of the pump beam. In this expression, ν_0 is the transition frequency between a hyperfine level of the $5^2S_{1/2}$ ground state and the ith hyperfine level of the excited $5^2P_{3/2}$ manifold, τ is the lifetime of the $5^2P_{3/2}$ state,Γ_i represents the sum over all spontaneous decay rates from the ith excited hyperfine level to all lower levels except the initial one, and T is the duration of the excitation (the time that the atoms remain in the laser beam).

The absorption cross section per atom is

$$\sigma_0 = \frac{16\pi^2 k\mu^2}{h\gamma}\frac{1}{4\pi\epsilon_0} \tag{5.3}$$

where $k = \frac{\omega}{c}$, the electric dipole moment μ satisfies

$$\mu^2 = \frac{2\epsilon_0 hc^3\Gamma_0}{2\omega_0^3} \tag{5.4}$$

and Γ_0 is the spontaneous decay rate peculiar to the resonant pair of hyperfine levels. The values of Γ_i and Γ_o reflect hyperfine branching ratios and satisfy the equation $\Gamma_i+\Gamma_o = \frac{1}{\tau}$. Large values for the Γ_i portend significant optical pumping, which implies enhanced saturation absorption signals. A large value of Γ_o , on the other hand, implies a strong transition moment but not necessarily a strong saturation signal.

While the previous discussion is somewhat dense, its significance is straight-forward: one can easily determine or estimate ν_0, τ, T, and $\delta\nu_{laser}$

With a little more effort, one can find values for Γ_o and Γ_i , and proceed to determine μ, σ_0, and I_{sat}. By measuring I_{pump}, one can then evaluate F and hence predict the power-broadened widths Δ of the saturated absorption signals. Hence, through these expressions, one can appreciate that greater pump intensities I_{pump} imply stronger but broader signals, and that large values of Γ_i imply small values of I_{sat} , which means that I_{pump} need not be large to produce sizeable saturated absorption signals in the presence of optical pumping. Finally, we see that if T is large compared to τ then in the limit of low laser power, the saturated absorption linewidth Δ is essentially $\delta\nu_{laser}$.

5.2. Aligning the Fabry-Perot

The chief challenge in using the Fabry-Perot cavity to monitor the laser frequency is alignment of the two cavity mirrors. First ensure that the laser beam enters into the Fabry-Perot cavity; the beam is often blocked when performing the spectroscopic measurements because light retro-reflected from the F-P cavity back into the diode laser can cause undesired instabilities.

Next, remove both mirrors and make sure the laser beam is parallel with the optical bench and falls at the center of the silicon detector. Locate the pinhole (or adjustable iris) and check that the laser goes through it. Place this in front of the front F-P mirror, then insert the back F-P mirror (the one nearest the detector). Look for the mirror's reflection on the surface of the pinhole and align the mirror until the reflection passes back through the pinhole. Now insert the front mirror and repeat. It is helpful to use the CCD camera to observe the reflection. Now turn on the SC100 frequency sweep and train the CCD on the detector.

Tweak up both mirrors until you see clear interference fringes on the detector. When properly aligned, the detector should produce an output voltage with a swing of $\approx$ 30 mV which is easily observed on the scope. Figure 4 shows a sample of actual data from this procedure. If you do not see fringes, it may be because the laser is not operating in its single mode regime. You will want to set the SC100 on its widest sweep range, and initially zero the SC100 offset. A diode current of about 54 mA and temperature of 18.0° C are good choices to begin with. Be sure to measure the F-P mirror separation so you can

calculate its free spectral range later. Experiment with the diode laser settings to determine for what ranges you get single-mode output.

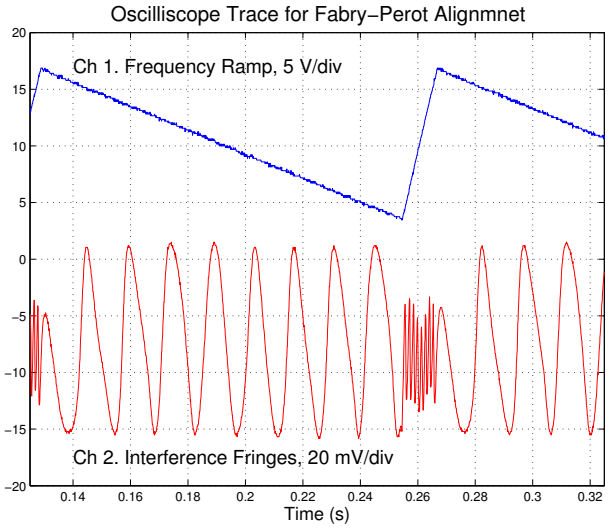

FIG. 4: Sample Data for the Oscilliscope reading of the Fabry-Perot Interferometer

5.2.1. *Saturated Absorption Spectra*

Figure 5 shows three types of absorption lineshapes that can be obtained from the experimental layout shown in Figure 3. To produce spectrum 1, both the pump and one of the probe beams must be blocked. Hence this spectrum, which records the absorption $A(\nu)$ of the vapor vertically versus laser frequency horizontally, is a conventional Doppler-broadened lineshape. The two large features in the center of the spectrum arise from the more abundant isotope ^{85}Rb while the outer lobes arise from ^{87}Rb. These features come in pairs because of the hyperfine interaction and hence splittings in the $5^2S_{1/2}$ ground state. The hfs splitting for ^{87}Rb, being nearly double that of ^{85}Rb, suggests that the former's nuclear magnetic moment is roughly double the latter's.

Trace 2 in Figure 5 was acquired with one pump and one probe beam. Various Lamb dips, most of which are not fully resolved, are now present. With only one probe beam, the Doppler character remains, but the trace shows unmistakably how saturated absorption appears as fatigue in the absorption capacity of the sample. Notice that in your measurements, traces on the scope may appear with different polarity and pedestals; however the difference will look like trace 3.

Finally in trace 3 we see the effects of using two probe beams. Here we have the differential signal A_{12}, and we see that saturated absorption laser spectroscopy reveals at least nine new features that were completely shrouded in trace 1. These new features arise from hfs splittings in the $5^2P_{3/2}$ state. Note from the flatness of the baseline

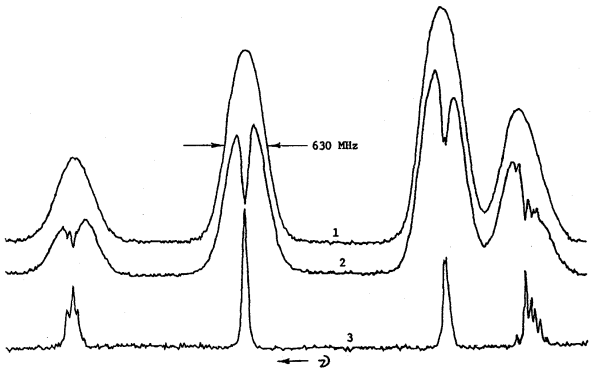

FIG. 5: Three different absorption spectra acquired with the setup of Fig. 3.

that all the Doppler character has been removed from this spectrum.

Align the pump and probe beams such that you can see data like those of traces 1 and 2. Make sure the laser is operating in its single-mode regime. You may need to block the beam from entering the F-P cavity to prevent laser instabilities from the F-P retroreflection into the laser.

5.2.2. *Balancing the detector*

The pump and two probe beams, the rubidium vapor cell, and the dual detector-amplifier are carefully positioned so that in the absence of a pump beam, the differential absorption signal $A_{12}(\nu)$ is null throughout the sweep. Even with the reintroduction of the pump beam, which crosses only one probe beam, the null in $A_{12}(\nu)$ persists as long as ν differs from ν_0. At resonance, however, one gets a pure saturation signal, devoid of Doppler character and riding on a flat baseline.

Neutral density filters attenuate the laser beams to optimize the tradeoff between signal size and signal width. Since the collimated beams have areas of about $5mm^2$, the probe and pump powers of 10 and 100 μW correspond to beam intensities of 2 and 20 $\frac{\mu W}{mm^2}$ respectively. Low laser noise obviates the need for beam chopping and synchronous detection.

Place neutral density filters in both the probe and pump beam paths, and align the balanced detector until you have data such as that of trace 3. Note that the detector sits on a translating stage which can be moved if you loosen the lock-down screw. A typical differential absorption signal $A_{12}(\nu)$ observed on the scope is 10's or 100's of millivolts high and exhibits a signal-to-noise (S/N) ratio of 50 or higher. The detector runs off of two nine-volt batteries to minimize noise; the power switch is **on** in the **up** position. **Please be sure to turn off the detector when done, so the batteries do not get drained.**

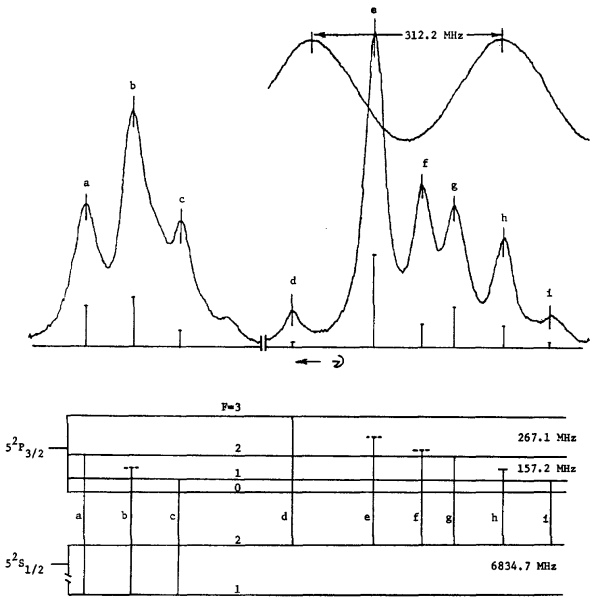

FIG. 6: Composite saturated absorption spectrum for ^{87}Rb and energy-level diagram.

5.2.3. *Getting data from the scope*

The oscilloscope you use in this experiment is an Agilent digital scope, with a floppy drive. You can store your data on a floppy, say in CSV (Comma-Separated-Values) format which can easily be imported into matlab for analysis. For this experiment, you may also want to have the scope average the signal, to reduce the noise. The scope is also connected directly to the local computer's COM-1 port and data may be sent directly to Matlab or another analysis program on Athena.

6. Analysis

An exploded version of trace 3 in Figure 5 appears in Figure 6. The lineshape shows nine transitions identified as "a" through "i" in the energy-level diagram. Features a, c, d, g, and i are normal $\Delta F = \pm 1, 0$ transitions, while features b, e, f, and h are "cross-over" resonances peculiar to saturated absorption spectroscopy. To determine the hfs splitting in the $5^2S_{1/2}$ ground state of ^{87}Rb, we use transition pairs (a,g), (b,h), and (c,i) because the transitions in each of these pairs terminate on a common upper level. Hence the frequency differences $\nu_{ag} = \nu_a - \nu_g, \Delta_{bh}$, and Δ_{ci} provide direct, redundant measures of the ground state hfs. The accepted value of this splitting is $\delta\nu\left(5^2S_{1/2},^{87}Rb\right) = 6834.682614(3)$ MHz according to Penselin et al. [Phys. Rev. 127, 524 (1962)].

To complete the determination of the ground state hfs, consider the panoramic scan in Figure 7. Included is a transmission interferogram that was produced with a 48.000 cm plane-parallel Fabry-Perot cavity while the laser scanned through the spectrum.

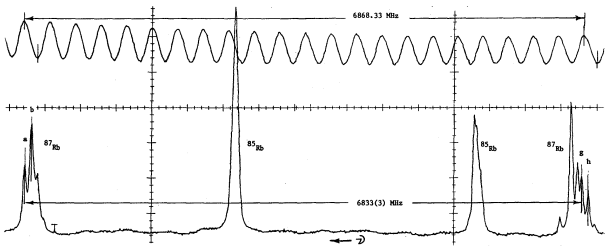

FIG. 7: Panoramic spectrum and interferogram for determination of $5^2S_{1/2}$ hfs. Please note that this particular spectrum was obtained using a research grade instrument and your own spectra may not look quite as nice.

Since the free spectral range (FSR) of this cavity is

$$\Delta\nu_{FRS} = \frac{c}{2n_{air}L} = \frac{2.99792 \times 10^{10}}{2 \times 1.000275 \times 48.000} = 312.197\,\text{MHz} \tag{6.1}$$

it follows that every period in the interferogram corresponds to a scan increment of 312.197 MHz. To calibrate the trace in Figure 7, we use 22 periods of the interferogram corresponding to a scan range of 22(312.197) = 6868.33 MHz and a linear distance Δx_{cal} along the chart. The linear distance between the spectral pair (a,g) is then measured and labelled Δx_{spec} . It follows that

$$\nu_{hfs}\left(5^2S_{1/2},^{87}Rb\right) = 6868.33\frac{x_{spec}}{\Delta x_{cal}} \tag{6.2}$$

For this particular chart, the result is $\nu_{hfs}\left(5^2S_{1/2},^{87}Rb\right) = 6833(5)MHz$, where the uncertainty reflects somewhat optimistically the accuracy with which one can locate the peaks on the interferogram. An advantage to this type of calibration, in which one uses a length of the interferogram essentially equal to the separation between the spectral features of interest, is that effects due to nonlinearities in the scan are largely suppressed. The agreement between our 6833(6) MHz and Penselin's 6834.682614 MHz is quite satisfactory. The resulting coupling constant is $A(5^2S_{1/2},^{87}Rb) = 3416(3)MHz$.

By returning to Figure 6, you can proceed to determine the hfs splittings and coupling constants for the $5^2P_{3/2}$ state. The pair of transitions (d,g) provide the basis for a determination of the F=3 to F=2 splitting, the accepted value of which is 267.1 MHz. Similarly the transition pair (g,i) permits a determination of the middle splitting. The smallest of the splittings cannot be determined from this spectrum. Once the experimental splittings have been determined, you should proceed to evaluate the coupling constants A and B by subtracting Eq 3.2 from itself as discussed above. The accepted values are $A(5^2P_{3/2},^{87}Rb) = 84.85MHz$ and $B(5^2P_{3/2},^{87}Rb) = 12.51MHz$.

6.1. Further Explorations

Once the basics of this experiment are understood, there are many avenues and variations to explore. The present version of the experiment uses laser beams that are horizontally polarized. Other polarizations are possible and the resulting effects on the lineshapes are interesting. You should experiment with different beam intensities to appreciate the tradeoff between signal strength and signal width. You should also think carefully about the nonlinearity of the laser scan and devise a method for measuring it. You might attempt also to identify the origin of the cross-over resonances and understand why they are so strong. In fluorescence spectroscopy, transition "d" would be much stronger than all the others. Why is it so weak here, and why is substantial laser power required in order to observe it?

6.2. Suggested Theoretical Topics

1. Derive Equation 3.1

2. Derive Equation 3.2

ACKNOWLEDGEMENTS This experiment and lab guide was designed by Prof. John Brandenberger, of Lawrence University who was a visiting Professor at MIT during the 1995-96 academic year. Several other students have made valuable contributions to the development of this experiment. They are John Heanue, Gregory Richardson, Victoria Carlton, Peter Yesley and Adam Brailove.

[1] M. S. Feld and V. S. Letokhov, Sci. Am. **229**, 69 (1973), dewey Library Basement.
[2] V. S. Letokhov and V. P. Chebotayev, in *Springer Series in Optical Sciences, Vol. 4* (Springer-Verlag, New York, 1977), pp. 1–35, qC454.L3.L46 Physics Department Reading Room.
[3] V. S. Letokhov, in *High Resolution Laser Spectroscopy*, edited by K. Shimoda (Springer-Verlag, New York, 1976), chap. 4, topics in Applied Physics, Vol. 13.
[4] P. G. P. et al., Phys. Rev. **21A**, 1955 (1980), qC.P579 Physics Department Reading Room and E-Journal.
[5] J. C. Camparo, Contemp. Phys. **27**, 443 (1985), qC.761 E-Journal.
[6] J. R. Brandenberger, Phys. Rev. **39A**, 64 (1989), qC.P579 Physics Department Reading Room and E-Journal.
[7] C. Wieman and L. Hollberg, Rev. Sci. Instrum. **62**, 1 (1991), qC.R453 Physics Department Reading Room and E-Journal.
[8] K. B. MacAdam, A. Steinbach, and C. Wieman, Am. J. Phys. **60**, 1098 (1992), qC.A513 Physics Department Reading Room and E-Journal.
[9] J. Neukammer, Optics. Comm **38**, 361 (1981).
[10] C. G. Aminoff and M. Pinard, J. Physique **43**, 273 (1982), science Library Journal Collection.
[11] S. Nakayama, J. Phys. Soc. Jap. **53**, 3351 (1984), qC.P582 Science Library Journal Collection.
[12] S. Nakayama, Jap. J. Appl. Phys. **23**, 879 (1984).
[13] G. Woodgate, *Elementary Atomic Structure* (Oxford University Press, 1980), chap. 9: Hyoerfine Structure and Isotopic Shift, pp. 168–187.

Quantum Information Processing (QIP)

MIT Department of Physics
(Dated: February 2, 2010)

This experiment will let you perform a series of simple quantum computations on a two spin system, demonstrating one and two quantum-bit quantum logic gates, and a circuit implementing the Deutsch-Jozsa quantum algorithm. You will use NMR techniques and manipulate the state of a proton and a carbon nucleus in a chloroform molecule, measuring ensemble nuclear magnetization. *WARNING: you should know Matlab well to successfully do this experiment!* You will measure: (1) the coupling constant describing the electron-mediated interaction between the proton and carbon nuclear spins of chloroform, (2) the classical input-output truth table for a controlled-NOT gate, (3) the numerical output of the Deutsch-Jozsa quantum algorithm, and (4) optionally, the output and oscillatory behavior of the Grover quantum search algorithm.

1. Preparatory questions

1. The NMR spectrum of ^{13}C chloroform has four peaks: two proton peaks (centered around $\sim$ 200 MHz in this experiment) and two carbon peaks (around $\sim$ 50 MHz). If the initial state of the system is described by a diagonal density matrix,

$$\rho = \begin{bmatrix} a & 0 & 0 & 0 \\ 0 & b & 0 & 0 \\ 0 & 0 & c & 0 \\ 0 & 0 & 0 & d \end{bmatrix} \tag{1.1}$$

(where the states are 00, 01, 10, and 11, with proton on left and carbon on right) then after a $R_x(\pi/2)$ readout pulse, the integrals of the two proton peaks (in the proton frequency spectrum) are given by $a-c$ and $b-d$, and the integrals of the two carbon peaks are given by $a-b$ and $c-d$. The spectrum is the fourier transform of the free induction decay signal, Eq.(3.21), for a given spin state ρ; see the Appendix for a detailed derivation. (a) Sketch the spectra you expect for the four cases when only one of a, b, c, and d is nonzero. (b) What peak integrals do you expect for $\rho = \rho_{therm}$, the thermal state of Eq.(3.25)? (c) What are the spectra if ρ is a CNOT gate applied to the thermal state, that is $\rho = U_{cn}\rho_{therm}U_{cn}^{\dagger}$? How about the near-CNOT?

2. Explicitly compute

$$U = \exp\left[i(n_x\sigma_x + n_y\sigma_y + n_z\sigma_z)\right]$$

and show this gives

$$U = \cos(|n|) + i\frac{n_x\sigma_x + n_y\sigma_y + n_z\sigma_z}{|n|}\sin(|n|)\,.$$

3. Give a sequence of pulses to implement a proper controlled-NOT, which has matrix elements of only one and zero, that is:

$$U_{cn} = \begin{bmatrix} 1 & 0 & 0 & 0 \\ 0 & 1 & 0 & 0 \\ 0 & 0 & 0 & 1 \\ 0 & 0 & 1 & 0 \end{bmatrix}$$

(up to an irrelevant overall phase). You may find it helpful to start with the near controlled-NOT operation of Eq.(3.7). You should need no more than four additional rotations about $\hat{x}$ and $\hat{y}$ axes, or just two rotations about $\hat{z}$ axes to transform the near-CNOT to a real CNOT. The Matlab script `qipgates.m` in the Junior Lab locker on Athena, under `matlab/qip`, is very helpful for this problem.

4. Consider the four possible (classical) functions which have one bit as input and one bit as output.

   - State the function $f_k(x)$ for each of these functions (k from 1 to 4). Sketch a classical circuit which implements each of these functions. Sketch a quantum circuit which implements each of these functions using rotation operations and CNOT gates (the quantum circuit will consist of two qubits, an input 'x' and an output 'y', such that 'x' remains unchanged by the circuit and 'y' encodes the function $f_k(x) \oplus y$). Particularly useful references are [1, 2]
   - State the four pulse sequences which implement the above quantum circuits (denote them as U_{f1}, U_{f2}, U_{f3}, and U_{f4}) comprised of rotations about $\hat{x}$ and $\hat{y}$ axes, and delay times τ during which free two-qubit evolution occurs according to Eq.(3.3).
   - Compute the 4×4 unitary matrices U_k corresponding to the four pulse sequences $U_k = R_{\bar{y}2}R_{y1}\,U_{fk}\,R_{y2}R_{\bar{y}1}$, for k from 1 to 4.

5. Compute the one-sided fourier transform (integral from $t = 0$ to $t = +\infty$) of $e^{i(\omega_0 t+\phi)}e^{-t/T_2}$ and relate your result to the parameters for the Lorentzian in Eq.(3.22).

Suggested schedule

Day 1: Measure ω_P, ω_C, and J, pulse widths for 90 degree rotations; estimate T_1, and T_2. Day 2: Implement near controlled-NOT gate and full controlled-NOT gate on the thermal spectrum, and characterize its peak amplitudes. Day 3: Implement the Deutsch-Jozsa algorithm, and characterize sources of error. Day 4: (if you have time) Implement the Grover algorithm.

2. Introduction

Information always has a physical representation, and physical systems are governed by Laws of Nature. The earliest mechanical computers represented their state using the positions of gears and cogs; these computed by using Newton's laws of classical mechanics. Modern electronic computers store information using the presence or absence of electronic charge on small semiconductor capacitors, and use laws of electricity and magnetism to process information. *Quantum* computers represent information using states of quantum systems, and perform computation by exploiting the laws of quantum physics. Since quantum mechanics is capable of transformations which are impossible classically, new feats of computation are enabled which can speed the solution of some interesting mathematical problems; this potential was first foreseen by Richard Feynman, who pointed out in 1982[3] that quantum systems are difficult to simulate using classical computers. This is because the amount of information necessary to completely describe a quantum state grows exponentially in its size; the wavefunction of an n spin-1/2 particle system is given by about 4^n real numbers. Feynman posed the question: how much computational power could be obtained by using the dynamics of quantum systems to solve classical problems?

Many early questions had to be answered before the potential for quantum information processing was to become evident. First was the thermodynamic cost of computation: for example, von Neumann believed it was necessary to dissipate $\approx k_B T$ of energy per elementary computational step[4]; however, it was then realized by Landauer[5] that energy dissipation is necessary only to *erase* information; in a closed (frictionless) computational system, there is no energy cost to computation! In part, von Neumann's belief came from the fact that gates such as the logical AND are irreversible; Bennett[6] then showed that all Boolean circuits can be made reversible with overhead (number of additional gates) only polynomial in the size of the original circuit. A whole field of reversible computation blossomed from this[7].

These insights brought quantum dynamics into compatibility with the idea of computation, since it was well known that closed quantum systems evolve unitarily, and the microscopic evolution of physical systems is reversible. Benioff[8] began by expressing classical computation as the dynamical behavior of a quantum system, and Feynman introduced various elementary quantum gates[9], but it was not until Deutsch's article in 1989[10] that a problem was found which could provably be solved faster than is possible with a classical computer. Essentially, this was the computation of $f(0) + f(1)$ in one evaluation of a function f which has a domain and range of one bit: $\{0, 1\}$.

Factoring & Search. Deutsch's result languished in relative obscurity until Peter Shor surprised the world in 1994, with his discovery of a quantum algorithm for factoring integers[11]. This result extended a quantum period-finding algorithm by Simon[12] and utilized a number-theoretic result to turn a period of a certain function into factors of L-digit integers, using $O(L^3)$ quantum gates, in contrast to the $O(2^{L^{1/3}})$ operations required by the best known classical algorithm. Subsequently, in 1996 Grover[13] discovered a quantum search algorithm which can be used to speed up a wide range of problems from requiring $O(N)$ steps to only $O(\sqrt{N})$.

Implementation. Large-scale implementation of these algorithms remains a significant experimental challenge, but their basic working principles are now readily demonstrated using nuclear magnetic resonance (NMR) techniques applied to small multi-spin molecules. This methodology[1, 2] involves some new averaging techniques to extract a signal as if the spins were initialized to a zero-temperature state (in reality, they are in a high-temperature Boltzmann distribution). However, implementation of single quantum-bit (qubit) and multiple-qubit logic gates is straightforward, as well as is measurement of the final result. NMR has been successfully used to demonstrate the Deutsch-Jozsa, Grover, and Shor quantum algorithms, as well as quantum error correction and simulation of quantum systems[14, 15].

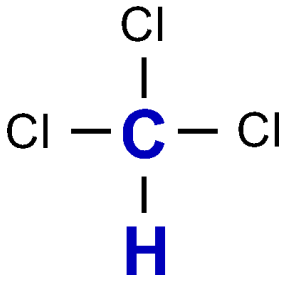

FIG. 1: Chloroform molecule.

In this lab, you will use a simple two-spin system comprised of the hydrogen (proton) and carbon nuclei of ^{13}C labeled chloroform (Fig. 1) to implement a series of quantum logic gates, beginning with single qubit rotation operations, and a simple quantum addition gate. You will then use these building blocks to implement the Deutsch-Jozsa algorithm. Optionally, you may also implement Grover's quantum search algorithm and observe its expected oscillatory behavior.

3. Theory: Quantum gates, circuits, and algorithms

Digital electronic computers are constructed from elementary building blocks known as *logic gates*, and the digital quantum computers we study here are similarly constructed from *quantum logic gates*. These are nothing more than unitary transforms which act on finite-dimensional Hilbert spaces. The physical systems are comprised of numbers of *quantum bits*, two-level quantum systems, whose states are acted upon by a sequence of unitary transforms describing a *quantum circuit*. Finally, a projective measurement collapses the state, giving a probabilistic sequence of classical bits as output. The meaning of this output is dependent on the *quantum algorithm* which is instantiated by the circuit. These algorithms solve certain problems faster than is known to be possible with classical algorithms, because quantum logic gates provide additional new transforms, impossible classically.

We quickly tour this theoretical arena beginning with a description of the basic quantum logic gates, how they are composed to form circuits which implement two basic quantum algorithms, and finally how the circuits are implemented with NMR. More information can be found in the literature[16].

3.1. Quantum gates and circuits

qubits. A single qubit is a vector $|\psi_1\rangle = c_0|0\rangle + c_1|1\rangle$ parameterized by two complex numbers satisfying $|c_0|^2 + |c_1|^2 = 1$. Operations on a qubit must preserve this norm, and thus are described by 2×2 unitary matrices. Similarly, two-qubit states are described by four-dimensional vectors $|\psi_2\rangle = c_{00}|00\rangle + c_{01}|01\rangle + c_{10}|10\rangle + c_{11}|11\rangle$, satisfying $\sum_k |c_k|^2 = 1$, and transforms are 4×4 unitary matrices. In vector form, $|\psi_1\rangle = \begin{bmatrix} c_0 \\ c_1 \end{bmatrix}$, and similarly $|\psi_2\rangle = [c_{00}c_{01}c_{10}c_{11}]^T$.

Measurement. When measured in the *computational basis* of $|0\rangle$ and $|1\rangle$, the single qubit state $|\psi_1\rangle$ produces 0 and 1 with probability $|c_0|^2$ and $|c_1|^2$, respectively. The two-qubit state behaves similarly. Note that the overall phase of a wavefunction is unmeasurable and has no physical meaning, so that $e^{i\theta}|\psi_1\rangle$ is indistinguishable from $|\psi_1\rangle$ for any θ. Thus, a single qubit is often visualized as a unit vector on a sphere (see the Appendix on Bloch sphere representations).

Single qubit gates. The Pauli matrices,

$$\sigma_x \equiv \begin{bmatrix} 0 & 1 \\ 1 & 0 \end{bmatrix} \quad \sigma_y \equiv \begin{bmatrix} 0 & -i \\ i & 0 \end{bmatrix} \quad \sigma_z \equiv \begin{bmatrix} 1 & 0 \\ 0 & -1 \end{bmatrix} \tag{3.1}$$

are important as *generators* of unitary transforms, and a good starting point for describing how a physical system performs quantum computation is to write down its Hamiltonian in terms of such matrices. A system with Hamiltonian H evolves under the Schrödinger equation $i\hbar\partial_t|\psi\rangle = H|\psi\rangle$, which has the solution $|\psi(t)\rangle = U|\psi(t=0)\rangle$, where $U = e^{-iHt/\hbar}$ is unitary.

Quantum logic gates are realized by turning on and off terms in a Hamiltonian via an external control mechanism. For example, a single qubit may be realized by a two-level spin sitting in a static $\hat{z}$-oriented magnetic field, described by the Hamiltonian $H_1 = \hbar\omega_1\sigma_z + \hbar P_{x1}(t)\sigma_x/2 + \hbar P_{y1}(t)\sigma_y/2$, where $P_{x1}(t)$ and $P_{x2}(t)$ are classical variables (c-numbers) resulting from externally controlled magnetic fields about the $\hat{x}$ and $\hat{y}$-axes (see the Appendix on magnetic resonance).

When P_{x1} is turned on, while $P_{y1} = 0$ (and let us assume for now we can neglect the $\hbar\omega_1$ term; this is done by moving into the rotating frame of the spin), the spin state transforms under $U = e^{-iP_{x1}t\sigma_x/2}$. For $P_{x1}t = \pi$, this gives $U = e^{-i\pi\sigma_x/2} = i\sigma_x$. It is easy to see this transform, known as a π rotation about $\hat{x}$, is analogous to a classical NOT gate, since $\sigma_x|\psi_1\rangle = c_1|0\rangle + c_0|1\rangle$; the probability amplitudes of 0 and 1 are reversed. We denote this transform as $R_x(\pi)$. **You will implement such NOT gates to prepare inputs from the initial state $|00\rangle$.**

What happens when $P_{x1}t = \pi/2$? This is called a $\pi/2$ rotation, and results in the transform

$$R_x(\pi/2) = \frac{1}{\sqrt{2}} \begin{bmatrix} 1 & -i \\ -i & 1 \end{bmatrix}, \tag{3.2}$$

which has no classical analogue! It might be thought of as a "square-root" of NOT, since performing this twice gives $R_x(\pi/2)R_x(\pi/2) = R_x(\pi)$, which we identified as a NOT. Similar rotations occur when P_{y1} is nonzero. In general, we can perform rotations $R_x(\theta)$ and $R_y(\theta)$ for any value of θ, by controlling P_{x1} and P_{y1} appropriately. Furthermore, by performing appropriate $\hat{x}$ and $\hat{y}$ rotations sequentially, we can construct rotations about the $\hat{z}$-axis, $R_z(\theta)$.

Two qubit gates. Now consider a two-qubit system described by the Hamiltonian

$$\begin{aligned} H &= \frac{\hbar\pi}{2} J\sigma_z^1\sigma_z^2 + \frac{\hbar P_{x1}(t)}{2}\sigma_x^1 + \frac{\hbar P_{y1}(t)}{2}\sigma_y^1 \\ &\quad + \frac{\hbar P_{x2}(t)}{2}\sigma_x^2 + \frac{\hbar P_{y2}(t)}{2}\sigma_y^2, \end{aligned} \tag{3.3}$$

where the superscripts describe which qubit the operators act upon, and J is a fixed *coupling constant* describing a first-order spin-spin coupling. This kind of coupling is common in liquid-state NMR systems such as that we will be working with. As before, the $P(t)$ terms describe classical controls used to effect single-qubit operations. We assume that each of the $P(t)$ can be turned on separately, and with a magnitude such that $|P(t)| \gg J$, so that while any single qubit operation is active, the J-coupling can be neglected, to very good approximation. This will be the case in our experiment, and the above Hamiltonian will describe our system excellently.

How are single qubit operations on a two-qubit system described mathematically? For example, R_{x1} denotes a $\pi/2$ rotation about $\hat{x}$ on qubit 1 (note that in this labguide, qubit 1 is the carbon nucleus; also we sometimes write R_x as short for $R_x(\pi/2)$). This implies that we wish to do nothing, i.e. the *identity* operation, to qubit 2. To express "do nothing to the second qubit and a R_x to the first qubit" we write $R_{x1} = I \otimes R_{x1}$, where $\otimes$ is the *tensor product* (or sometimes, *Kronecker product*) operator. More about this, and the mathematics used for composite quantum systems, is described in the Appendix. With matlab, you can compute the matrix $R_{x1} = \texttt{kron}(I, R_x)$. Similarly, $\sigma_z^1\sigma_z^2$ is the matrix $\sigma_z \otimes \sigma_z$.

Consider the sequence of operations $U_{ncn} = R_{x1} - \tau - R_{\bar{y}1}$, where τ stands for a free evolution period (with all $P(t) = 0$) of time $1/2J$, and R_{x1} and R_{y1} are $\pi/2$ rotations acting on the first qubit. Note that this sequence is written with time going left to right, but when multiplying unitary transforms the first operator goes on the *right*. Using a Dirac ket labeling of $|c_2c_1\rangle$ (that is, the first qubit has its label on the right), and writing the matrix rows and columns in the natural numerical order of 00, 01, 10, 11 (left to right, and top to bottom), we obtain

$$\begin{aligned} U_{ncn} &= R_{\bar{y}1}\tau R_{x1} && (3.4)\\ &= \left[I \otimes R_{\bar{y}}\right] e^{-i(\pi/4)\sigma_z\otimes\sigma_z} \left[I \otimes R_x\right] && (3.5)\\ &= \frac{1}{\sqrt{2}}\begin{bmatrix} 1 & 1 & 0 & 0\\ -1 & 1 & 0 & 0\\ 0 & 0 & 1 & 1\\ 0 & 0 & -1 & 1\end{bmatrix} \frac{1}{\sqrt{-i}}\begin{bmatrix} -i & 0 & 0 & 0\\ 0 & 1 & 0 & 0\\ 0 & 0 & 1 & 0\\ 0 & 0 & 0 & -i\end{bmatrix}\\ &\quad \times \frac{1}{\sqrt{2}}\begin{bmatrix} 1 & -i & 0 & 0\\ -i & 1 & 0 & 0\\ 0 & 0 & 1 & -i\\ 0 & 0 & -i & 1\end{bmatrix} && (3.6)\\ &= \frac{1}{\sqrt{-i}}\begin{bmatrix} -i & 0 & 0 & 0\\ 0 & 1 & 0 & 0\\ 0 & 0 & 0 & -i\\ 0 & 0 & -1 & 0\end{bmatrix}. && (3.7)\end{aligned}$$

This two-qubit gate is interesting: acting on each of the four computational basis input states $|00\rangle$, $|01\rangle$, $|10\rangle$, $|11\rangle$, we obtain $U|00\rangle = -i|00\rangle$, $U|01\rangle = |01\rangle$, $U|10\rangle = -|11\rangle$, $U|11\rangle = -i|10\rangle$. If we denote the input as $|xy\rangle$, we find that the output from measuring $U|xy\rangle$ gives the classical bits x' and y' such that $x' = x$ and $y' = x \oplus y$, where $\oplus$ is binary addition modulo two ($0 \oplus 0 = 0, 0 \oplus 1 = 1 \oplus 0 = 1, 1 \oplus 1 = 0$). This quantum gate is thus an analog of a classical XOR gate. It is possible to insert further rotations about the $\hat{z}$-axes of the two qubits in order to make all the matrix elements equal to 1; the resulting operation is known as a *controlled*-NOT (or CNOT) gate, and the one given above, with non-ideal phases, is a "near" CNOT. **You will implement the quantum controlled-NOT gate and confirm its classical input-output truth table.**

In drawing these circuits graphically, let the top line be qubit 1, and the bottom qubit 2, such that an $\oplus$ on the bottom line represents R_{x2}^2, that is a π pulse on qubit 2. The vertical line connecting a solid dot with an $\oplus$ is a symbol for a **cnot** gate.

3.2. Quantum algorithm: Deutsch-Jozsa

We are now ready to explore the first non-trivial quantum algorithm ever invented, the Deutsch-Jozsa algorithm, and solve the following problem: give a function $f(x)$ which accepts one bit as input and produces one bit as output, what is $f(0) \oplus f(1)$? Equivalently: give a coin, is it a fake (both sides have heads or tails), or fair (heads one one side, tails on the other)? Clearly, any classical computer must evaluate the function (look at both sides of the coin) at least twice to answer this question. On the other hand, a quantum computer need only evaluate f once!

Here is how it works. We use two qubits, one to store the argument x, and the other to store the value of $f(x)$. In our basis this looks like $|x\ f(x)\rangle$. The two qubits are initialized in the state $|\psi_0\rangle = |00\rangle$. We then perform $U_1 = R_{y2}(\pi/2)R_{\bar{y}1}(\pi/2)$ to the state (note that $R_{\bar{y}1}(\pi/2) = R_{y1}(-\pi/2)$ is simply a rotation about the $-\hat{y}$ axes), obtaining

$$\begin{aligned} |\psi_1\rangle &= U_1|\psi_0\rangle && (3.8)\\ &= \left[R_{y2}(\pi/2)|0\rangle\right] \otimes \left[R_{\bar{y}1}(\pi/2)|0\rangle\right] && (3.9)\\ &= \left[\frac{|0\rangle + |1\rangle}{\sqrt{2}}\right] \otimes \left[\frac{|0\rangle - |1\rangle}{\sqrt{2}}\right] && (3.10)\\ &= \frac{1}{2}\left[|00\rangle - |01\rangle + |10\rangle - |11\rangle\right]. && (3.11)\end{aligned}$$

Now a unitary transform U_f implementing f is applied; this is defined to give $U_f|xy\rangle = |x\rangle|f(x) \oplus y\rangle$. (There are other ways f could be implemented in such a reversible, unitary manner, but they are all equivalent for our purposes.) The result is the state $|\psi_2\rangle$,

$$\begin{aligned} |\psi_2\rangle &= U_f|\psi_1\rangle && (3.12)\\ &= \frac{1}{2}\Big[|0\rangle|f(0)\rangle - |0\rangle|f(0) \oplus 1\rangle\Big]\\ &\qquad +|1\rangle|f(1)\rangle - |1\rangle|f(1) \oplus 1\rangle] && (3.13)\\ &= \frac{1}{2}\Big[(-1)^{f(0)}|0\rangle(|0\rangle - |1\rangle)\Big].\\ &\qquad +(-1)^{f(1)}|1\rangle(|0\rangle - |1\rangle)\Big] && (3.14)\\ &= \left[\frac{(-1)^{f(0)}|0\rangle + (-1)^{f(1)}|1\rangle}{\sqrt{2}}\right] \otimes \left[\frac{|0\rangle - |1\rangle}{\sqrt{2}}\right] && (3.15)\end{aligned}$$

The simplification from the second to third lines above occurs because $0 \oplus 1 = 1$, but $1 \oplus 1 = 0$. Note that

the state of the first qubit (the one on the right) remains unchanged. We now apply two final single-qubit rotations, $U_2 = R_{\bar{y}2}(\pi/2)R_{y1}(\pi/2)$, giving $|\psi_3\rangle$. Recalling that $R_{\bar{y}}(\pi/2)|0\rangle = (|0\rangle - |1\rangle)/\sqrt{2}$, and $R_{\bar{y}}(\pi/2)|1\rangle = (|0\rangle + |1\rangle)/\sqrt{2}$,

$$|\psi_3\rangle = U_2|\psi_2\rangle \tag{3.16}$$

$$= \left[R_{\bar{y}2}(\pi/2)\frac{(-1)^{f(0)}|0\rangle + (-1)^{f(1)}|1\rangle}{\sqrt{2}}\right] \otimes |0\rangle \tag{3.17}$$

$$= \left[\frac{(-1)^{f(0)}(|0\rangle - |1\rangle) + (-1)^{f(1)}(|0\rangle + |1\rangle)}{2}\right] \otimes |0\rangle \tag{3.18}$$

$$= \left[\frac{(-1)^{f(0)} + (-1)^{f(1)}}{2}|0\rangle + \frac{-(-1)^{f(0)} + (-1)^{f(1)}}{2}|1\rangle\right] \otimes |0\rangle\,. \tag{3.19}$$

Note how the first qubit (the one on the right) is left in its original state, $|0\rangle$. As for the second qubit (the one on the left): by inspection, we see that if $f(0) = f(1)$, then $f(0) \oplus f(1) = 0$ and measurement of the second qubit gives 0; otherwise $f(0) \oplus f(1) = 1$, and the measurement gives 1. This is the desired result.

Summarizing, the two-qubit Deutsch-Jozsa algorithm can be expressed as the sequence of operations

$$R_{\bar{y}2}R_{y1}\,U_{fk}\,R_{y2}R_{\bar{y}1} \tag{3.20}$$

acting on the initial state $|00\rangle$, where U_{fk} implements the k^{th} of the four possible functions $f_k(x)$, and each of the R's denotes a $\pi/2$ rotation. These functions can be described by the truth tables

x	$f_1(x)$	$f_2(x)$	$f_3(x)$	$f_4(x)$
0	0	1	0	1
1	0	1	1	0

In one evaluation of f, the quantum algorithm distinguishes between $k = \{1, 2\}$ and $k = \{3, 4\}$, whereas classically this would require two evaluations.

The action of this quantum circuit may be understood as having *interfered* two computational pathways to obtain the final answer. Indeed, the rotation operations are like beamsplitters, and the structure of the algorithm is that of a complex, four-path interferometer. A generalization of this structure is used in the quantum factoring algorithm. **You will construct quantum circuits for the four possible functions U_f, implement the Deutsch-Jozsa algorithm, and observe the measurement result.**

3.3. Quantum algorithm: Grover (optional)

In this lab, you may optionally implement the Grover quantum search algorithm on two qubits. The theory and implementation procedure for this optional part are described in the Appendix.

3.4. Implementation with NMR

This experiment utilizes an NMR apparatus which allows complex pulse sequences to be applied simultaneously at two different frequencies, to control and observe the proton and carbon spins inside molecules of $^{13}CHCl_3$. You are expected to have already completed Experiment #12, Spin Echos / Pulsed NMR, and know the basic physics of NMR. Below is some additional information specific to this quantum computation experiment.

Magnetization readout. The principal output of an experiment is the free induction decay (FID) signal $V(t)$ for spin k, mathematically given as

$$V(t) = -V_0 \mathrm{tr}\left[e^{-iHt}\rho e^{iHt}(i\sigma_x^k + \sigma_y^k)\right]\,, \tag{3.21}$$

where σ_x^k and σ_y^k operate only on the kth spin, and V_0 is a constant factor dependent on coil geometry, quality factor, and maximum magnetic flux from the sample volume. This signal originates from the pickup coils detecting the magnetization of the sample in the $\hat{x}-\hat{y}$ plane. In the laboratory frame, this signal will oscillate at a frequency equal to the precession frequency ω_0 of the nuclei; however, $V(t)$ is usually mixed down with an oscillator locked at ω_0, then fourier transformed.

Notice how the voltage is *complex* valued; this is achieved using a superheterodyne receiver (much like that employed in the 21-cm Radio Astrophysics MIT Junior Lab experiment), and allows one to differentiate between a spin circulating clockwise or counterclockwise. The voltage signal also decays exponentially, as e^{-t/T_2}, so that the fourier transform signal of each spin resonance line is a complex-valued Lorentzian $g(\omega)$,

$$g(\omega) = \frac{\alpha\Gamma}{i(\omega - \omega_0) + \Gamma}\,, \tag{3.22}$$

where ω_0 is the center frequency of the line, $\alpha = |\alpha|e^{i\arg\alpha}$ is the (complex-valued) height of the peak, and 2Γ is the full-width at half-max. You will read out $|0\rangle$ and $|1\rangle$ states (which are along the $\hat{z}$ axes) by tipping them into the $\hat{x} - \hat{y}$ plane, such that they are either $|+y\rangle$ or $|-y\rangle$ states. By convention, the local oscillator reference phase is set such that these states correspond to peaks which are positive, with $\arg\alpha = 0$, or negative, with $\arg\alpha = \pi$.

For a single (uncoupled) spin, the FID has only a single frequency. Two coupled spins will produce *four* frequencies; these occur as two pairs, in this experiment centered around the proton frequency ($\approx$ 200 MHz) and the carbon frequency ($\approx$ 50 MHz). The reason each spin's line is split into two is because of the coupling; as schematically shown in Fig. 2, we can think of what happens as one spin seeing the magnetic field of the other.

In chloroform, we observe that each line is split by $J \approx 215$ Hz, due to a Fermi-contact interaction mediated by electrons in the chemical bond between the carbon and proton. The spectra will appear much like the data shown in Fig. 3.

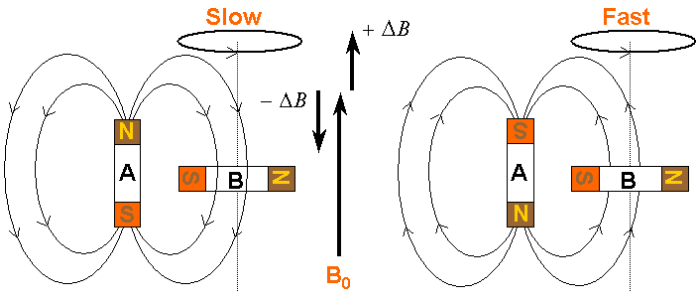

FIG. 2: Semiclassical explanation for spin-spin coupling, showing two spins in a strong magnetic field B_0. Each spin produces its own local magnetic field, which is seen by its neighbor. When spin A is spin-up, its field subtracts from that seen by B, thus causing it to precess slower. When A is spin-down, its field adds, causing B to precess faster. A is a quantum spin which only has two states.

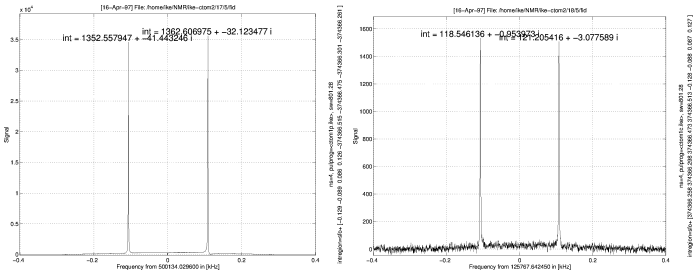

FIG. 3: Proton (left) and carbon (right) spectra of $^{13}CHCl_3$, showing ≈ 215 Hz J coupling.

The input state preparation problem. *(This discussion requires knowledge of basic density matrices and statistical mechanics; it is optional (you can do the lab without fully understanding it) but essential to how the experiment works.)* NMR systems would be ideal for quantum computation if not for one problem which particularly concerns this experiment: NMR is typically applied to physical systems in equilibrium at room temperature, where the spin energy $\hbar\omega$ is much less than $k_B T$. This means that the initial state of the spins is nearly completely random. Traditional quantum computation requires the system be prepared in a pure state (i.e. $|00\rangle$, as describe above); how can quantum computation be performed with a system which is in a high entropy mixed state?

Mathematically, we may write the initial state as the thermal equilibrium state (note our sign convention here),

$$\rho = \frac{e^{+\beta H}}{\mathcal{Z}}, \tag{3.23}$$

where $\beta = 1/k_B T$, and $\mathcal{Z} = \mathrm{tr}\, e^{+\beta H}$ is the usual partition function normalization, which ensures that $\mathrm{tr}(\rho) = 1$. Since $\beta \approx 10^{-4}$ at modest fields for typical nuclei at room temperature, the high temperature approximation

$$\rho \approx 2^{-n}\left[1 + \beta H\right] \tag{3.24}$$

is appropriate, for a system of n spins. For the two-spin chloroform molecule, the initial state is approximately

$$\rho \approx \frac{I}{4} + 10^{-4}\begin{bmatrix} 5 & 0 & 0 & 0 \\ 0 & 3 & 0 & 0 \\ 0 & 0 & -3 & 0 \\ 0 & 0 & 0 & -5 \end{bmatrix}, \tag{3.25}$$

since $\omega_H \approx 4\omega_C$, by virtue of the approximate factor of four difference in the gyromagnetic factor for the proton compared with the carbon.

Initialization solution: temporal labeling. This experiment uses the following technique to extract a signal from only the $|00\rangle$ initial state; it is based on two important facts: quantum operations are linear, and the observables measured in NMR are traceless. Suppose a two spin system starts out with the density matrix

$$\rho_1 = \begin{bmatrix} a & 0 & 0 & 0 \\ 0 & b & 0 & 0 \\ 0 & 0 & c & 0 \\ 0 & 0 & 0 & d \end{bmatrix}, \tag{3.26}$$

where a, b, c, and d are arbitrary positive numbers satisfying $a+b+c+d = 1$. We can use a circuit P constructed from controlled-NOT gates to obtain a state with the permuted populations

$$\rho_2 = P\rho_1 P^\dagger = \begin{bmatrix} a & 0 & 0 & 0 \\ 0 & c & 0 & 0 \\ 0 & 0 & d & 0 \\ 0 & 0 & 0 & b \end{bmatrix}, \tag{3.27}$$

and similarly,

$$\rho_3 = P^\dagger \rho_1 P = \begin{bmatrix} a & 0 & 0 & 0 \\ 0 & d & 0 & 0 \\ 0 & 0 & b & 0 \\ 0 & 0 & 0 & c \end{bmatrix}. \tag{3.28}$$

A unitary quantum computation U is applied to each of these states, to obtain (in three separate experiments, which may be performed at different times) $C_k = U\rho_k U^\dagger$.

By linearity,

$$\sum_{k=1,2,3} C_k = \sum_k U\rho_k U^\dagger \tag{3.29}$$

$$= U\left[\sum_k \rho_k\right]U^\dagger \tag{3.30}$$

$$= (4a-1)U\begin{bmatrix}1&0&0&0\\0&0&0&0\\0&0&0&0\\0&0&0&0\end{bmatrix}U^\dagger + (1-a)\begin{bmatrix}1&0&0&0\\0&1&0&0\\0&0&1&0\\0&0&0&1\end{bmatrix}. \tag{3.31}$$

In NMR, observables M (such as Pauli σ_x and σ_y) for which $\mathrm{tr}(M) = 0$ are the only ones ever measured; thus,

$$\mathrm{tr}\left(\sum_k C_k M\right) = \sum_k \mathrm{tr}\left(LC_k M\right) \tag{3.32}$$

$$= (4a-1)\,\mathrm{tr}\left(U\begin{bmatrix}1&0&0&0\\0&0&0&0\\0&0&0&0\\0&0&0&0\end{bmatrix}U^\dagger M\right) \tag{3.33}$$

$$= (4a-1)\,\mathrm{tr}\left(U|00\rangle\langle 00|U^\dagger\right). \tag{3.34}$$

We find that the sum of the measured signals from the three experiments gives us a result which is proportional to what we would have obtained had the original system been prepared in a pure state $|00\rangle\langle 00|$ instead of in the arbitrary state of Eq.(3.26).

States which are of the form $\rho = 2^{-n}(1-\epsilon)I + \epsilon U|00\ldots0\rangle\langle 00\ldots0|U^\dagger$ (where U is any unitary operator), are called 'effective pure states', or 'pseudopure' states[14]. There are many strategies for preparing such states, and in general they all incur some cost. Effective pure states make it possible to observe zero temperature dynamics from a system which equilibrates to a high temperature state, as long as the coupling of the system to its high temperature environment is sufficiently small. This is the way it is used in NMR quantum computation.

4. Experimental Apparatus

The experimental apparatus consists of a specially prepared chemical sample containing $^{13}CHCl_3$, a NMR spectrometer, and a control computer. A schematic of the Bruker acquisition system is shown in Figure 4.

You will be using a special Bruker Avance 200 NMR spectrometer located in Junior Lab room 4-361 for this experiment. It is primarily controlled by a Linux workstation running Bruker's xwin-nmr; you will interact with the spectrometer through an Athena workstation next to it, which speaks to xwin-nmr over the network, using matlab as your interface. Your main task is to design and implement sequences of pulses (a "pulse program") for the quantum circuits and algorithms described above. You will acquire data, compare with theoretical expectations, and explain likely sources of error and how they could be dealt with.

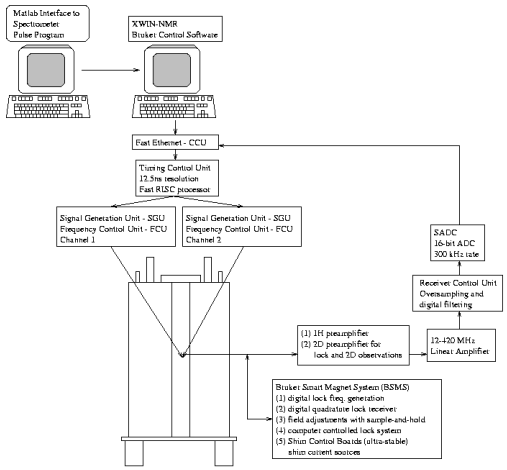

FIG. 4: An overview of the Bruker acquisition system.

4.1. Sample

The 7% by weight $^{13}CHCl_3$ sample is prepared in a flame-sealed 5mm glass tube (Fig. 5) and mounted in a special "spinner" which allows the tube to be rapidly spun to average away transverse inhomogeneities in the B_0 axial field. The solvent is d6-acetone; the deuterium in the solvent is used to produce a lock signal which is picked up by the NMR probe and used in an active feedback loop to stabilize the axial magnetic field from drift.

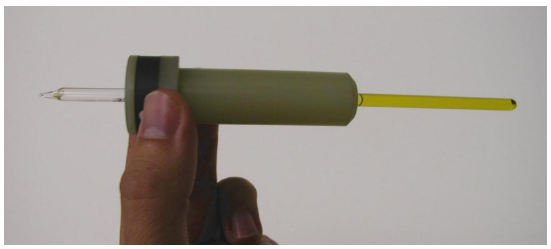

FIG. 5: Picture of a typical NMR sample in a spinner.

4.2. NMR Spectrometer hardware

The spectrometer is constructed from radiofrequency (RF) electronics and a large superconducting magnet with a proton NMR frequency at about 200 MHz, within the bore of which is held the sample in a glass tube, as shown in Figure 6. There, the static $\hat{z}$-oriented magnetic field B_0 is carefully trimmed to be uniform over approximately 1 cm^3 to better than one part in 10^9. Orthogonal saddle coils lying in the transverse plane allow small, oscillating magnetic fields to be applied along the $\hat{x}$ and $\hat{y}$ directions. These fields can be rapidly pulsed on and off to manipulate nuclear spin states. The same coils are also part of tuned circuits which are used to pick up the RF signal generated by the precessing nuclei (much like how a spinning magnet inductively generates an alternating current in a nearby coil).

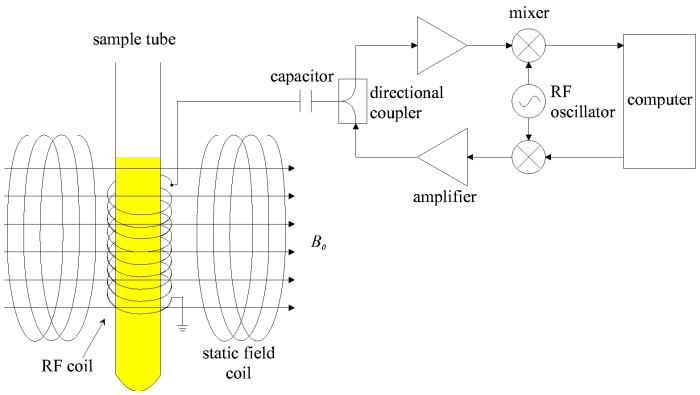

FIG. 6: Schematic diagram of an NMR apparatus.

A typical experiment begins with a long waiting period in which the nuclei are allowed to thermalize to equilibrium; this is on the order of 60 seconds for our sample. Under control of the computer, RF pulses are then applied to effect the desired transformation on the state of the nuclei. The high power pulse amplifiers are then quickly switched off and a sensitive pre-amplifier is enabled, to measure the FID, which is then fourier transformed to obtain a frequency spectrum with peaks whose areas are functions of the spin states.

There are many important practical issues which lead to observable imperfections. For example, spatial inhomogeneities in the static magnetic field cause nuclei in different parts of the fields to precess at different frequencies. This broadens lines in the spectrum. An even more challenging problem is the homogeneity of the RF field, which is generated by a coil which must be orthogonal to the B_0 magnet; this geometric constraint and the requirement to simultaneously maintain high B_0 homogeneity usually forces the RF field to be inhomogeneous and generated by a small coil, leading to imperfect control of the nuclear system. Also, pulse timing, and stability of power, phase, and frequency are important issues.

4.3. Control system and software environment

Two Linux computers are used in this experiment. The QIP workstation is the main controller for the Bruker spectrometer; it will be setup in a server configuration for you, and you should not need to interact with it under normal operation. The main workstation used in this experiment is an Athena Linux terminal. The Athena computer communicates with the other computer over the network to control the spectrometer and perform experiments. The main MATLAB functions you will use are

- `NMRCalib(pw,phref,d1)` – applies one pulse of width `pw` to the proton and carbon channels, for calibration of the center frequencies, the J coupling, the phase references, and the 90 degree pulse widths of the proton and carbon. A matlab structure containing the proton and carbon spectra, as specified below, is returned. The pulse performs a R_x rotation. `d1` is the delay time to wait before starting the sequence.
- `NMRRunPulseProg(pw90,phref,pulses,phases, delays,tavgflag,nucflag,d1)` – runs a pulse program, as specified by `pulses`, `phases`, `delays` using the 90 degree pulse width `pw90` specified, returning a structure containing the proton and carbon spectra, phased according to `phref`, as described below. If `tavgflag` is 1 (that is the default, if this parameter is left out), then the averaging procedure for temporal labeling is performed; otherwise, no averaging is performed and just a single pair of spectra (one proton, one carbon) are taken. `nucflag` specifies whether both proton and carbon spectra are acquired (the default case), or just one. `d1` is the delay time to wait before starting the sequence.

The function arguments follow the following form:

- `pw` = pulse width (for `NMRCalib`) in [μs]
- `pw90` = 90-degree pulse width array (proton,carbon) in [μs]
- `d1` = delay time to wait before pulse sequence in [s]; the default value is 50 seconds, which should be long enough for the sample to re-equilibrate between excitations.
- `phref` = vector of two scalar elements $[\phi_p \phi_c]$ specifying the proton and carbon phase references, in units of [deg]. The spectra are multiplied by $\exp(i\phi_p)$ and $\exp(i\phi_c)$ by the program.
- `pulses` = $2\times N_p$ (two row, and N_p column) matrix specifying what pulse widths to apply for proton and carbon. N_p is the total number of pulses. The first row gives the proton pulse widths, and the second row gives the carbon pulse widths, in units

of `pw90`. For example, [1 0; 0 1] describes a sequence of two 90-degree pulses, the first on the proton, and the second on the carbon.

- `phases` = $2\times N_p$ matrix specifying the phases of the proton and carbon pulses. The first row gives the proton phases, and the second row the carbon phases. Phases are 0, 1, 2, 3 for rotations about the $\hat{x}$, $\hat{y}$, $-\hat{x}$, and $-\hat{y}$ axes, respectively.

- `delays` = $1\times N_p$ vector specifying the delays, in [ms], to perform after each pulse. The first element in this vector specifies the delay after the first pulse, and so forth. Note that the delays vector, the pulses matrix, and the phases matrix must all have the same number of columns.

- `nucflag` = 0 is acquire both spectra (the default), 1 is proton only, 2 is carbon only. The spect structure that is returned will have only the corresponding elements set.

- `tavgflag` = 1 (the default) is to perform temporal labeling, 0 is no temporal labeling.

The proton and carbon spectra must be taken sequentially, one at a time, because the machine only has a single receiver. And if the averaging procedure for temperal labeling is performed, then this requires three experiments (with two spectra each) to be taken, so you have to be patient while the data is taken.

Each of these procedures returns (and saves) a data structure containing the proton and carbon spectra. Specifically, the returned or saved structure `spect` has fields:

- **spect.hfreq**: proton frequency scale data [Hz] - relative to hsfo

- **spect.cfreq**: carbon frequency scale data [Hz] - relative to csfo

- **spect.hspect**: proton spectral data phased according to hphase

- **spect.cspect**: carbon spectral data phased according to cphase

- **spect.cfid**: carbon free induction decay data

- **spect.hfid**: proton free induction decay data

- **spect.tacq** acquisition time [sec]

- **spect.hsfo**: proton transmitter frequency [MHz]

- **spect.csfo**: carbon transmitter frequency [MHz]

- **spect.dt**: date-time marker [string]

- **spect.hpeaks**: integrals of proton peaks phased according to hphase

- **spect.cpeaks**: integrals of carbon peaks phased according to cphase

- **spect.hphase**: phase value for proton spectra [radians]

- **spect.cphase**: phase value for carbon spectra [radians]

- **spect.pp**: pulse program structure containing `spect.pp.pulses`, `spect.pp.phases`, `spect.pp.delays`

- **spect.tavgflag**: flag indicating if temporal labeling was done [binary]

- **spect.nucflag**: flag indicating if one or both of the proton and carbon spectra were acquired [0/1/2]. Normally set to 1 or 2 but not 0.

- **spect.craw**: cell array of the three carbon spectra added together when temperal labeling is done

- **spect.hraw**: cell array of the three proton spectra added together when temporal labeling is done

These two procedures will also save the entire spect structure in a date-time stamped file (e.g., `spect-07Mar02-182304.mat`, i.e. `spect-date-time.mat`). You can load in this structure for later analysis.

5. OBSERVATIONS and MEASUREMENTS

5.1. OVERVIEW

A typical experiment will involve the following steps:

1. Measure phase references, and J.

2. Measure the pulse widths required to implement $R_x(\pi/2)$ rotations on the proton and carbon spins.

3. Measure T_1 and T_2 of the sample.

4. Implement a controlled-NOT gate and measure its input-output truth table.

5. Implement the Deutsch-Jozsa quantum algorithm and test its four cases.

6. (optional) Implement the Grover algorithm, test its four cases, and observe the predicted theoretical oscillation.

5.2. DETAILED PROCEDURE & ANALYSIS

You will need an instructor or graduate TA to introduce you to the spectrometer during the first lab session. It is a very sensitive system and there are special safety precautions so please request help before you begin! Start by ensuring the Junior Lab chloroform sample is in the spectrometer, and taking a sample spectrum to make sure things are working normally. The technical staff may also need to *shim* the magnetic field to optimize its homogeneity. Each time you begin, you will want to quickly check your basic measurements (of the proton and carbon frequencies, and 90 degree pulse widths) again. Login to the Athena workstation, and then:

- **1.** Start `/usr/local/bin/matlab`
- **2.** `addpath /home/nmrqc/matlab`
- **3.** `NMRStartup`

You should now have all the proper Junior Lab QIP scripts in your path and can control the NMR machine. You may check that the network connection to the spectrometer is up by running the script `testnmrx`. If the connection is down, you will get the error message "do_nmr_command failed". In this case, you will need to go to the Bruker console and run the command `netnmr2` inside xwin-nmr; a staff member can help with this. Aborting commands while communicating over the network may also require you to restart `netnmr2`.

5.2.1. *Measurement of* `phref`, ω_P, ω_C, *and* J

Run `NMRCalib` with `pw`=5, and `phref`=[0 0]. The output is the structure `spect` (type 'help NMRCalib' for more) and 2 plots will show up, one for carbon and one for proton.

The data you obtain at first will have complex-valued peak integrals, because the phase reference of the receiver is not set properly (that is the role of `phref`). By plotting `spect.hspect` versus `spect.hfreq`, determine what value of ϕ you need, such that $e^{i\phi\pi/180} \times$ `spect.hspect` is real-valued (and appears as in Fig. 7). Do similarly for the carbon. Then run `NMRCalib` again with these two phase values in `phref`, and it will give you properly phased spectra. Note that you do not need an absolutely perfect phase setting for this experiment to work properly: having the imaginary component be $\langle 10\%$ of the real component is acceptable.

Example: The matlab commands

```
spect = NMRCalib(5,[10 34])
figure;
plot(real(spect.hfid));
figure;
plot(spect.hfreq,spect.hspect);
```

apply a 5 μs pulse to the proton, measure the proton and carbon spectra, and plot these in two figures. `10` and `34` are used as the phase reference angles; they should be chosen (by you) such that the spectra are real. The two plot commands plot the proton FID and the proton spectra. You can use `plot(spect.hfreq,exp(i*x)*spect.hspect)` to change the phase by `x` radians.

Analysis: Plot the free induction decay data (`spect.hfid` and `spect.cfid`) as functions of time (`spect.tacq` is the total acquisition time for each FID); this is the data that is fourier transformed to give the spectral data. Plot the absolute value of the spectral data (`spect.{hspect,cspect}`) versus frequency (`spect.{hfreq,cfreq}`), and note the four Lorentzian lines. The RF frequency of the carrier has to be set to exactly the center of the two split lines, for both the proton and carbon (this is how one works in the rotating frame). Be sure to write down the filenames in which your spectral data are saved, as you take them. Carefully measure the splitting between the lines, J, by fitting Lorentzians to the spectral data. J should not change between experiments, and is not a function of the magnetic field strength, but the proton and carbon frequencies may drift slightly from session to session, and also depending on how well the sample is shimmed. When fitting Lorentzians to the lines to obtain the best center positions, refer back to Eq.(3.22).

The ideal thermal spectrum can be computed as the fourier transform of Eq.(3.21), using the thermal density matrix of Eq.(3.25) as the initial state ρ. It is useful to know that if the initial state is a diagonal density matrix $\rho = \mathrm{diag}(a, b, c, d)$, then after a $R_x(\pi/2)$ readout pulse, the peak integrals for the proton peaks are $a - c$ and $b - d$, and the carbon peaks are $a - b$ and $c - d$. For a voltage scale reference of $V_0 = 1$, the integrals of the two peaks in the proton spectrum should be $+8$ and $+8$, while the carbon spectrum should have integrals $+2$ and $+2$, as shown in Fig. 7. **Write down the four peak integrals from your real-valued spectra as your reference thermal spectrum peak integral values and assign their values to the theoretical ratios (+8 or +2.**

You must be careful of the phase of the signals in this lab, and be aware of how the phase is referenced. Ideally, we wish a 90 degree pulse about $\hat{x}$ to result in a real-valued peak (i.e. a Lorentzian of Eq.(3.22) with $\arg\alpha = 0$). Always be sure that a single $R_x(\pi/2)$ pulse indeed gives a spectrum with no net imaginary component! From studying Eq.(3.22), you should note that because of Γ being nonzero, you will always see some imaginary spectral component, but the integrated area of the peak will be zero. The phase tells us the relative phase of the $|0\rangle$ and $|1\rangle$ components of the proton and carbon qubits; equivalently, this can be visualized as their point along the equator of the Bloch sphere. The qubits start along $+\hat{z}$, and then get tipped by a $R_x(\pi/2)$

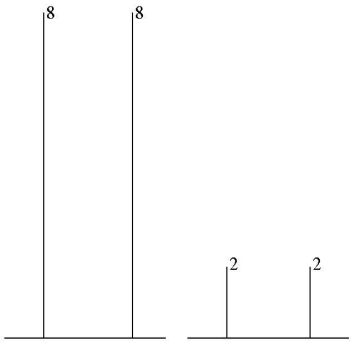

FIG. 7: Thermal spectra for proton (left) and carbon (right): stick figures with nominal peak integrals.

onto $+\hat{y}$, and by convention we choose that to give us a real valued peak. Thus, a $R_y(\pi/2)$ pulse, which tips $+\hat{z}$ onto $+\hat{x}$ should give us a purely imaginary valued peak; you may check that this is true using `NMRRunPulseProg`.

5.2.2. *Calibration of* 90 *degree pulse widths*

Run `NMRCalib` with a set of different pulse widths to determine the number of microseconds required for a $\pi/2$ pulse on the carbon and $\pi/2$ on the proton. Note that they are different, not in the least because the two channels use different RF power amplifiers (why else might they be different?). The best estimate comes from taking a regularly spaced set of pulse widths, and fitting an exponentially damped sinusoid to the points given by peak height versus pulse width (why does the sinusoid exponentially decay?). **On a first pass, do not spend too much time getting your calibrations absolutely perfect; it is important that you get through to finishing the lab.**

Example: The matlab commands

```
peaks = [];
pwtab = linspace(1,15,8);
for pw = pwtab
  sd = NMRCalib(pw,[10 34]);
  peaks = [peaks ; sd.hpeaks sd.cpeaks]
end
figure;
plot(pwtab,real(peaks(:,1)));
figure;
plot(pwtab,real(peaks(:,3)));
```

will measure the proton and carbon spectra for 8 different peak widths from 1 to 15 microseconds, and plot the real part of the left peak integrals as a function of pulse width. `[10 34]` is a vector which specifies the phase references; be sure to replace this with your own values. Note that each signal acquisition takes $\approx$ 50 seconds (by default), so the script as given above will take $\approx 50 * 8 * 2 = 13$ minutes.

Analysis: Take the peak integrals from each of the experiments and plot them as a function of the pulse widths. (You should compare the peak integrals given by the program to what you get from Lorentzian linefits.) Fit an exponentially decaying sinusoid to the proton data and to the carbon data, and from this determine the optimal 90 degree pulse widths for the two nuclei. What sources of error contribute to your pulse width calibrations?

5.2.3. *Measurement of* T_1 *and* T_2

T_1 is measured using a 180 – Δt – 90 "inversion-recovery" pulse sequence, and fitting an exponential decay to the resulting data of peak height versus Δt. Use `NMRRunPulseProg` for this; construct a pulse program with appropriate pulse widths, phases, and delays to perform the experiment. **Be aware that each FID acquisition takes 50 seconds or more, because the system must re-equilibrate between excitations. Do not setup an experiment that will take too long to complete**. The purpose of this part is to familiarize yourself with the system, and to put a lower bound on T_1 and T_2 so that you can convince yourself that the quantum information processing part of the experiment should work.

Example: The matlab commands

```
peaks = [];
dtab = linspace(1,8000,5);
pulses=[2 1;0 0]
phases=[0 0 ;0 0]
nucflag = 0
for delay = dtab
  sd = NMRRunPulseProg([7.3 5.5],[10 34],
     pulses,phases,[delay 0],0,nucflag);
  peaks = [peaks ; sd.hpeaks ]
end
figure;
plot(dtab,real(peaks(:,1)));
```

will perform an inversion recovery T_1 measurement on the proton, taking 5 datapoints with delays from 1 millisecond to 8 seconds. Note that the units of delay is **milliseconds**. `pulses` specifies that the first pulse should be a π pulse on the proton, followed by a $\pi/2$ pulse on the proton. `phases` specifies that all the pulses are along $+\hat{x}$. Note that `[7.3 5.5]` give the $\pi/2$ pulse widths for proton and carbon, in this example, and should be replaced with your actual measured values; similarly for the phase reference values.

Analysis: Measure data to calculate T_1, for both the proton and carbon. Be warned that T_1 is on the order

of 1 to 30 seconds, and you must wait $\geq 5T_1$ between spectra for the sample to re-equilibrate. Also estimate T_2 from the linewidths, obtained by fitting the Lorentzians (and using your answer to prep question #5). Why does the complex amplitude of the Lorentzians vary as they do when you change Δt, particularly on the time scale of 2 to 8 milliseconds?

5.2.4. *Characterization of controlled-*NOT *and its truth table*

Write a pulse sequence for `NMRRunPulseProg` to implement the "near"controlled-NOT gate (with strange phases), $U_{ncn} = R_{\bar{y}1}\tau R_{x1}$, where τ is a $1/2J$ delay, and also your "real" controlled-NOT gate (which you obtained as an answer to prep question #3), U_{cn}.

1. Apply U_{ncn} and a readout pulse ($R_x(\pi/2)$) to the thermal state, and take both proton and carbon spectra; there should be only one readout pulse and it should correspond to the nucleus you are acquiring data for. (What should these spectra look like?)
2. Setup single and two-pulse sequences to prepare all four possible classical inputs (00, 01, 10, 11), using temporal labeling to prepare the initial 00. Then apply U and a readout pulse, to confirm the classical truth table of the CNOT.
3. Repeat the two above steps for your own CNOT pulse sequence, U_{cn}.

You will need to have a proper U_{cn} to proceed to the next step of this lab!

Example: The matlab commands

```
pulses=[0 0 1;1 1 0]
phases=[0 0 0;0 3 0]
delays=[1/2/J 0 0]
tavgflag = 0
nucflag = 1
sd = NMRRunPulseProg([7.3 5.5],[10 34],
       pulses,phases,delays,tavgflag,nucflag);
```

applies a near-CNOT gate with one readout pulse on the proton.

The first row of `pulses` specifies that only one pulse should be applied to the proton, and this is a $\pi/2$ pulse in the third time interval. The second row of `pulses` specifies that $\pi/2$ pulses are applied to the carbon, in the first and second time intervals. The `phases` matrix specifies that the proton pulse should be about $\hat{x}$ (since `phases(1,3)=0`), and the carbon pulses should be about $\hat{x}$ and $-\hat{y}$. And the delays vector specifies that a delay of $1/2J$ (*in milliseconds*!) occurs after the first pulse is applied; this implements the τ free-evolution unitary operator involved in the construction of the near-CNOT of Eq.(3.4).

To obtain a similar spectrum, but for the carbon, you will need to set `nucflag=2` and move the readout pulse to the carbon. `tavgflag=0` tells the machine not to do temporal averaging, so that it applies the pulse sequence to a thermal spectrum. To apply the pulse sequence to the state $|00\rangle$, obtained by temporal averaging, simply set `tavgflag=1`. To apply the sequence to other pure inputs, such as $|01\rangle$, you will need to add additional pulses.

Analysis: Write down the four peak integrals you obtain for the near-CNOT applied to the thermal spectrum. Refering back to prep question #1, and the four reference peak integrals you obtained in the first part of this lab, **compare your peak integrals to make sure you have the right ratios**. That is, let P_{H1}, P_{H2}, P_{C1}, P_{C2} be the reference peak integrals, and P^{cn}_{H1} etc. be the peak integrals for the CNOT applied to the thermal state. Compute P^{cn}_{H1}/P_{H1}, P^{cn}_{H2}/P_{H2}, P^{cn}_{C1}/P_{C1}, P^{cn}_{C2}/P_{C2}, and compare P_{H1}/P_{C1} versus P^{cn}_{H1}/P^{cn}_{C1}. If you see the right peak integral ratios, then you have successfully implemented a logic operation on two nuclear spins – your first simple quantum computation!

Be sure to estimate your errors - where do they come from, and are your results within a standard deviation of the ideal theoretical prediction? Also verify that you are able to create the 00, 01, 10, and 11 states by acquiring corresponding spectra; note that a 0 is a positive real peak, and a 1 is a negative real peak. How close is your output to the theoretical ideal?

Show that for these inputs (the thermal state and the computational basis states) the proton and carbon spectra should be the same whether you implement the ideal CNOT, with all the proper phases, or the "near" CNOT, on the thermal state (or indeed, on any classical input state).

If the spins are in a computational basis state (i.e. 00, 01, 10, or 11), then readout of the proton (or carbon) spectrum alone actually gives full information about the state; only one of the two spectra need be acquired. How does one obtain the state from one spectrum, and why is this possible?

5.2.5. *Implementation of Deutsch-Jozsa quantum algorithm*

The Deutsch-Jozsa algorithm has four possible cases, corresponding to the four possible functions mapping one bit to one bit. Let these be f_1, f_2, f_3, and f_4. In prep question #4, you found pulse sequences to implement these functions. As a hint: U_{f2} needs just one pulse, $U_{f3} = U_{cn}$, and U_{f4} is a simple modification of U_{f3}. Put these together with the theoretical discussion above sequences implementing the full algorithm for four cases. Specifically, translate Eq.(3.20) into pulses. You should be able to fit the sequences into at most eight pulses on each spin. For example, for $k = 1$ the pulse sequence is simply $R_{\bar{y}2}R_{y1}R_{y2}R_{\bar{y}1}$, since U_{f1} is the identity operation.

Write pulse programs for all these four cases, adding readout pulse, and run `NMRRunPulseProg` to acquire the data. It is helpful to translate your pulses into matrices and confirm theoretically that their product gives the expected theoretical result, and matches your experimental observations.

Analysis: Be sure to set your phase reference `phref` properly (as in the calibration step above) such that plotting the reference thermal spectra gives you a positive set of peak parameters α. With the same `phref`, you should find that all the output spectra from the Deutsch-Jozsa experiments give real-valued peak integrals, if all your gates (and in particular, your CNOT gate) are correct.

You should obtain the same spectra for the $k = 1$ and $k = 2$ cases, and a different spectrum for the $k = 3$ and $k = 4$ cases. Verify that this is the case. Note that just as for the controlled-NOT gate experiment, only one of the two (proton and carbon) spectra are needed to fully distinguish the outputs of the two-qubit Deutsch-Jozsa algorithm.

What sources of error contribute to getting non-ideal spectra? **Compute the theoretically expected spectra, and propagate errors from all your measurements and calibrations to obtain an estimate of how far you expect to be off from the ideal; are you within one standard deviation and if not, why?**

Further optional topics: Can you identify where the quantum behavior of the spin system is uniquely required for this algorithm to work? What choice of assignment of qubits to spins did you use, and what happens if you reverse this?

6. Suggested advanced topics

6.1. NMR techniques for quantum computation with other physical systems

The techniques you learned in this lab for quantum computation with NMR are actually extremely similar to what is employed to perform quantum computations with other atomic, molecular, and optical implementations. For example, the Deutsch-Jozsa algorithm was recently implemented[17] on a trapped Ca ion, using pulses of laser light similar to the RF pulses used in this lab. Investigate how quantum bits are realized using trapped ions or superconductors and describe how pulsed excitations implement quantum computations in those systems.

6.2. Entangled states in NMR

One of the most intriguing aspects of quantum systems is a property known as *entanglement*; it is widely believed that entanglement is necessary to achieve any significant computational speedup (or nontrivial cryptographic protocol with qubits) – although this necessity remains unproven in general. By definition, a pure state of two systems A and B in a state $|\psi_{AB}\rangle$ is entangled if and only if it cannot be written as a tensor product, that is, there does not exist $|\psi_A\rangle$ and $|\psi_B\rangle$ such that $|\psi_{AB}\rangle = |\psi_A\rangle \otimes |\psi_B\rangle$. Of such entangled states, the most well studied are the four two-qubit states

$$|\Psi^+\rangle = \frac{|00\rangle + |11\rangle}{\sqrt{2}} \tag{6.1}$$

$$|\Psi^-\rangle = \frac{|00\rangle - |11\rangle}{\sqrt{2}} \tag{6.2}$$

$$|\Phi^+\rangle = \frac{|01\rangle + |10\rangle}{\sqrt{2}} \tag{6.3}$$

$$|\Phi^-\rangle = \frac{|01\rangle - |10\rangle}{\sqrt{2}} \tag{6.4}$$

Give quantum circuits for creating these four states from the initial state $|00\rangle$, describe how to implement this on the two-qubit chloroform system used in this lab, and explain what the measured output signal should be.

[1] D. G. Cory, A. F. Fahmy, and T. F. Havel, Proc. Nat. Acad. Sci. USA **94**, 1634 (1997).
[2] N. Gershenfeld and I. L. Chuang, Science **275**, 350 (1997).
[3] R. P. Feynman, Int. J. Theor. Phys. **21**, 467 (1982).
[4] H. Leff and R. Rex, *Maxwell's Demon: Entropy, Information, Computing* (Princeton University Press, Princeton, NJ, 1990).
[5] R. Landauer, IBM J. Res. Dev. **5**, 183 (1961).
[6] C. H. Bennett, IBM J. Res. Dev. **17**, 525 (1973).
[7] E. Fredkin and T. Toffoli, Int. J. Theor. Phys. **21**, 219 (1982).
[8] P. Benioff, J. Stat. Phys. **22**, 563 (1980).
[9] R. P. Feynman, Optics News p. 11 (1985).
[10] D. Deutsch, Proc. R. Soc. London A **425**, 73 (1989).
[11] P. W. Shor, in *Proceedings, 35th Annual Symposium on Foundations of Computer Science* (IEEE Press, Los Alamitos, CA, 1994), pp. 124–134.
[12] D. Simon, in *Proceedings, 35th Annual Symposium on Foundations of Computer Science* (IEEE Press, Los Alamitos, CA, 1994), pp. 116–123.
[13] L. K. Grover, in *28th ACM Symposium on Theory of Computation* (Association for Computing Machinery, New York, 1996), p. 212.
[14] D. Cory, R. Laflamme, E. Knill, L. Viola, T. Havel, N. Boulant, G. Boutis, E. Fortunato, S. Lloyd, R. Martinez, et al., Fortschr. Phys. **48**, 875 (2000).
[15] L. Vandersypen, C. Yannoni, and I. Chuang, in *to appear in The encyclopedia of NMR (supplement)*, edited by

D. Grant and R. Harris (John Wiley and Sons, West Sussex, England, 2001).
[16] M. Nielsen and I. Chuang, *Quantum computation and quantum information* (Cambridge University Press, Cambridge, England, 2000).
[17] Guilde, Riebe, Lancaster, Becher, Eschner, Haffner, Schmidt-Kaler, Chuang, and Blatt, Nature **421**, 48 (2003).

APPENDIX A: BLOCH SPHERE REPRESENTATION OF A SINGLE QUBIT

Recall that a single qubit in the state $a|0\rangle + b|1\rangle$ can be visualized as a point (θ, ϕ) on the unit sphere, where $a = \cos(\theta/2)$, $b = e^{i\phi}\sin(\theta/2)$, and a can be taken to be real because the overall phase of the state is unobservable. This is called the Bloch sphere representation, and the vector $(\cos\phi\sin\theta, \sin\phi\sin\theta, \cos\theta)$ is called the Bloch vector.

The Pauli matrices give rise to three useful classes of unitary matrices when they are exponentiated, the *rotation operators* about the $\hat{x}$, $\hat{y}$, and $\hat{z}$ axes, defined by the equations:

$$\begin{aligned} R_x(\theta) &\equiv e^{-i\theta X/2} = \cos\frac{\theta}{2} I - i\sin\frac{\theta}{2} X \\ &= \begin{bmatrix} \cos\frac{\theta}{2} & -i\sin\frac{\theta}{2} \\ -i\sin\frac{\theta}{2} & \cos\frac{\theta}{2} \end{bmatrix} \qquad \text{(A1)} \\ R_y(\theta) &\equiv e^{-i\theta Y/2} = \cos\frac{\theta}{2} I - i\sin\frac{\theta}{2} Y \\ &= \begin{bmatrix} \cos\frac{\theta}{2} & -\sin\frac{\theta}{2} \\ \sin\frac{\theta}{2} & \cos\frac{\theta}{2} \end{bmatrix} \qquad \text{(A2)} \\ R_z(\theta) &\equiv e^{-i\theta Z/2} = \cos\frac{\theta}{2} I - i\sin\frac{\theta}{2} Z \\ &= \begin{bmatrix} e^{-i\theta/2} & 0 \\ 0 & e^{i\theta/2} \end{bmatrix}. \qquad \text{(A3)} \end{aligned}$$

One reason why the $R_{\hat{n}}(\theta)$ operators are referred to as rotation operators is the following fact. Suppose a single qubit has a state represented by the Bloch vector $\vec{\lambda}$. Then the effect of the rotation $R_{\hat{n}}(\theta)$ on the state is to rotate it by an angle θ about the $\hat{n}$ axis of the Bloch sphere. This explains the rather mysterious looking factor of two in the definition of the rotation matrices.

An arbitrary unitary operator on a single qubit can be written in many ways as a combination of rotations, together with global phase shifts on the qubit. A useful theorem to remember is the following: Suppose U is a unitary operation on a single qubit. Then there exist real numbers α, β, γ and δ such that

$$U = e^{i\alpha} R_x(\beta) R_y(\gamma) R_x(\delta)\,. \qquad \text{(A4)}$$

APPENDIX B: FUNDAMENTAL EQUATIONS OF MAGNETIC RESONANCE

The magnetic interaction of a classical electromagnetic field with a two-state spin is described by the Hamiltonian $H = -\vec{\mu}\cdot\vec{B}$, where $\vec{\mu}$ is the spin, and $B = B_0\hat{z} + B_1(\hat{x}\cos\omega t + \hat{y}\sin\omega t)$ is a typical applied magnetic field. B_0 is static and very large, and B_1 is usually time varying and several orders of magnitude smaller than B_0 in strength, so that perturbation theory is traditionally employed to study this system. However, the Schrödinger equation for this system can be solved straightforwardly without perturbation theory, in terms of which the Hamiltonian can be written as

$$H = \frac{\omega_0}{2} Z + g(X\cos\omega t + Y\sin\omega t)\,, \qquad \text{(B1)}$$

where g is related to the strength of the B_1 field, and ω_0 to B_0, and X, Y, Z are the Pauli matrices as usual. Define $|\phi(t)\rangle = e^{i\omega t Z/2}|\chi(t)\rangle$, such that the Schrödinger equation

$$i\partial_t|\chi(t)\rangle = H|\chi(t)\rangle \qquad \text{(B2)}$$

can be re-expressed as

$$i\partial_t|\phi(t)\rangle = \left[e^{i\omega Zt/2} H e^{-i\omega Zt/2} - \frac{\omega}{2} Z\right]|\phi(t)\rangle\,. \qquad \text{(B3)}$$

Since

$$e^{i\omega Zt/2} X e^{-i\omega Zt/2} = (X\cos\omega t - Y\sin\omega t)\,, \qquad \text{(B4)}$$

(B3) simplifies to become

$$i\partial_t|\phi(t)\rangle = \left[\frac{\omega_0 - \omega}{2} Z + gX\right]|\phi(t)\rangle\,, \qquad \text{(B5)}$$

where the terms on the right multiplying the state can be identified as the effective 'rotating frame' Hamiltonian. The solution to this equation is

$$|\phi(t)\rangle = e^{i\left[\frac{\omega_0-\omega}{2} Z + gX\right]t}|\phi(0)\rangle\,. \qquad \text{(B6)}$$

The concept of *resonance* arises from the behavior of this solution, which can be understood to be a single qubit rotation about the axis

$$\hat{n} = \frac{\hat{z} + \frac{2g}{\omega_0-\omega}\hat{x}}{\sqrt{1 + \left(\frac{2g}{\omega_0-\omega}\right)^2}} \qquad \text{(B7)}$$

by an angle

$$|\vec{n}| = t\sqrt{\left(\frac{\omega_0-\omega}{2}\right)^2 + g^2}\,. \qquad \text{(B8)}$$

When ω is far from ω_0, the spin is negligibly affected by the B_1 field; the axis of its rotation is nearly parallel

with $\hat{z}$, and its time evolution is nearly exactly that of the free B_0 Hamiltonian. On the other hand, when $\omega_0 \approx \omega$, the B_0 contribution becomes negligible, and a small B_1 field can cause large changes in the state, corresponding to rotations about the $\hat{x}$ axis. The enormous effect a small perturbation can have on the spin system, when tuned to the appropriate frequency, is responsible for the 'resonance' in nuclear magnetic resonance.

In general, when $\omega = \omega_0$, the single spin rotating frame Hamiltonian can be written as

$$H = g_1(t)X + g_2(t)Y\,, \tag{B9}$$

where g_1 and g_2 are functions of the applied transverse RF fields.

APPENDIX C: STATE TOMOGRAPHY

How does one debug a quantum computer? A classical computer is analyzed by measuring its internal state at different points in time. Analogously, for a quantum computer, an essential technique is the ability to measure its density matrix – this is called *state tomography*.

Recall that the density matrix of a single qubit can be expressed as

$$\rho = \frac{1}{2}\left[1 + \sum_k r_k \sigma_k\right], \tag{C1}$$

where σ_k are the Pauli matrices and r_b is a real, three-component vector. Because of the trace orthogonality property of Pauli matrices,

$$\mathrm{tr}(\sigma_k \sigma_j) = 2\delta_{kj}\,, \tag{C2}$$

it follows that ρ can be reconstructed from the three measurement results

$$r_k = \langle \sigma_k \rangle = \mathrm{tr}(\rho \sigma_k)\,. \tag{C3}$$

Measurement of the usual observable in NMR, (3.21), preceded by the appropriate single qubit pulses, allows us to determine $\langle \sigma_k \rangle$, and thus obtain ρ. Similar results hold for larger numbers of spins. In practice, it is convenient to measure just the traceless deviation of ρ from the identity; this is called the deviation density matrix.

APPENDIX D: QUANTUM ALGORITHM: GROVER (OPTIONAL)

In this lab, you may optionally implement the Grover quantum search algorithm on two qubits.

1. Theory

Another quantum algorithm which solves a problem faster than is possible classically is Grover's quantum search algorithm: for a problem size of four elements ($n = 2$ qubits), we are given the set $x = \{0, 1, 2, 3\}$ for which $f(x) = 0$ except at one value x_0, where $f(x_0) = 1$. The goal is to find x_0, which can be classically accomplished by evaluating $f(x)$ an average of 2.25 times. In comparison, the quantum algorithm finds x_0 by evaluating $f(x)$ only once.

Three operators are required: the oracle operator O (which performs a phase flip based on the function $f(x)$), the Hadamard operator on two qubits $H^{\otimes 2}$, and the conditional phase shift operator P. The oracle O flips the sign of the basis element corresponding to x_0; for $x_0 = 3$, this is

$$O = \begin{bmatrix} 1 & 0 & 0 & 0 \\ 0 & 1 & 0 & 0 \\ 0 & 0 & 1 & 0 \\ 0 & 0 & 0 & -1 \end{bmatrix}, \tag{D1}$$

Denoting free evolution period of time $1/2J$ as τ, we find that $O = R_{y1}R_{x1}R_{\bar{y}1}R_{y2}R_{x2}R_{\bar{y}2}\,\tau$ (up to an irrelevant overall phase factor) for the $x_0 = 3$ case, where each of the rotations is by the angle $\pi/2$. $H^{\otimes 2}$ is the operator

$$H^{\otimes 2} = \frac{1}{\sqrt{2}}\begin{bmatrix} 1 & 1 \\ 1 & -1 \end{bmatrix} \otimes \frac{1}{\sqrt{2}}\begin{bmatrix} 1 & 1 \\ 1 & -1 \end{bmatrix} \tag{D2}$$

which can be implemented as $H^{\otimes 2} = R_{x1}(\pi)R_{y1}(\pi/2)R_{x2}(\pi)R_{y2}(\pi/2)$. And the operator P,

$$P = \begin{bmatrix} 1 & 0 & 0 & 0 \\ 0 & -1 & 0 & 0 \\ 0 & 0 & -1 & 0 \\ 0 & 0 & 0 & -1 \end{bmatrix} \tag{D3}$$

is simply realized as $P = R_{y1}R_{\bar{x}1}R_{\bar{y}1}R_{y2}R_{\bar{x}2}R_{\bar{y}2}\,\tau$, where again the angles are $\pi/2$. From these, we construct the Grover iteration $G = H^{\otimes 2}PH^{\otimes 2}O$. This operator can be simplified straightforwardly by eliminating unnecessary operations which obviously cancel.

Let $|\psi_k\rangle = G^k H^{\otimes 2}|00\rangle$ be the state after k applications of the Grover iteration to the initial state. We find that the amplitude $\langle x_0|\psi_k\rangle \approx \sin((2k+1)\theta)$, where $\theta = \arcsin(1/2)$; this periodicity is a fundamental property of the quantum search algorithm, and is a natural feature to test in an experiment. For $x_0 = 3$, we find $|\psi_1\rangle = |11\rangle$, which is the desired result. Indeed, for the other three possible values of x_0 we also find $|\psi_1\rangle = |x_0\rangle$. Another feature of the algorithm is that $|x_0\rangle = |\psi_1\rangle = -|\psi_4\rangle = |\psi_7\rangle = -|\psi_{10}\rangle$, a period of 3 if the overall sign is disregarded. **You may (optionally) implement Grover's algorithm and observe all four cases of x_0. Time permitting, you may also confirm the predicted oscillatory behavior.**

2. Implementation of Grover quantum algorithm

The Grover algorithm for two qubits has four possible cases, corresponding to searching one of the four special elements x_0, x_1, x_2 or x_3. Construct the individual circuit elements, P and O using just Z-rotation, time delays and Hadamard gates. Then simplify your sequences using the tricks below and keeping in mind that Z-rotations and time delays commute:

$$H = Z^2\bar{Y} \tag{D4}$$

$$H = X^2Y \tag{D5}$$

$$Z\bar{Y}\bar{Z} = X \tag{D6}$$

Do not simplify the first two Hadamard gates. You will be able to specify the number of grover iterations you wish to apply.

Write pulse programs for all these four cases, and run `NMRRunPulseProg` to acquire the data.

APPENDIX E: INTERFACE TO BRUKER'S XWIN-NMR

This appendix contains some reference information about the QIP experiment software configuration which you will generally not need to know for this lab, but may be helpful for instructors when debugging problems.

`netnmr2` is a C program (called an "au" script) which runs under xwin-nmr. It is a server which listens on a special socket port for commands sent from Matlab over TCP/IP. Under xwin-nmr, you can start a `netnmr2` process by typing "netnmr2" into the xwin-nmr command prompt line; it will respond with a message saying that the server is running. You can check to see if a `netnmr2` server is already running by typing "show cmd". You can kill a process by typing "kill" – then click on the process to kill.

Matlab speaks to `netnmr2` using a MEX function, `nmrx`. This function can send text commands to xwin-nmr, read parameters, run experiments, and retrieve data. For example, `nmrx('zg')` sends the "zg" command to xwin-nmr, which is "zero-go"; it zeros memory then runs an experiment. This command waits until the experiment is done, then returns control to matlab.

APPENDIX F: MATHEMATICS OF COMPOSITE QUANTUM SYSTEMS

Given quantum systems A and B, how does one properly describe the composite quantum system represented "$A + B$" by the combination of the two subsystems? In quantum mechanics, the answer is the *tensor product*.

Suppose V and W are vector spaces of dimension m and n respectively. For convenience we also suppose that V and W are Hilbert spaces. Then $V \otimes W$ (read 'V tensor W') is an mn dimensional vector space. The elements of $V \otimes W$ are linear combinations of 'tensor products' $|v\rangle \otimes |w\rangle$ of elements $|v\rangle$ of V and $|w\rangle$ of W. In particular, if $|i\rangle$ and $|j\rangle$ are orthonormal bases for the spaces V and W then $|i\rangle \otimes |j\rangle$ is a basis for $V \otimes W$. We often use the abbreviated notations $|v\rangle|w\rangle$, $|v, w\rangle$ or even $|vw\rangle$ for the tensor product $|v\rangle \otimes |w\rangle$. For example, if V is a two-dimensional vector space with basis vectors $|0\rangle$ and $|1\rangle$ then $|0\rangle \otimes |0\rangle + |1\rangle \otimes |1\rangle$ is an element of $V \otimes V$. In terms of vector notation, for example, where $|0\rangle = (10)^T$ and $|1\rangle = (01)^T$, the tensor product $|0\rangle \otimes |1\rangle = (0100)^T$, and $|0\rangle \otimes |0\rangle = (1000)^T$, and so forth.

By definition the tensor product satisfies the following basic properties:

1. For an arbitrary scalar z and elements $|v\rangle$ of V and $|w\rangle$ of W,
$$z\left(|v\rangle \otimes |w\rangle\right) = (z|v\rangle) \otimes |w\rangle = |v\rangle \otimes (z|w\rangle)\,. \tag{F1}$$
2. For arbitrary $|v_1\rangle$ and $|v_2\rangle$ in V and $|w\rangle$ in W,
$$(|v_1\rangle + |v_2\rangle) \otimes |w\rangle = |v_1\rangle \otimes |w\rangle + |v_2\rangle \otimes |w\rangle. \tag{F2}$$
3. For arbitrary $|v\rangle$ in V and $|w_1\rangle$ and $|w_2\rangle$ in W,
$$|v\rangle \otimes (|w_1\rangle + |w_2\rangle) = |v\rangle \otimes |w_1\rangle + |v\rangle \otimes |w_2\rangle. \tag{F3}$$

For matrices, the tensor product is also known as the *Kronecker product*. For example, suppose A is an m by n matrix, and B is a p by q matrix. Then we have the matrix representation:

$$A \otimes B \equiv \overbrace{\left.\begin{bmatrix} A_{11}B & A_{12}B & \dots & A_{1n}B \\ A_{21}B & A_{22}B & \dots & A_{2n}B \\ \vdots & \vdots & \vdots & \vdots \\ A_{m1}B & A_{m2}B & \dots & A_{mn}B \end{bmatrix}\right\} mp}^{nq}. \tag{F4}$$

In this representation terms like $A_{11}B$ denote p by q submatrices whose entries are proportional to B, with overall proportionality constant A_{11}. For example, the tensor product of the vectors $(1, 2)$ and $(2, 3)$ is the vector

$$\begin{bmatrix} 1 \\ 2 \end{bmatrix} \otimes \begin{bmatrix} 2 \\ 3 \end{bmatrix} = \begin{bmatrix} 1 \times 2 \\ 1 \times 3 \\ 2 \times 2 \\ 2 \times 3 \end{bmatrix} = \begin{bmatrix} 2 \\ 3 \\ 4 \\ 6 \end{bmatrix}. \tag{F5}$$

The tensor product of the Pauli matrices X and Y is

$$X \otimes Y = \begin{bmatrix} 0 \cdot Y & 1 \cdot Y \\ 1 \cdot Y & 0 \cdot Y \end{bmatrix} = \begin{bmatrix} 0 & 0 & 0 & -i \\ 0 & 0 & i & 0 \\ 0 & -i & 0 & 0 \\ i & 0 & 0 & 0 \end{bmatrix}. \tag{F6}$$

In Matlab, you can use the function `kron` for the Kronecker product.

APPENDIX G: HOW PROTON AND CARBON SPECTRA ARISE FROM THE DENSITY MATRIX

A two-spin density matrix

$$\rho = \begin{bmatrix} a & 0 & 0 & 0 \\ 0 & b & 0 & 0 \\ 0 & 0 & c & 0 \\ 0 & 0 & 0 & d \end{bmatrix} \tag{G1}$$

produces a proton spectrum with peak areas $a - c$ and $b - d$ for the $\omega_P - J/2$ and $\omega_P + J/2$ peaks, respectively, after a $R_x(\pi/2) \otimes I$ proton readout pulse is applied. The same density matrix also produces a carbon spectrum with peak areas $a - b$ and $c - d$ for the $\omega_C - J/2$ and $\omega_C + J/2$ peaks, respectively, after a $I \otimes R_x(\pi/2)$ carbon readout pulse is applied.

Here, we prove this claim, based on the fact that the voltage in the pick-up coil for spin k is given by

$$V(t) = -V_0 \mathrm{tr}\left[e^{-iHt}\rho e^{iHt}(i\sigma_x^k + \sigma_y^k)\right], \tag{G2}$$

where H is the Hamiltonian for the two-spin system, σ_x^k and σ_y^k operate only on the kth spin, and V_0 is a constant factor dependent on coil geometry, quality factor, and maximum magnetic flux from the sample volume.

1. The readout operator

Let $R_{xP} = R_x(\pi/2) \otimes I$ denote a $\pi/2$ readout pulse on the proton, and R_{xC} similarly for the carbon. Our goal is to compute

$$V_P(t) = -V_0 \mathrm{tr}\left[e^{-iHt} R_{xP}\rho R_{xP}^\dagger e^{iHt}[(i\sigma_x + \sigma_y) \otimes I]\right], \tag{G3}$$

and similarly for the carbon. It is helpful first to move into the rotating frame of the proton and carbon, in which case nothing changes except we utilize the Hamiltonian

$$H = \frac{J}{4}\sigma_z \otimes \sigma_z\,, \tag{G4}$$

representing the spin-spin coupling. Utilizing the cyclic property of the trace, $V_P(t)$ can be written as

$$V_P(t) = -V_0 \mathrm{tr}\left[\rho R_{xP}^\dagger e^{iHt}[(i\sigma_x + \sigma_y) \otimes I]e^{-iHt} R_{xP}\right], \tag{G5}$$

at which point it is useful to define

$$\hat{M}_P = -R_{xP}^{\dagger} e^{iHt} \left[(i\sigma_x + \sigma_y) \otimes I \right] e^{-iHt} R_{xP} \qquad \text{(G6)}$$

as our proton magnetization "readout operator," such that $V_P(t) = V_0 \mathrm{tr}(\rho \hat{M}_P)$. Explicitly working this out in terms of matrix products, we obtain:

$$\begin{aligned}
\hat{M}_P &= -R_{xP}^{\dagger} e^{iHt} \begin{bmatrix} 0 & 0 & 0 & 0 \\ 0 & 0 & 0 & 0 \\ 2\,i & 0 & 0 & 0 \\ 0 & 2\,i & 0 & 0 \end{bmatrix} e^{-iHt} R_{xP} && \text{(G7)} \\
&= -R_{xP}^{\dagger} \begin{bmatrix} e^{\frac{i}{4}J\,t} & 0 & 0 & 0 \\ 0 & e^{\frac{-i}{4}J\,t} & 0 & 0 \\ 0 & 0 & e^{\frac{-i}{4}J\,t} & 0 \\ 0 & 0 & 0 & e^{\frac{i}{4}J\,t} \end{bmatrix} \begin{bmatrix} 0 & 0 & 0 & 0 \\ 0 & 0 & 0 & 0 \\ 2\,i & 0 & 0 & 0 \\ 0 & 2\,i & 0 & 0 \end{bmatrix} \begin{bmatrix} e^{\frac{-i}{4}J\,t} & 0 & 0 & 0 \\ 0 & e^{\frac{i}{4}J\,t} & 0 & 0 \\ 0 & 0 & e^{\frac{i}{4}J\,t} & 0 \\ 0 & 0 & 0 & e^{\frac{-i}{4}J\,t} \end{bmatrix} R_{xP} && \text{(G8)} \\
&= -R_{xP}^{\dagger} \begin{bmatrix} 0 & 0 & 0 & 0 \\ 0 & 0 & 0 & 0 \\ 2\,ie^{-\frac{i}{2}J\,t} & 0 & 0 & 0 \\ 0 & 2\,i\,e^{\frac{i}{2}J\,t} & 0 & 0 \end{bmatrix} R_{xP} && \text{(G9)} \\
&= -\begin{bmatrix} \frac{1}{\sqrt{2}} & 0 & \frac{i}{\sqrt{2}} & 0 \\ 0 & \frac{1}{\sqrt{2}} & 0 & \frac{i}{\sqrt{2}} \\ \frac{i}{\sqrt{2}} & 0 & \frac{1}{\sqrt{2}} & 0 \\ 0 & \frac{i}{\sqrt{2}} & 0 & \frac{1}{\sqrt{2}} \end{bmatrix} \begin{bmatrix} 0 & 0 & 0 & 0 \\ 0 & 0 & 0 & 0 \\ 2\,ie^{-\frac{i}{2}J\,t} & 0 & 0 & 0 \\ 0 & 2\,i\,e^{\frac{i}{2}J\,t} & 0 & 0 \end{bmatrix} \begin{bmatrix} \frac{1}{\sqrt{2}} & 0 & \frac{-i}{\sqrt{2}} & 0 \\ 0 & \frac{1}{\sqrt{2}} & 0 & \frac{-i}{\sqrt{2}} \\ \frac{-i}{\sqrt{2}} & 0 & \frac{1}{\sqrt{2}} & 0 \\ 0 & \frac{-i}{\sqrt{2}} & 0 & \frac{1}{\sqrt{2}} \end{bmatrix} && \text{(G10)} \\
&= \begin{bmatrix} e^{\frac{-i}{2}J\,t} & 0 & -ie^{-\frac{i}{2}J\,t} & 0 \\ 0 & e^{\frac{i}{2}J\,t} & 0 & -i\,e^{\frac{i}{2}J\,t} \\ -ie^{-\frac{i}{2}J\,t} & 0 & -e^{\frac{-i}{2}J\,t} & 0 \\ 0 & -i\,e^{\frac{i}{2}J\,t} & 0 & -e^{\frac{i}{2}J\,t} \end{bmatrix}. && \text{(G11)}
\end{aligned}$$

Similarly, we find that the analogous carbon magnetization "readout operator" $\hat{M}_C$ is

$$\begin{aligned}
\hat{M}_C &= -R_{xC}^{\dagger} e^{iHt} \left[I \otimes (i\sigma_x + \sigma_y) \right] e^{-iHt} R_{xC} && \text{(G12)} \\
&= -R_{xC}^{\dagger} e^{iHt} \begin{bmatrix} 0 & 0 & 0 & 0 \\ 2\,i & 0 & 0 & 0 \\ 0 & 0 & 0 & 0 \\ 0 & 0 & 2\,i & 0 \end{bmatrix} e^{-iHt} R_{xC} && \text{(G13)} \\
&= \begin{bmatrix} e^{\frac{-i}{2}J\,t} & -ie^{-\frac{i}{2}J\,t} & 0 & 0 \\ -ie^{-\frac{i}{2}J\,t} & -e^{\frac{-i}{2}J\,t} & 0 & 0 \\ 0 & 0 & e^{\frac{i}{2}J\,t} & -i\,e^{\frac{i}{2}J\,t} \\ 0 & 0 & -i\,e^{\frac{i}{2}J\,t} & -e^{\frac{i}{2}J\,t} \end{bmatrix}. && \text{(G14)}
\end{aligned}$$

2. The proton and carbon spectra

$\hat{M}_P$ and $\hat{M}_C$ are very useful, because they now allows us to compute the free induction decay signal for the proton (centered in frequency around ω_P) and carbon (centered about ω_C) for any state ρ. For the state in Eq.(G1), we obtain the proton FID

$$V_P(t) = V_0 \mathrm{tr}(\rho \hat{M}_P) \tag{G15}$$

$$= V_0 \mathrm{tr} \left(\begin{bmatrix} a & 0 & 0 & 0 \\ 0 & b & 0 & 0 \\ 0 & 0 & c & 0 \\ 0 & 0 & 0 & d \end{bmatrix} \begin{bmatrix} e^{\frac{-i}{2}Jt} & 0 & -ie^{-\frac{i}{2}Jt} & 0 \\ 0 & e^{\frac{i}{2}Jt} & 0 & -ie^{\frac{i}{2}Jt} \\ -ie^{-\frac{i}{2}Jt} & 0 & -e^{\frac{-i}{2}Jt} & 0 \\ 0 & -ie^{\frac{i}{2}Jt} & 0 & -e^{\frac{i}{2}Jt} \end{bmatrix} \right) \tag{G16}$$

$$= V_0 \left[(a-c)e^{-iJt/2} + (b-d)e^{iJt/2} \right] . \tag{G17}$$

And for the carbon FID,

$$V_C(t) = V_0' \mathrm{tr}(\rho \hat{M}_C) = V_0 \left[(a-b)e^{-iJt/2} + (c-d)e^{iJt/2} \right] . \tag{G18}$$

Note that in general, it is likely that the proton and carbon signals have different voltage scale factors V_0, since they are usually detected by different pick-up coils in an experimental apparatus, and this is reflected in the use of V_0' in the last equation above.

These equations may also be used to show why application of two simultaneous readout pulses (to proton and carbon) in one experiment may give different final voltage signals than applying one readout pulse at a time and doing two experiments.

APPENDIX H: MATLAB SCRIPT QIPGATES.M

This is a Matlab script which defines quantities useful for computing what you should obtain theoretically in this experiment. The theory describes the experiment extremely well, so what you obtain with matlab is what you can obtain in the experiment.

```
%
% File:   qipgates.m
% Date:   26-Feb-03
% Author: I. Chuang <ichuang@mit.edu>
%
% Standard QC gates; with proper sign convention to be
% consistent with MIT Junior Lab quantum information processing labguide

global hadamard cnot cphase sx sy sz si rx ry rz N zz xx yy

%%%%%%%%%%%%%%%%%%%%%%%%%%%%%%%%%%%%%%%%%%%%%%%%%%%%%%%%%%%%%%%%%%%%%%%%%%%%%%%
% pauli matrices

sx = [0 1; 1 0];
sy = [0 -i; i 0];
sz = [1 0; 0 -1];
si = [1 0; 0 1];

pauli = {sx,sy,sz};
```

```
%%%%%%%%%%%%%%%%%%%%%%%%%%%%%%%%%%%%%%%%%%%%%%%%%%%%%%%%%%%%%%%%%%%%%%%%%%%%
% two-qubit interaction terms

zz = kron(sz,sz);
xx = kron(sx,sx);
yy = kron(sy,sy);
zi = kron(sz,si);
iz = kron(si,sz);
ii = kron(si,si);

%%%%%%%%%%%%%%%%%%%%%%%%%%%%%%%%%%%%%%%%%%%%%%%%%%%%%%%%%%%%%%%%%%%%%%%%%%%%
% single qubit rotations (acting on 1 qubit: 2x2 unitaries)

rx = expm(-i*pi/4*sx);
ry = expm(-i*pi/4*sy);
rz = expm(-i*pi/4*sz);


%%%%%%%%%%%%%%%%%%%%%%%%%%%%%%%%%%%%%%%%%%%%%%%%%%%%%%%%%%%%%%%%%%%%%%%%%%%%
% single qubit rotations (acting on 1 of 2 qubits: 4x4 unitaries)

rx1 = kron(si,rx);
rx2 = kron(rx,si);
ry1 = kron(si,ry);
ry2 = kron(ry,si);
rz1 = kron(si,rz);
rz2 = kron(rz,si);

%%%%%%%%%%%%%%%%%%%%%%%%%%%%%%%%%%%%%%%%%%%%%%%%%%%%%%%%%%%%%%%%%%%%%%%%%%%%
% one-qubit computational basis states

psi0 = [1 ; 0];
psi1 = [0 ; 1];

%%%%%%%%%%%%%%%%%%%%%%%%%%%%%%%%%%%%%%%%%%%%%%%%%%%%%%%%%%%%%%%%%%%%%%%%%%%%
% two-qubit computational basis states

psi00 = kron(psi0,psi0);
psi01 = kron(psi0,psi1);
psi10 = kron(psi1,psi0);
psi11 = kron(psi1,psi1);

%%%%%%%%%%%%%%%%%%%%%%%%%%%%%%%%%%%%%%%%%%%%%%%%%%%%%%%%%%%%%%%%%%%%%%%%%%%%
% two-qubit Hamiltonian (for CHCl3) & coupled evolution gate

ham = zz;
tau = expm(-i*pi/4*zz);

%%%%%%%%%%%%%%%%%%%%%%%%%%%%%%%%%%%%%%%%%%%%%%%%%%%%%%%%%%%%%%%%%%%%%%%%%%%%
% standard ideal quantum logic gates

hadamard = [1 1 ; 1 -1]/sqrt(2);
cnot = [1 0 0 0 ; 0 1 0 0 ; 0 0 0 1 ; 0 0 1 0];
cphase = [1 0 0 0 ; 0 1 0 0 ; 0 0 1 0 ; 0 0 0 -1];
```

```
%%%%%%%%%%%%%%%%%%%%%%%%%%%%%%%%%%%%%%%%%%%%%%%%%%%%%%%%%%%%%%%%%%%%%%%%%%%%
% Example: near-controlled-not

Uncnot = ry1' * tau * rx1;

%%%%%%%%%%%%%%%%%%%%%%%%%%%%%%%%%%%%%%%%%%%%%%%%%%%%%%%%%%%%%%%%%%%%%%%%%%%%
% Example: effect of Uncnot on thermal state density matrix

rho_therm = [5 0 0 0; 0 3 0 0; 0 0 -3 0; 0 0 0 -5];
rho_out = Uncnot * rho_therm * Uncnot';

%%%%%%%%%%%%%%%%%%%%%%%%%%%%%%%%%%%%%%%%%%%%%%%%%%%%%%%%%%%%%%%%%%%%%%%%%%%%
% Example: Deutsch-Jozsa

Uf1 = [ 1 0 0 0 ; 0 1 0 0 ; 0 0 1 0 ; 0 0 0 1 ];
Uf2 = [ 0 1 0 0 ; 1 0 0 0 ; 0 0 0 1 ; 0 0 1 0 ];
Uf3 = [ 1 0 0 0 ; 0 1 0 0 ; 0 0 0 1 ; 0 0 1 0 ];
Uf4 = [ 0 1 0 0 ; 1 0 0 0 ; 0 0 1 0 ; 0 0 0 1 ];

Udj1 = ry2' * ry1 * Uf1 * ry2 * ry1';
Udj2 = ry2' * ry1 * Uf2 * ry2 * ry1';
Udj3 = ry2' * ry1 * Uf3 * ry2 * ry1';
Udj4 = ry2' * ry1 * Uf4 * ry2 * ry1';

Out1 = Udj1 * psi00;
Out2 = Udj2 * psi00;
Out3 = Udj3 * psi00;
Out4 = Udj4 * psi00;
```